ABSTRACT

Title of dissertation: EXAMINING QUINONE CONTRIBUTION TO THE OPTICAL PROPERTIES OF CHROMOPHORIC DISSOLVED ORGANIC MATTER

Rachel Ashmore, Doctor of Philosophy, 2024

Dissertation directed by: Dr. Neil V. Blough
University of Maryland Department of Chemistry

Chromophoric Dissolved Organic Matter (CDOM) in natural waters is largely responsible for absorption of light and photochemistry in the water, impacting environmental reactions and aquatic life. The composition of CDOM is greatly varied based on source, photochemical reactions, and natural cycles. The impact of quinone moieties on this structure and photochemical and redox reactions involving CDOM remains the subject of controversy. To investigate the impact of quinone structure on optical properties, model quinone compounds were thoroughly characterized by their optical properties and reactions with sodium dithionite and sodium sulfite. A series of methyl-substituted *p*-benzoquinones, a methoxy *p*-benzoquinone, and a range of napthoquinones and anthraquinones were investigated. These model compounds were characterized according to their quinone and hydroquinone molar absorptivities and fluorescence quantum yields. Sodium dithionite reduction of quinones and the impact of structure on the products of this reaction was investigated by reducing the quinones with both sodium dithionite and sodium sulfite and comparing the optical properties of the products to those of the quinone and hydroquinone. The spectra of

dithionite reduced *p*-benzoquinones and napthoquinones suggested the presence of products other than the hydroquinone. Sulfite is produced in solution as a result of dithionite reduction of quinones. Model quinones were therefore also reduced with sodium sulfite to investigate the impact of this side reaction on the dithionite reduction products. High performance liquid chromatography (HPLC) was used to further investigate and quantify the products of dithionite reduction of quinones and the importance of sulfite interference. Although some of the model quinones react with sulfite to form a proposed sulfonated hydroquinone product, based on the observed extent of this reaction in dithionite reductions, the structures of quinones likely to be found in CDOM, and their relatively small contribution to CDOM optical properties, the sulfite reaction was determined to not significantly impact the study of quinone moieties in CDOM.

Dithionite selectively reduces quinones, while borohydride reduces ketones, aldehydes, and quinones. Therefore, in CDOM samples, dithionite can be used to isolate the effects of quinone moieties on the optical properties. Dithionite reduction was used to analyse CDOM standards and natural water extracts from the North Pacific Ocean and the Chesapeake Bay to investigate quinone contribution to their optical properties. These results are compared to borohydride reduction results from Cartisano and McDonnell to compare the contribution of quinones to that of ketones and aldehydes. (*1*, *2*) Dithionite reduction showed small impacts on absorbance and fluorescence, whereas significant changes in both were observed for borohydride reduction. Therefore, the optical changes observed under borohydride reduction are attributed to primarily ketones and aldehydes rather than quinones. Model quinones showed significant changes in fluorescence intensity due to dithionite reduction, which are largely not observed for CDOM standards and natural water extracts, further supporting the conclusion that their role in CDOM optical properties is small.

EXAMINING QUINONE CONTRIBUTION TO THE OPTICAL PROPERTIES OF CHROMOPHORIC DISSOLVED ORGANIC MATTER

by

Rachel Ashmore

Dissertation submitted to the Faculty of the Graduate School of the
University of Maryland, College Park in partial fulfillment
of the requirements for the degree of
Doctor of Philosophy
2024

Advisory Committee:
Dr. Neil V. Blough, Chair/Advisor
Dr. Akua Asa-Awuku
Dr. Sang Bok Lee
Dr. Alice Mignerey
Dr. Amy Mullin

© Copyright by
Rachel Ashmore
2024

Acknowledgments

When I think about all of the people who have loved and supported me on this journey, I don't know how I can possibly thank you all. Of course, I'd like to thank Dr. Neil Blough for all of your guidance, encouragement, science arguments, and mentorship over the last 7 years. I would not be the scientist or the person I am today without you and for that I will be forever grateful. This work would not have been possible without the work of Dr. Rossana Del Vecchio, Dr. Carmen Cartisano, and Dr. Shannon McDonnell. I would be remiss if I did not also thank Jaden Force and Mari Suzuki for their contributions. I'd like to thank my committee members, Dr. Akua Asa-Awuku, Dr. Sang Bok Lee, Dr. Alice Mignerey, and Dr. Amy Mullin for your support and guidance throughout this process.

I am also incredibly thankful to have worked with Dr. Jason Khan and Professor Natalia White in addition to Dr. Blough as a teaching assistant throughout my graduate career. All of you have shaped the teacher I have become. Special thanks to Natalia White and Dr. Gili Marbach-Ad for their support and participation in my work toward the University Teaching and Learning Center Scholar Program completion.

I'd like to thank previous group members Dr. Danielle Le Roux, Dr. Shannon McDonnell, and Dr. Marla Bianca for their friendship and support throughout my time at UMD.

My professors at Millersville University also deserve my thanks and appreciation for encouraging me to go to graduate school in the first place and preparing me for this experience. I could not be more grateful for the education and mentorship I received, especially from Dr. Edward Rajaseelan and Dr. Michael S. Elioff.

On a more personal note, I'd like to thank God for always working things out in the end and walking with me on this road of life (and sometimes dragging me along). I'd like to thank all of my family and friends for their love and support throughout not just graduate school, but always. It means more than you know.

I'd especially like to thank my best friend, Diandra Soemardi. Thank you for putting up with my highs and lows and especially my really lows. I genuinely do not think I could have done this without you. A piece of my heart is always with you across the globe.

Finally and most importantly of all, I owe everything I am and everything I've done to my mom, Lynette Ashmore. I *know* I couldn't have done this without you. From day 1 you have been my strongest supporter, my biggest cheerleader, my safe place, and my favorite person in the world. Thank you for every heart-to-heart, every sacrifice, and every "I'm proud of you". Thank you for always expecting my best, and for being there for me at my worst. Love you forever.

Front Matter

0.1 List of Acronyms

DOM Dissolved Organic Matter

POM Particulate Organic Matter

CDOM Chromophoric Dissolved Organic Matter

UV ultra-violet

HS Humic Substances

HA Humic Acids

FA Fulvic Acids

IHSS International Humic Substances Society

ESHA Elliot Soil Humic Acid

LHA Leonardite Humic Acid

PLFA Pony Lake Fulvic Acid

SRHA Suwanee River Humic Acid

SRFA Suwanee River Fulvic Acid

SRNOM Suwanee River Natural Organic Matter

LAC Lignin, alkali, carboxylated

SPE solid phase extraction

SEC Size-Exclusion Chromatography

NMR nuclear magnetic resonance

ESI-MS electrospray ionisation mass spectrometry

FTIR Fourier-transform infrared spectroscopy

QSE quinine sulfate equivalents

ROS Reactive Oxygen Species

DIC Dissolved Inorganic Carbon

NOM Natural Organic Matter

EAC electron accepting capacity

DER direct electrochemical reduction

MER mediated electrochemical reduction

MEO mediated electrochemical oxidation

ECC electron-carrying capacity

HPLC High Performance Liquid Chromatography

0.2 List of Figures

1.1 CDOM Production and Consumption. Adapted from (*8*) CDOM may enter waters through atmospheric deposition, runoff from terrestrial sources, sediment release, and microbial production. It may be removed from the system by photobleaching, carbon/nitrogen/phosphorous cycling, greenhouse gas release, and microbial decomposition. 2

1.2 Components of a whole water sample and the processes used to separate them. Adapted from (*2*). The whole water sample is first filtered to remove particulate matter. The sample is then extracted on a C18 column to collect the DOM, while salts pass through. The organic material retained on the column is eluted with methanol, then the methanol is evaporated off to leave the organic matter collected as a solid. This is redissolved into a small amount of ultrapure water. This yield a highly concentrated CDOM extract that is then studied. 6

1.3 (Left) Absorbance of 5.42 mg/L LHA (Right) Fluorescence Emission Spectra at increasing excitation wavelength (Right) for 0.87 mg/L LHA 7

1.4 Charge transfer model of individual chromophores and charge transfer interactions combining to form the absorption spectra of CDOM. Adapted from Cartisano 2019(*1*) 9

1.5 Quinone, Semiquinone, and Hydroquinone (*76*) 13

1.6 Products of reduction of ketones, alde hydes, and quinones with sodium borohydride and sodium dithionite under anoxic conditions and products of subsequent aeration.(*48*) R = organic structure for ketones and aldehydes, R = H, or organic structure for quinones. Rs may differ from each other within a structure. 16

1.7 Absorption Spectra of LHA (black), Dithionite added to a mQ water blank (blue), and Dithionite added to the LHA sample (red) 17

1.8 Quinone content found by Del Vecchio et al. (bars) using dithionite reduction compared to Aeschbacker et al. based on electrochemical measurement (stars) (*48*) 19

1.9 DER, MER, and MEO set up in (*101*) 20

2.1 Model Quinones Studied 24

2.2 Absorption and fluorescence spectra for *p*-benzoquinone and methyl-*p*-benzoquinone. *p*-benzoquinone and methyl-*p*-benzoquinone fluorescence is 5-point smoothed. 30
2.3 Absorption and fluorescence spectra for 2,5-dimethyl-*p*-benzoquinone and 2,6-dimethyl-*p*-benzoquinone. 2,5-dimethyl-*p*-benzoquinone and 2,6-dimethyl-*p*-benzoquinone fluorescence is 5-point smoothed. 32
2.4 Absorption and fluorescence spectra for 2,3-dimethyl-*p*-benzoquinone and trimethyl-*p*-benzoquinone. 2,3-dimethyl-*p*-benzoquinone and trimethyl-*p*-benzoquinone fluorescence is 5-point smoothed. 33
2.5 Absorption and fluorescence spectra for duroquinone and 2,3-dimethoxy-5-methyl-*p*-benzoquinone. Duroquinone and 2,3-dimethoxy-5-methyl-*p*-benzoquinone fluorescence is 5-point smoothed. 34
2.6 Absorption and fluorescence spectra for naphthoquinones 37
2.7 Absorption and fluorescence spectra for anthraquinones 38

3.1 Mechanism of the reduction of carbonyl functional group with hydroquinone demonstrating the release of two molecules of SO_2 (*97*) 42
3.2 Mechanism of sulfite addition to quinone molecule. 43
3.3 UV-Visible spectrum of potassium ferricyanide used for dithionite quantification. 47
3.4 UV-Visible Spectra for *p*-benzoquinone, methyl-*p*-benzoquinone, 2,3-dimethyl-*p*-benzoquinone, and 2,5-dimethyl-*p*-benzoquinone. Quinone spectra is shown in black, hydroquinone spectra is shown in blue, substoichiometric dithionite reduced spectra is shown in red dashed line, and excess sulfite reduced spectra is shown in solid red line. 54
3.5 UV-Visible Spectra for 2,6-dimethyl-*p*-benzoquinone, trimethyl-*p*-benzoquinone, duroquinone, and 2,3-dimethoxy-5-methyl-*p*-benzoquinone. Quinone spectra is shown in black, hydroquinone spectra is shown in blue, substoichiometric dithionite reduced spectra is shown in red dashed line, and excess sulfite reduced spectra is shown in solid red line. 55
3.6 UV-Visible Spectra for naphthoquinone, juglone, and 5,8-dihydroxy-1,4-naphthoquinone. Quinone spectra is shown in black, hydroquinone spectra is shown in blue, substoichiometric dithionite reduced spectra is shown in red dashed line, and excess sulfite reduced spectra is shown in solid red line. 56
3.7 UV-Visible Spectra for anthraquinone-1,5-disulfonic acid and anthraquinone-2,6-disulfonic acid. Quinone spectra is shown in black, hydroquinone spectra is shown in blue, substoichiometric dithionite reduced spectra is shown in red dashed line, and excess sulfite reduced spectra is shown in solid red line. 56
3.8 Hydroquinone (blue) and dithionite reduced (green) spectra for 2,5-dimethyl-*p*-benzoquinone, 2,6-dimethyl-*p*-benzoquinone, 2,3-dimethyl-*p*-benzoquinone, and trimethyl-*p*-benzoquinone. 59

3.9 Hydroquinone (blue) and dithionite reduced (green) spectra for juglone, and 5,8-dihydroxy-1,4-naphthoquinone 60
3.10 Example Chromatagraph (Duroquinone) highlighting peaks used for calculations. 61

4.1 Location of NPO sample site. Figure is from Bianca 2020(*32*) with arrow and label added for clarity. 68
4.2 Chesapeake Bay area sample sites.(*2*) 70
4.3 [Left] Absorption spectra of CDOM standards normalized to their absorbance at 350 nm [Right] The log of the normalized absorbances of the CDOM standards. 73
4.4 Log of normalized absorbance and change due to reduction for untreated and dithionite reduced ESHA, LHA, and LAC 75
4.5 og of normalized absorbance and change due to reduction for untreated and dithionite reduced PLFA, SRFA, and SRHA 76
4.6 Log of normalized absorbance and change due to reduction for untreated and dithionite reduced SRNOM 77
4.7 (Right) Fluorescence in QSE scaled to absorbance at 240 nm for ESHA, LHA, and LAC (Left) Change in Fluorescence in QSE scaled to absorbance at 240 nm due to dithionite reduction for ESHA, LHA, and LAC. Fluorescence spectra were obtained using excitation wavelengths from 240-600 in 20nm increments and collecting the emission spectra from 290-800nm. . . . 78
4.8 (Right) Fluorescence in QSE scaled to absorbance at 240 nm for PLFA, SRFA, and SRHA (Left) Change in Fluorescence in QSE scaled to absorbance at 240 nm due to dithionite reduction for PLFA, SRFA, and SRHA. Fluorescence spectra were obtained using excitation wavelengths from 240-600 in 20nm increments and collecting the emission spectra from 290-800nm. 79
4.9 (Right) Fluorescence in QSE scaled to absorbance at 240 nm for SRNOM (Left) Change in Fluorescence in QSE scaled to absorbance at 240 nm due to dithionite reduction for SRNOM. Fluorescence spectra were obtained using excitation wavelengths from 240-600 in 20nm increments and collecting the emission spectra from 290-800nm. 80
4.10 (Left) Absorbance normalized to 350 nm for NPO samples with increasing depth (Right) Log of the normalized absorbance of NPO samples with increasing depth 81
4.11 (Left) Log of Absorbance normalized to 350 for untreated and dithionite reduced NPO surface, 500 m, and 600 m samples. (Right) Change in log of absorbance normalized to 350 nm for NPO surface, 500, and 600 m . . . 82
4.12 (Left) Log of Absorbance normalized to 350 for untreated and dithionite reduced NPO 800, 1000, and 1500 m samples. (Right) Change in log of absorbance normalized to 350 nm for NPO 800, 1000, and 1500 m samples 83

4.13 (Left) Log of Absorbance normalized to 350 for untreated and dithionite reduced NPO 800, 1000, and 1500 m samples. (Right) Change in log of absorbance normalized to 350 nm for NPO 2500, 3500, and 4500 m samples 84
4.14 (Left) Fluorescence intensity normalized to the absorbance at 240 for the untreated sample, shown for untreated and dithionite reduced NPO surface, 500 m, and 600 m samples. (Right) Change in this fluorescence value due to dithionite reduction for NPO surface, 500, and 600 m samples. Fluorescence spectra were obtained using excitation wavelengths from 240-600 in 20nm increments and collecting the emission spectra from 290-800nm. . . . 85
4.15 (Left) Fluorescence intensity normalized to the absorbance at 240 for the untreated sample, shown for untreated and dithionite reduced NPO 800, 1000, and 1500 m samples. (Right) Change in this fluorescence value due to dithionite reduction for NPO 800, 1000, and 1500 m samples. Fluorescence spectra were obtained using excitation wavelengths from 240-600 in 20nm increments and collecting the emission spectra from 290-800nm. 86
4.16 (Left) Fluorescence intensity normalized to the absorbance at 240 for the untreated sample, shown for untreated and dithionite reduced NPO 2500, 3500, and 4500 m samples. (Right) Change in this fluorescence value due to dithionite reduction for NPO 2500, 35000, and 4500 m samples. Fluorescence spectra were obtained using excitation wavelengths from 240-600 in 20nm increments and collecting the emission spectra from 290-800nm. . 87
4.17 (Left) Absorbance normalized to 350 nm for Chesapeake Bay samples with increasing depth (Right) Log of the normalized absorbance of Chesapeake Bay samples with increasing depth 88
4.18 (Left) Log of Absorbance normalized to 350 for untreated and dithionite reduced Susquehanna River, Sassafras River, and Patapsco River samples. (Right) Change in log of absorbance normalized to 350 nm for Susquehanna River, Sassafras River, and Patapsco River samples 89
4.19 (Left) Log of Absorbance normalized to 350 for untreated and dithionite reduced Mid Bay, Severn River, and South River 2020 samples. (Right) Change in log of absorbance normalized to 350 nm for Mid Bay, Severn River, and South River 2020 samples. 90
4.20 (Left) Log of Absorbance normalized to 350 for untreated and dithionite reduced South River 2021, Harris Creek, and Miles River samples. (Right) Change in log of absorbance normalized to 350 nm for South River 2021, Harris Creek, and Miles River samples. 91
4.21 (Left) Log of Absorbance normalized to 350 for untreated and dithionite reduced Tred Avon River samples from October 2020, November 2020, and 2021. (Right) Change in log of absorbance normalized to 350 nm for Tred Avon River samples from October 2020, November 2020, and 2021. . 92

4.22 Log of Absorbance normalized to 350 for untreated and dithionite reduced Choptank River, Patuxant River, and York River samples. (Right) Change in log of absorbance normalized to 350 nm for Choptank River, Patuxant River, and York River samples 93
4.23 (Left) Fluorescence intensity normalized to the absorbance at 240 for the untreated sample, shown for untreated and dithionite reduced Susquehanna River, Sassafras River, and Patapsco River samples. (Right) Change in this fluorescence value due to dithionite reduction for Susquehanna River, Sassafras River, and Patapsco River samples. Fluorescence spectra were obtained using excitation wavelengths from 240-600 in 20nm increments and collecting the emission spectra from 290-800nm. 94
4.24 (Left) Fluorescence intensity normalized to the absorbance at 240 for the untreated sample, shown for untreated and dithionite reduced Mid Bay, Severn River, and South River 2020 samples. (Right) Change in this fluorescence value due to dithionite reduction for Mid Bay, Severn River, and South River 2020 samples. Fluorescence spectra were obtained using excitation wavelengths from 240-600 in 20nm increments and collecting the emission spectra from 290-800nm. 95
4.25 (Left) Fluorescence intensity normalized to the absorbance at 240 for the untreated sample, shown for untreated and dithionite reduced South River 2021, Harris Creek, and Miles River samples. (Right) Change in this fluorescence value due to dithionite reduction for South River 2021, Harris Creek, and Miles River samples. Fluorescence spectra were obtained using excitation wavelengths from 240-600 in 20nm increments and collecting the emission spectra from 290-800nm. 96
4.26 (Left) Fluorescence intensity normalized to the absorbance at 240 for the untreated sample, shown for untreated and dithionite reduced Tred Avon River samples from October 2020, November 2020, and 2021. (Right) Change in this fluorescence value due to dithionite reduction for Tred Avon River samples from October 2020, November 2020, and 2021. Fluorescence spectra were obtained using excitation wavelengths from 240-600 in 20nm increments and collecting the emission spectra from 290-800nm. . . . 97
4.27 (Left) Fluorescence intensity normalized to the absorbance at 240 for the untreated sample, shown for untreated and dithionite reduced Choptank River, Patuxent River, and York River samples. (Right) Change in this fluorescence value due to dithionite reduction for Choptank River, Patuxent River, and York River samples. Fluorescence spectra were obtained using excitation wavelengths from 240-600 in 20nm increments and collecting the emission spectra from 290-800nm. 98

1 Preliminary results from replicating the work of Del Vecchio et. al. (*48*) . . 109
2 Calibration curve concentrations and representative spectra for *para*-benzoquinone. 110

3 Calibration curve concentrations and representative spectra for methyl-*para*-benzoquinone. 111
4 Calibration curve concentrations and representative spectra for 2,3-dimethyl-*para*-benzoquinone. 111
5 Calibration curve concentrations and representative spectra for 2,5-dimethyl-*para*-benzoquinone. 112
6 Calibration curve concentrations and representative spectra for 2,6-dimethyl-*para*-benzoquinone. 112
7 Calibration curve concentrations and representative spectra for trimethyl-*para*-benzoquinone. 113
8 Calibration curve concentrations and representative spectra for duroquinone. 113
9 Calibration curve concentrations and representative spectra for 2,3-dimethoxy-5-mehtyl-*para*-benzoquinone. 114
10 Calibration curve concentrations and representative spectra for naphthoquinone. 114
11 Calibration curve concentrations and representative spectra for juglone . . . 115
12 Calibration curve concentrations and representative spectra for 5,8-dihydroxynapthoquinone 115
13 Calibration curve concentrations and representative spectra for anthraquinone-1,5-disulfonic acid. 116
14 Calibration curve concentrations and representative spectra for anthraquinone-2,6-disulfonic acid. 116
15 Absorption spectra for (Left) dithionite additions to a mQ blank and (Right) dithionite additions to a sample of potassium ferricyanide. 117
16 Absorption spectra of ferricyanide and ferrocyanide produced by dithionite reduction of ferricyanide. A line is placed at 420 nm to emphasize that only the ferricyanide absorbs at this wavelength. 118
17 Blank subtracted dithionite fluorescence intensity presented as obtained. . . 119
18 HPLC chromatographs of 2,3-dimethyl-*p*-benzoquinone, 2,3-dimethyl-*p*-benzohydroquinone, and dithionite reduced 2,3-dimethyl-*p*-benzoquinone. Quinone peak is highlighted by black box. Hydroquinone peak is highlighted by red box. 120
19 HPLC chromatographs of 2,5-dimethyl-*p*-benzoquinone, 2,5-dimethyl-*p*-benzohydroquinone, and dithionite reduced 2,5-dimethyl-*p*-benzoquinone. Quinone peak is highlighted by black box. Hydroquinone peak is highlighted by red box. 121
20 HPLC chromatographs of 2,6-dimethyl-*p*-benzoquinone, 2,6-dimethyl-*p*-benzohydroquinone, and dithionite reduced 2,6-dimethyl-*p*-benzoquinone. Quinone peak is highlighted by black box. Hydroquinone peak is highlighted by red box. 122

21 HPLC chromatographs of trimethyl-*p*-benzoquinone, trimethyl-*p*-benzohydroquinone, and dithionite reduced trimethyl-*p*-benzoquinone. Quinone peak is highlighted by black box. Hydroquinone peak is highlighted by red box. 123
22 HPLC chromatographs of duroquinone, durohydrquinone, and dithionite reduced duroquinone. Quinone peak is highlighted by black box. Hydroquinone peak is highlighted by red box. 124
23 HPLC chromatographs of 1,4-naphtoquinone, naphthohydroquinone, and dithionite reduced 1,4-naphthoquinone. Quinone peak is highlighted by black box. Hydroquinone peak is highlighted by red box. 125
24 HPLC chromatographs of juglone, hydroxyjuglone, and dithionite reduced juglone. Quinone peak is highlighted by black box. Hydroquinone peak is highlighted by red box. 126
25 HPLC chromatographs of 5,8-dihydroxy-1,4-naphthoquinone, naphthalene-1,4,5,8-tetraol, and dithionite reduced 5,8-dihydroxy-1,4-naphthoquinone. Quinone peak is highlighted by black box. Hydroquinone peak is highlighted by red box. 127
26 HPLC Chromatagraph of 2,3-dimethyl-*p*-benzoquinone 128
27 HPLC Chromatagraph of 2,3-dimethyl-*p*-benzohydroquinone 129
28 HPLC Chromatagraph of 2,3-dimethyl-*p*-benzoquinone reduced with excess dithionite 130
29 HPLC Chromatagraph of 2,3-dimethyl-*p*-benzoquinone for dithionite titration 131
30 HPLC Chromatagraph of 2,3-dimethyl-*p*-benzoquinone following dithionite titration 132
31 HPLC Chromatagraph of duroquinone 133
32 HPLC Chromatagraph of durohydroquinone 134
33 HPLC Chromatagraph of duroquinone for dithionite titration 134
34 HPLC Chromatagraph of duroquinone following dithionite titration 135
35 2,3 and 2,5-dimethyl*p*-benzoquinone over time with substoichiometric sulfite addition. Quinone, hydroquinone, and excess sulfite spectra are shown for reference as dotted lines. 137
36 2,6 and trimethyl*p*-benzoquinone over time with substoichiometric sulfite addition. Quinone, hydroquinone, and excess sulfite spectra are shown for reference as dotted lines. 138
37 Duroquinone and napthoquinone over time with substoichiometric sulfite addition. Quinone, hydroquinone, and excess sulfite spectra are shown for reference as dotted lines. 139
38 Juglone and anthraquinone-1,5-disulfonic acid over time with substoichiometric sulfite addition. Quinone, hydroquinone, and excess sulfite spectra are shown for reference as dotted lines. 140
39 Absorption spectra of 2-acetylnaphthone with dithionite 142
40 Absorption spectra of 4-hydroxybenzaldehyde with dithionite 143

0.3 List of Tables

2.1 Molar absorptivity at major wavelengths and fluorescence quantum yields for methyl-substituted range of quinones. Quantum yield values given as $<$ indicate that fluorescence emission is indistinguishable from zero under the experimental conditions. 35
2.2 Molar absorptivity at major wavelengths and fluorescence quantum yields for polycyclic range of quinones. 39

3.1 Stoichiometry of quinone disappearance and hydroquinone appearance for model quinone samples. 64

4.1 Estimated quinone content in CDOM standards, compared to Del Vecchio et. al. (*48*) and Aeschbacher et. al. (*101*) 100
4.2 Estimated quinone content for NPO samples, scaled to match the absorbance of 100 mg/L LAC 101
4.3 Estimated quinone content for Chesapeake Bay samples, scaled to match the absorbance of 100 mg/L LAC 103

A.1 Stoichiometry of reduction of quinones by sulfite, based on disappearance of quinone absorbance peak and sulfite concentration calculated from mass and volume. 141

Table of Contents

Acknowledgements ii
0.1 List of Acronyms . . . iv
0.2 List of Figures . . . vi
0.3 List of Tables . . . xiii

1 Introduction 1
1.1 Chromophoric Dissolved Organic Matter (CDOM) Origins and Importance 1
1.1.1 CDOM Definition . . . 1
1.1.2 Lignin and Humic Substances . . . 3
1.1.3 CDOM Reference Standards . . . 4
1.1.4 CDOM analysis . . . 5
1.2 Environmental Impact of CDOM and Role of Quinone Moieties . . . 12
1.2.1 Aquatic Photochemistry . . . 12
1.2.2 Redox Interactions . . . 14
1.3 Quinones in CDOM - Quantification . . . 15
1.3.1 Contribution of Quinones to the Optical Properties of HS . . . 15
1.3.2 Electrochemical Analysis . . . 18
1.4 Description of Thesis . . . 20

2 Model Quinone Characterization 22
2.1 Introduction . . . 22
2.2 Materials and Methods . . . 25
2.2.1 Materials . . . 25
2.2.2 Optical Measurements . . . 25
2.2.3 Molar Absorptivities and Fluorescence Quantum Yields . . . 26
Quinone Stock Preparation . . . 26
UV-Visible Spectra and Molar Absorptivities . . . 27
Fluorescence Spectra and Quantum yields . . . 27
2.2.4 Calculations . . . 29
2.3 Results and Discussion . . . 29
2.3.1 Optics . . . 29

2.4 Conclusion . . . 39

3 Characterization of Optics, Stoichiometry, and Products of Reduction of Model Quinones 41
3.1 Introduction . . . 41
3.1.1 Reduction of Quinones in CDOM by Sodium Dithionite and Sulfite 41
3.1.2 Dithionite quantification . . . 46
3.1.3 Examination of Reduction Products by HPLC . . . 47
3.2 Materials and Methods . . . 48
3.2.1 Materials . . . 48
3.2.2 Optical Measurements . . . 48
HPLC . . . 48
Optical Changes Following Dithionite Reduction . . . 49
3.2.3 Sulfite Reductions . . . 50
3.2.4 Dithionite Reduction HPLC Analysis . . . 50
3.3 Results and Discussion . . . 52
3.3.1 Optics . . . 52
Evidence of sulfonated hydroquinone product . . . 52
3.3.2 Stoichiometry/LC . . . 61
3.4 Conclusions . . . 65

4 Quinone Contribution to Optical Properties of CDOM Standards and Natural Waters 66
4.1 Introduction . . . 66
4.2 Experimental . . . 71
4.2.1 Absorbance Measurements and Quinone quantification . . . 71
4.2.2 Fluorescence Measurements . . . 72
4.3 Results and discussion . . . 73
4.3.1 Influence of quinones on Optical Properties . . . 73
4.3.2 CDOM Standards . . . 73
4.3.3 NPO C-18 Extracts . . . 77
4.3.4 Chesapeake Bay C-18 Extracts . . . 81
4.3.5 Estimated Quinone Content . . . 99
4.4 Conclusions . . . 102

5 Conclusions and Future Work 104
5.1 Summary . . . 104
5.2 Future Directions . . . 106
5.2.1 Model Quinones . . . 106
5.2.2 CDOM Characterization in Lakes and Rivers . . . 107
5.2.3 Photochemical activity of Quinones in CDOM . . . 107

A Supporting Information 108

A.1 Chapter 1 Supplemental 108
A.1.1 Beer's Law 108
A.2 Chapter 2 Supplemental 109
A.2.1 Calibration Curve Concentrations and Representative Spectra 109
A.3 Chapter 3 Supplemental 110
A.3.1 Dithionite Quantification 110
A.3.2 HPLC Chromatographs 117
A.3.3 Comparison of 2,3-dimethyl-*p*-benzoquinone and duroquinone LC chromatographs 117
A.3.4 Quinone-Sulfite Reactions Over Time 136
A.3.5 Sulfite Reduction Stoichiometry 136
A.3.6 *p*-benzoquinone and methyl-*p*-benzoquinone 136
A.4 General Supplemental 141
A.4.1 Ketone and Aldehyde Dithionite Reduction Controls 141

Chapter 1: Introduction

1.1 Chromophoric Dissolved Organic Matter (CDOM) Origins and Importance

1.1.1 CDOM Definition

Aquatic ecosystems, including inland freshwater, marine waters, and estuaries where the two mix, contain Dissolved Organic Matter (DOM) and Particulate Organic Matter (POM), which are collectively referred to as Natural Organic Matter (NOM). The portion of organic matter that we refer to as "dissolved" is that which passes through a very small (0.2-1.0 μm) filter (*3*). The absorbing and emitting portion of DOM over the ultra-violet (UV) and visible wavelengths is called Chromophoric Dissolved Organic Matter (CDOM) or Colored Dissolved Organic Matter.

Organic matter is composed of organic molecules containing carbon, nitrogen, phosphorous, and sulfur(*3*), derived from a range of biomolecules including lignin, proteins, amino acids, and anthropogenic sources of organic compounds. (*4*) Dissolved organic matter, although only a portion of natural organic matter, is the most mobile and active portion of organic matter (*5*). Because it is dissolved, it is easily transported through water systems from the inland lakes and rivers through estuaries and into the ocean. Much of this material is derived from the cycling of carbon in terrestrial environments, but terrestrially produced DOM is partly consumed or degraded by microbes, photochemistry, or absorp-

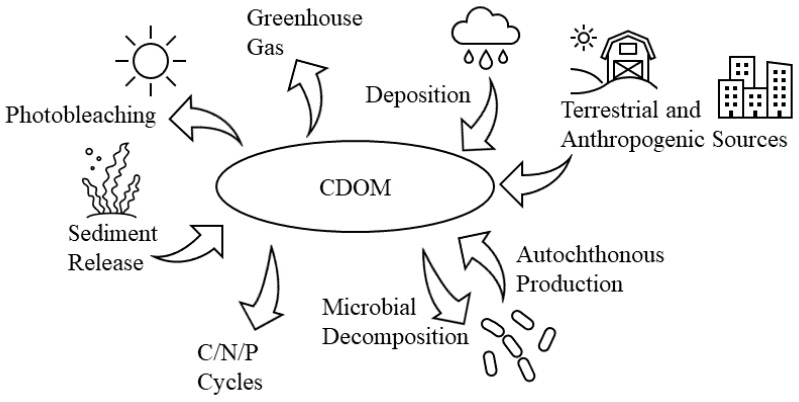


Figure 1.1: CDOM Production and Consumption. Adapted from (*8*) CDOM may enter waters through atmospheric deposition, runoff from terrestrial sources, sediment release, and microbial production. It may be removed from the system by photobleaching, carbon/nitrogen/phosphorous cycling, greenhouse gas release, and microbial decomposition.

tion into soils and sediments during its transportation to the ocean. (*5*) DOM is active in the carbon cycle through respiration by microbes, releasing CO_2 into the atmosphere.(*5*). Marine DOM generally contains smaller molecules from these terrestrial sources, but is also autochthonously produced by microbes, and this fraction greatly impacts its optical properties.(*6*)

CDOM comes from a wide range of sources both autochthonous, meaning produced within the system, and allochthonous, meaning originating from outside the system. (*7*) Autochronous sources of CDOM include decomposition of microorganisms and plants within the system, microbial production, and release from sediments. (*8*) Allochthonous CDOM can enter a system from runoff, groundwater, precipitation, and anthropogenic waste.(*8*) A diagram of these sources and removal processes of CDOM in natural water systems is shown in Figure 1.1.

These different sources impact DOM composition, which impacts its optical properties and reactivity. (*9–12*) More importantly, the reactions that CDOM undergoes in the environment impact its structure and properties. CDOM is consumed as part of the microbial

food chain.(*3*). It also takes part in carbon, nitrogen, and phosphorous cycling in the environment (*3*). A significant portion of CDOM is removed by its photodegradation, releasing smaller molecules and inorganic carbon, especially CO_2. (*3*, *13*) As a result, in areas of greater photochemical activity (i.e. surface waters) CDOM molecular weight is typically lower than in deeper waters as the higher molecular weight CDOM is photodegraded (*14*).

1.1.2 Lignin and Humic Substances

Lignin is a polymer found in plants that gives them structure and rigidity and the ability to transport water and nutrients. (*15*) The degradation products of lignin, along with possibly tannins, are thought to be the main source of CDOM in rivers and estuaries. (*14*, *16*) Anthropogenic impacts on CDOM include changes in land use and inputs from wastewater and agriculture. (*17*)

Lignin, its degradation products, proteins, lipids, nucleic acids, polysaccharides, and other molecules that result from the decomposition of dead plants and microbes form a class of compounds referred to as Humic Substances (HS). (*18*) Humic substances can be defined by 3 fractions: insoluble humin, Humic Acids (HA) which are soluble at pH $<$2, and Fulvic Acids (FA) which are soluble regardless of pH. (*19*) These labels don't necessarily reflect different classes of compounds, merely different functional categories that can be studied.(*19*) Humic substances are an often studied portion of DOM and organic molecules in soils. (*11*, *19–28*)

Understanding of humic substance structure has proved challenging. Reviews by Sutton (*19*) and Piccolo (*22*) in the early 2000's approached the "polymer model" of humic substance structure critically. In this understanding of humic substance structure, they are thought to be large polymeric macromolecules. The alternate view presented is that of weakly associated smaller heterogeneous molecules. (*22*) Supporters of the polymer

model (*29*) argue that Size-Exclusion Chromatography (SEC) results have been insufficient to prove the supramolecular association model, and that the polymer model still best explains experimental results. However, newer results from nuclear magnetic resonance (NMR), electrospray ionisation mass spectrometry (ESI-MS), and Fourier-transform infrared spectroscopy (FTIR) have shown support for the supramolecular model, showing smaller molecular weights that can be attributed to these smaller associated molecules(*19*, *30–32*). However, these methods could also be missing some portions of high molecular weight material that are not easily ionized. (*30*, *32*) This conflict among many in the field of humic substance studies show how complex and difficult it is to fully characterize these species.

1.1.3 CDOM Reference Standards

Because HS are difficult to characterize and incredibly variably in structure, the International Humic Substances Society (IHSS) was formed in 1981. Prior to this, it was nearly impossible to compare work between labs.(*33*) The IHSS collects and processes a number of humic substances which can then be used by researchers around the world to compare their results with each other. (*33*) Since these samples are collected and isolated at the same time and in the same way, it provides a "known" class of CDOM/HS standards so that different labs or the same lab at different times can compare techniques and results on a sample that should give consistent results. Due to the complex nature of CDOM itself, these standards do not have known molecular structures, but they are thoroughly characterized by elemental composition, acidic functional groups, amino acid composition, ^{13}C NMR, ^{1}H NMR, sedimentation rate, FTIR, and fluorescence.(*33*) The standards used in this study are Elliot Soil Humic Acid (ESHA), Leonardite Humic Acid (LHA), Pony Lake Fulvic Acid (PLFA), Suwanee River Humic Acid (SRHA), Suwanee River Fulvic Acid (SRFA), and Suwanee

River Natural Organic Matter (SRNOM). The Suwanee River is in Georgia in an area containing a great deal of peat and decomposing vegetation.(*33*) Elliot soil comes from the prairie lands of the central U.S. in Illinois.(*33*) Leonardite is produced by the oxidation of coal and collected from Gascoyne Mine in North Dakota.(*33*) Pony Lake is a pond in the Antarctic surrounded by no plants, suggesting that all the DOM contained in this sample is due to microbial production in the lake.(*34*)Lignin, alkali, carboxylated (LAC) from Sigma-Aldrich is also studied. These samples represent a wide range of CDOM sources, from plant decay to coal oxidation to microbial production to lignin from wood and bark. This allows an examination of the difference in structure and properties of humic substances from different sources.

1.1.4 CDOM analysis

Figure 1.2 shows the categories of organic matter contained within a whole water sample, and the methods used to separate and study them. As discussed, filtration is used to separate DOM from POM, but when working with a whole water sample, the solution will still contain salts. Additionally, the CDOM is often incredibly dilute, and therefore requires highly sensitive methods to characterize its properties and reactions. By extracting the DOM using solid phase extraction (SPE), the salts can be separated and the CDOM concentrated into a more easily studied concentration. This process, however, can impact the composition of the CDOM itself.(*16*, *35*) Sleighter and Hatcher determined that C18 extraction eliminates aliphatic amines and amides as well as tannin-like compounds due to their ionic and more polar natures, respectively. (*16*) Andrew et al. observed that C18 extraction favored long wavelength absorbing and emitting materials, but the changes in optical properties due to borohydride reduction were comparable for whole water and extracted samples. This suggests that although long-wavelength absorbance may be over

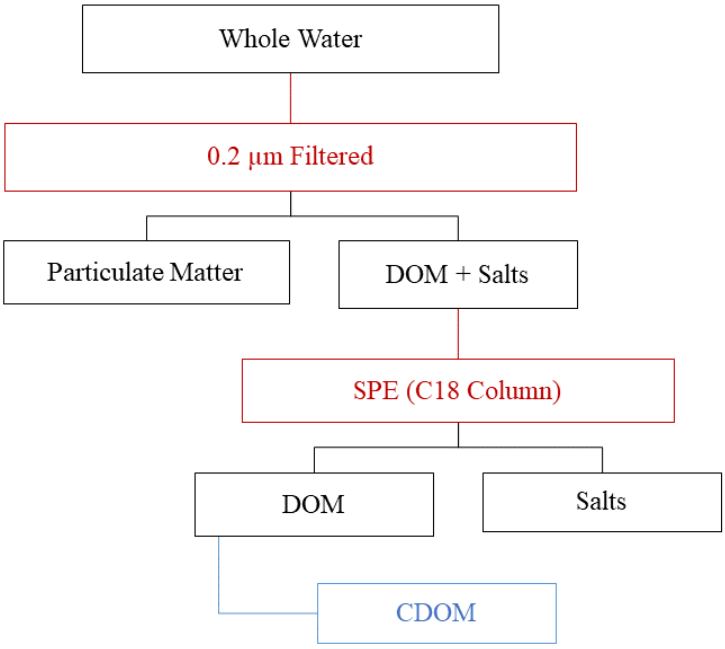


Figure 1.2: Components of a whole water sample and the processes used to separate them. Adapted from (*2*). The whole water sample is first filtered to remove particulate matter. The sample is then extracted on a C18 column to collect the DOM, while salts pass through. The organic material retained on the column is eluted with methanol, then the methanol is evaporated off to leave the organic matter collected as a solid. This is redissolved into a small amount of ultrapure water. This yield a highly concentrated CDOM extract that is then studied.

represented, in general the extracts represent the natural water samples fairly well. (*35*)

CDOM and humic substances are often studied by UV-Visible absorbance and fluorescence spectroscopy (*6*, *11*, *14*, *23–27*, *33*, *36–41*) and by examining the optical properties of these materials, conclusions can be drawn about their structure and activity. CDOM absorbs light in the ground-level solar spectrum over the ultra-violet and visible range. (*42*). The absorption spectra typically resembles an exponential decay in shape, with high absorbance in the UV/near UV region, and low absorbance in the long wavelength range. (*42*).

The fluorescence spectrum of CDOM, like the absorbance, is unstructured. It shows broad emission that shifts to longer wavelengths and lower intensity as excitation wave-

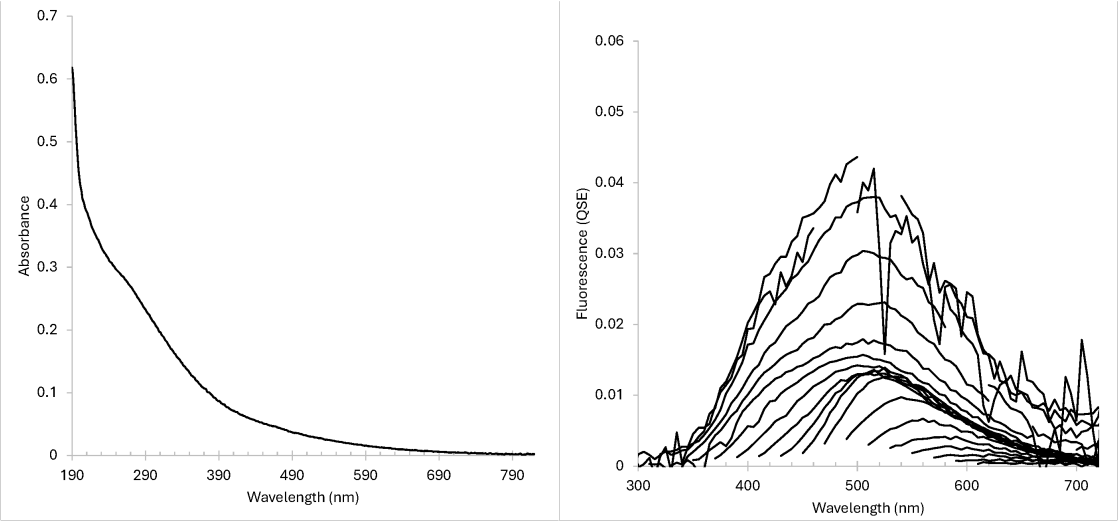


Figure 1.3: (Left) Absorbance of 5.42 mg/L LHA (Right) Fluorescence Emission Spectra at increasing excitation wavelength (Right) for 0.87 mg/L LHA

length increases.(*43*). A sample absorption and fluorescence spectra of LHA is shown in figure 1.3.

Due to the complex nature of CDOM and its variability in different aquatic environments, relating the optical properties of absorption and fluorescent emission to the structure and photochemical properties of CDOM has proven difficult and somewhat controversial. There are two competing models used to try to explain the absorbance and fluorescence properties of CDOM - the superposition model and the electronic interaction model. In the superposition model, the absorption and emission spectra of CDOM is thought to arise from the sum of many individual absorbing and emitting chromophores within the dissolved organic matter sample.(*43*) In the electronic interaction model, the spectra is instead attributed to not only the absorption and emission of its individual chromophores, but also from charge transfer interactions between electron acceptor and donor chromophores within the CDOM.(*43*)

According to the superposition model, a solution containing multiple independently

absorbing and fluorescing species will have an absorbance and fluorescence corresponding to the sum of these individual spectra. Additionally, most organic compounds absorb at wavelengths shorter than 400 nm (the visible spectrum). Conjugated aromatic species and quinones can n $\rightarrow \pi_*$ transitions that occur out into the visible wavelength region, but this absorbance at long wavelength is typically weak. (*32*) However, in cases where the species interact with each other, the spectra will not be the simple sum of components, but also have absorbance and fluorescence resulting from the electronic interactions between the components. These interactions can cause stronger absorbance further into the visible region than the aforementioned conjugated aromatic species or quinones. Thus, the superposition model cannot explain the long wavelength absorption or the complex emission, but these are accounted for in the electronic interaction model.(*11*, *23*, *43–47*) A visual depiction of the charge transfer model is shown in figure 1.4.

The broad, unstructured absorbance at long wavelengths in CDOM supports the electronic interaction model, as does the red-shifting of its fluorescence emission as excitation wavelength increases. In the case of the superposition model, the long wavelength absorbances would be more defined into individual species or absent entirely. The fluorescence shifts implies that the fluorescence of CDOM is not due to distinct species, but a range of species and electronic interactions. (*43*)

Charge transfer results from electron donors and electron acceptors within CDOM.(*11*, *23*, *43*, *46*) Electron donating groups may include phenolic and substituted aromatic carboxylic acid groups, while electron accepting groups include aromatic ketones/aldehydes and quinones.(*48*) The typical regions of absorbance and a theoretical structure of CDOM showing these donors, acceptors, and charge transfer processes is shown in figure 1.4.

Though the electronic interaction model can account for many of the optical and photochemical properties of CDOM, additional studies are needed to better understand the types of individual absorbing and emitting species within CDOM that are responsible for

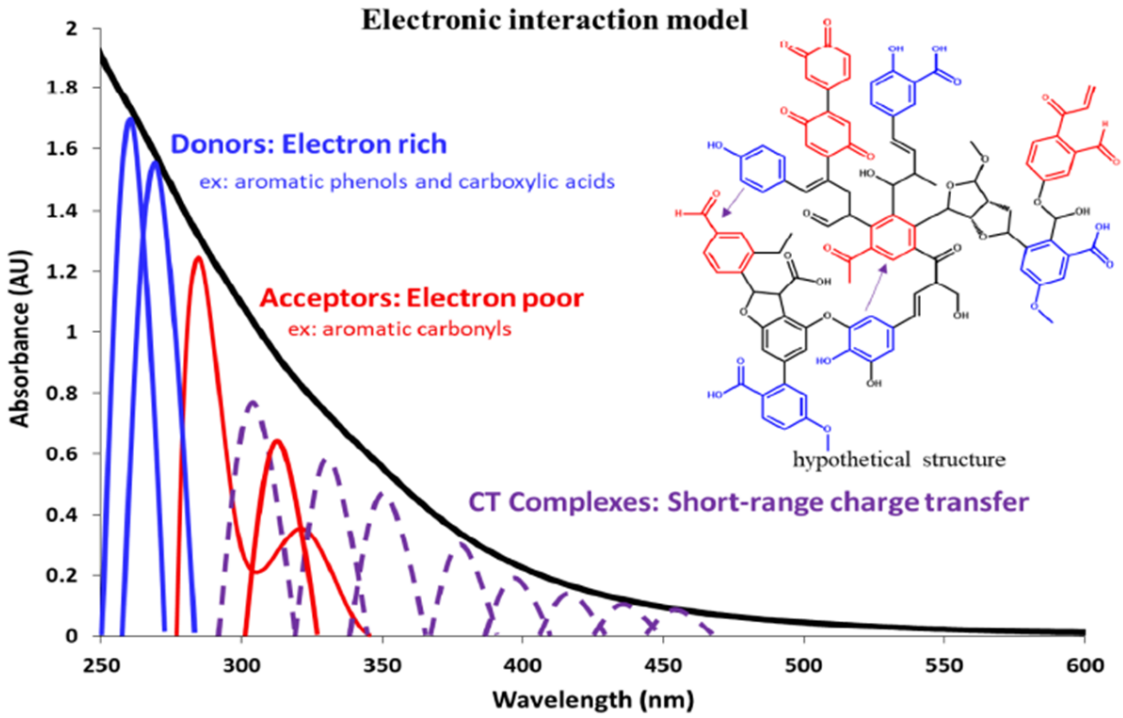


Figure 1.4: Charge transfer model of individual chromophores and charge transfer interactions combining to form the absorption spectra of CDOM. Adapted from Cartisano 2019(*1*)

its unique optical properties.

Beyond simply comparing absorption spectra of CDOM samples, some ratios and relations are applied to compare these spectra quantitatively and draw conclusions about the samples' properties.

Spectral Slope is defined according to equation 1.1, where $a(\lambda) = 2.303A(\lambda)/l$. $A(\lambda)$ is the absorbance of the solution and l is the pathlength of the cell in meters.(*39*) $a(\lambda)$ is the absorption coefficient at wavelength λ, and $a(r)$ is the absorbance at the reference wavelength *r*.

$$a(\lambda) = a(r)e^{S(r-\lambda)} \tag{1.1}$$

The spectral slope coefficient, S, defines the rate of exponential decline of CDOM absorbance with increasing wavelength. (*49*). This parameter is often utilized in studies of CDOM. (*2*, *11*, *13*, *14*, *35*, *36*, *38*, *43*, *49–58*) It has been shown to decrease as molecular weight and aromaticity increase, and to be larger for fulvic acids as compared to humic acids. (*49*, *59*, *60*)

Similarly to spectral slope, the ratio of the absorbance of CDOM at 250 and 365 nm, called the E_2:E_3 ratio (*50*) is used to analyse CDOM samples for molecular size, structure, and DOC. (*21*, *50*, *61*) E_2:E_3, like spectral slope, decreases with molecular size as high molecular weight components of CDOM absorb at longer wavelengths. (*50*) E_2:E_3 is also correlated with aromaticity (*21*).

Both spectral slope and E_2:E_3 are also used to measure changes in CDOM, such as those occurring during photobleaching processes, or to compare differences between CDOM in different samples. (*38*, *55*, *56*)

Fluorescence relationships are also utilized in studies of CDOM. This includes analysis of quantum yields for different samples or for the same sample before and after chemical

reduction and/or photochemical exposure. (*2*, *11*, *12*, *14*, *23*, *35*, *39*, *62*)

Quantum yield is defined as the fluorescence of a substance per absorption unit (*39*). It is calculated by equation 1.2.(*39*)

$$\phi(\lambda) = [FI(\lambda)a_{\mathrm{r}}\phi_{\mathrm{r}}]/[a(\lambda)FI_{\mathrm{r}}] \tag{1.2}$$

As mentioned earlier, $a(\lambda)$ is the absorption coefficient of the sample, in this case at the excitation wavelength. FI is the corrected integrated fluorescence intensity of the fluorescence emission due to excitation at the same excitation wavelength. Likewise, a_r is the absorption coefficient of the reference material at its excitation wavelength, FI_r is the corrected integrated fluorescence intensity of the fluorescence emission of the reference at this excitation wavelength, and ϕ_r is the quantum yield of the reference material at this exciation wavelength. Quinine sulfate is often used as a reference in CDOM fluorescence studies (*11*, *12*, *14*, *23*, *39*, *62*), due to its fluorescence at comparable wavelengths to CDOM(*2*). It is utilized herein as a quantum yield standard. It's ϕ_r is 0.51 in 0.1 N H_2SO_4 using an excitation wavelength of 350 nm. (*39*)

In addition to using quinine sulfate as a reference standard for calculating quantum yields, fluorescence studies of natural waters often scale the emission spectra to quinine sulfate units (*1*, *2*, *13*, *14*, *63*, *64*). Using quinine sulfate units accounts for instrument-specific biases. (*40*)

To put fluorescence spectra into quinine sulfate equivalents (QSE), equation 1.3 was used, where F_{QSE} is the fluorescence intensity of the sample in qse, F_s is the blank subtracted fluorescence intensity of the sample as measured by the instrument, and FI_{QS} is the integrated fluorescence intensity of a sample of 10 ppb quinine sulfate in 0.1 N H_2SO_4

excited at 350 nm, measured the same day as the sample fluorescence.

$$F_{\mathrm{QSE}} = F_{\mathrm{s}}/[FI_{\mathrm{QS}}/10] \tag{1.3}$$

1.2 Environmental Impact of CDOM and Role of Quinone Moieties

1.2.1 Aquatic Photochemistry

The three main roles of CDOM in the environment are: 1) it determines light depth penetration and photochemical reactivity in surface waters 2) facilitates carbon, nitrogen, and phosphorous cycling which supports phytoplankton and bacteria in these environments 3) and a portion of the global carbon pool, which can impact climate change. (*8*)

The absorption of light by CDOM is an important part of the natural water ecosystem. Not only is CDOM the main determinant of the optical properties of the water; it also prevents UV and blue light penetration to deeper waters.(*8*, *43*) Effectively, this largely limits photochemical reactions to surface waters and can protect organisms in the water system from the harmful effects of UV-light. (*8*, *43*, *65*) While CDOM may benefit organisms through this protection, it also photochemically produces reactive oxygen species (ROS) such as hydrogen peroxide, superoxide, singlet dioxygen, the hydroxyl radical, and organic peroxyl radicals. (*66*) Reactive oxygen species may have harmful effects on organisms(*4*, *13*). These reactive oxygen species can harm organisms by reacting with proteins, lipids, and nucleic acids, as well as damaging enzymes and DNA.(*4*). They may also have some positive effects of improving iron uptake and oxidizing manganese oxides, allowing them to play active roles in biogeochemical cycles. (*4*) Exposure to UV radiation also affects CDOM availability as a food source to microorganisms. (*65*, *67*)

Reactive Oxygen Species (ROS) as well as triplet excited states of CDOM formed by exposure to light are involved in several environmental reactions.(*4*, *66*, *68–71*) These

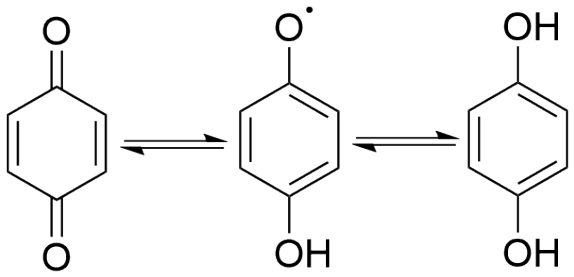


Figure 1.5: Quinone, Semiquinone, and Hydroquinone (*76*)

reactive intermediates act to degrade the CDOM and produce smaller molecules - both smaller molecular weight DOM and inorganic molecular products.(*54*, *68*). This includes producing bioavailable DOM and Dissolved Inorganic Carbon (DIC) (*69*). Photoreaction of CDOM also forms COS, CO, CO_2 gases and volatile organic compounds which can have important atmospheric and environmental impacts. (*13*, *72*). Photochemically excited DOM and the ROS it produces affect contaminant transformation and degradation(*9*, *43*, *73*), trace metal speciation (*65*, *68*, *71*, *74*), and degradation of DOM into lower molecular weight products and inorganic carbon and nitrogen(*10*, *13*, *58*, *65*).

Studies have employed individual quinone compounds as models for the activity of the quinone moieties in CDOM. (*52*, *75*) These studies support the involvement of quinones in some photochemical reactions. Irradiation produced ROS in a fashion consistent with quinones being a photochemically active component of CDOM. (*52*, *75*)

Quinones in CDOM exist in one of three forms – the quinone, the semiquinone radical, and the hydroquinone. (*76*) These quinones can interact with each other and the environment, undergoing charge transfer processes as well as undergo addition reactions with nucleophiles like hydroxide. (*76*)

1.2.2 Redox Interactions

Humic substances act as redox mediators in environmental systems, both as an electron donor and accceptor. (*77–82*) Quinones are thought to be the main moiety involved in electron accepting capacities (EAC) in HS/CDOM(*78–80*, *83–86*), although they may not be the only structure responsible. (*81*, *87*) In terms of electron donating/antioxidant properties, phenolic groups within the HS/CDOM may stabilize the HS/CDOM within the environment and decrease reduction of pollutants by quenching reactive oxygen species and donating electrons to radical intermediates. (*88*)

Redox reactions of HS/CDOM are involved in reduction of metals and organic compounds in the environment. (*81*) These reactions therefore influence the toxicity of these contaminants as well as their breakdown. (*84*, *89*) They affect the speciation, mobility, toxicity, and bioavailability of redox sensitive elements - arsenic, chromium, copper, iron, mercury, and selenium (*77*). NOM redox processes are involved in carbon cycling and microbial interactions (*85*) such as reduction and respiration.

Iron respiration/iron bioreduction contributes to biogeochemical cycling of carbon, oxygen, phosphorous, sulfur, and nitrogen, as well as driving bio-purification of groundwater contaminants. (*90*) There is evidence that quinones play a significant role as electron accepting groups in CDOM, particularly in photochemical and redox reactions in the environment.(*52*, *76*) Quinones not only act as an electron transfer mediator in biogeochemical processes such as iron bioreduction and contaminant degradation(*76*), but also can contribute to the optical properties of CDOM(*48*).

Iron bioreduction is an indispensable part of the biogeochemical cycling of iron, and contaminant degradation reduces toxic species in the environment.(*76*) Since quinones in CDOM are thought to both contribute to CDOM optical properties and are redox-active constituents in important environmental processes, understanding the optical properties of

quinones in CDOM and their reduction to hydroquinones is vital.

1.3 Quinones in CDOM - Quantification

1.3.1 Contribution of Quinones to the Optical Properties of HS

In charge transfer interactions, electron accepting species are thought to be aromatic ketones/aldehydes and quinones. In examining the contribution of quinones in particular to the optical properties of CDOM, there has been conflicting conclusions.(*48*, *91*) Some studies claim small, reversible changes in HS fluorescence upon reduction of quinones in CDOM (*24*, *86*, *92*), others claim significant contribution of the quinone/hydroquinones to the fluorescence of HS. (*83*, *93*). In light of this controversy, both quantitative analysis of quinone content and investigation of their contribution to the optical properties of CDOM is necessary.(*23*)

Sodium borohydride irreversibly reduces ketones and aldehydes to their alcohols, but it also reversibly reduces quinones to hydroquinones under anoxic, meaning absent of O_2, conditions. (*12*, *48*, *94*) Therefore, using sodium borohydride under anoxic conditions, all three functional groups are reduced, but most hydroquinones are expected to return to their quinone forms upon exposure to air. (*48*) Sodium dithionite can only reduce ketones and aldehydes at elevated temperatures (*95–99*), therefore at room temperature it can be employed to selectively reduce quinones under anoxic conditions. A diagram of the reaction products of ketone, aldehyde, and quinone reduction using borohydride and dithionite under N_2 and the product upon aeration is shown in figure 1.6.

In the work of Del Vecchio et. al.(*48*), the contribution of quinones to the optical properties of CDOM standards (SRFA, LAC, PLFA, LHA, and ESHA) is compared to the contribution of ketones and aldehydes to the optical properties via reduction of these standards using sodium borohydride and sodium dithionite. (*48*) Further, the quinone content

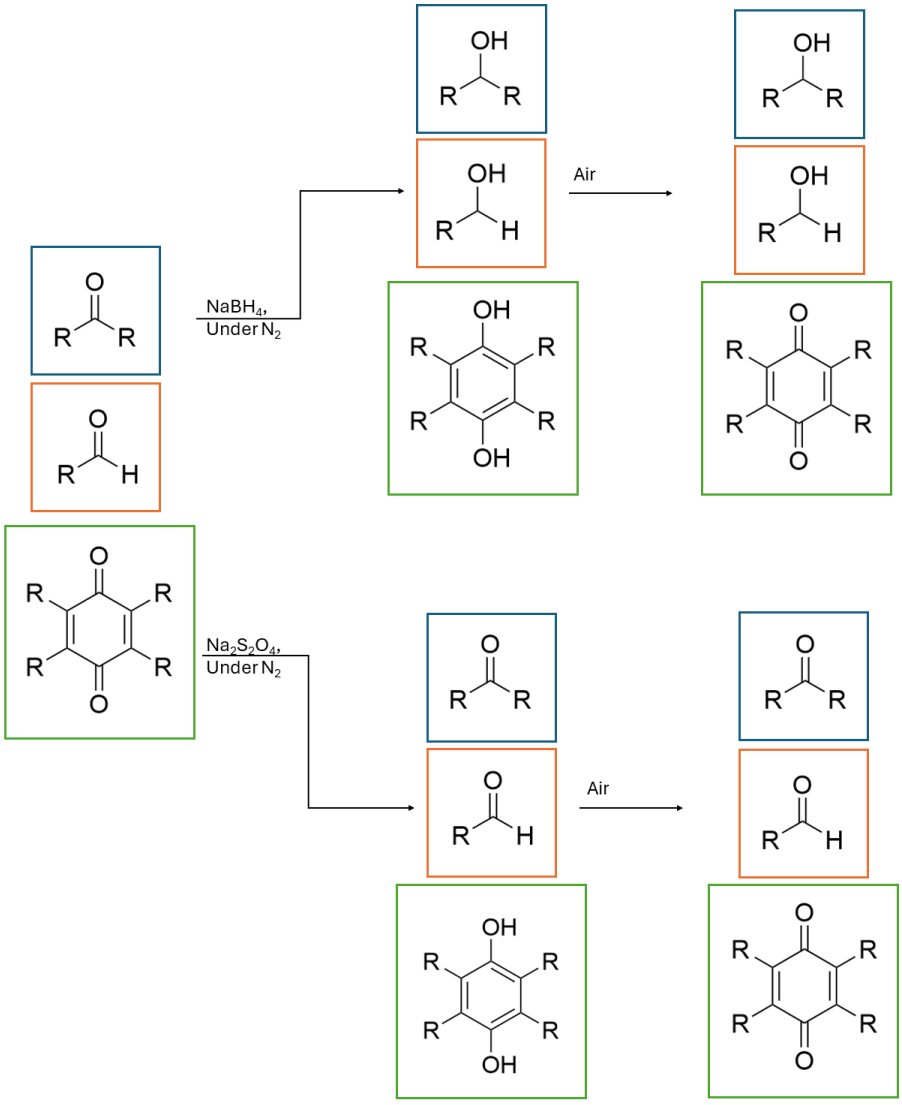


Figure 1.6: Products of reduction of ketones, alde hydes, and quinones with sodium borohydride and sodium dithionite under anoxic conditions and products of subsequent aeration.(*48*) R = organic structure for ketones and aldehydes, R = H, or organic structure for quinones. Rs may differ from each other within a structure.

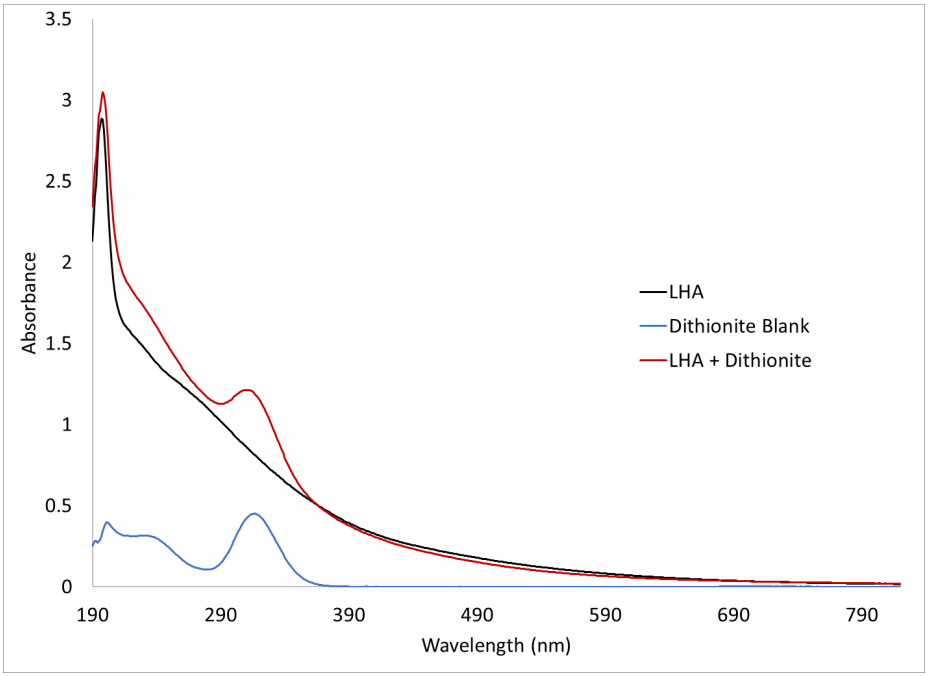


Figure 1.7: Absorption Spectra of LHA (black), Dithionite added to a mQ water blank (blue), and Dithionite added to the LHA sample (red)

in these standards is quantified by dithionite reduction. (*48*)

Sodium dithionite absorbs strongly at 316 nm, with a molar absorptivity of 8000 M^{-1} cm^{-1}.(*48*, *100*). A brief explanation of the Beer-Lambert law and the relation of concentration to absorbance is given in A.1.1 By injecting the same quantity of a dithionite stock into a mQ water blank and the HS sample, the quinone content of the HS sample was be calculated by the reacted dithionite. The concentration of dithionite added to the sample was calculated by the absorbance at 316 nm of the blank. Then, the increase of the absorbance in the CDOM sample at 316 nm was used to calculate excess dithionite. The excess dithionite was subtracted from the dithionite added to the sample to calculate the dithionite reacted, which is attributed to the quinone content of the sample. The absorption spectra for one trial of an LHA dithionite reduction is shown in figure 1.7, and the calculations are shown in equations 1.4-1.8.

Quinone Content of Sample (Q) = Dithionite Consumed by reduction of quinones (DC)

(1.4)

Quinone Content of Sample (Q) = Dithionite Consumed by reduction of quinones (DC)

(1.5)

DC = Dithionite added to sample (DA) - Excess Dithionite in Sample (DE) (1.6)

DA = Dithionite Added to Blank =

$$\frac{Abs_{316}(Blank, PostDithioniteAddition) - Abs_{316}(Blank, PreDithioniteAddition)}{\varepsilon_{316}(Dithionite)} \quad (1.7)$$

$$DE = \frac{Abs_{316}(Sample, PostDithioniteAddition) - Abs_{316}(Sample, PreDithioniteAddition)}{\varepsilon_{316}(Dithionite)} \quad (1.8)$$

Using these methods and calculations, Del Vecchio et al. quantified the quinone content of SRFA, LAC, PLFA, LHA, and ESHA. These results are shown in figure 1.8, compared to electrochemical results from Aeschbacker et al. (*101*), which will be discussed in section 1.3.2.

In addition to quantifying quinone content of these standards, Del Vecchio et al. (*48*) examined the change in optical properties (absorbance and fluorescence) with borohydride and dithionite reduction. They concluded that there was little contribution of quinones to fluorescence in CDOM standards and almost no effect on absorbance, but reduction of ketones and aldehydes significantly impacted optical properties. Therefore ketones and aldehydes seem to be the more relevant compounds as charge transfer acceptors.(*48*)

1.3.2 Electrochemical Analysis

As discussed in section 1.2.2, quinones are thought to be a major redox-reversible group in HS/CDOM. (*78–80*, *83–86*). Aeschbacher et al. examined quinone content of HS standards by electrochemical reduction and oxidation and related these results to the quinone

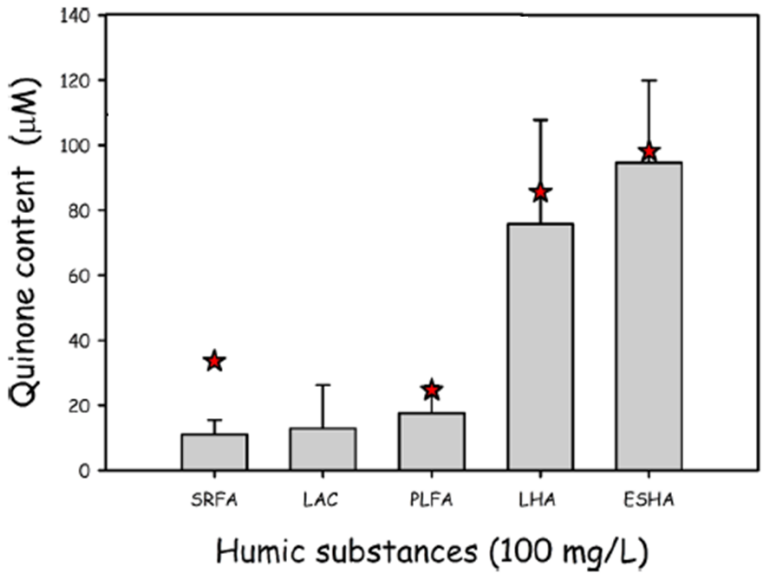


Figure 1.8: Quinone content found by Del Vecchio et al. (bars) using dithionite reduction compared to Aeschbacker et al. based on electrochemical measurement (stars) (*48*)

content of these samples.(*101*)

Aeschbacher et. al. directly measured electron accepting capacity (EAC) of several model HS, including ESHA, LHA, PLFA, and SRFA (*101*). They used direct electrochemical reduction (DER), mediated electrochemical reduction (MER), and mediated electrochemical oxidation (MEO) to measure the electrons transferred in solutions of SRHA, SRFA, ESHA, LHA, and PLFA, as well as Elliott Soil Fulvic Acid, Pahokee Peat Humic Acid Standard, Pahokee Peat Humic Acid Reference, Pahokee Peat Fulvic Acid Standard, Waskish Peat Humic Acid Reference, Nordic Aquatic Humic Acid Reference, and Nordic Aquatic Fulvic Acid Reference. The electrochemical cell set up is shown in figure 1.9.

The EACs of the HS were determined from MER. The working electrode was reticulated vitreous carbon, the reference electrode was Ag/AgCl, and the auxiliary (counter) electrode was platinum wire. Diquat dibromide monohydrate was used as the electron mediator. The electrons transferred was calculated as the integrated reductive and oxidative

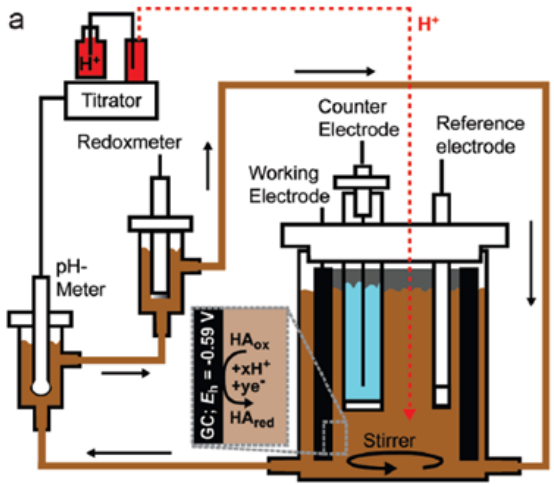


Figure 1.9: DER, MER, and MEO set up in (*101*)

currents over time. Measured redox potentials fell in the range of those measured for model quinone compounds. They concluded therefore that quinones were predominantly responsible for the electron transfer observed. Therefore, measured EAC was used as the quinone concentration to compare to optical measurements by Del Vecchio et. al. (*48*)

Similarly, Ratasuk and Nanny (*81*) determined the electron carrying capacities of HS samples using catalytic reduction. The trend in EAC from Aeschbacher et. al. closely followed the trend in EAC found by Ratasuk and Nanny. (*101*) Ratasuk and Nanny, however, concluded that quinones are not the only contributing species to their measured electron-carrying capacity (ECC). They attributed 21-56% of total ECC to non-quinone sites in the HA/FA.

1.4 Description of Thesis

The role of quinones in the redox activity and their contribution to the optical properties of CDOM/HS remains unclear. The goal of the following thesis is to elucidate the role of quinones in the optical properties of CDOM and HS and estimate the quinone content in

these samples.

In approaching this question, it became clear that a thorough study of model quinones was necessary to fully understand the role of these moieties in CDOM and to quantify them. Preliminary studies, which are described in A.1, highlighted the need for a more concrete understanding of the reaction of quinones themselves before applying this knowledge to quinone content in the complex system of CDOM in natural waters. First, the optical properties of a series of model quinones were thoroughly characterised. This includes absorption and fluorescence spectra, molar absorptivities at major peaks, and fluorescence quantum yields of the quinone and hydroquinone forms. This information was then used to investigate the chemical reduction of these quinones as a standard against which to compare the chemical reduction of CDOM. Since CDOM/HS include many different structures, it can be hard to differentiate how reactions effect specific functional groups. By first examining quinones in isolation, these effects can then be compared to observations of CDOM optical properties. The optical characterization of a series of model quinone compounds is described in Chapter 2. Following characterization, the quinones were reduced using sodium dithionite and the products separated by High Performance Liquid Chromatography (HPLC). Model quinones were also reduced using sodium sulfite to investigate a possible mechanism for the loss of quinone product in the dithionite reduction. These results are presented in Chapter 3. Finally, HS standards and C18 extracts of natural water samples from the North Pacific Ocean and the Chesapeake Bay were reduced using sodium dithionite to investigate the impact of quinone moieties on their optical properties and estimate quinone content in these samples. These results are provided in Chapter 4.

Chapter 2: Model Quinone Characterization

2.1 Introduction

As discussed in Chapter 1, quinone moieties are thought to contribute to the optical and redox properties of CDOM. In terms of the optical properties of CDOM, the electronic interaction model requires the presence of electron donors and electron acceptors within CDOM. Electron donating groups include phenolic and substituted aromatic carboxylic acid groups, while electron accepting groups include aromatic ketones/aldehydes and quinones.(*48*) There is evidence that quinones play a significant role as electron accepting groups in CDOM, particularly in photochemical and redox reactions in the environment.(*76*) Quinones may not only contribute to the optical properties in CDOM,(*48*) but also act as an electron transfer mediator in biogeochemical processes such as iron bioreduction and contaminant degradation.(*76*) Iron bioreduction is an indispensable part of the biogeochemical cycling of iron, and contaminant degradation reduces toxic species in the environment. Since quinones in CDOM are thought to both contribute to CDOM optical properties and are redox-active constituents in important environmental processes, understanding the optical properties of quinones in CDOM and their reduction reactions is vital.

To better understand CDOMs varied and complex structure, model compounds can be used to probe specific reactions, functional groups, mechanisms within a more isolated system. (*12*, *52*, *75*, *102*) Thorough characterization of the optical properties of model quinones allows these optical properties to be compared to those of CDOM/HS

and draw conclusions about the possible contribution of quinones to the optical properties of CDOM/HS.

The role of quinones in CDOM optical properties remains the subject of some controversy(*48*, *103*) In addition, there exists poor characterization of the optical properties of quinones themselves.

In this chapter, the characterization of a series of model quinone compounds is discussed. The model compounds consist of a series of methyl-substituted *p*-benzoquinones, naphthoquinones, and anthraquinones. Naphthoquinones and anthraquinones have been suggested to be good representatives of naturally occurring quinones, and anthraquinone has been used as a model compound for CDOM quinone studies.(*52*, *76*) The structures of the model quinones are shown in figure 2.1. These quinones and their hydroquinones were characterized by absorbance and fluorescence, the molar absorptivities of each major absorption peak were found, and the fluorescence quantum yields were calculated. In Chapter 3, this information will be used investigate the reactions of these quinones with dithionite and sulfite both qualitatively and quantitatively through the changes in the optical properties of the quinones due to reduction.

Previous work by Ma et. al. (*12*) on model quinone and CDOM reduction using sodium borohydride suggested that the optical changes observed in CDOM following borohydride reduction could not be attributed solely to the influence of quinones, and in fact it was postulated that ketones and aldehydes likely played a larger role due to the irreversible changes observed for CDOM samples. (*12*) The model quinone studies employed at this time were mainly used to compare optical changes. Molar absorptivities were estimated in Ma's study from a single measurement. (*12*) In addition, the suite of quinones studied encompassed a wide range of different structures. Therefore, these characterization studies were repeated utilizing calibration curves, triplicate trials, and a narrowly focused suite of compounds to investigate structural effects.

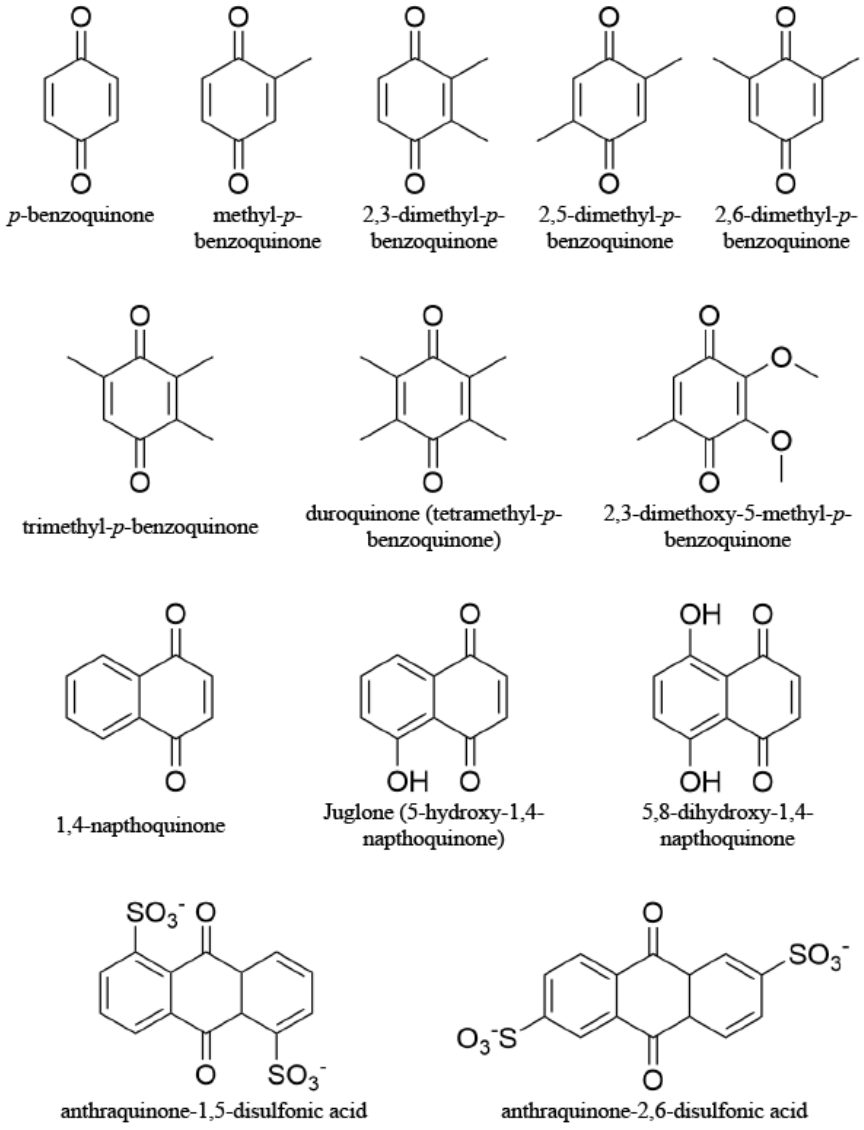


Figure 2.1: Model Quinones Studied

2.2 Materials and Methods

2.2.1 Materials

Quinones were used as received from the supplier – *para*-quinone, methyl-*p*-benzoquinone, 2,6-dimethyl-*p*-benzoquinone, duroquinone, 2,3-dimethoxy-5-methyl-*p*-benzoquinone, 1,4-naphthoquinone, juglone, 58-dihydroxy-1,4-naphthoquinone, and anthraquinone-1,5-disulfonic acid from Sigma-Aldrich, 2,3-dimethyl-p-benzoquinone from BOC Sciences, 2,5-dimethyl-p-benzoquinone and anthraquinone-2,6-disulfonic acid from ACROS Organics, and trimethyl-*p*-benzoquinone from ALFA.

Ultrapure water was obtained by filtering deionized water through a Sartorius Arium mini benchtop filtration system. methanol was used as received from Fisher Chemical Phosphate buffer was made from sodium phosphate monobasic and dibasic from Sigma-Aldrich dissolved in ultrapure water to make a solution of pH 7. Quinine Sulfate was used as received from sigma, dissolved in 0.1 N H_2SO_4 received from EM Science. Sodium borohydride was used as received from ACROS organics. N_2 from AirGas was used for anoxic experiments. The N_2 was passed through oxygen scrubbers to further ensure complete anoxic conditions in samples.

2.2.2 Optical Measurements

Absorption spectra were collected on a Shimadzu UV-Visible 2401PC Spectrophotometer from 190-820nm in 1 nm increments in a 1 cm quartz cuvette. Each spectra was blank subtracted using a sample of mQ water in the same cuvette.

Fluorescence spectra were collected on a Fluoro-Max 4 (Horiba) instrument, using an excitation wavelength corresponding to the longest absorption peak for each of the quinone and hydroquinone. Emission spectra were collected from an additional 10 nm above the

excitation wavelength to just before the second-order Raleigh scattering peak, or to 800 nm.

For *p*-benzoquinones, all quinones were excited at 428 and 350nm, and all *p*-benzohydroquinones were excited at 280nm. The quinone was diluted as necessary to keep the absorbance at the excitation wavelength <0.1 absorbance units. Excitation wavelengths used are in Table 1 along with the corresponding quantum yield). Excitation and emission bandpasses were set to 3 nm and emission spectra collected at increments of 1 nm. Each spectra was blank subtracted using a sample of mQ water in the same cuvette. Occasionally, the Raman peak from water was over or under corrected and this negative peak had to be removed manually. In these cases, intermediate wavelengths were filled in as to make a straight line from the last point before the Raman band to the first point after. Quantum yields were calculated as previously reported using quinine sulfate as a reference.(*12*) Emission intensities for quinone and hydroquinone fluorescence spectra were Quinine Sulfate Equivalents as previously reported ((*1*, *2*, *32*)). For samples where the fluorescence was <0.01 QSE, a five-point average was applied to the spectra to reduce the noise.

2.2.3 Molar Absorptivities and Fluorescence Quantum Yields

Quinone Stock Preparation

The quinone solid was dissolved in minimal methanol $\leq 5\%$ of the total volume) and diluted with ultrapure water and 1 mM phosphate buffer, to a final concentration of 0.001-5 mM of the quinone and 0.5-1 mM pH 7 phosphate buffer. Quinone stocks were remade each day. Exact concentrations for absorbance and fluorescence spectra are given with the spectra.

UV-Visible Spectra and Molar Absorptivities

For quinone molar absorptivities, calibration curves were composed of at least 5 concentrations of the quinone giving absorbance at the wavelength maximum of below 2.3, which has been determined to be the linear range of the instrument (*1*). Concentrations used for calibration curves and sample spectra are given in Supporting Information figure S1.

Each quinone was also reduced using sodium borohydride to obtain the spectra of the hydroquinone and to find the molar absorptivity of the hydroquinone peak. A very small quantity of borohydride ($<$1 mg) was transferred directly into cuvettes containing 3 mL of the quinone diluted with the pH 7 phosphate buffer to minimize pH effects. Reduced spectra were taken as soon as possible following reduction, though in some cases the excess borohydride caused bubbles from H_2 gas evolution which interfered with optical measurements and spectra were taken after 10-15 minutes when gas evolution had slowed or stopped. The reduction was considered complete when the quinone absorbance peaks were no longer discernible, and the hydroquinone peak was clearly visible. For hydroquinone molar absorptivity calculations, either the five concentrations of quinone were reduced to give the hydroquinone spectra and a calibration curve composed, or three samples of the same concentration of quinone were reduced to ensure reproducibility and acquire uncertainties, with the molar absorptivity calculated as absorbance divided by concentration, as the path length was 1 cm.

Fluorescence Spectra and Quantum yields

***P*-benzoquinones** The quinone stock was diluted such that the absorbance at 428nm $<$0.1 absorbance units. The UV-Vis spectra was collected in triplicate and the fluorescence spectra with an excitation wavelength of 428 nm was collected in triplicate. If necessary,

the stock was further diluted so that the absorbance at 350 nm was ¡0.1 absorbance units. The UV-Vis spectra was collected in triplicate and the fluorescence spectra with an excitation wavelength of 350 nm was collected in triplicate. The stock was diluted a final time such that the absorbance of the hydroquinone would be <0.1 at 280 nm based on the molar absorptivity. Three cuvettes containing 3 mL of the quinone at this concentration were deoxygenated by delivering N_2 through Teflon tubing directly into the sample for 10-15 minutes. Cuvettes were capped with Teflon septa and a Teflon tube inserted into the septa used as a vent. A small amount of sodium borohydride (<1mg) was directly added to each cuvette to produce the hydroquinone as determined by the absorbance spectra. The UV-Vis and fluorescence spectra with an excitation wavelength of 280 were collected in triplicate.

Naphthoquinones and Anthraquinones Borohydride reduction was conducted as described for *p*-benzoquinones. For naphthoquinone, the quinone excitation wavelength was 362 nm. The quinone samples were not diluted prior to borohydride reduction and the hydroquinone samples were excited at 332 nm. For juglone, the quinone was excited at 428 nm. The quinone was diluted such that the absorbance of the reduced sample would fall below 0.1 absorbance units at 332 nm, which was used as the excitation wavelength. For 5,8-dihydroxy-naphtoquinone, the excitation wavelength was 518 nm for the quinone and 364 nm for the hydroquinone. The sample was not diluted prior to borohydride reduction.

Anthraquinones were reduced using excess sodium dithionite to give they hydroquinone spectra. Dithionite reduction methods are described in detail in Chapter 3.

For anthraquinone-1,5-disulfonic acid, the quinone was excited at 324 nm and the hydroquinone was excited at 480 nm. For anthraquinone-2,6-disulfonic acid, the quinone was excited at 328 and 450 nm and the hydroquinone was excited at 450 nm.

2.2.4 Calculations

For quinone molar absorptivities, calibration curves were composed of at least 5 concentrations of the quinone giving absorbance at the wavelength maximum of below 2.3, which has been determined to be within the linear range of the instrument(*1*). Concentrations used for calibration curves and sample spectra are given in Supporting Information A.2. Excitation wavelengths used are shown with corresponding quantum yields. The fluorescence spectra of quinine sulfate was used as a reference standard, and quantum yields were calculated as previously reported.(*12*)

2.3 Results and Discussion

2.3.1 Optics

***P*-benzoquinones** Absorbance and fluorescence spectra are shown for the model quinone compounds and their hydroquinone counterparts in figures 2.2, 2.3, 2.4, and 2.5. Absorption spectra are shown as solid lines, fluorescence spectra are shown as dashed lines, and dotted lines are placed at the excitation wavelength for each fluorescence spectra. Longer wavelength fluorescence spectra for quinones is shown in black, and the shorter wavelength spectra is shown in red. Hydroquinone spectra are shown in blue. Note that these absorption spectra were taken in dilute conditions to negate inner filter effects. Absorption spectra acquired under higher concentrations are provided in supporting information A.2. Molar absorptivities of each quinone and hydroquinone peak and fluorescence quantum yields are given in table 2.1.

As discussed in Ma et. al. (*12*), the longest, lowest intensity absorption band of the quinones, occurring around 420 nm for the *p*-benzoquinone, methyl-*p*-benzoquinone, 2,5-dimethyl-*p*-benzoquinone, and 2,6-dimethyl-*p*-benzoquinone, represents the n $\rightarrow \pi^*$ tran-

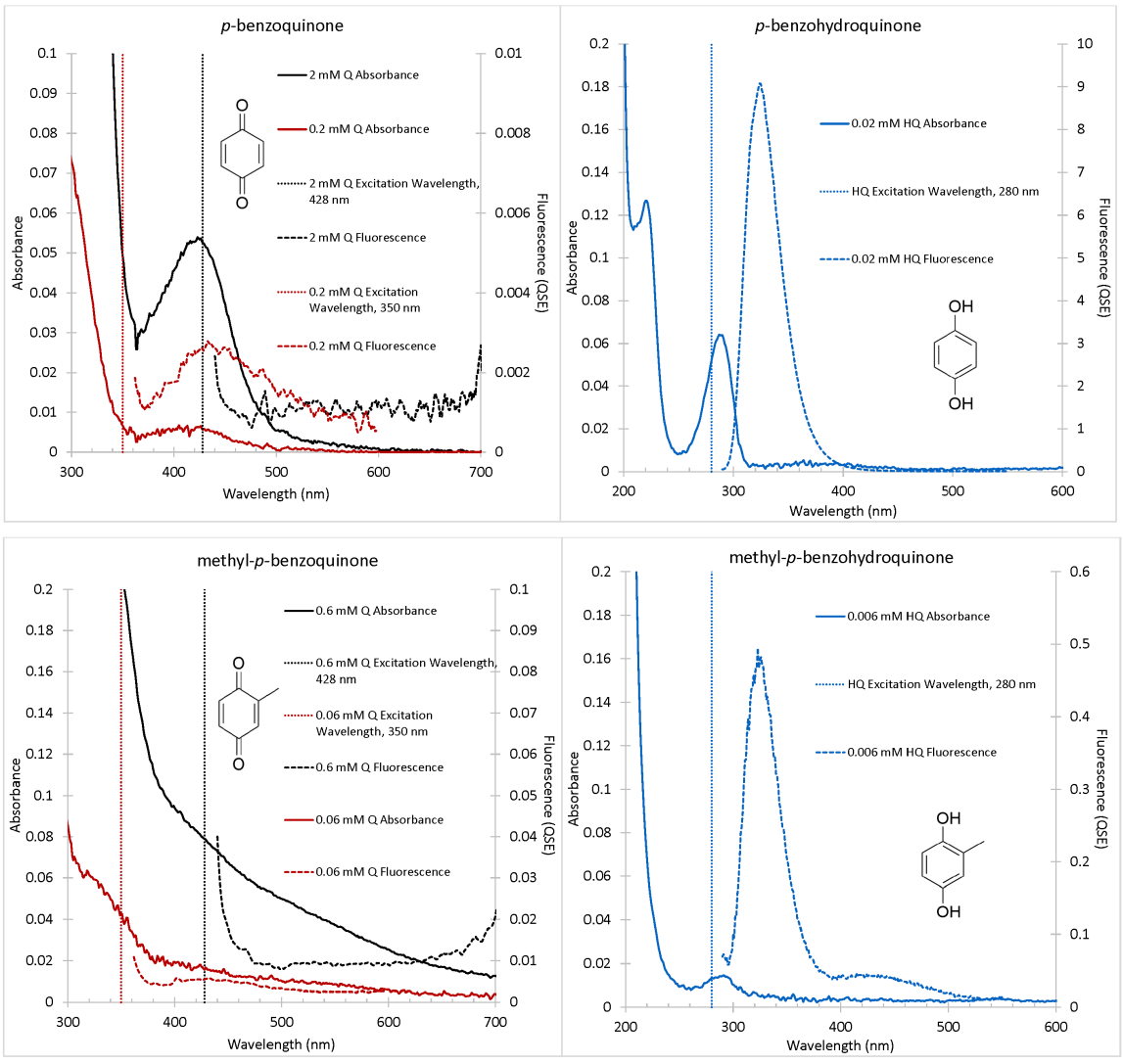


Figure 2.2: Absorption and fluorescence spectra for *p*-benzoquinone and methyl-*p*-benzoquinone. *p*-benzoquinone and methyl-*p*-benzoquinone fluorescence is 5-point smoothed.

sition, while the largest and second largest bands, occurring around 260 and 320 nm, respectively for these quinones represent the $\pi \rightarrow \pi^*$ transitions. (*12*)

For 2,3-dimethyl-*p*-benzoquinone, trimethyl-*p*-benzoquinone, and duroquinone, the ~420 nm peak is not evident due to the ~350 nm peak, which shifts to longer wavelength relative to the other compounds (~325 nm), and the usually ~420 nm peak shifts towards the blue, obscuring it within the ~350 nm peak for these compounds. Structurally, these compounds all contain methyl groups substituted in the 2,3 positions, which appears to lower the energy of the $\pi \rightarrow \pi^*$, so that its and that of the n $\rightarrow \pi^*$ become indistinguishable

All hydroquinones of the monocyclic methyl-substituted quinones showed an absorbance peak around 280 nm, due to the loss of conjugation from the quinone carbonyl groups. Methyl-substitution did not show much impact on the hydroquinone absorbance, suggesting structural substitutions to be less important in the hydroquinone than the quinone.

Trimethyl-*p*-benzoquinone can be compared to 2,3-dimethoxy-5-methyl-*p*-benzoquinone to observe the effect of methoxy substitution as compared to methyl substitution. The methoxy substution shifts the $\pi \rightarrow \pi^*$ transition to 408 nm, as compared to 351 nm for trimethyl-*p*-benzoquinone. Their hydroquinone peaks remain at comparable wavelengths (284 for trimethyl-*p*-benzohydroquinone and 286 for 2,3-dimethoxy-5-methyl-*p*-benzohydroquinone).

Wavelength maxima of absorption bands reported in table 2.1 are in agreement with previous work by Ma et. al. (*12*); however, molar absorptivity values differed somewhat. This is likely due to the difference in methods- molar absorptivities were found by Ma et. al. (*12*) from a single absorbance measurement, whereas standard curves were utilized here.

Naphthoquinones and Anthraquinones Absorbance and fluorescence spectra are shown for the model quinone compounds and their hydroquinone counterparts in figures 2.6 and 2.7. Molar absorptivities of each quinone and hydroquinone peak and fluorescence quan-

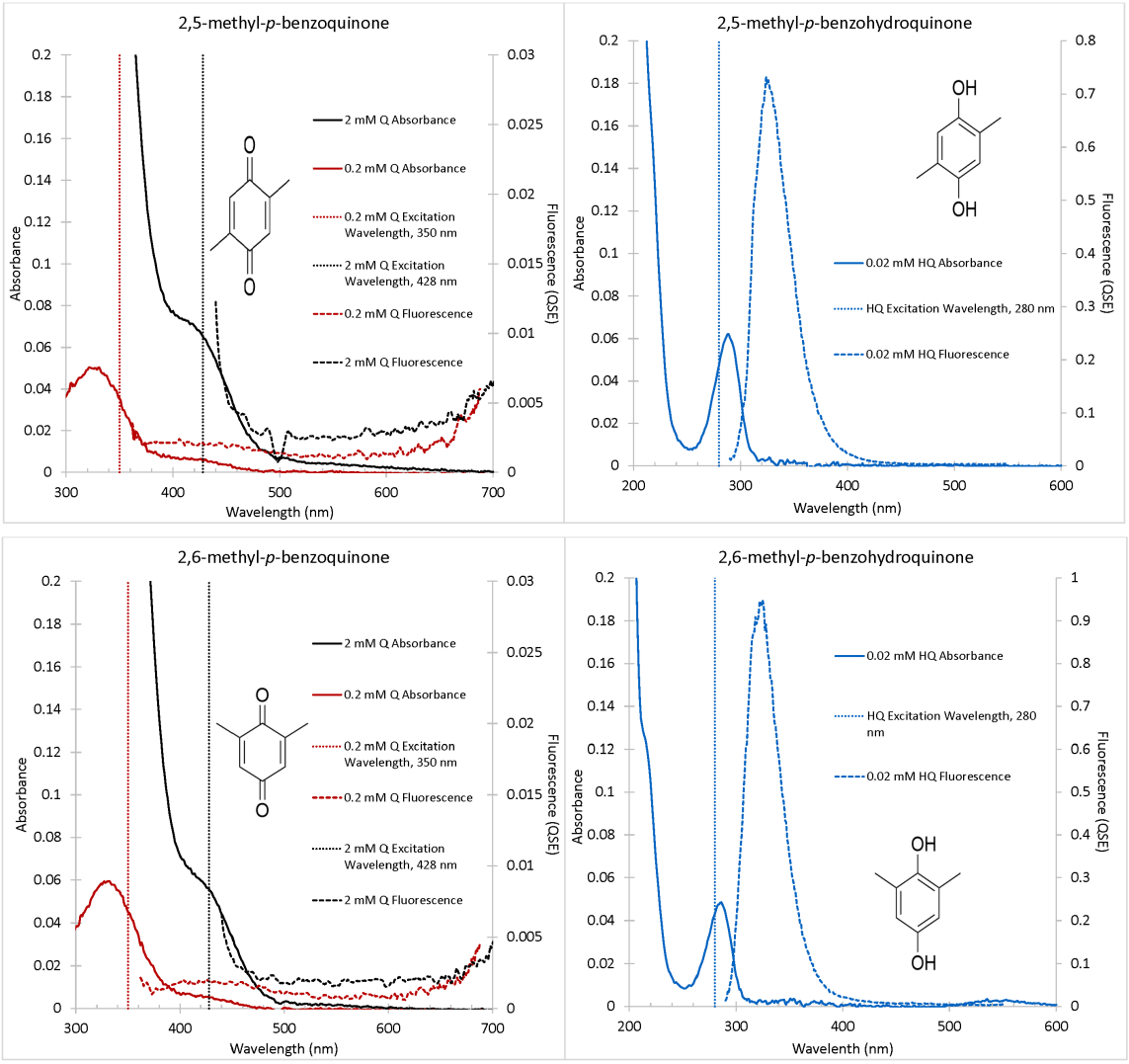


Figure 2.3: Absorption and fluorescence spectra for 2,5-dimethyl-*p*-benzoquinone and 2,6-dimethyl-*p*-benzoquinone. 2,5-dimethyl-*p*-benzoquinone and 2,6-dimethyl-*p*-benzoquinone fluorescence is 5-point smoothed.

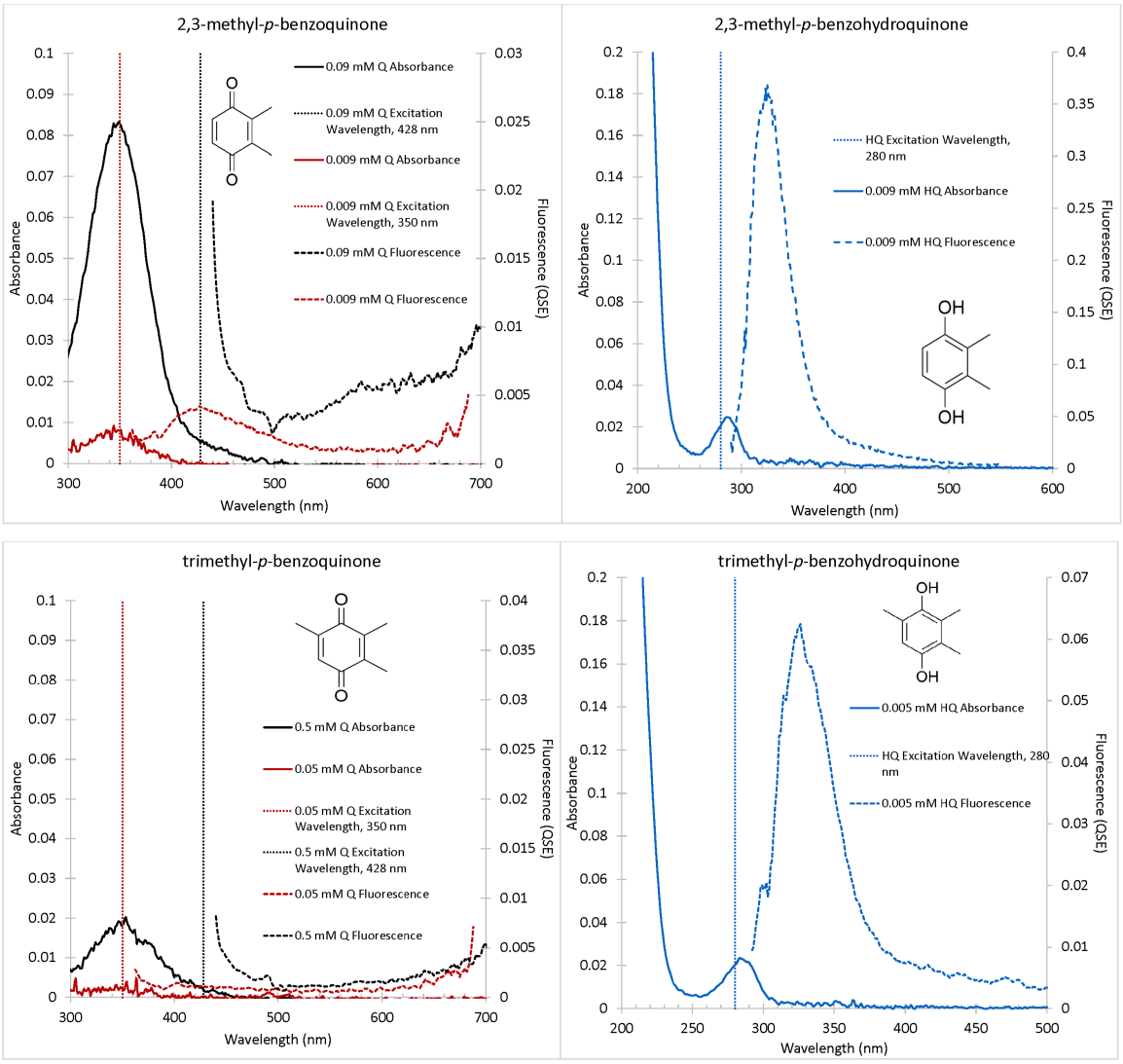


Figure 2.4: Absorption and fluorescence spectra for 2,3-dimethyl-*p*-benzoquinone and trimethyl-*p*-benzoquinone. 2,3-dimethyl-*p*-benzoquinone and trimethyl-*p*-benzoquinone fluorescence is 5-point smoothed.

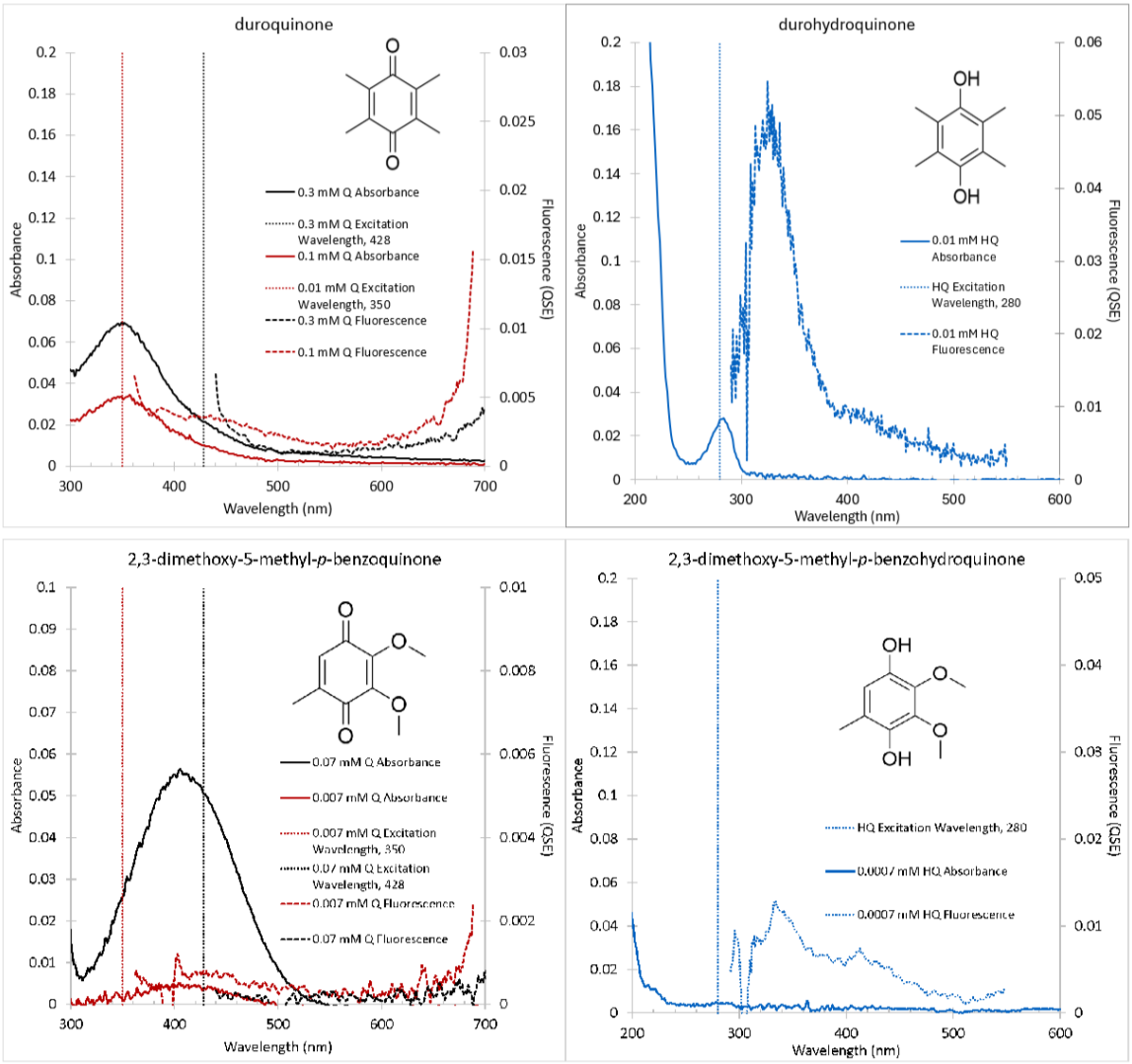


Figure 2.5: Absorption and fluorescence spectra for duroquinone and 2,3-dimethoxy-5-methyl-*p*-benzoquinone. Duroquinone and 2,3-dimethoxy-5-methyl-*p*-benzoquinone fluorescence is 5-point smoothed.

Quinone	Quinone or Hydroquinone	Wavelength (nm)	Molar Absorptivity	Wavelength (nm)	Fluorescence Quantum Yield
p -benzoquinone	Q	246	18300 ± 100		
		293	379 ± 5	350	<9.75x10-4
		424	28.9 ± 0.2	428	<1.77x10-4
	HQ	222	4520 ± 30	280	$9.98\times10^{-2} \pm 1.83\times10^{-2}$
		288	2280 ± 10		
methyl-*p* -benzoquinone	Q	250	17700 ± 300		
		324	530 ± 10	350	$<7.15\times10^{-4}$
		420	43.5 ± 0.4	428	$<1.40\times10^{-3}$
	HQ	288	2700 ± 200	280	$2.62\times10^{-2} \pm 4.63\times10^{-3}$
2,3-dimethyl-*p* -benzoquinone	Q	254	16900 ± 100	350	$<6.25\times10^{-4}$
		350	910 ± 10	428	$<1.48\times10^{-4}$
	HQ	287	2500 ± 40	280	$1.36\times10^{-2} \pm 5.07\times10^{-4}$
2,5-dimethyl-*p* -benzoquinone	Q	256	19600 ± 300		
		328	261.3 ± 0.6	350	$<1.02\times10^{-3}$
		416	37.2 ± 0.2	428	$<1.34\times10^{-4}$
	HQ	288	3250 ± 40	280	$1.01\times10^{-2} \pm 1.14\times10^{-3}$
2,6-dimethyl-*p* -benzoquinone	Q	258	20570 ± 50		
		332	354 ± 2	350	$<1.64\times10^{-4}$
		424	37.7 ± 0.2	428	$<4.37\times10^{-4}$
	HQ	286	2730 30	280	$1.71\times10^{-2} \pm 7.66\times10^{-4}$
trimethyl-*p* -benzoquinone	Q	260	19500 ± 300	350	$<3.95\times10^{-4}$
		351	405.1 ± 0.6	428	$<7.91\times10^{-4}$
	HQ	284	2710 ± 20	280	$3.70\times10^{-3} \pm 5.36\times10^{-4}$
duroquinone	Q	270	19200 ± 100	350	$<1.74\times10^{-3}$
		352	228 ± 2	428	$<2.16\times10^{-3}$
	HQ	284	2070 ± 60	280	$5.71\times10^{-3} \pm 5.20\times10^{-4}$
2,3-dimethoxy-5-methyl-*p* -benzoquinone	Q	268	15080 ± 80	350	$<3.95\times10^{-3}$
		408	750 ± 6	428	$<1.66\times10^{-4}$
	HQ	286	3020 ± 10	280	$1.13\times10^{-3} \pm 2.64\times10^{-5}$

Table 2.1: Molar absorptivity at major wavelengths and fluorescence quantum yields for methyl-substituted range of quinones. Quantum yield values given as $<$ indicate that fluorescence emission is indistinguishable from zero under the experimental conditions.

tum yields are given in table 2.2.

The wavelength maxima are less defined in the absorption spectra for the polycyclic compounds than for the *p*-benzoquinones. Naphthoquinone is fairly straightforward, with a $\pi \rightarrow \pi^*$ transition showing at 342 nm. As it becomes substituted with hydroxy groups, this peak shifts towards longer wavelengths and widens, showing a maximum of 429 nm for juglone and 514 nm for 5,8-dihydroxy-1,4-naphthoquinone, as well as displaying a shoulder for juglone and $\sim$3 humps for 5,8-dihydroxy-1,4-naphthoquinone.

Reduction of anthraquinones by borohydride does not form the hydroquinone product; instead it produces a mixture of anthrone isomers. (*104*). This being the case, the anthraquinones were reduced with sodium dithionite to give the hydroquinone peak. The absorbance spectra given by dithionite reduction matches the hydroquinone spectra observed by Ma et. al. (*12*) for photochemical reduction of these compounds, excluding the additional peak at 316 nm from the excess dithionite. The molar absorptivities and quantum yields for the anthrahydroquinones are calculated at wavelengths where dithionite does not absorb to avoid interference from this peak.

The molar absorptivities given in 2.1 and 2.2 were used to calculate concentrations of quinone stocks in the reduction experiments in Chapter 3, and the spectra of known quinone and hydroquinone samples were used to compare to dithionite and sulfite reduced spectra to examine products.

The fluorescence quantum yields calculated were generally on the same order of magnitude as those reported by (*12*). Generally, quinone quantum yields were very small, in most cases indistinguishable from zero for the *p*-benzoquinones, while most hydroquinone quantum yields were on the order of 10^{-2}. Fluorescence quantum yields of CDOM are typically on the order of 10^{-2} (*12*), so it is unlikely that these quinones themselves are contributing to the fluorescence emission of CDOM. The reported values are the average between 3 measurements and the reported errors are the standard deviation between the 3

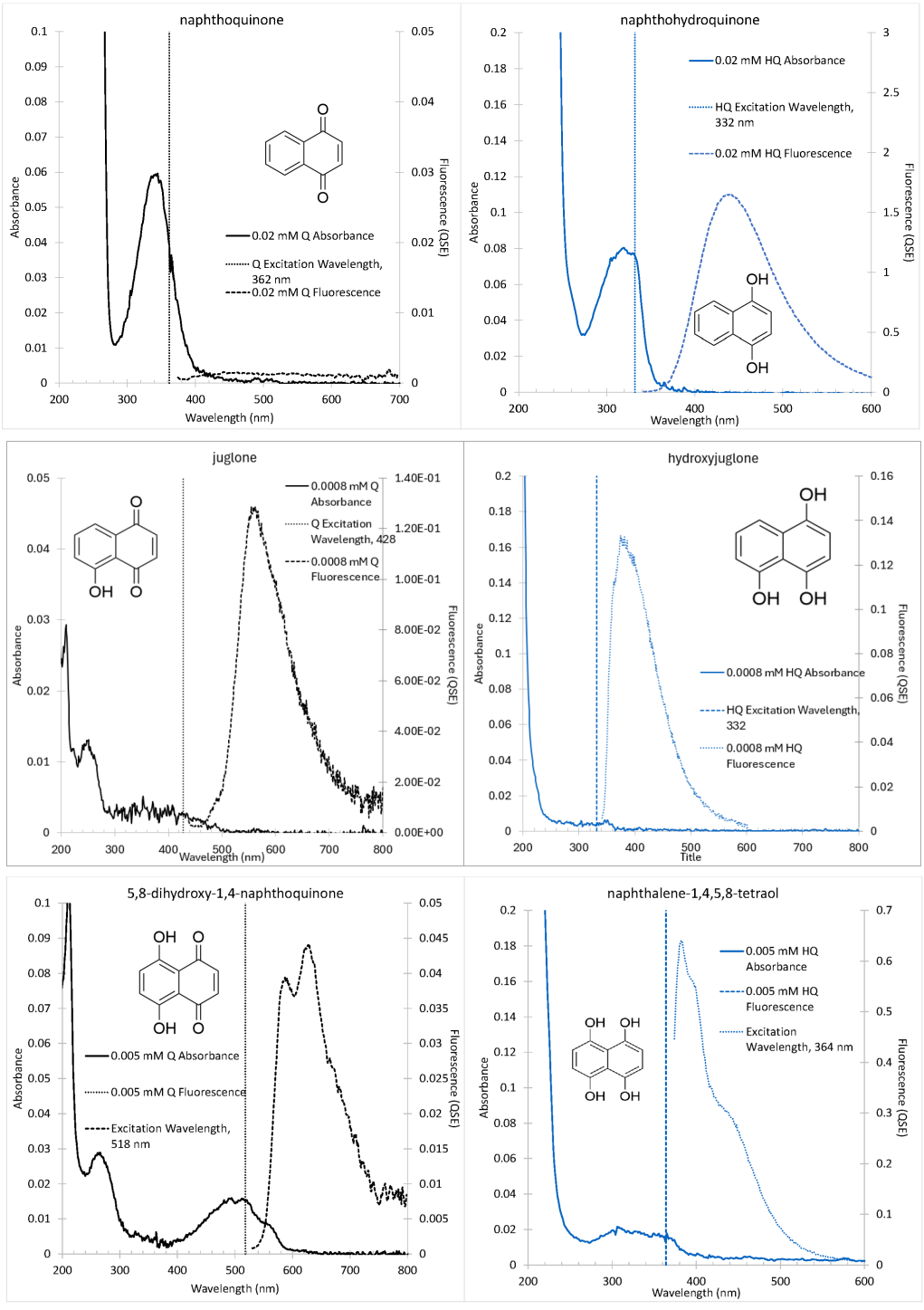


Figure 2.6: Absorption and fluorescence spectra for naphthoquinones

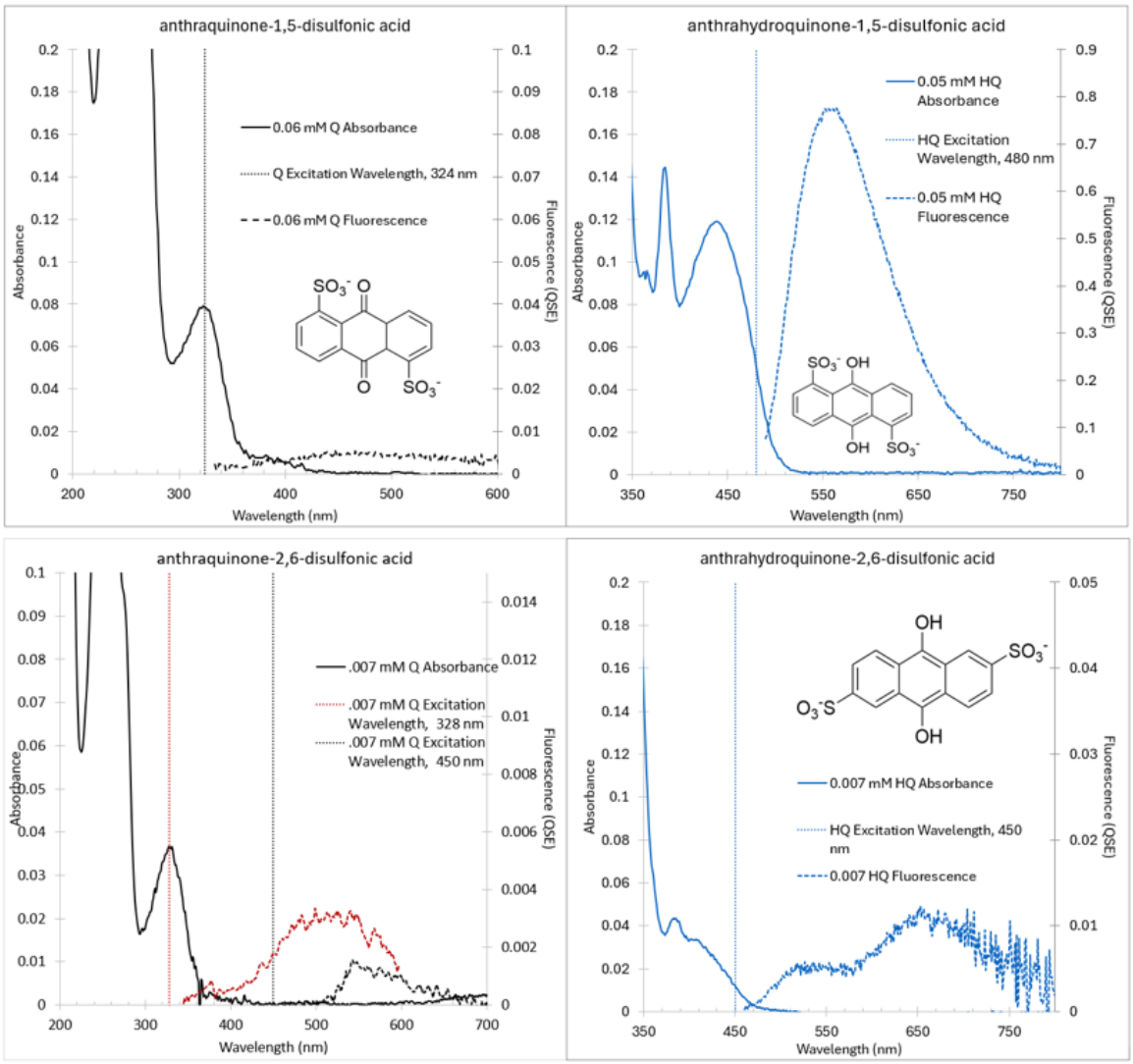


Figure 2.7: Absorption and fluorescence spectra for anthraquinones

Quinone	Quinone or Hydroquinone	Wavelength (nm)	Molar Absorptivity	Wavelength (nm)	Fluorescence Quantum Yield
naphthoquionone	Q	252	22740 ± 80		
		342	2960 ± 50	362	$<9.25\times10^{-5}$
	HQ	242	14100 ± 500		
		320	3000 ± 200	332	$2.4\times10^{-2} \pm 0.9\times10^{-2}$
juglone (5-Hydroxy-1,4-naphthoquinone)	Q	209	32800 ± 300		
		250	13800 ± 200		
		429	3280 ± 70	428	$1.42\times10^{-2} \pm 1.94\times10^{-4}$
	HQ	280	2195 ± 6.000		
		334	1280 ± 90	324	$1.59\times10^{-1} \pm 6.85\times10^{-2}$
5,8-dihydroxy-1,4-naphthoquinone	Q	265	5730 ± 60.0		
		514	3530 ± 70.0	518	$8.72\times10^{-3} \pm 4.00\times10^{-4}$
	HQ	364	2500 ± 200.0	364	$1.42\times10^{-1} \pm 6.95\times10^{-2}$
anthraquinone-1,5-disulfonic acid disodium salt	Q	258	17000 ± 300		
		324	1400 ± 200	324	$<3.48\times10^{-3}$
	HQ	384	2505 ± 13.7		
		439	3035 ± 4.02	480	$8.17\times10^{-2} \pm 7\times10^{-3}$
anthraquinone-2,6-disulfonic acid disodium salt	Q	209	30980 ± 70		
		257	46500 ± 100		
		328	5220 ± 10	328	$<6.09\times10^{-4}$
	HQ	385	6145 ± 441	450	$1.02\times10^{-2} \pm 3\times10^{-3}$

Table 2.2: Molar absorptivity at major wavelengths and fluorescence quantum yields for polycyclic range of quinones.

measurements.

2.4 Conclusion

Molar absorptivity and fluorescence quantum yields were determined for a series of model quinones, including a series of *p*-benzoquinones and a series of polycyclic quinones. The trends in their molar absorptivities with structure are examined, showing substitution at the 2 and 3 positions in the *p*-benzoquinones compounds brings the $\pi \rightarrow \pi^*$ transition to lower energy and making the $n \rightarrow \pi^*$ transition indistinguishible from this peak. In the polycyclic compounds, the $\pi \rightarrow \pi^*$ transition is brought to lower energy with -OH substitution for naphthoquinone, and anthraquinone shows the effect of sulfonate groups on the band gap of the hydroquinone. *P*-benzoquinones show little fluorescence, whereas their hydroquinone counterparts show fluorescence quantum yields on the order of 10^{-2}. Polycyclic quinones generally do show fluorescence, although their hydroquinone counterparts

also have greater fluorescence quantum yields.

Chapter 3: Characterization of Optics, Stoichiometry, and Products of Reduction of Model Quinones

3.1 Introduction

3.1.1 Reduction of Quinones in CDOM by Sodium Dithionite and Sulfite

Given the importance of the structure and properties of CDOM and the reactions of quinones contained therein, the quinone content and the changes in optical properties resulting from quinone reduction in CDOM were studied by reaction with sodium dithionite. Quinones can be selectively reduced by dithionite under anoxic conditions.(*12*, *23*, *48*, *105*) This reaction is shown to occur at a 1:1 stoichiometry for select quinones.(*106*).

Dithionite is used because it reacts rapidly with quinones, but not with ketones and aldehydes. Ketones and aldehydes can be reduced by dithionite, but the time scale is much longer and the reaction conditions generally more rigorous, involving higher temperatures or flow reactor set-ups.(*95*, *96*, *98*, *99*) In principle, the quinones would be expected to react at a 1:1 stoichiometric ratio with the dithionite, as dithionite has 2 reducing equivalents and a quinone has 2 reducible carbonyl groups. Dithionite in solution forms 2 SO_2^- in solution, each of which is one reducing equivalent. This is shown in equation 3.1. The expected 1:1 stoichiometry of dithionite used to quinone reduced has been shown for lawsone, 9,10-anthraoquinone-2,6-disulfonic acid, and 9,10-anthraquinone-2-sulfonic acid,8 all of which are resonance stabilized and therefore less reactive than benzoquinones.(*76*).

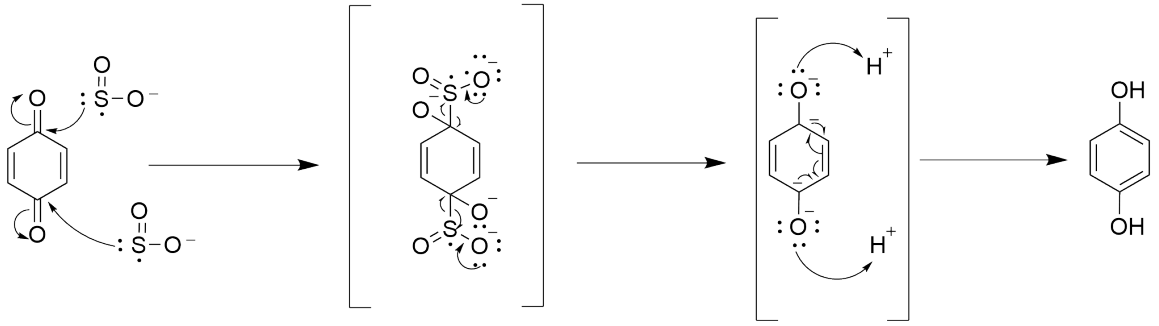


Figure 3.1: Mechanism of the reduction of carbonyl functional group with hydroquinone demonstrating the release of two molecules of SO_2 (*97*)

The expected reaction is shown in equation 3.2 The proposed mechanism of the reduction of a quinone with dithionite is given in figure 3.1, based off of the proposed mechanism of dithionite reduction of ketones and aldehydes given by Gassman et. al. (*97*).

$$S_2O_4{}^{2-} \longrightarrow 2SO_2{}^{-} \tag{3.1}$$

$$Q + 2SO_2{}^{-} \longrightarrow H_2Q + 2SO_2 \tag{3.2}$$

Upon reduction of the quinone by the dithionite, SO_2 is produced in solution, which reacts with water to form sulfurous acid, shown in equation 3.3

$$SO_2 + H_2O \longrightarrow H_2SO_3 \tag{3.3}$$

The sulfurous acid forms bisulfite and sulfite in solution in equilibrium according to equations 3.4 and 3.5. The Ka for the deprotonation of suflurous acid to bisulfite is $Ka_1=1.6\text{x}10^{-2}$(*107*) and the Ka for the deprotonation of bisulfite to sulfite is $Ka_2=6.4\text{x}10^{-8}$ (*107*). Therefore, the reduction of quinones by dithionite results in the formation of sulfite in solution around neutral pH, with a pKa of 7.2.

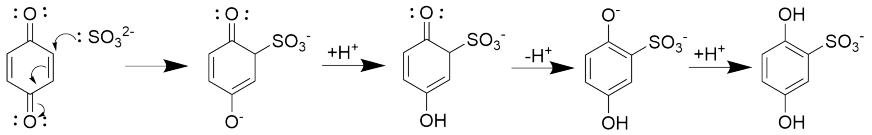


Figure 3.2: Mechanism of sulfite addition to quinone molecule.

$$H_2SO_3(aq) \rightleftharpoons HSO_3^-(aq) + H_3O^+(aq) \tag{3.4}$$

$$HSO_3^-(aq) \rightleftharpoons SO_3^{2-}(aq) + H_3O^+(aq) \tag{3.5}$$

Because of this formation of sulfite as a product of dithionite reduction and the reduction of quinones by sulfite, this was investigated as a possible side reaction occurring with the dithionite reduction of certain quinones, particularly *p*-benzoquinones, and the degree of its interference in quinone quantification was investigated.

Previous studies have investigated the effects of pH and the reduction potential of the quinone/hydroquinone system on the products of these quinones' reactions with sulfite. Sulfite reacts with quinones to form hydroquinone and sulfonated hydroquinones(*108*), the ratio and degree of sulfonation depending on reaction conditions and the quinone reactivity. At low pH, the primary product is the hydroquinone, but as pH rises above 4.5, the only product is the hydroquinone monosulfonate. Thus, at pH 7, the reaction of *p*-quinone with sulfite will form entirely hydroquinone monosulfonate. At alkaline pH, some hydroquinone disulfite is formed. (*108*). The mechanism for sulfonation of the benzoquinone is shown in 3.2.

In addition to pH effects, both the products and the kinetics of the quinone and sulfite reaction depend on the difference in their reduction potential. The redox potentials of quinones affect the products of its reaction with sulfite according to the ΔE = $E_{quinone}$-$E_{sulfite}$: (*109*)

1. Large and positive ΔE favor redox reactions - the formation of the hydroquinone product.

2. Smaller ΔE favors 1,4-addition of the sulfite - the formation of the sulfonated hydroquinone product.

3. Negative differences, where the reduction potential of the quinone is less than that of sulfite, will result in a very slow addition reaction, if it occurs at all.

The first order rate constant increases with ΔE for the reaction between the quinone and sulfite, regardless of whether ΔE is positive or negative, meaning that larger differences in reduction potential will result in a faster reaction regardless of whether the hydroquinone or the sulfonated hydroquinone is forming.(*109*, *110*) Greater resonance stabilization due to higher ring numbers lowers E_0 of the quinone. (*76*)

Many reactions of quinones are reversible; however, addition reactions and side reactions may result in irreversible side products that remove the quinones from the reactive pool. The result of these reactions is that quinones with low reactivity, likely with attached rings or electron-donating substituents, will eventually be the main quinone compounds present in the environment.(*76*)

Previous studies have shown qualitatively that quinones will react with both dithionite and sulfite (*108*, *110–117*), but the stoichiometry of these reactions is not well studied. Additionally, the scope of previous studies on reaction products and kinetics is limited, so further studies on a greater range of quinones are necessary. Previous studies on sulfite reactions with quinones also tend to focus on the process of pulp bleaching or the reaction of these compounds in wine.(*118*, *119*) Due to this focus, these studies do not encompass a wide range of substituted quinones.

Environmental studies often focus on anthraquinones and naphthoquinones.(*76*) Anthraquinones are especially prevalent in natural sources, particularly fungi and lichens. Many of these anthraquinones are methoxy derivatives.(*105*) Methoxy groups are also

abundant in CDOM precursors such as lignin.(*120*, *121*) Anthraquinones, naphthoquinones, and methoxy-substituted quinones are therefore the most environmentally relevant quinone species and the most likely to be found within CDOM samples.

The exact structure of quinones found in CDOM is not well known, and therefore it is important to understand how different structures and substitutions may affect the reactivity of different quinones in CDOM. In addition, there is little to no data relating the reaction of sodium dithionite with various quinones in relation to their reactivity with sulfite. There is also limited data regarding the kinetics of these reactions for a range of quinones, which is important if side reactions with sulfite are occurring within the experimental time frame of the dithionite reduction, as that will affect the stoichiometry and products of the dithionite reduction.

Model quinones were reacted with sodium dithionite, sodium sulfite, and sodium borohydride to examine the differences in the reduction products of a variety of substituted quinones with a variety of reduction potentials. The quinones studied are shown in Figure 2.1. These quinones represent a variety of methyl-substituted quinones to examine the effect of the number of substituted ring positions and their structural arrangement on reactivity. 2,3-dimethoxy-5-methyl-*p*-benzoquionone was also tested and compared to trimethyl-*p*-benzoquinone to demonstrate changes in reactivity due to methoxy-substitution rather than methyl-substitution.

In addition to elucidating the stoichiometry and optical changes in quinones as a result of reduction with dithionite, the sulfite reaction studies also carry environmental relevance. Sulfur species in the environment can form sulfite, and if the quinones react with sulfite, both quinone reactions and the sulfur cycle would be affected.(*76*, *122*) For example, sulfite species in the environment which result from acid rain could react with more reactive quinones in the environment.

A clearer understanding of the reaction of a variety of model quinones with dithionite

and sulfite will allow a greater understanding of the reactions of the quinones within CDOM with these compounds. This study will thus allow a greater theoretical and experimental understanding of these results.

3.1.2 Dithionite quantification

As discussed in Chapter 1 and supplemental information A.1, dithionite absorbs strongly at 316 nm and this absorbance peak can be used to quantify it. However, dithionite is very sensitive to oxygen in the system, and therefore requires very precise anaerobic techniques. A comparison of dithionite quantification by its absorbance at 316 nm versus substoichiometric additions of dithionite to potassium ferricyanide is given in supplemental information figure 15. Substoichiometric dithionite addition to a sample of potassium ferricyanide gives a more accurate and much more precise calculation of dithionite concentration between trials. Therefore rather than using dithionite absorbance in a sample of ultrapure water, dithionite was quantified by ferricyanide addition. Ferricyanide has a molar extinction coefficient of 1020 M^{-1} cm^{-1} at 420 nm. Its reduction product, ferrocyanide, does not absorb at this wavelength, therefore ferricyanide loss can be calculated spectroscopically. Absorption spectra of ferricyanide and ferrocyanide are provided in supplemental information figure 16.

Ferricyanide was used to quantify the dithionite added at each step, using the disappearance of the absorbance for ferricyanide, its molar absorptivity of 1020 at 420 nm, and the ratio of 1 equivalent of dithionite reduces 2 equivalents of ferricyanide (*100*). The reduction half reaction for ferricyanide is given in equation 3.6. The action of dithionite as a reducing agent was discussed in equations 3.1 and 3.2. An example of the absorption change due to addition of dithionite to a ferricyanide sample is shown in figure 3.3. The concentration of the dithionite is then the change in the absorbance divided by the molar

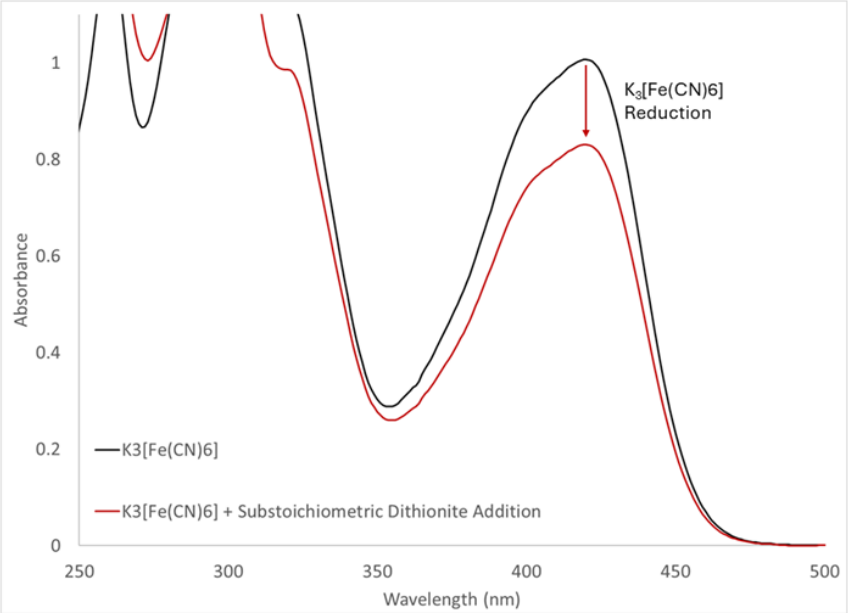


Figure 3.3: UV-Visible spectrum of potassium ferricyanide used for dithionite quantification.

extinction coefficient divided by 2. This calculation is shown in equation 3.7.

$$[\mathrm{Fe(CN)6}]^{3-} + \mathrm{e}^{-} \leftrightarrow [\mathrm{Fe(CN)6}]^{4-} \tag{3.6}$$

$$\text{Concentration of Dithionite} = \frac{\Delta A(ferricyanide)}{1020 * 2} \tag{3.7}$$

3.1.3 Examination of Reduction Products by HPLC

The quinone reacted can be calculated by the disappearance of the quinone absorbance peak, however, due to the overlap of spectra and observed differences in the dithionite reduced spectra as compared to the borohydride reduced spectra, HPLC was used to separate and quantify the reduction products.

In addition to examining optical differences between the reduction of model quinones using sodium dithionite and sodium sulfite, the stoichiometry of the dithionite reduction was be examined using HPLC. HPLC separated injected mixtures by polarity of the components, so the hydroquinone will elute from the column faster than the quinone. This method was only applied to dithionite reductions on monocyclic and naphthoquinone compounds because since the sulfonated hydroquinone would be ionic, it cannot be separated by HPLC, the studied anthraquinone compounds could not be separated for the same reason. Not only can HPLC separate the quinone and hydroquinone (since they are often difficult to distinguish by UV-Vis alone), but it can also quantify them. In this way, we can examine the stoichiometry of quinone reduced and hydroquinone formed by dithionite reduction. This gives us insight into the stoichiometry and products of this reaction.

3.2 Materials and Methods

3.2.1 Materials

A list of model quinones, suppliers, and sample preparation is provided in section 2.2.

3.2.2 Optical Measurements

A description of UV-Vis and fluorescence measurements is given in 2.2

HPLC

HPLC chromatagraphs were collected using a Shimadzu LC-20AT HPLC-UV, which has a sample loop volume of 20 μL. The column is a Gemini 5μ C18 110 Å column measuring 100x4.60 mm. The mobile phase was a 50:50 Methanol:1 mM Acetate Buffer (pH 4) in mQ water for the mono-cyclic quinones. For the naphthoquinones, a gradient elu-

tion was used consisting of 30:70 Methanol:1 mM Acetate Buffer (pH 4) in mQ water for the first 5 minutes, 40:60 for the next 5 minutes, and 50:50 for 10 minutes. These mobile phases were selected because they were able to separate the quinone and hydroquinone within a 20-minute time frame with relatively narrow peaks. Acetate buffer was used to ensure hydroquinones were protonated to minimize pH effects. These mobile phases yielded the best separation of quinone and hydroquinone within a 20 minute elution time.

Optical Changes Following Dithionite Reduction

To investigate the effect of dithionite reduction on the fluorescence spectra of the quinones and hydroquinones, three cuvettes containing the quinone stock diluted to a concentration where the absorbance of the quinone at the excitation wavelength was ¡0.1 absorbance units were deoxygenated using N_2 delivered through Teflon tubing directly into the sample for ¿30 minutes. Cuvettes were capped with Teflon septa and a Teflon tube inserted into the septa used as a vent. An additional cuvette containing potassium ferricyanide was also set up to quantify the dithionite added to each quinone sample.

The dithionite stock solution was prepared by deoxygenating a vial containing $\sim$ 5 mg of sodium dithionite by passing N_2 over the solid in the vial, deoxygenating a vial containing 1 mL of 0.01 N NaOH and another vial containing 10 mL of 0. 01 N NaOH. To obtain a sufficiently small concentration of sodium dithionite without introducing oxygen to the system, 1 mL of the 10 mL NaOH solution was transferred using a gas-tight syringe to the vial containing solid dithionite. Once the solid was dissolved, 10-300 μL of this solution (determined by estimated concentration from mass of dithionite used) was transferred to the 1 mL vial of NaOH. This was then used as the dithionite stock in the quinone reduction. An aliquot (20-300 μL) of this solution was transferred to both a quinone sample and a ferricyanide sample under anoxic conditions. If the excess dithionite peak was

not observed, additional aliquots were added to both cuvettes until the peak was observed. The fluorescence emission spectra at an excitation wavelength similar to that used for the hydroquinone was collected for each cuvette.

3.2.3 Sulfite Reductions

Sulfite reduction was conducted following the observed dissimilarities between borohydride and dithionite reduced spectra. This procedure was similar to that of the dithionite reduction. Two sulfite stock solutions were prepared. One vial of 10 mL 0.100 M phosphate buffer and one vial of 1-1.5 mL 0.100 M phosphate buffer were deoxygenated as above and 5 mg of sodium sulfite added to each vial. The 10 mL vial was used for substoichiometric sulfite additions. The concentration was calculated from the mass of sodium sulfite and volume of solvent. This sulfite stock was added by two aliquots 20-100 μL to the quinone sample, deoxygenated as above, to observe substoichiometric changes in the spectra due to substoichiometric sulfite reduction. Then, an aliquot of the excess sulfite stock from the 1-1.5 mL vial was added to the sample to observe the spectra of the reduced quinone.

3.2.4 Dithionite Reduction HPLC Analysis

In order to relate model quinones optical properties to those of CDOM and investigate the reaction of quinones in CDOM reduction methods, model quinones were reacted with substoichiometric dithionite and the sample separated by High Performance Liquid Chromatography (HPLC).

Three cuvettes containing 3 mL of the quinone sample at a concentration where the absorbance of the longest wavelength peak was within the linear range of the instrument were deoxygenated using N_2 delivered through Teflon tubing directly into the sample for

>30 minutes. Cuvettes were capped with Teflon septa and a Teflon tube inserted into the septa used as a vent.

Three additional cuvettes containing 3 mL of a potassium ferricyanide solution in 0.5 mM phosphate buffer were deoxygenated the same way.

To obtain the untreated quinone chromatogram, 100 μL of the quinone stock 0.02-1.2 mM (exact concentration given with spectra) was injected into the HPLC. To obtain the hydroquinone chromatagram, <1 mg of sodium borohydride was added to the same concentration of quinone and 100 μL of this solution was injected into the HPLC.

The UV-Visible spectra of the deoxygenated quinone and potassium ferricyanide was measured.

The dithionite stock solution was prepared by deoxygenating a vial containing 5mg of sodium dithionite by passing N_2 over the solid in the vial, deoxygenating a vial containing 1 mL of 0.01 N NaOH and another vial containing 10 mL of 0. 01 N NaOH. To obtain a sufficiently small concentration of sodium dithionite without introducing oxygen to the system, 1 mL of the 10 mL NaOH solution was transferred using a gas-tight syringe to the vial containing solid dithionite. Once the solid was dissolved, 10-300 μL of this solution (determined by estimated concentration from mass of dithionite used) was transferred to the 1 mL vial of NaOH. This was then used as the dithionite stock in the quinone reduction. A small amount (10-20 μL) of this solution was transferred to both a quinone sample and a ferricyanide sample. If there was no discernible change in the quinone absorbance spectra, additional dithionite was added to both cuvettes until a change was observed. A 100 μL aliquot of the partially reduced sample was injected into the HPLC. This was repeated in triplicate with the remaining prepared cuvettes. For one cuvette, dithionite was added the partially reduced sample until the excess dithionite peak was observed at 316 nm. A 100 μL aliquot of the excess dithionite reduced sample was injected into the HPLC.

3.3 Results and Discussion

3.3.1 Optics

Evidence of sulfonated hydroquinone product

The absorbance spectra of the untreated quinone, the hydroquinone, and the substoiciometric dithionite reduced quinone are shown in figures 3.4 and 3.5 for the methyl-subsutitued series of quinones and 2,3-dimethoxy-5-methyl-*p*-benzoquinone. The spectra of the substiochiometric dithionite reduction is used to avoid interference by the absorbance of dithionite itself at 316 nm. The dithionite reduced spectra, in general, did not match the hydroquinone spectra and could not be explained as a superposition of the hydroquinone and quinone spectra, as would be expected in a substoichiometric reduction. Instead, the spectra showed not only the remaining untreated quinone and the formation of hydroquinone, but a unique shape not entirely accounted for by these two contributions. A possible explanation for this shape is the formation of an additional product other than the hydroquinone.

As discussed in the introduction to this chapter, dithionite reduction produces SO_2, forming sulfite ions in solution. To investigate the influence of this possible side reaction, quinones were reacted with dissolved sodium sulfite. The spectra of the sulfite reduced quinone is shown with the substoichiometric dithionite reduced spectra and the hydroquinone spectra in figures 3.4 and 3.5. Some quinones, namely trimethyl-*p*-benzoquinone, duroquinone, 2,3-dimethoxy-5-methyl-*p*-benzoquinone, and anthraquinone-1,5-disulfonic acid, show little to no reaction with the sulfite. In cases where a reaction with sulfite is observed, the sulfite reduced spectra is distinct from the hydroquinone spectra, indicating the primary product of sulfite reduction is not hydroquinone. This supports the conclusion that the sulfite primarily undergoes the addition reaction under these conditions, forming

the sulfonated hydroquinone product. The spectra of the sulfite-reduced quinone generally serves to explain some of the observed differences between the hydroquinone and dithionite reduced spectra, as the tentatively assigned ”sulfonated hydroquinone” peak appears to factor into the shape of the dithionite reduced spectra. The exception to this is duroquinone, which did not react with sulfite and the substoichiometric dithionite reduced spectra can be attributed to the formation of a small amount of hydroquinone in addition to the remaining unreacted quinone. Structurally, duroquinone does not have any positions to which the sulfite could undergo addition, therefore since that is the primary reaction of the quinones with sulfite under these conditions, no reaction is observed. Based on the shape of their respective absorption spectra upon reduction with sulfite, the 2,3-dimethoxy-5-methyl-*p*-benzoquinone appears more reactive than the trimethyl-*p*-benzoquinone, indicating the methoxy groups increase the quinones reactivity to sulfite addition. Both compounds, however, show mild reactivity to sulfite. Although the dithionite reduced spectra for all but the duroquinone differ somewhat from the hydroquinone and quinone spectra, they generally suggest relatively small interference by the assigned ”sulfonated hydroquinone”. In most cases, a small shoulder is observed in the range of the sulfonated hydroquinone peak, or the hydroquinone peak shifts towards longer wavelength, but not as far as the sulfonated hydroquinone peak.

For the polycyclic quinones, the spectra for the quinone, hydroquinone, substoichiometric dithionite reduced and sulfite reduced samples are given in figures 3.6 and 3.7. These show very interesting spectral shapes under different reducing agents. Naphthoquinone reacted with sulfite produces long wavelength absorbance that is not observed in the untreated or hydroquinone spectra. It appears to contribute slightly to the dithionite reduced spectra, but the shape around 300-350 nm suggests greater contribution by the hydroquinone than the sulfite reduced product.

For juglone, the effect of sulfite reduction more closely resembles what is seen in the

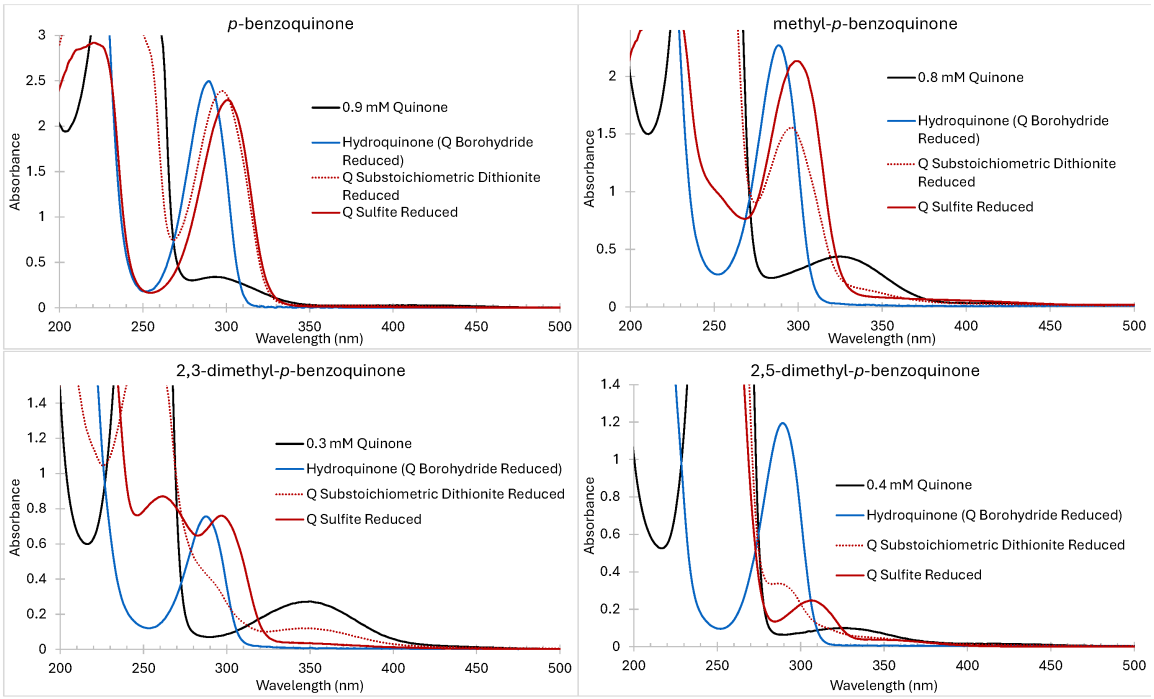


Figure 3.4: UV-Visible Spectra for *p*-benzoquinone, methyl-*p*-benzoquinone, 2,3-dimethyl-*p*-benzoquinone, and 2,5-dimethyl-*p*-benzoquinone. Quinone spectra is shown in black, hydroquinone spectra is shown in blue, substoichiometric dithionite reduced spectra is shown in red dashed line, and excess sulfite reduced spectra is shown in solid red line.

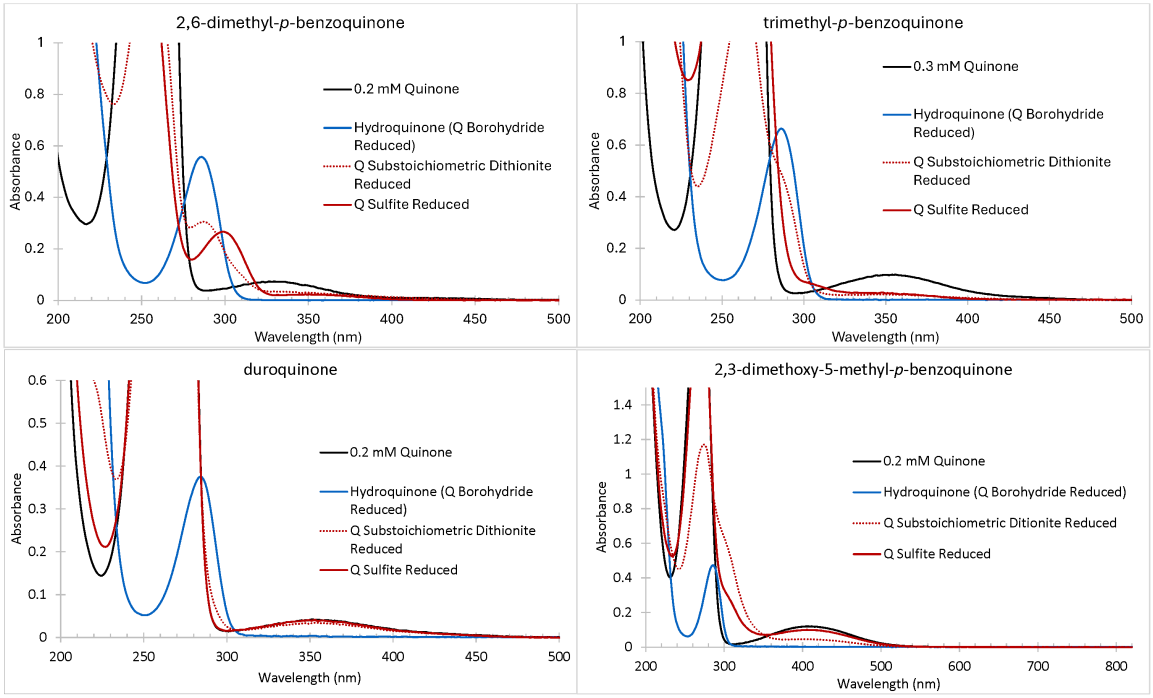


Figure 3.5: UV-Visible Spectra for 2,6-dimethyl-*p*-benzoquinone, trimethyl-*p*-benzoquinone, duroquinone, and 2,3-dimethoxy-5-methyl-*p*-benzoquinone. Quinone spectra is shown in black, hydroquinone spectra is shown in blue, substoichiometric dithionite reduced spectra is shown in red dashed line, and excess sulfite reduced spectra is shown in solid red line.

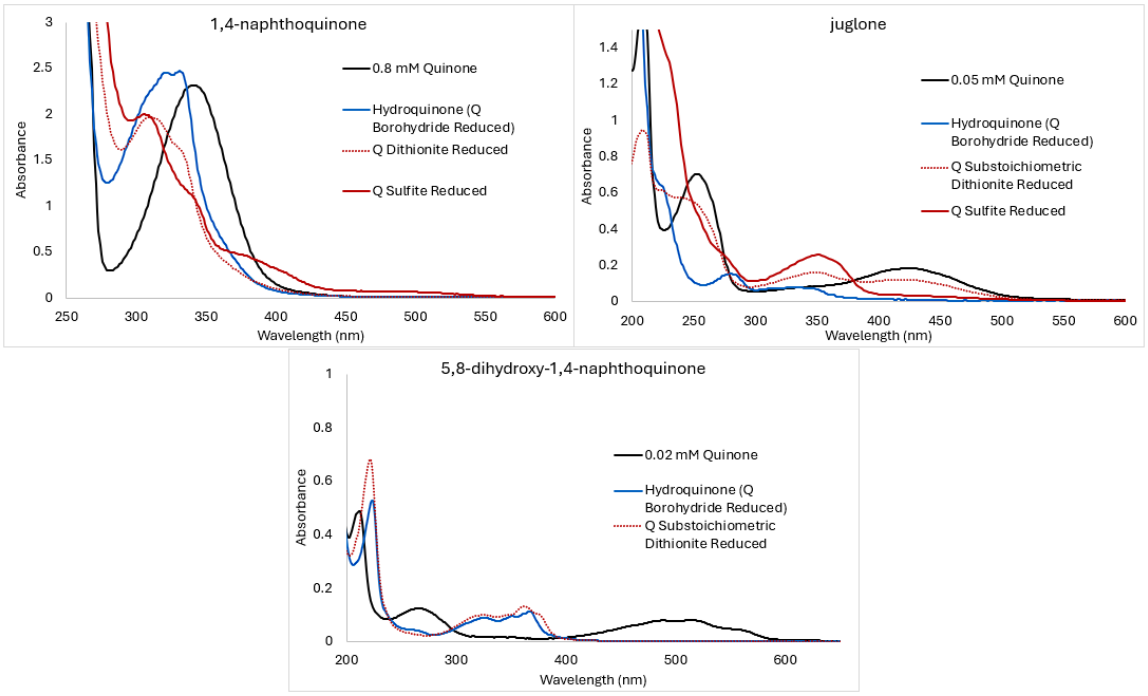


Figure 3.6: UV-Visible Spectra for naphthoquinone, juglone, and 5,8-dihydroxy-1,4-naphthoquinone. Quinone spectra is shown in black, hydroquinone spectra is shown in blue, substoichiometric dithionite reduced spectra is shown in red dashed line, and excess sulfite reduced spectra is shown in solid red line.

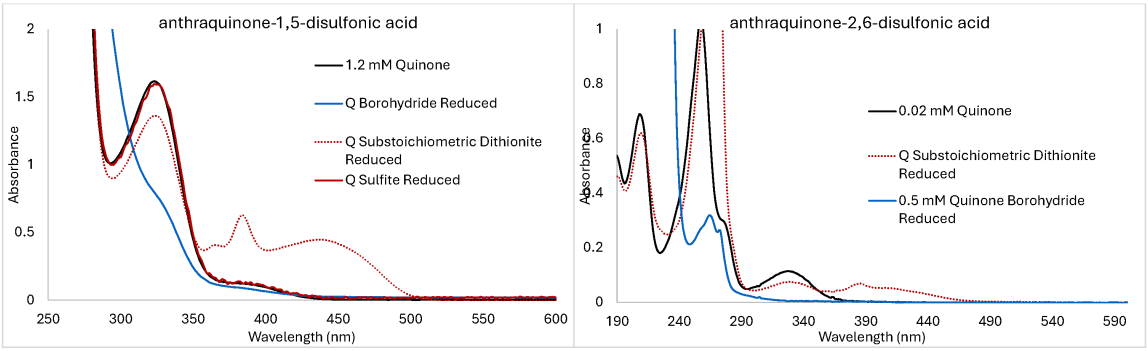


Figure 3.7: UV-Visible Spectra for anthraquinone-1,5-disulfonic acid and anthraquinone-2,6-disulfonic acid. Quinone spectra is shown in black, hydroquinone spectra is shown in blue, substoichiometric dithionite reduced spectra is shown in red dashed line, and excess sulfite reduced spectra is shown in solid red line.

monocyclic compounds - that is, a red shift of the absorbance peak as compared to the hydroquinone. The dithionite reduced spectra resembles a mixture of the absorbance from the quinone and hydroquinone, suggesting little impact of sulfite reactions. The spectra of dithionite reduced 5,8-dihydroxy-1,4-naphthoquinone closely resembles that of the hydroquinone, although slight differences in shape, especially around 350-400 nm are observed. This suggests that there is possibly a small contribution of sulfite side reactions, but it does not impact the absorbance significantly.

For both anthraquinones, the observed spectra for the dithionite reduced anthraquinone closely resembles the observed hydroquinone spectra by Ma et. al. (*12*) for photochemically reduced anthraquinone. This spectra is attributed as the hydroquinone spectra in this case rather than the borohydride reduced spectra. The borohydride reduction does not form the same spectra; rather, it reduces the intensity of the quinone spectra. Borohydride reduction of anthraquinones forms anthrones rather than the hydroquinone(*104*). Anthraquinone-1,5-disulfonic acid was not observed to react with sulfite.

An investigation of the reaction of sulfite with the quinones over time is given in supplemental information A.3. In summary, although sulfite continued to reduce the quinones over time, the majority of the reaction occurred within the first 20 minutes, within the time frame of the dithionite reduction experiments.

Since pure dithionite itself doesn't fluoresce, (see supplemental information A.3), the quinones were reacted with excess dithionite and the fluorescence shape and intensity compared to that of the hydroquinone. This spectra is given in figures 3.8 and 3.9.

This comparison is not necessarily quantitative in nature, given that *p*-benzoquinones were excited at 288 nm rather than the 280 nm excitation wavelength used in hydroquinone reductions, as this made the Raman peak easier to correct given the generally lower fluorescence intensity in the dithionite reduced samples. The main point of interest in this comparison is the shape of the spectra and the relative magnitude. In order to compare

the relative magnitude of fluorescence in this samples where concentration differed, the fluorescence is normalized to the intensity of the hydroquinone fluorescence at its peak in QSE and, if the borohydride reduced and dithionite reduced samples differed in concentration, the intensity of the dithionite reduced spectra was multiplied by the ratio of the concentration of the borohydride reduced sample to the dithionite reduced sample.

For *p*-benzoquinones, the shape of the hydroquinone and dithionite reduced spectra are very similar. The comparative magnitude differs. In 2,3-dimethyl-*p*-benzoquinone, the magnitudes are very similar. For 2,5-dimethyl-*p*-benzoquinone, they hydroquinone fluorescence approximately twice as intensely as the dithionite reduced sample, and for 2,6-dimethyl-*p*-benzoquinone this effect is reversed.

For naphthoquinone, the dithionite reduced fluorescence spectra closely resembles that of the hydroquinone. Juglone shows a much lower fluorescence intensity in the dithionite reduced sample, and a different shape, with a sharper peak at 370 nm and a broader, longer wavelength fluorescence. The 5,8-dihydroxy-napthoquinone, in contrast, shows greater intensity of fluorescence in the dithionite reduced spectra and a loss of long wavelength fluorescence. The fluorescence spectra of these compounds suggest a greater difference in the dithionite reduced compounds as compared to the hydroquinones produced by borohydride reduction than their respective absorption spectra would indicate.

These optical changes as a result of different reducing agents suggest that the dithionite reduction may form both hydroquinone and the sulfonated hydroquinone product in many of the model quinone systems. The occurrence of this side reaction makes quantification of quinones reacted with dithionite complicated. To investigate the degree of interference of the sulfite side reactions, dithionite reduced quinones were investigated using HPLC.

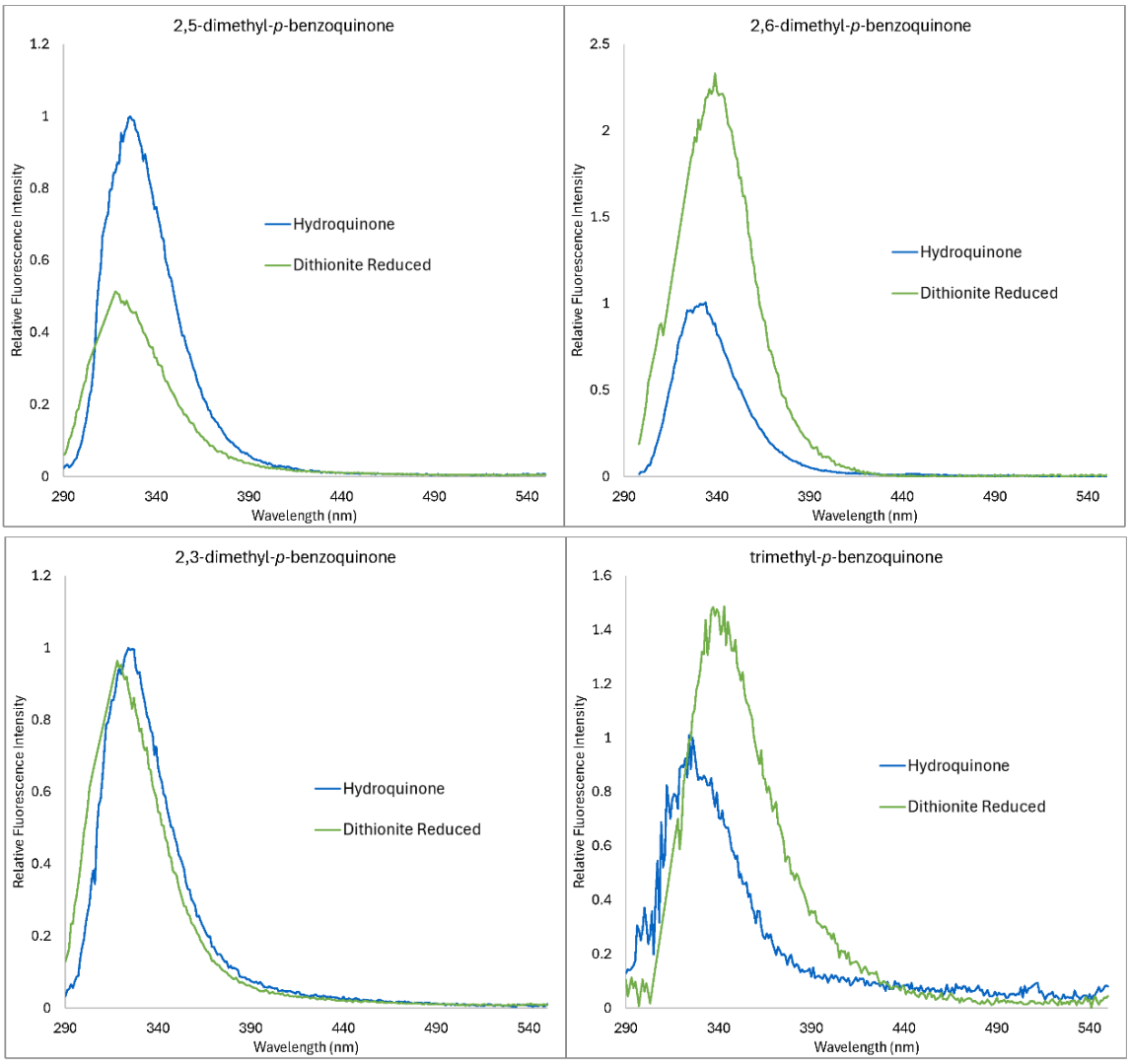


Figure 3.8: Hydroquinone (blue) and dithionite reduced (green) spectra for 2,5-dimethyl-*p*-benzoquinone, 2,6-dimethyl-*p*-benzoquinone, 2,3-dimethyl-*p*-benzoquinone, and trimethyl-*p*-benzoquinone.

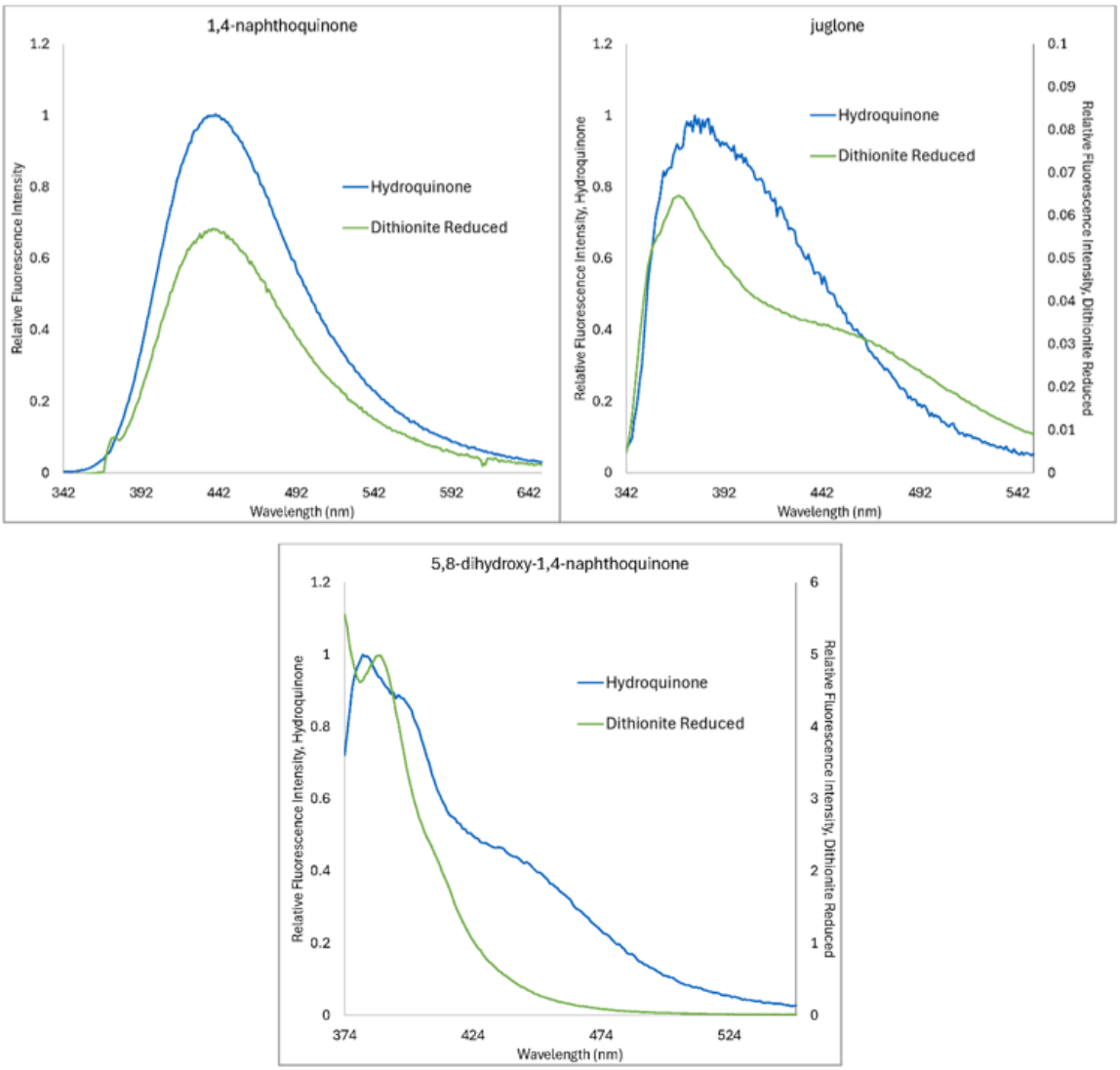


Figure 3.9: Hydroquinone (blue) and dithionite reduced (green) spectra for juglone, and 5,8-dihydroxy-1,4-naphthoquinone

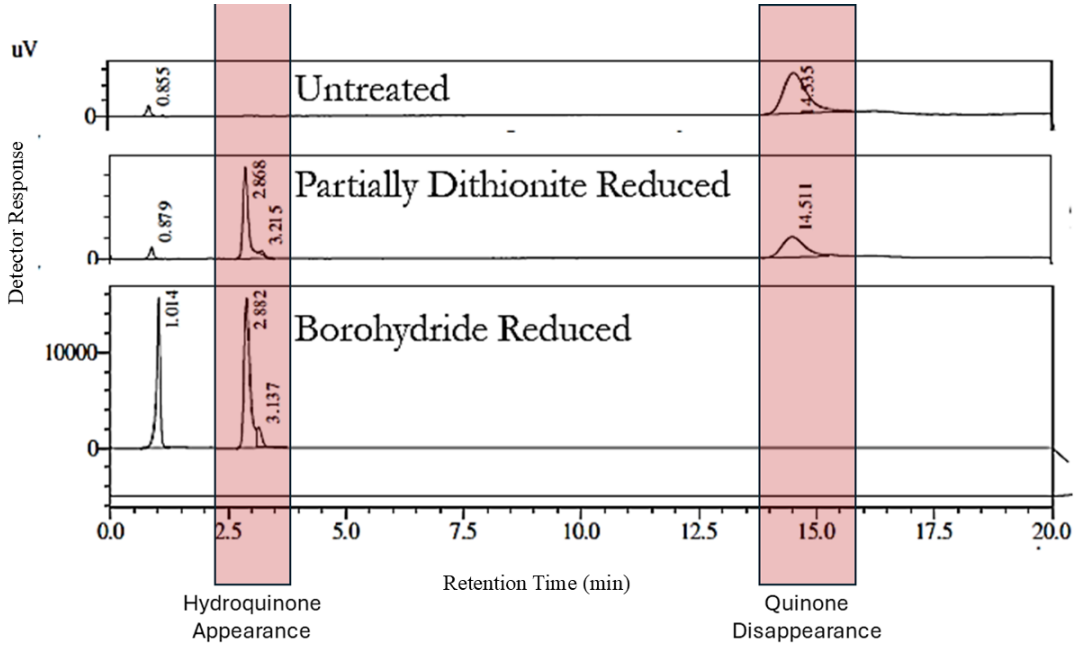


Figure 3.10: Example Chromatagraph (Duroquinone) highlighting peaks used for calculations.

3.3.2 Stoichiometry/LC

In order to distinguish the products of the dithionite reactions and investigate possible side reactions, the HPLC chromatographs of the substoichiometric dithionite reduced quinone samples were measured and compared to that of their untreated, borohydride, and excess dithionite reduced chromatagraphs. Sample LC chromatographs are given in supporting information. A.3

In this way, it was possible to quantify the disappearance of the quinone and the appearance of the hydroquine due to the addition of dithionite. An example of the chromatographs for the untreated, hydroquinone, and substoichiometric dithionite reduced sample for duroquinone is given in figure 3.10 The quinone and hydroquinone peaks are highlighted.

Using the peak areas of the chromatograph and comparing with the quinone and hydroquinone chromatographs, the quinone and hydroquinone in each substoichiometric dithion-

ite reduction was quantified as the % lost and % gained, respectively. The concentration of the quinone lost and the hydroquinone formed were divided by the concentration of dithionite added to the sample to obtain a stoichiometry of the quinone reduced to dithionite added and hydroquinone formed to dithionite added. An example calculation including chromatographs is given in supporting information. Quinone Disappearance:

$$\frac{\text{Peak area of Partially Dithionite Reduced Sample at Q retention time}}{\text{Peak Area of Untreated Sample at Q retention time}} =$$

Fraction of Quinone Remaining (Qfrac) = Qfrac*Total Quinone Concentration =

Concentration of Quinone Remaining

Total Quinone Concentration – Concentration of Quinone Remaining = Quinone

Reduced

$$\frac{Quinone\ Reduced}{Concentration\ of\ Dithionite\ added\ to\ Sample} = \text{Stoichiometry of Quinone Reduction}$$

based on Quinone Disappearance

(3.8)

Hydroquinone Formation:

$$\frac{\text{Peak area of Partially Dithionite Reduced Sample at HQ retention time}}{\text{Peak Area of Borohydride Reduced Sample at HQ retention time}} =$$

Fraction of Hydroquinone Formed (HQfrac)

HQfrac*Total Quinone Concentration= Concentration of Hydroquinone

Formed

$$\frac{Hydroquinone\ Formed}{Concentration\ of\ Dithionite\ added\ to\ Sample} = \text{Stoichiometry of Quinone}$$

Reduction based on Hydroquinone Formation

(3.9)

The stoichiometry of the quinone loss and hydroquinone formation for the model quinones is given in table 3.1 Based on whether these ratios are 1) equivalent to dithionite addition and 2) equivalent to each other, we can draw conclusions about the stoichiometry of dithionite reduction, possible side reductions by sulfite, and products.

As discussed in respect to the optical changes, duroquinone is not reactive to the sulfite side reaction. Therefore, its stoichiometry of reduction by dithionite is approximately 1:1, and the hydroquionone appearance matches this ratio. The juglone and 5,8-dihydroxy-1,4-naphthoquinone were not able to be effectively separated on the HPLC chromatograph, so only their quinone disappearance is calculated. In general, hydroquinone appearance resembles the expected stoichiometry of 1 hydroquinone formed per equivalent of dithionite added. This ratio also follows largely as expected for the quinone disappearance, except for 2,3-dimethyl-*p*-benzoquinone, 2,5-dimethyl-*p*-benzoquinone, naphthoquinone, and juglone, which are much larger than expected. It should be noted however that with the exception of the 2,3-dimethyl-*p*-benzoquinone, these ratios have very high error relative to the value, so they should not be used quantitatively. These ratios would require a deeper investigation to explain which is outside the scope of the current work. A more in depth discussion comparing LC results for 2,3-dimethyl-*p*-benzoquinone and duroquinone is given in Supplemental Information A.3. Based on the value for most of the quinones and the high error in the majority of diverging results, the dithionite reduction of the model quinones was concluded to primarily produce the hydroquinone, noting that there may be some interference by sulfite side reactions and so quantification of quinone content in CDOM based on dithionite reduction should be treated as an estimate rather than an exact value.

Quinone	Stoichiometry of Reduction based on Quinone Disappearance	Stoichiometry of Reduction based on Hydroquinone Appearance
2,3-dimethyl-p-benzoquinone	5.6±0.6	1.9±0.3
2,5-dimethyl-p-benzoquinone	4.7±2.8	1.1±0.2
2,6-dimethyl-p-benzoquinone	1.6±0.3	1.18±0.09
trimethyl-p-benzoquinone	1.6±0.4	1.05±0.05
duroquinone	1.2±0.1	1.18±0.06
naphthoquinone	5.3±2.9	1.9±1.3
juglone	4.1±2	n/a
5,8-dihydroxy-1,4-naphthoquinone	0.6±0.2	n/a

Table 3.1: Stoichiometry of quinone disappearance and hydroquinone appearance for model quinone samples.

3.4 Conclusions

The dithionite reduced spectra of model quinones did not produce the expected sum of the partial quinone and hydroquinone spectra, but showed some contribution from a unique shape which was attributed to formation of a sulfonated hydroquinone resulting from sulfite produced as a product of the reduction. Sulfite reduction of quinones is supported by literature (*109*, *110*). This sulfite reduction has not previously been linked to the reaction of quinones with dithionite. However, upon reduction by dithionite, sulfite is formed in solution which then can react with the quinones. It is proposed that the discrepancy between the quinone reacted by dithionite and the hydroquionone formed by dithionite for the model quinones, except duroquinone, is due to this reaction with sulfite forming the sulfonated hydroquinone product in addition to the hydroquinone formed by dithionite reduction. The dithionite reduction forms the hydroquinone as expected, but the sulfite produced in this reduction then may go on to react with additional quinones in the sample to produce sulfonated hydroquinone. In general, more reactive quinones with available sites for the addition of SO_3 were more reactive to sulfite. Duroquinone, with no available substitution sites, does not react at all, nor does the anthraquinone, due to its stability. The LC studies were not applied to the anthraquinones due to their ionic nature and the absense of evidence of sulfite side reactions based on the absorption spectra.

Since hydroquinone appearance basically follows from dithionite addition, this method was applied to CDOM samples to study the impact on fluorescence of the quinone moieties and to approximate a quinone content, bearing in mind that we cannot quantify sulfite side reactions.

Chapter 4: Quinone Contribution to Optical Properties of CDOM Standards and Natural Waters

4.1 Introduction

As discussed in Chapter 1, aquatic ecosystems contain CDOM. CDOM is composed of a range of organic molecules, including quinones. Quinones in CDOM are thought to be redox active, photochemically active, and contribute to charge transfer interactions in the optical properties of CDOM. (*48*, *52*, *76*)

The subject of the contribution of quinones to CDOM optical properties is a source of controversy. (*24*, *83*, *86*, *92*, *93*, *123*). Some studies report significant or even primary contribution of quinones to fluorescence emission, (*123*, *124*), others report minor and reversible changes in fluorescence emission due to the reduction of quinones (*24*, *86*, *92*)

To investigate the contribution of quinones to the optical properties of CDOM, Del Vecchio et. al. (*48*) compared the results of borohydride reduction of CDOM standards to that of dithionite reduction. Borohydride irreversibly reduces ketones and aldehydes and reversibly reduces quinones under anoxic conditions, while dithionite does not reduce ketones and aldehydes and reversibly reduces quinones under anoxic conditions. (*48*). Borohydride reduction of CDOM standards resulted in significant loss of absorption and increase in fluorescence emission, which were largely irreversible. (*48*). Dithionite reduction showed small, reversible changes in absorbance and fluorescence. Therefore, it was tentatively concluded that ketones and aldehydes show greater impact on the optical proper-

ties of CDOM standards than do quinones.(*48*). Similar spectral changes upon borohydride reduction are observed elsewhere. (*1*, *125*)

CDOM optical properties have also been observed as a function of pH for CDOM standards. (*1*) Increasing pH reversibly increases absorbance, suggesting the presence of phenols and carboxylic acids in these samples. (*1*)

In this chapter, the CDOM standards were examined using the methods described in Chapter 3 for dithionite reduction to compare to previous results from Del Vecchio et. al. (*48*) and electrochemical results from Aeschbacher et. al.(*101*) Natural water extracts from the North Pacific Ocean (NPO) at varying depths and from locations in the Chesapeake Bay and its tributaries were studied using the same methods.

CDOM standards studied were Elliot Soil Humic Acid (ESHA), Leonardite Humic Acid (LHA), Lignin Activated Carbon (LAC), Pony Lake Fulvic Acid (PLFA), Suwanee River Humic Acid (SRHA), Suwanee River Fulvic Acid (SRFA), and Suwanee River Natural Organic Matter. (SRNOM).

The location of the North Pacific Ocean sampling is shown in figure 4.1. NPO extracts were collected in December 2014 at Station ALOHA at 22 ° 45' N and 158° 00' W using a surface pumping system to collect water from 2-15 m depth and a rosette sampler to collect deeper water samples. Samples were acidified, filtered through a 0.2 μm filter, and drawn over C18 columns. The columns were rinsed with water to remove salts and stored in the dark at 4° C. DOM was eluted with methanol and vacuum evaporated until dry. The dried sample was then redissolved in ultrapure water and pH adjusted to neutral pH. This extract was then stored frozen until use. (*1*)

NPO extracts were previously studied under borohydride reduction and pH titration. (*1*) Like the CDOM standards, borohydride reduction resulted in significant loss of absorption and increase in fluorescence. Absorption also increased with pH for both the untreated and reduced samples. These results are given in much greater detail in (*1*). A map of the

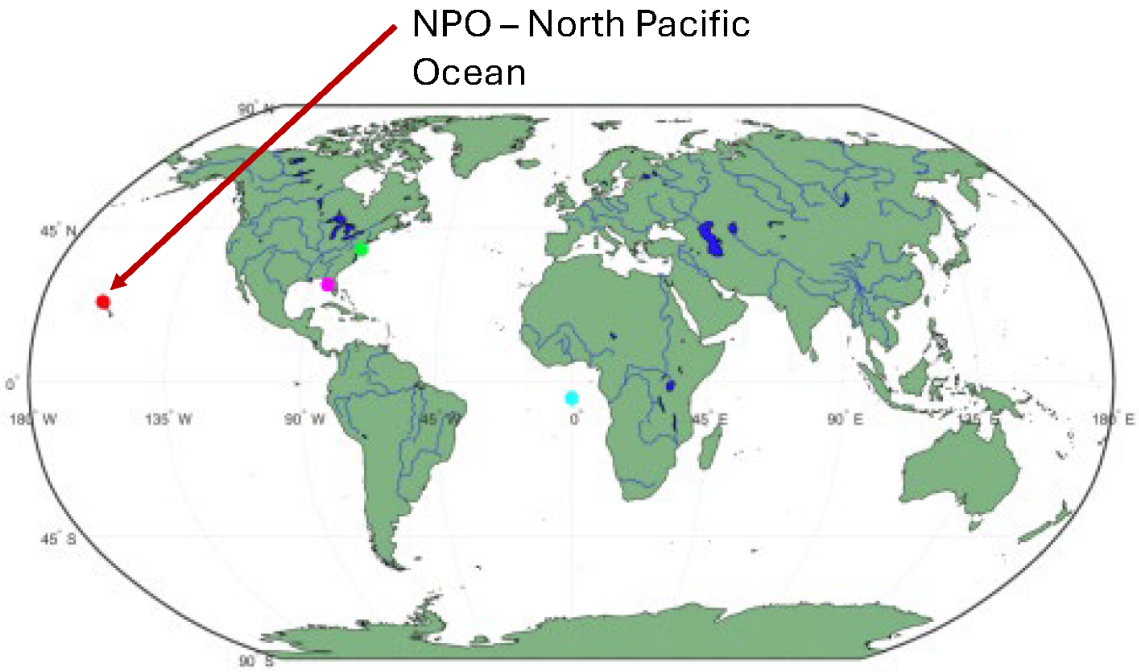


Figure 4.1: Location of NPO sample site. Figure is from Bianca 2020(*32*) with arrow and label added for clarity.

Chesapeake Bay area sample sources is shown in figure 4.2. Chesapeake bay samples were collected by the Maryland Department of Energy or off of piers in the Chesapeake bay from August 2021-March 2022 (*2*) Samples were collected from the top 1 meter of water and 0.2 μm filtered. The samples were acidified to pH 2 and drawn over C18 columns. The DOM was eluted from the columns using methanol, vacuum evaporated, redissolved in ultrapure water, and pH adjusted back to neutral pH.

Borohydride reduction and pH titration of the Chesapeake bay samples showed absorbance loss and fluorescence increase comparable to the NPO samples, although optical changes were more intense in the bay samples. (*2*) These results are discussed in much greater detail in (*2*).

These previous analysis are mentioned to show that for the CDOM standards and natural water extracts examined in this study, borohydride reduction is shown to significantly impact CDOM optical properties, indicating the presence of carbonyl groups - ketones, aldehydes, and quinones. Therefore, results from dithionite reduction are compared to these results to draw conclusions about the relative contribution of quinone moieties to these observed changes.

Natural water extracts are often used to study the CDOM structure and properties of natural water samples. The bulk water samples are typically very dilute in terms of CDOM concentration, so direct study on these samples requires highly sensitive techniques. (*2*, *35*) It has been found that while the extraction methods used may preferentially extract higher molecular weight material, in terms of the structural and optical properties the extracts were very similar to bulk CDOM samples, and thus good representatives of the bulk samples. (*35*)

Since naturally occurring quinones are largely from plant sources (*105*, *120*, *121*), or from anthropogenic sources(*76*), it is expected that quinone content will be higher from terrestrial sources (inland lakes and rivers) than in the ocean. Thus the Chesapeake Bay

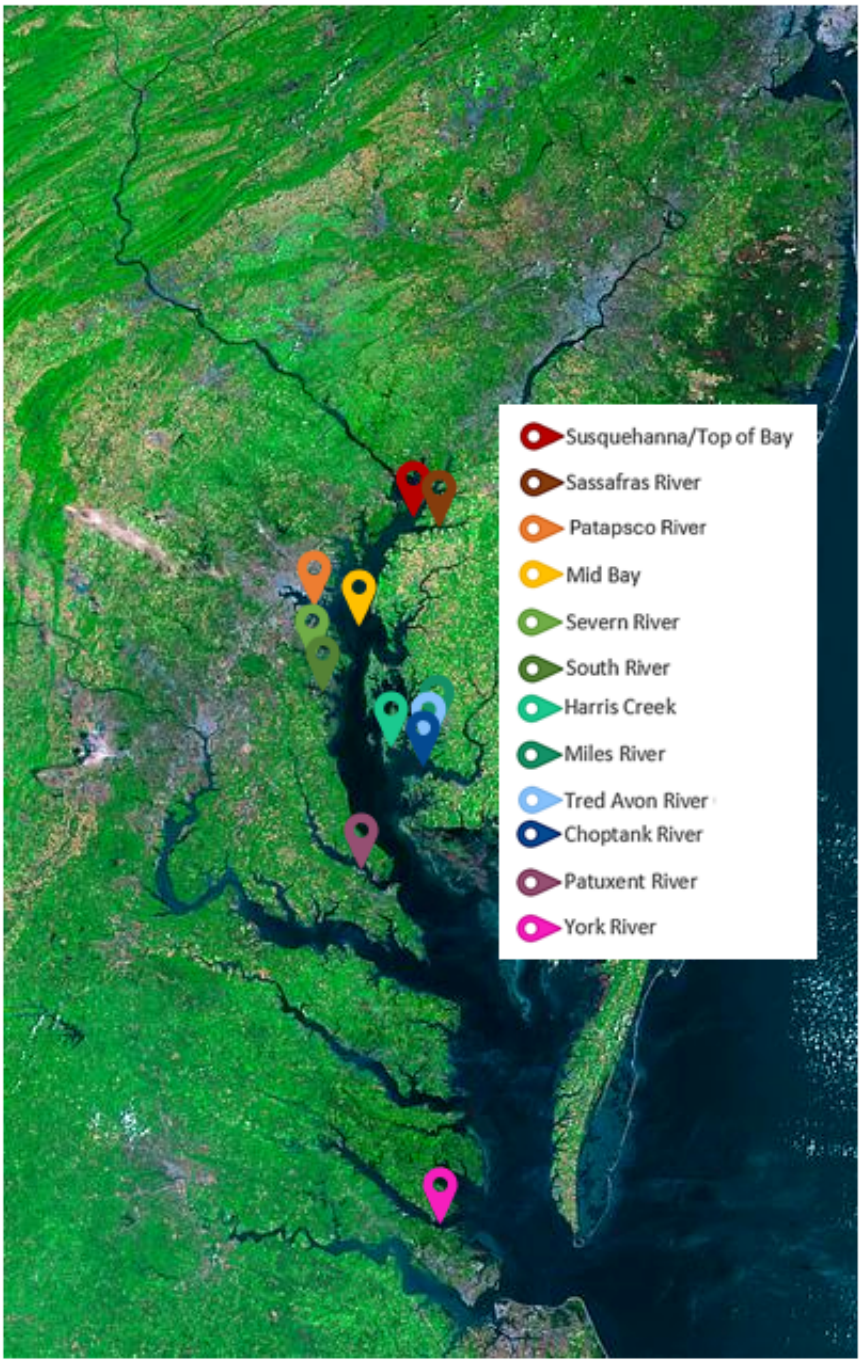


Figure 4.2: Chesapeake Bay area sample sites.(*2*)

area samples, particularly the river tributaries, are expected to have a higher quinone content than NPO samples. The quinone content from CDOM standards will also likely be higher, as they are from inland river and lake soil samples rather than natural water samples themselves.

4.2 Experimental

4.2.1 Absorbance Measurements and Quinone quantification

CDOM standards were received from International Humic Substances Society (IHSS). These standards include Elliot Soil Humic Acid (ESHA), Leonardite Humic Acid (LHA), Lignin Activated Carbon (LAC), Pony Lake Fulvic Acid (PLFA), Suwanee River Humic Acid (SRHA), Suwanee River Fulvic Acid (SRFA), and Suwanee River Natural Organic Matter (SRNOM). They were dissolved in ultrapure water and 0.5mM phosphate buffer to make 100mg/L solution, then diluted as noted for dithionite reduction experiments. C18 extracts were used as received from (*1*) and (*2*). They were diluted in ultrapure water to an absorbance within the linear range of the instrument for quinone quantification experiments.

The methods from 3.2.1 were adapted to the CDOM standards and natural water samples. The untreated UV-Vis spectra for the untreated sample was collected as described in 2.2. The absorbance spectra of the potassium ferricyanide sample was also collected prior to dithionite reduction. As before, 1 mL of deoxygenated N/100 NaOH was transferred to a vial of 5mg sodium dithionite to make the dithionite stock. However, for these experiments, since the quinone content is expected to be very small, this stock was further diluted by transferring 10-100 μL of this stock to another vial of 1 mL N/100 NaOH. This vial was then used for the reduction of the CDOM sample and the ferricyanide. Ten to twenty microliters of this stock was transferred anaerobically to both the CDOM and the ferricyanide,

then the UV-Visible spectra of both were collected. This process was repeated, increasing the volume of the addition as needed up to 100 μL, until the dithionite absorbance was observed in the CDOM sample, indicating that it was in excess.

Dithionite in each addition was quantified by disappearance of the ferricyanide absorbance as discussed in chapter 3. To calculate the estimated quinone content, for the addition to the CDOM where dithionite was seen in excess, the excess dithionite was calculated by the increase in absorbance at 316nm using a molar absorptivity of 8000 M^{-1} cm^{-1} for the dithionite. (*100*). Then, the dithionite reacted was calculated by subtracting this excess dithionite value from the sum of the dithionite added in all additions as calculated from the ferricyanide sample. This value is equivalent to the estimated quinone content in that sample. For CDOM standards, these values were scaled to 100 mg/L of the CDOM.

4.2.2 Fluorescence Measurements

The CDOM and natural water extracts were diluted to an absorbance ¡0.1 absorbance units at 240 nm. The fluorescence spectra was collected as a excitation-emission matrix, using excitation wavelengths from 240-600 in 20nm increments and collecting the emission spectra from 290-800nm using Rayleigh Masking 1st and 2nd order corrections. The wavelength ranges where Rayleigh scattering occurred were removed from final spectra. Bandpasses were set to 4 nm. The spectra were collected for the untreated sample and the sample with excess dithionite added as described in Ch. 3.

Fluorescence spectra are blank subtracted, and baseline corrected as necessary. The fluorescence difference spectra are calculated as the fluorescence of the untreated sample subtracted from the fluorescence of the reduced sample. The values are averaged between different excitation wavelengths and the three trials to show one average change in fluores-

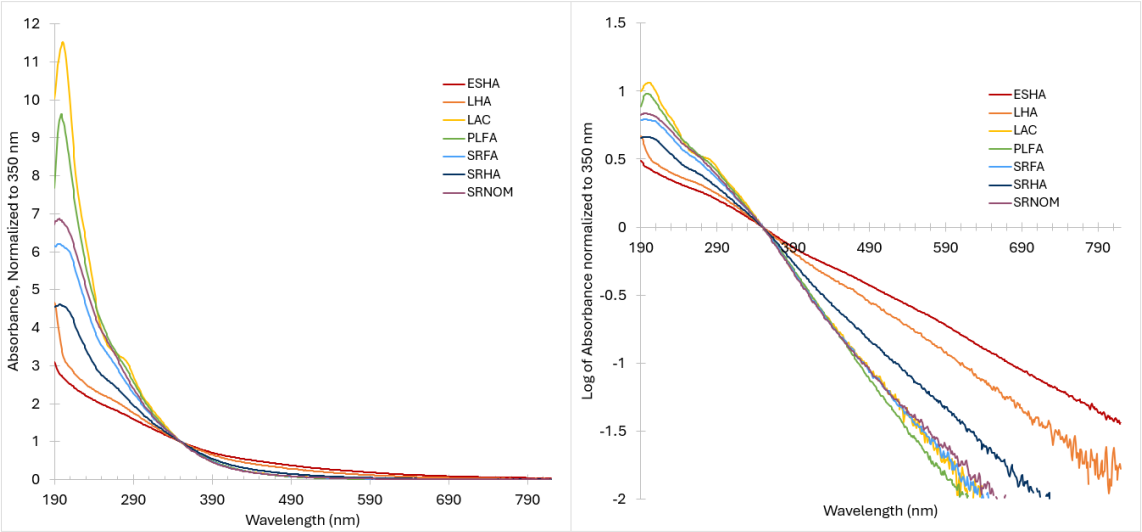


Figure 4.3: [Left] Absorption spectra of CDOM standards normalized to their absorbance at 350 nm [Right] The log of the normalized absorbances of the CDOM standards.

cence vs. wavelength.

4.3 Results and discussion

4.3.1 Influence of quinones on Optical Properties

4.3.2 CDOM Standards

The absorbance spectra of the CDOM Standards are shown in figure 4.3. Although CDOM spectra are similar in shape, different samples show more or less absorbance in certain bands/regions due to different functional groups and degree of charge transfer. These standards represent a range of sources of CDOM. ESHA and LHA show the greatest proportional long wavelength absorption, suggesting a significant degree of charge transfer interactions in these samples; meanwhile LAC and PLFA show the greatest proportional short wavelength absorbance, suggesting high relative content of electron-rich phenol and carboxylic acid species and lesser contribution by electron acceptors and charge transfer.

To examine the relative impact of quinone moieties on this absorption, the change in absorption due to dithionite reduction of these standards is given in figures 4.4, 4.5, and 4.6. This data is presented as the log of the absorbance of each standard normalized to its absorbance ate 350 nm. This is done to present data in a format that is (largely) independent of concentration, and to emphasize changes in shape at long wavelength that would otherwise be difficult to see. ESHA and LHA show a decrease in long wavelength absorption, though the effect is much more pronounced in ESHA, consistent with a loss of long wavelength charge transfer interactions with the reduction of quinone moieties. The remaining samples show little change, if anything a slight increase at longer wavelengths in absorbance, but this is difficult to state definitively as absorbance is small in these samples. Data points with log(Abs/Abs 350)$<$-2 is excluded from these plots because the fluorescence is indistinguishable from noise.

The fluorescence of these samples prior to and following dithionite reduction is shown in figures 4.7, 4.8, and 4.9. The fluorescence data is presented in units of Quinine Sulfite Equivalents divided by the absorbance of the sample at 240 nm, the first excitation wavelength in the EEMS scan. This is done to give a magnitude which is independent of concentration within normal limits of fluorescence ($<$0.1 absorbance). ESHA shows a slight loss of fluorescence at long wavelength, consistent with the reduction of quinone moieties decreasing charge transfer interactions within the sample. Otherwise, samples showed little to no change that could be distinguished from noise in the measurement. If anything, a slight increase in fluorescence at shorter wavelengths can be observed, consistent with the formation of hydroquinone moieties from quinones, but there is no corresponding loss of long wavelength fluorescence in these samples, suggesting what quinones may be present have little impact on the charge transfer interactions in these samples. (*48*) Del Vecchio et. al. (*48*) observed a significant increase in fluorescence upon dithionite reduction, which was not observed in this study. This may be partially due to pH effects, since their studies

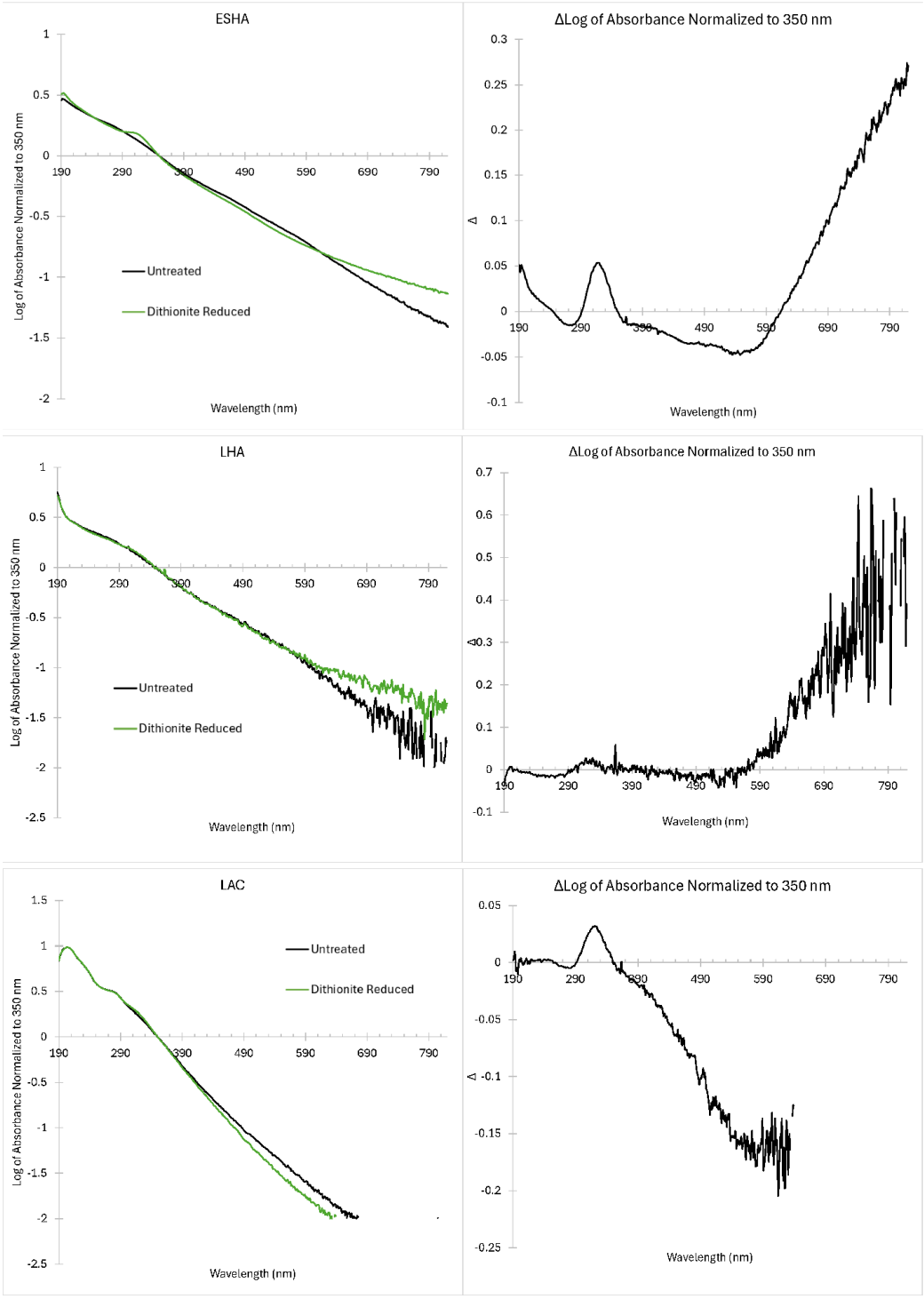


Figure 4.4: Log of normalized absorbance and change due to reduction for untreated and dithionite reduced ESHA, LHA, and LAC

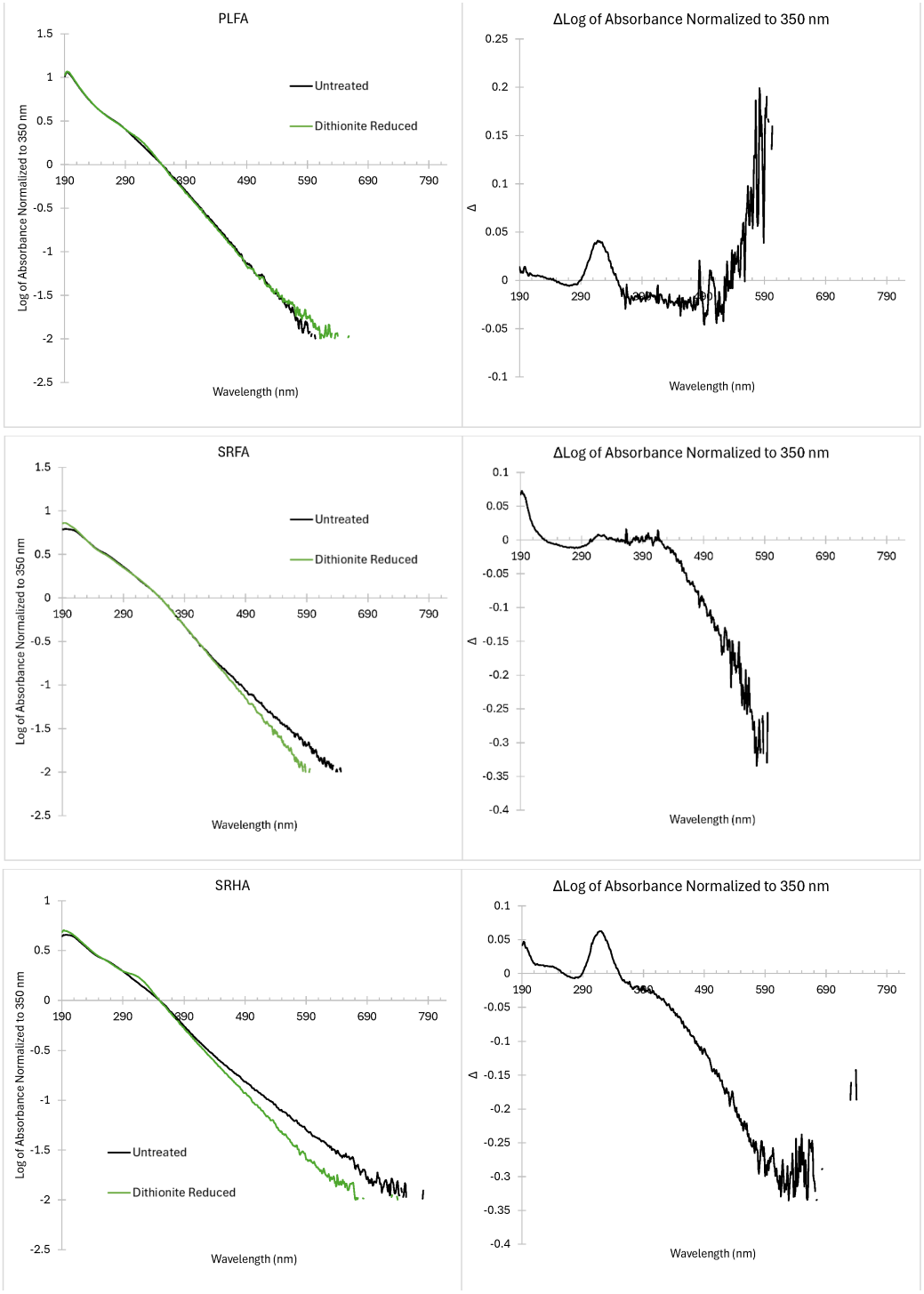


Figure 4.5: og of normalized absorbance and change due to reduction for untreated and dithionite reduced PLFA, SRFA, and SRHA

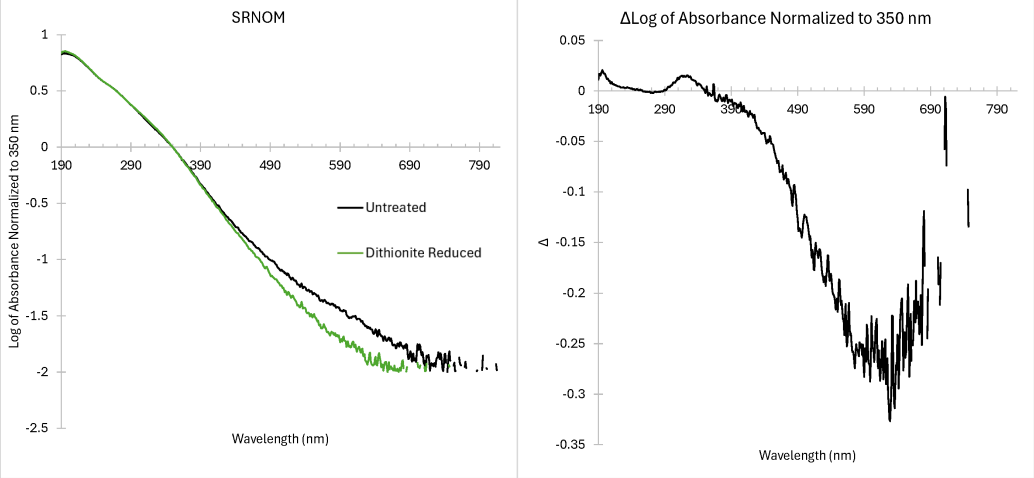


Figure 4.6: Log of normalized absorbance and change due to reduction for untreated and dithionite reduced SRNOM

were run at pH 10 and in this study samples were buffered at pH 7; but further studies on the pH effects on the fluorescence change of CDOM upon dithionite reduction would need to be investigated to confirm this.

As compared to borohydride reduction of the CDOM standards, which showed significant changes in both absorbance and fluorescence (*48*), dithionite reduction showed little impact on the optical properties of the CDOM standards. These results suggest that aldehydes and ketones are the primary carbonyl compounds in CDOM responsible for the observed optical properties rather than quinone structures.

4.3.3 NPO C-18 Extracts

The absorbance of the North Pacific Ocean (NPO) samples normalised to their absorbance at 350 nm, and the natural log of the normalized absorbance, are shown in figure 4.10. Plotting the natural log of the absorbance allows more detailed comparison than is allowed by the very similar absorption spectra. The log of the absorption normalized to the absorption at 350 nm for the untreated and dithionite reduced NPO extracts are given

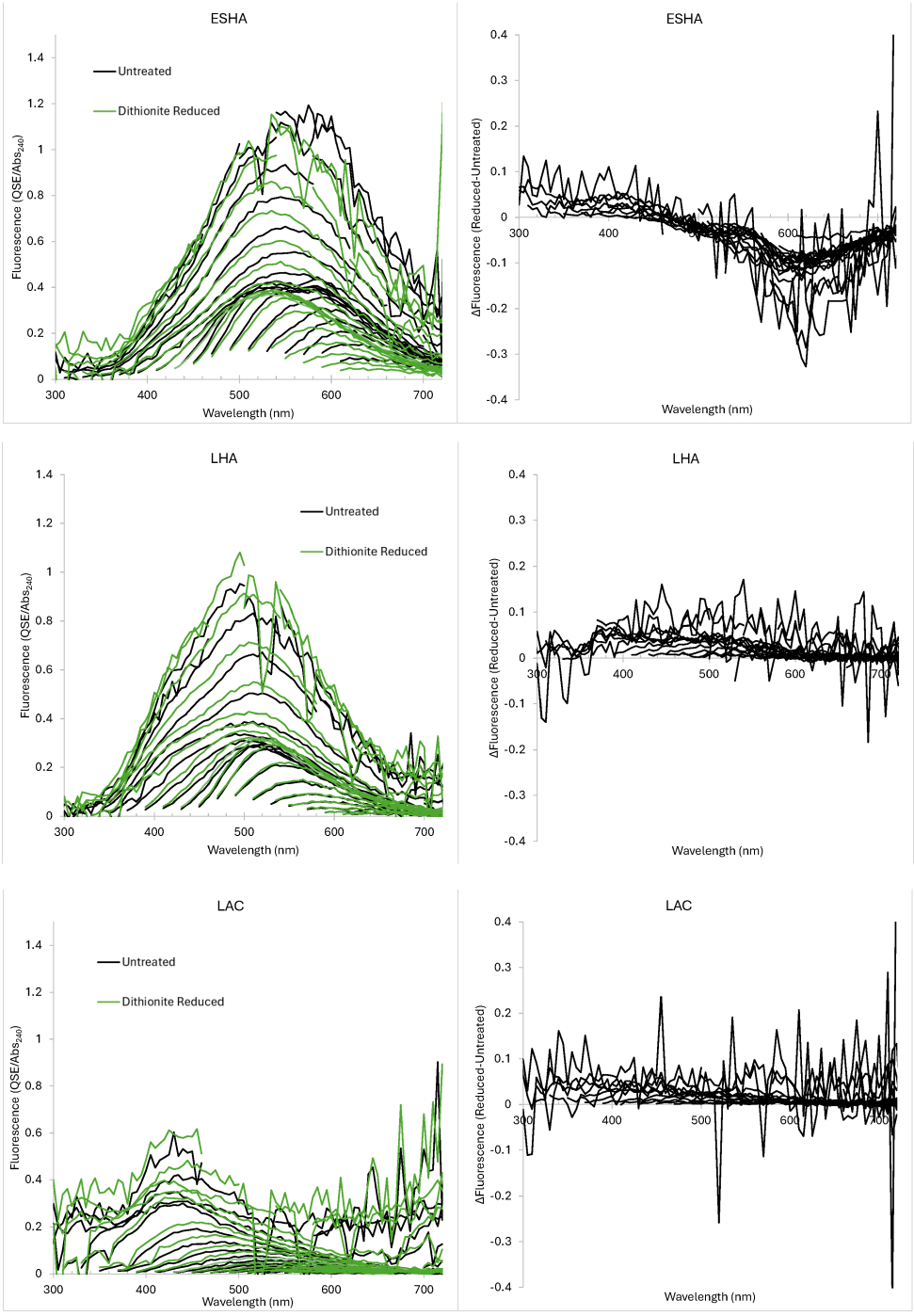


Figure 4.7: (Right) Fluorescence in QSE scaled to absorbance at 240 nm for ESHA, LHA, and LAC (Left) Change in Fluorescence in QSE scaled to absorbance at 240 nm due to dithionite reduction for ESHA, LHA, and LAC. Fluorescence spectra were obtained using excitation wavelengths from 240-600 in 20nm increments and collecting the emission spectra from 290-800nm.

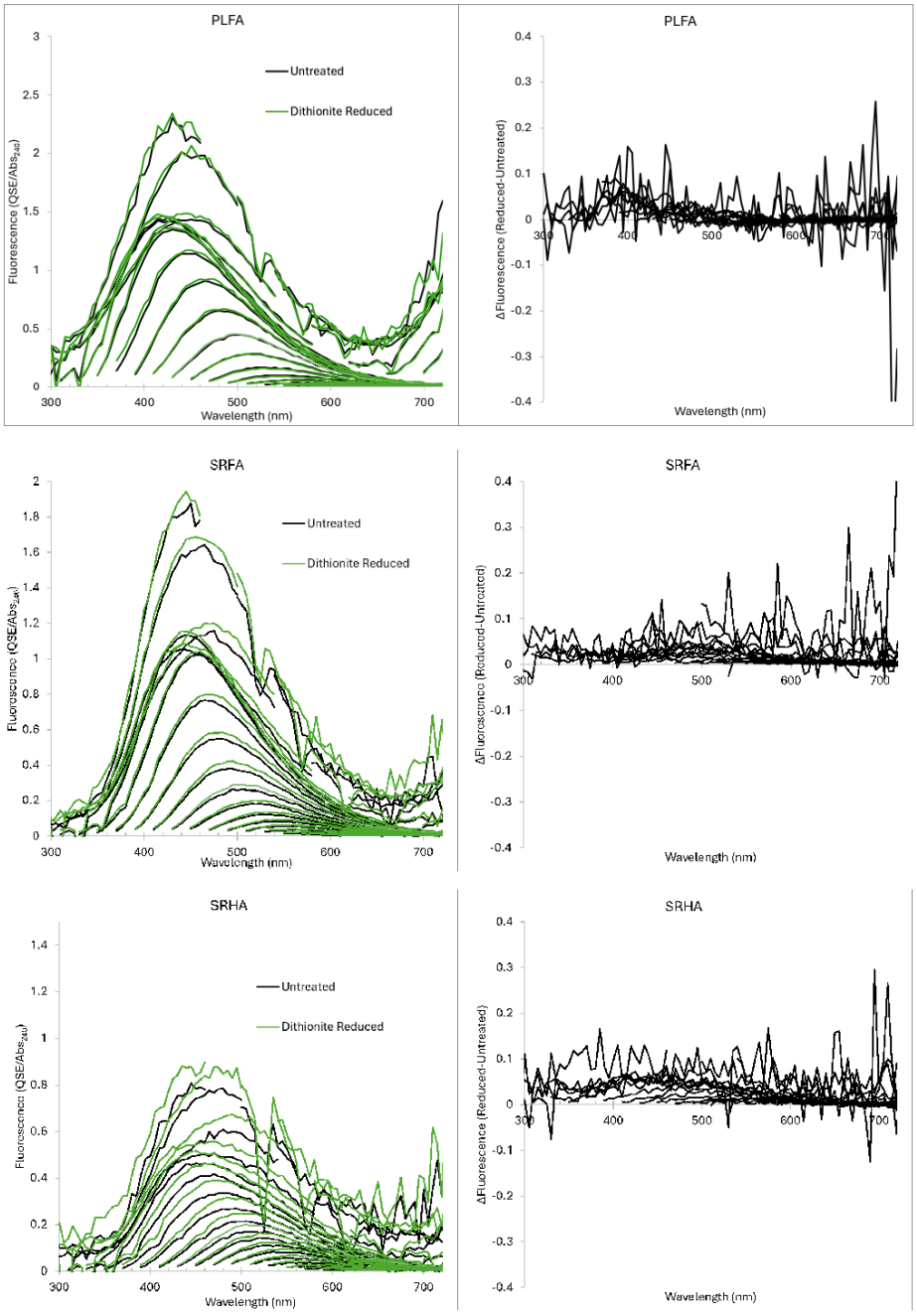


Figure 4.8: (Right) Fluorescence in QSE scaled to absorbance at 240 nm for PLFA, SRFA, and SRHA (Left) Change in Fluorescence in QSE scaled to absorbance at 240 nm due to dithionite reduction for PLFA, SRFA, and SRHA. Fluorescence spectra were obtained using excitation wavelengths from 240-600 in 20nm increments and collecting the emission spectra from 290-800nm.

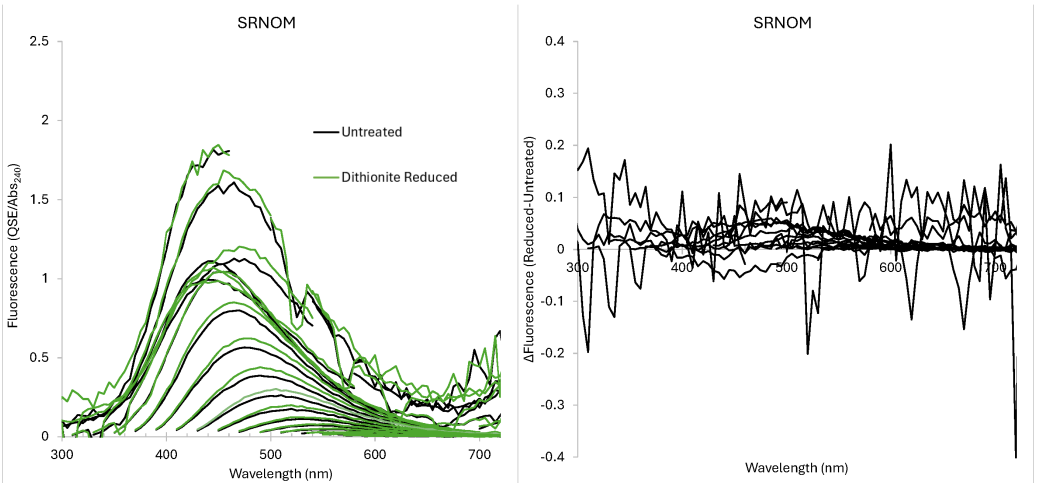


Figure 4.9: (Right) Fluorescence in QSE scaled to absorbance at 240 nm for SRNOM (Left) Change in Fluorescence in QSE scaled to absorbance at 240 nm due to dithionite reduction for SRNOM. Fluorescence spectra were obtained using excitation wavelengths from 240-600 in 20nm increments and collecting the emission spectra from 290-800nm.

in figures 4.11 , 4.12, and 4.13. To the right of these log spectra is the change between the untreated and dithionite reduced samples. Data points below log(abs/abs350) = -2 are excluded because they are indistinguishable from instrument noise. Aside from the excess dithionite peak observed at 316 nm, little change in the absorbance is observed due to dithionite reduction. There is a small loss of absorbance at wavelengths $<$350 nm for the surface NPO sample, so there may be some loss of charge transfer interactions in surface waters due to reduction of quinones. This difference is much smaller than the changes observed for borohydride reduction, (*1*, *2*), indicating that the impact of quinones is significantly less than that of ketones and aldehydes on these interactions.

The fluorescence spectra prior to and following dithionite reduction reported in units of QSE/Abs(240) is shown in figures 4.14, 4.15, and 4.16, and the change in fluorescence due to the reduction is shown to the right of the spectra.

There is very little observed change in the fluorescence for NPO samples due to dithionite reduction. For borohydride reduction of the same samples, significant increases of fluo-

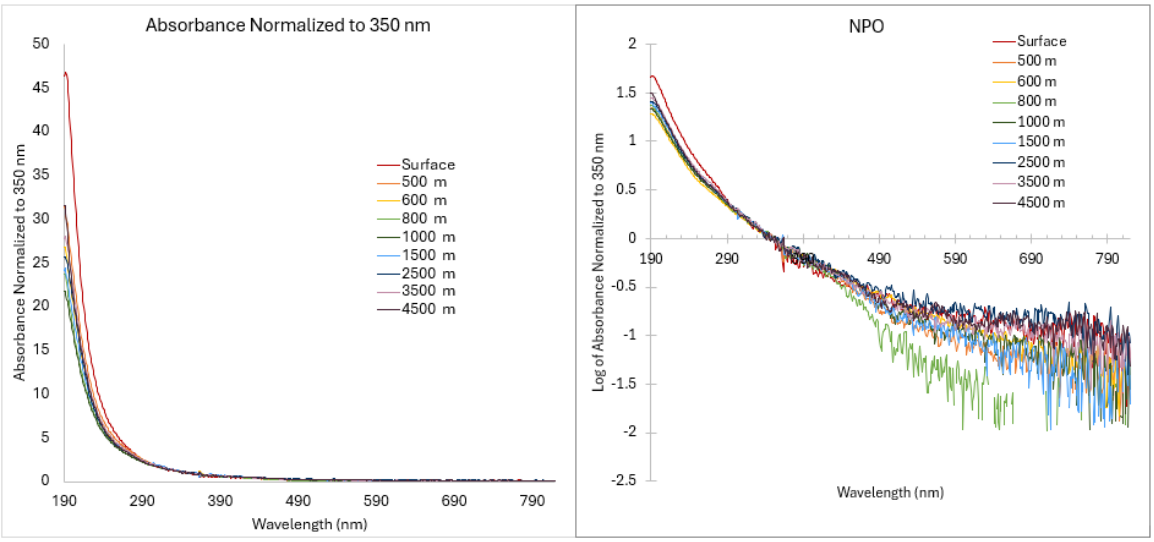


Figure 4.10: (Left) Absorbance normalized to 350 nm for NPO samples with increasing depth (Right) Log of the normalized absorbance of NPO samples with increasing depth

rescence intensity are observed. (*1*) This supports the conclusion that quinones contribute little to the optical properties of CDOM in the ocean and that ketones and aldehydes are far more relevant to the optical properties of marine CDOM than quinones. This follows from the earlier conclusions that the CDOM samples with the greatest quinone contribution were sources that contained a lot of vegetation or coal (ESHA, LHA, Suwanee River standards), and less quinone contribution was found due to microbial production (PLFA), which would be most relevant for the ocean samples.

4.3.4 Chesapeake Bay C-18 Extracts

Absorption spectra normalized to the absorbance at 350 nm and the natural log of normalized absorbance spectra for Chesapeake Bay area samples is shown in figure 4.17. The natural log of the normalized absorbance spectra for the untreated and dithionite reduced extracts are shown in figures 4.18, 4.19, 4.20, 4.21, and 4.22. There is very little observable change in absorbance due to dithionite reduction in the Chesapeake bay extracted samples.

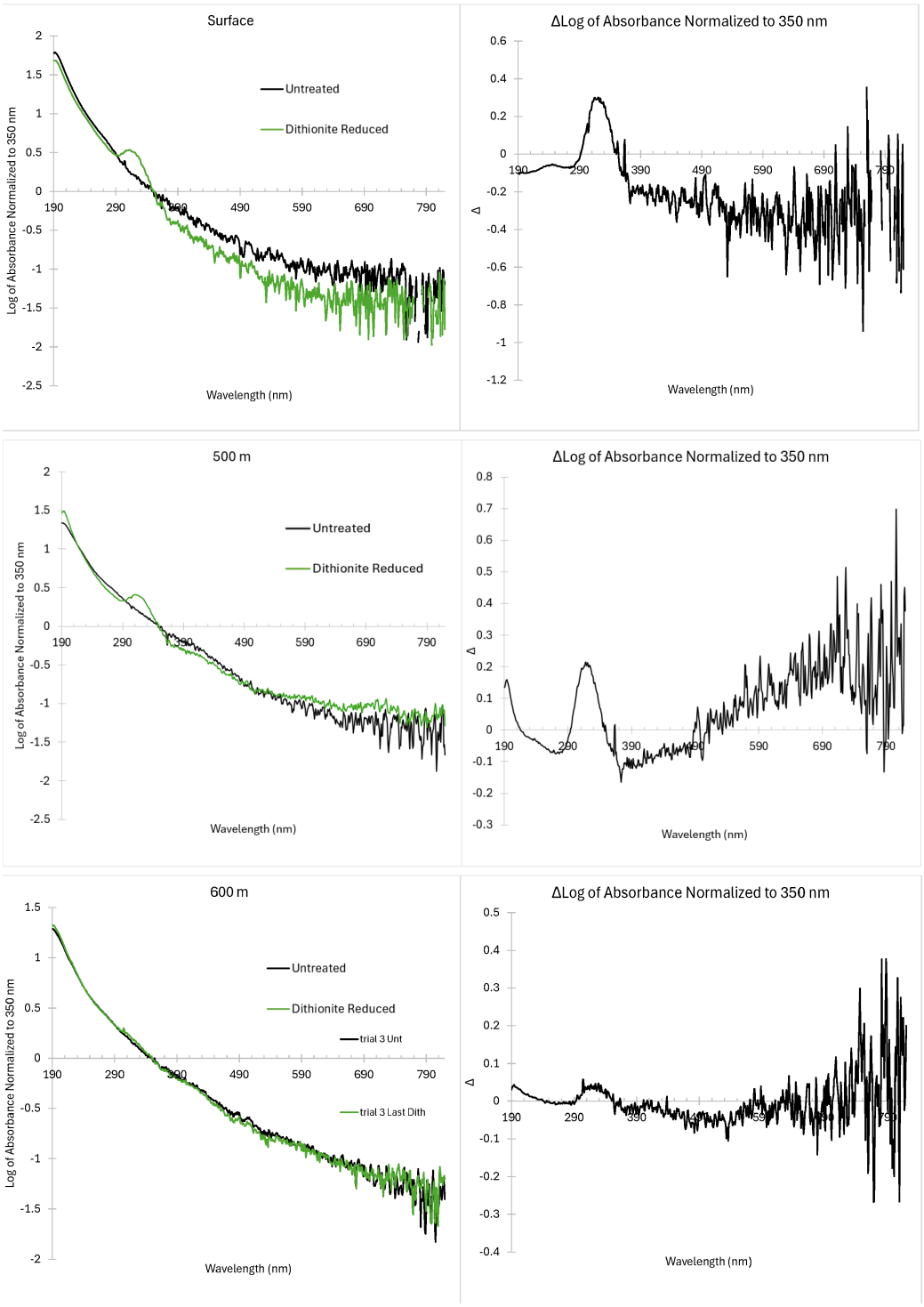


Figure 4.11: (Left) Log of Absorbance normalized to 350 for untreated and dithionite reduced NPO surface, 500 m, and 600 m samples. (Right) Change in log of absorbance normalized to 350 nm for NPO surface, 500, and 600 m

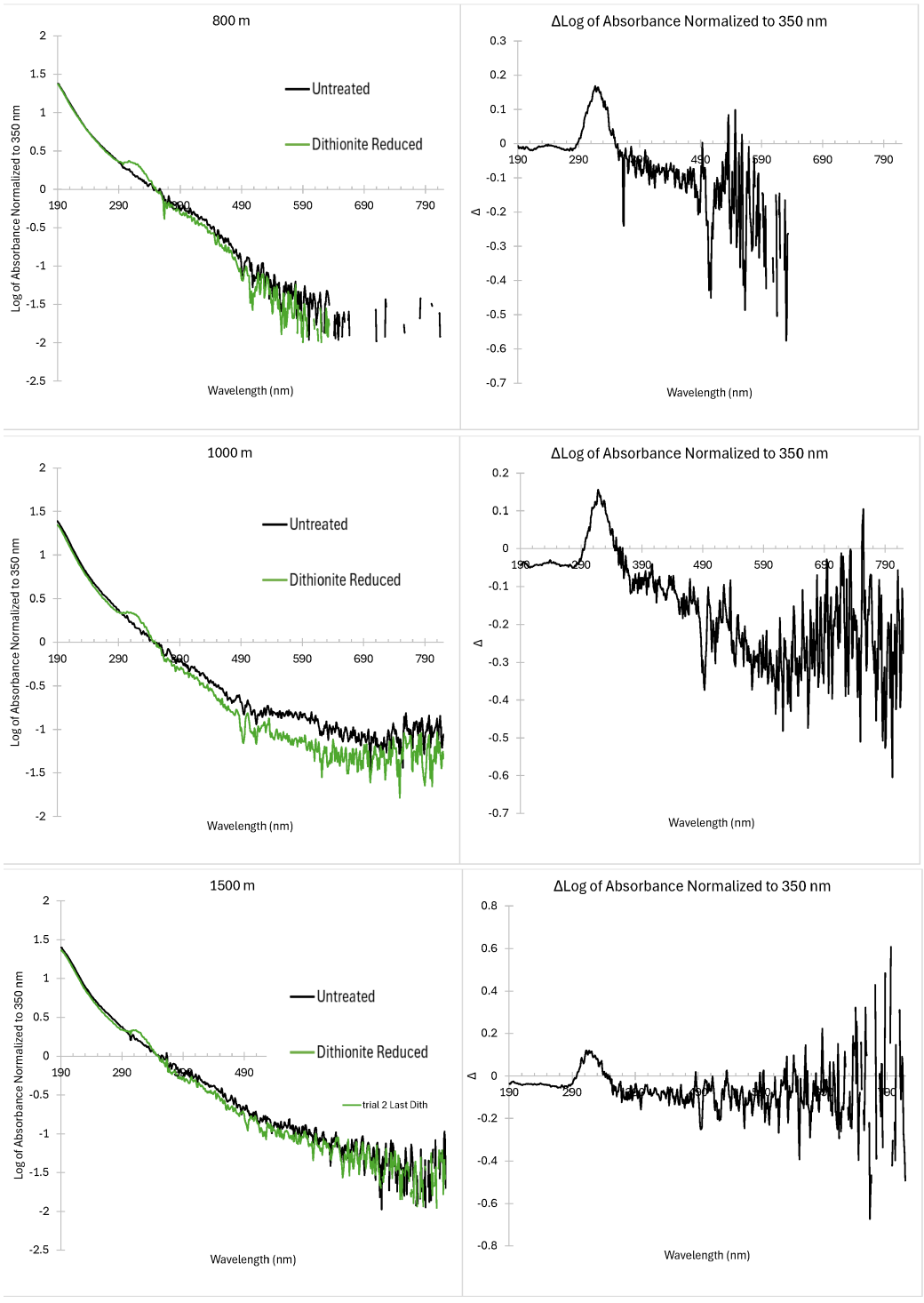


Figure 4.12: (Left) Log of Absorbance normalized to 350 for untreated and dithionite reduced NPO 800, 1000, and 1500 m samples. (Right) Change in log of absorbance normalized to 350 nm for NPO 800, 1000, and 1500 m samples

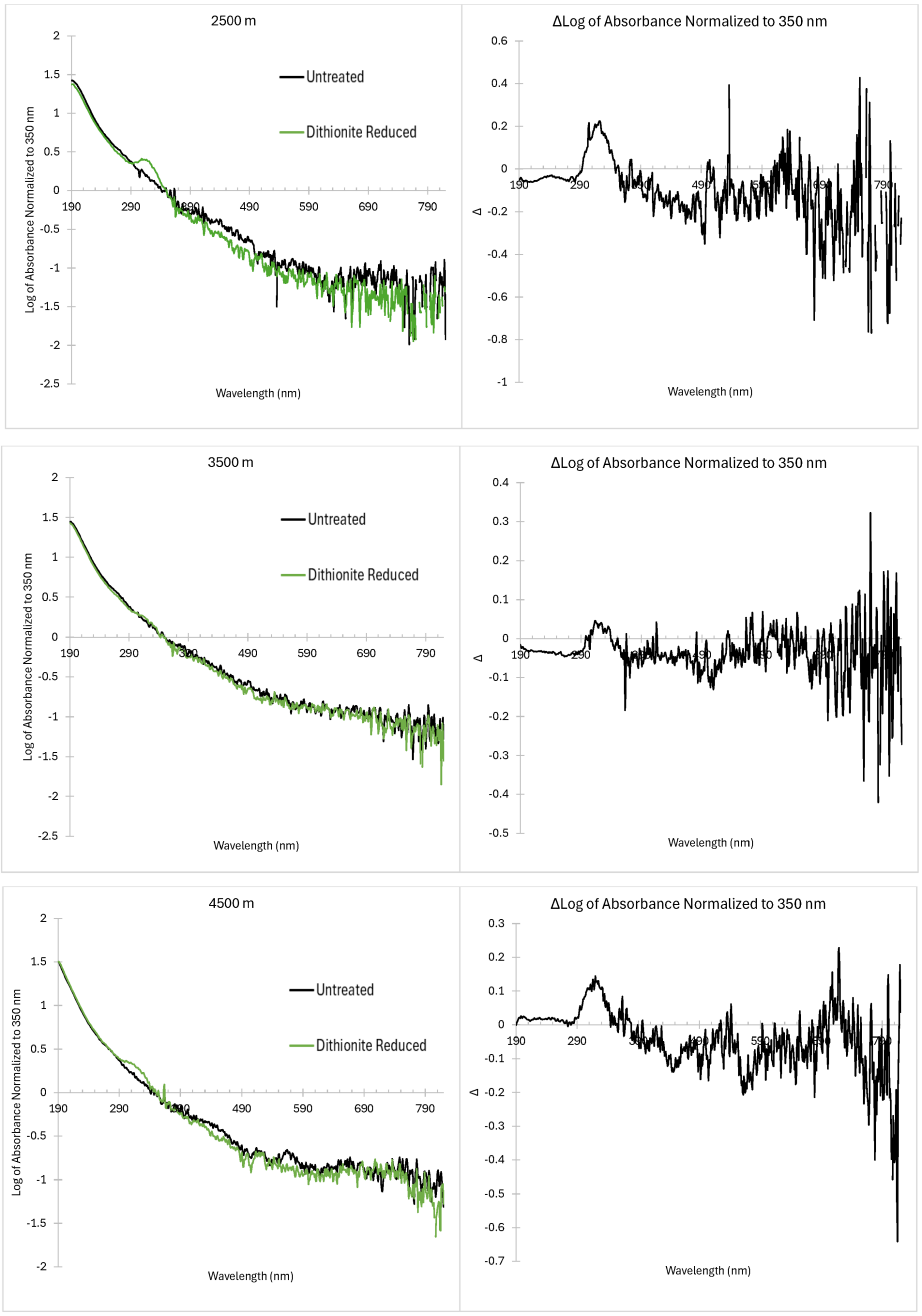


Figure 4.13: (Left) Log of Absorbance normalized to 350 for untreated and dithionite reduced NPO 800, 1000, and 1500 m samples. (Right) Change in log of absorbance normalized to 350 nm for NPO 2500, 3500, and 4500 m samples

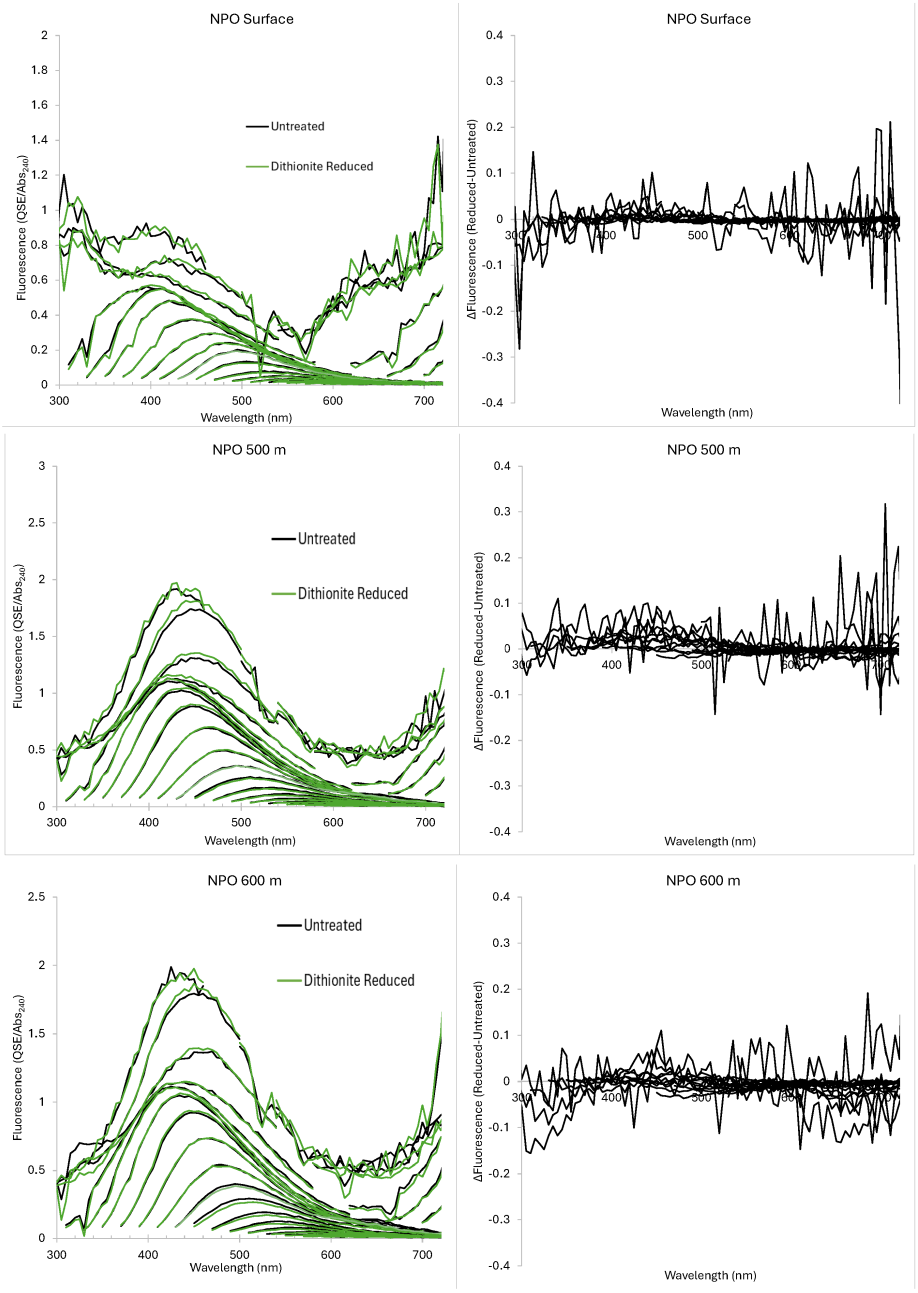


Figure 4.14: (Left) Fluorescence intensity normalized to the absorbance at 240 for the untreated sample, shown for untreated and dithionite reduced NPO surface, 500 m, and 600 m samples. (Right) Change in this fluorescence value due to dithionite reduction for NPO surface, 500, and 600 m samples. Fluorescence spectra were obtained using excitation wavelengths from 240-600 in 20nm increments and collecting the emission spectra from 290-800nm.

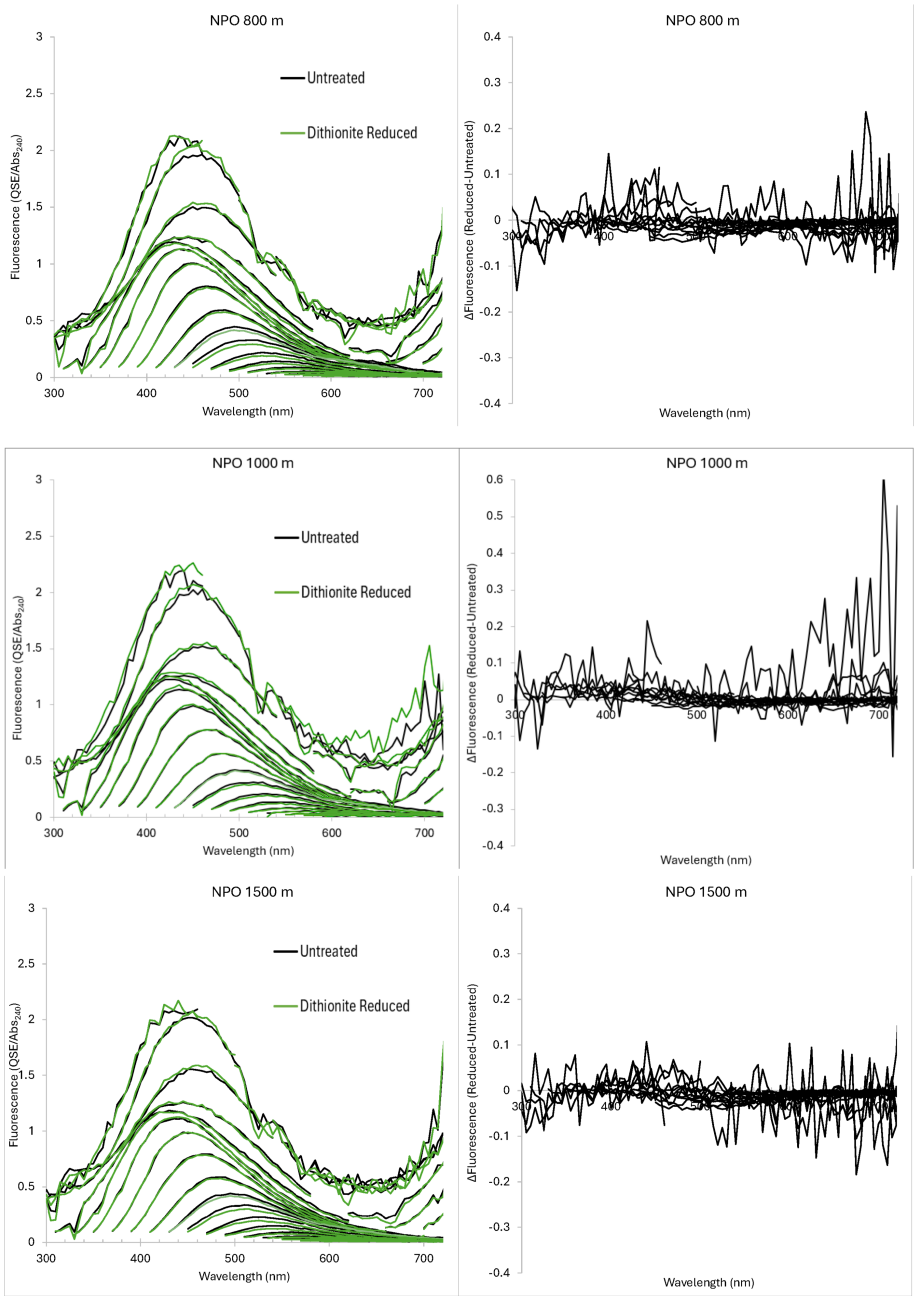


Figure 4.15: (Left) Fluorescence intensity normalized to the absorbance at 240 for the untreated sample, shown for untreated and dithionite reduced NPO 800, 1000, and 1500 m samples. (Right) Change in this fluorescence value due to dithionite reduction for NPO 800, 1000, and 1500 m samples. Fluorescence spectra were obtained using excitation wavelengths from 240-600 in 20nm increments and collecting the emission spectra from 290-800nm.

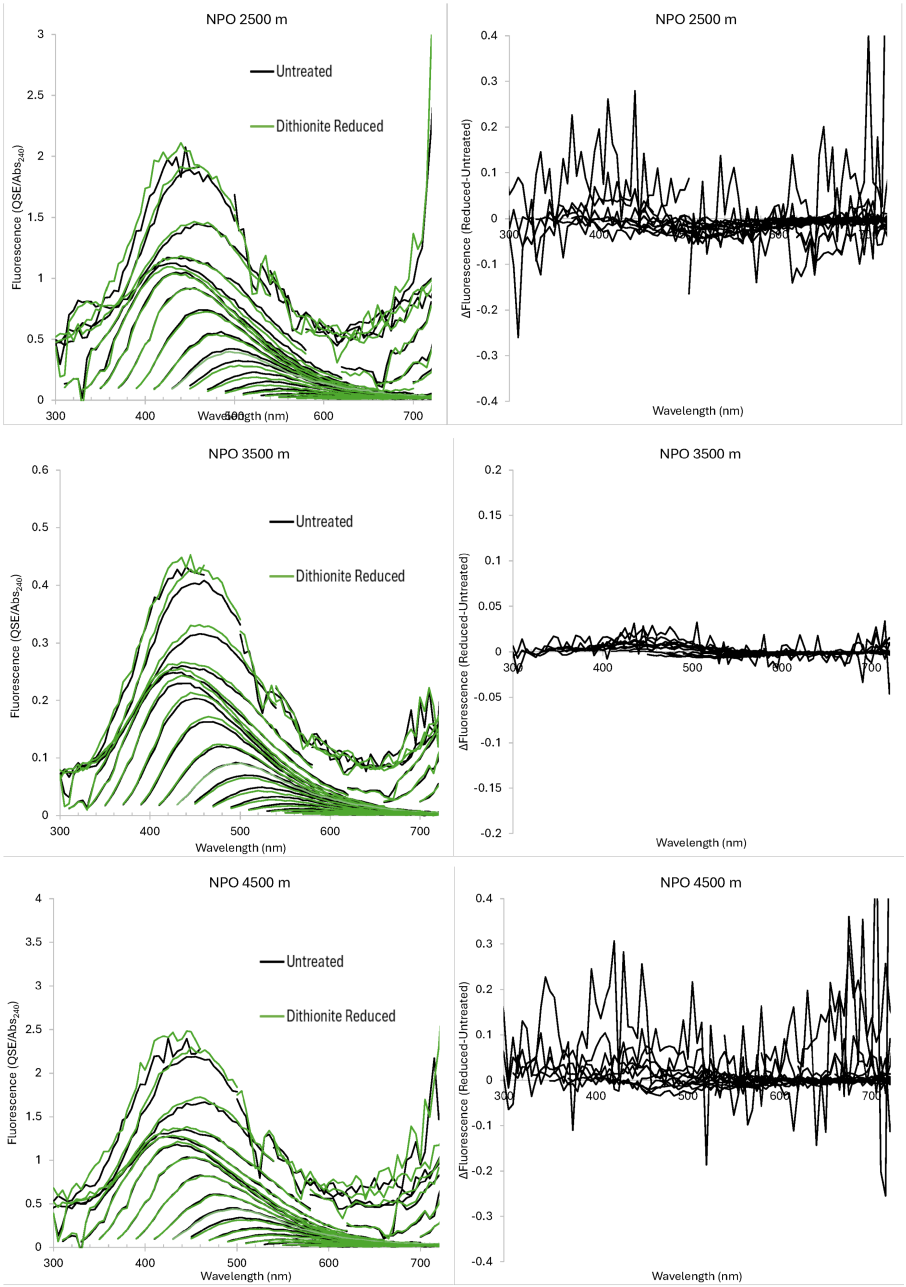


Figure 4.16: (Left) Fluorescence intensity normalized to the absorbance at 240 for the untreated sample, shown for untreated and dithionite reduced NPO 2500, 3500, and 4500 m samples. (Right) Change in this fluorescence value due to dithionite reduction for NPO 2500, 35000, and 4500 m samples. Fluorescence spectra were obtained using excitation wavelengths from 240-600 in 20nm increments and collecting the emission spectra from 290-800nm.

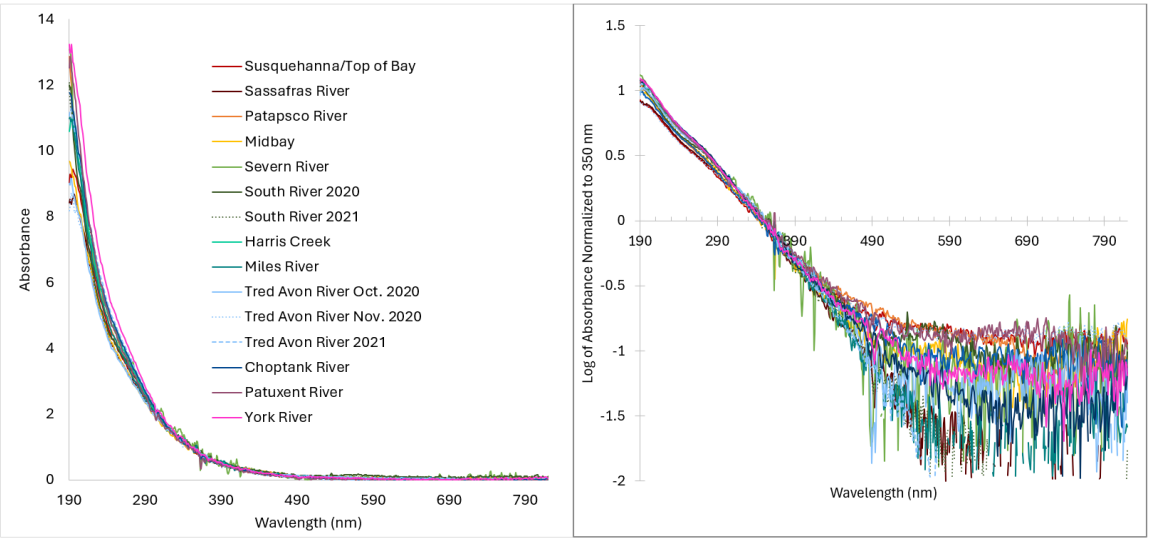


Figure 4.17: (Left) Absorbance normalized to 350 nm for Chesapeake Bay samples with increasing depth (Right) Log of the normalized absorbance of Chesapeake Bay samples with increasing depth

A very small loss of absorbance may be observed in the Susquehanna River, Patapso River, Choptank River, and York River samples.

The fluorescence spectra prior to and following dithionite reduction reported in units of QSE/Abs(240) is shown in figures 4.23, 4.24, 4.25, 4.26, and 4.27; and the change in fluorescence due to the reduction is shown to the right of the spectra. Very little change in the fluorescence due to dithionite reduction is observed.

Comparing the dithionite reduction spectra to that of borohydride reduction(*2*), much like the ocean samples, borohydride reduction shows much greater changes to the absorption and fluorescence of these samples than does dithionite reduction, again supporting that ketones and aldehydes are the primary contributors to the optical properties of these samples over quinones. Much like in this work, little difference was observed between the different samples from the Chesapeake Bay due to borohydride reduction(*2*). This suggests that the samples in the Bay area are not largely different from one another, despite coming from different locations within the Bay or being measured at different times (*2*).

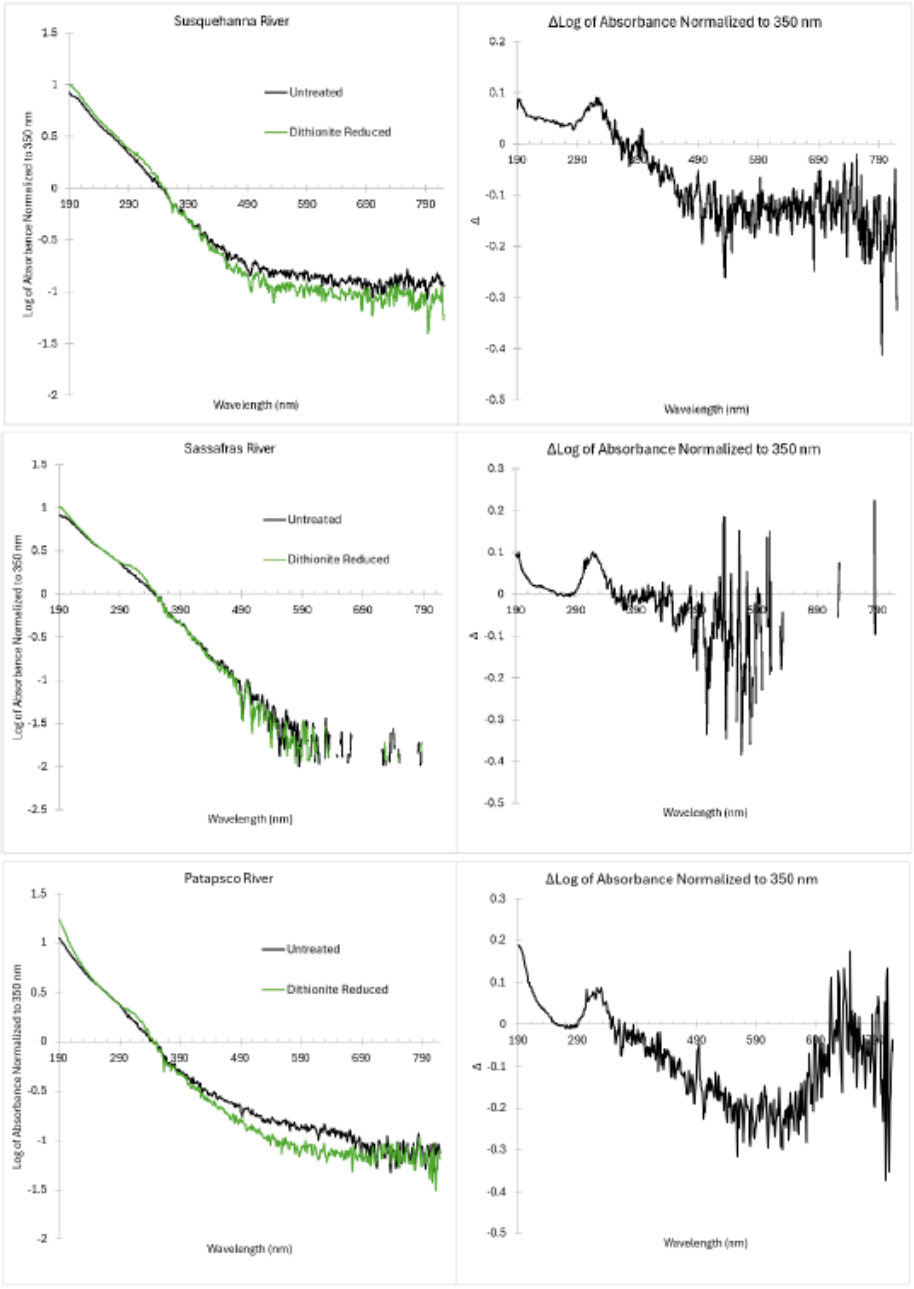


Figure 4.18: (Left) Log of Absorbance normalized to 350 for untreated and dithionite reduced Susquehanna River, Sassafras River, and Patapsco River samples. (Right) Change in log of absorbance normalized to 350 nm for Susquehanna River, Sassafras River, and Patapsco River samples

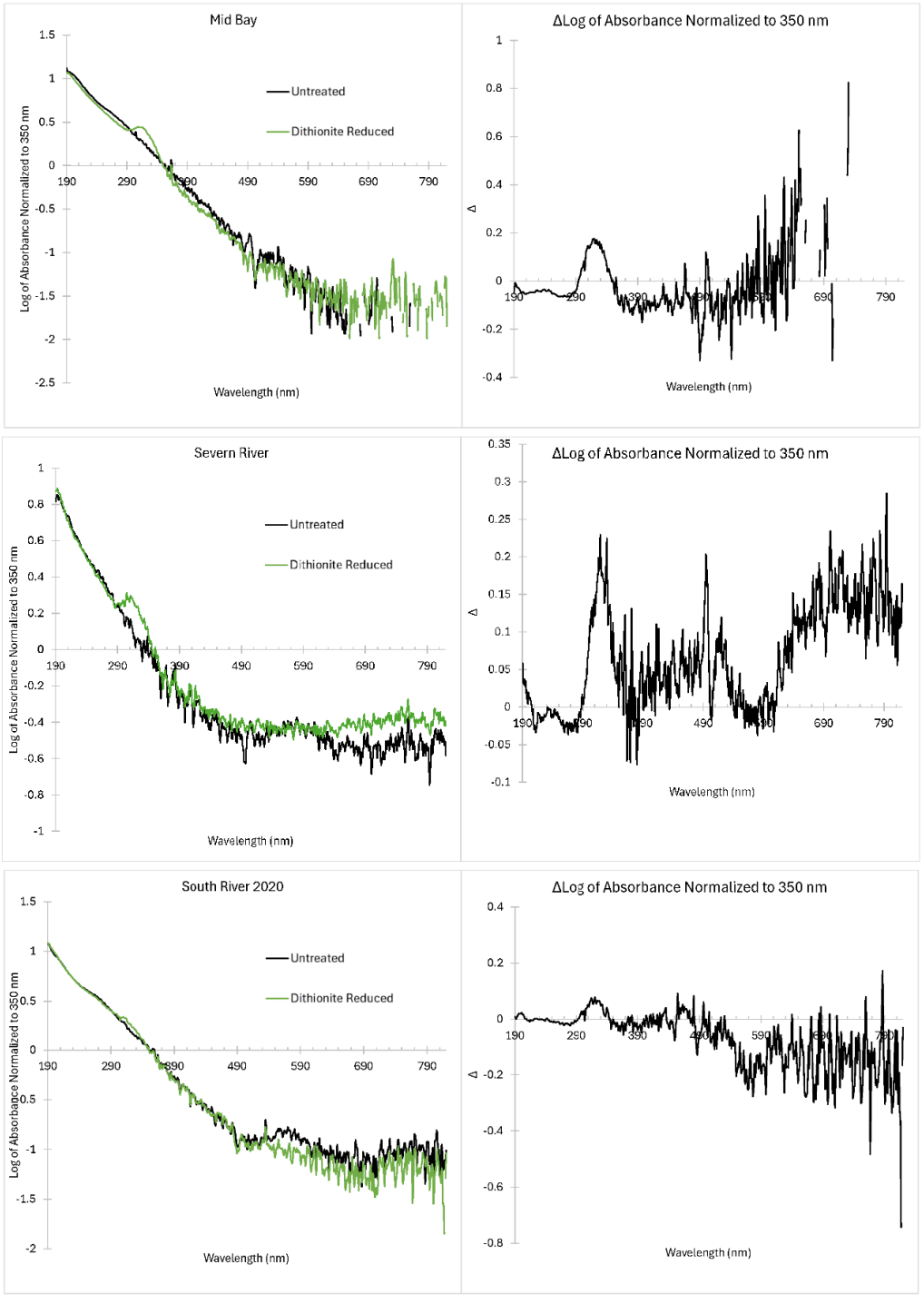


Figure 4.19: (Left) Log of Absorbance normalized to 350 for untreated and dithionite reduced Mid Bay, Severn River, and South River 2020 samples. (Right) Change in log of absorbance normalized to 350 nm for Mid Bay, Severn River, and South River 2020 samples.

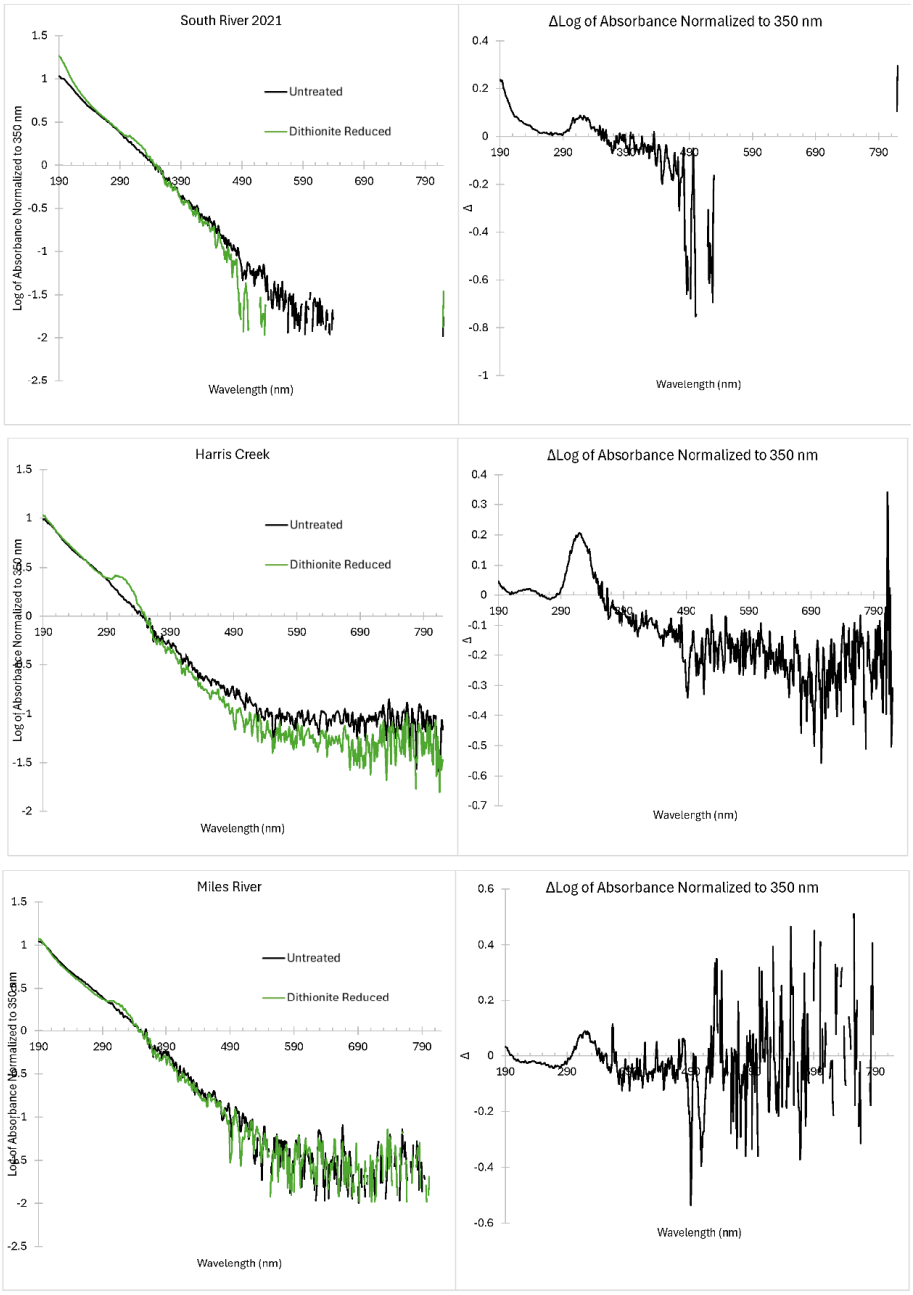


Figure 4.20: (Left) Log of Absorbance normalized to 350 for untreated and dithionite reduced South River 2021, Harris Creek, and Miles River samples. (Right) Change in log of absorbance normalized to 350 nm for South River 2021, Harris Creek, and Miles River samples.

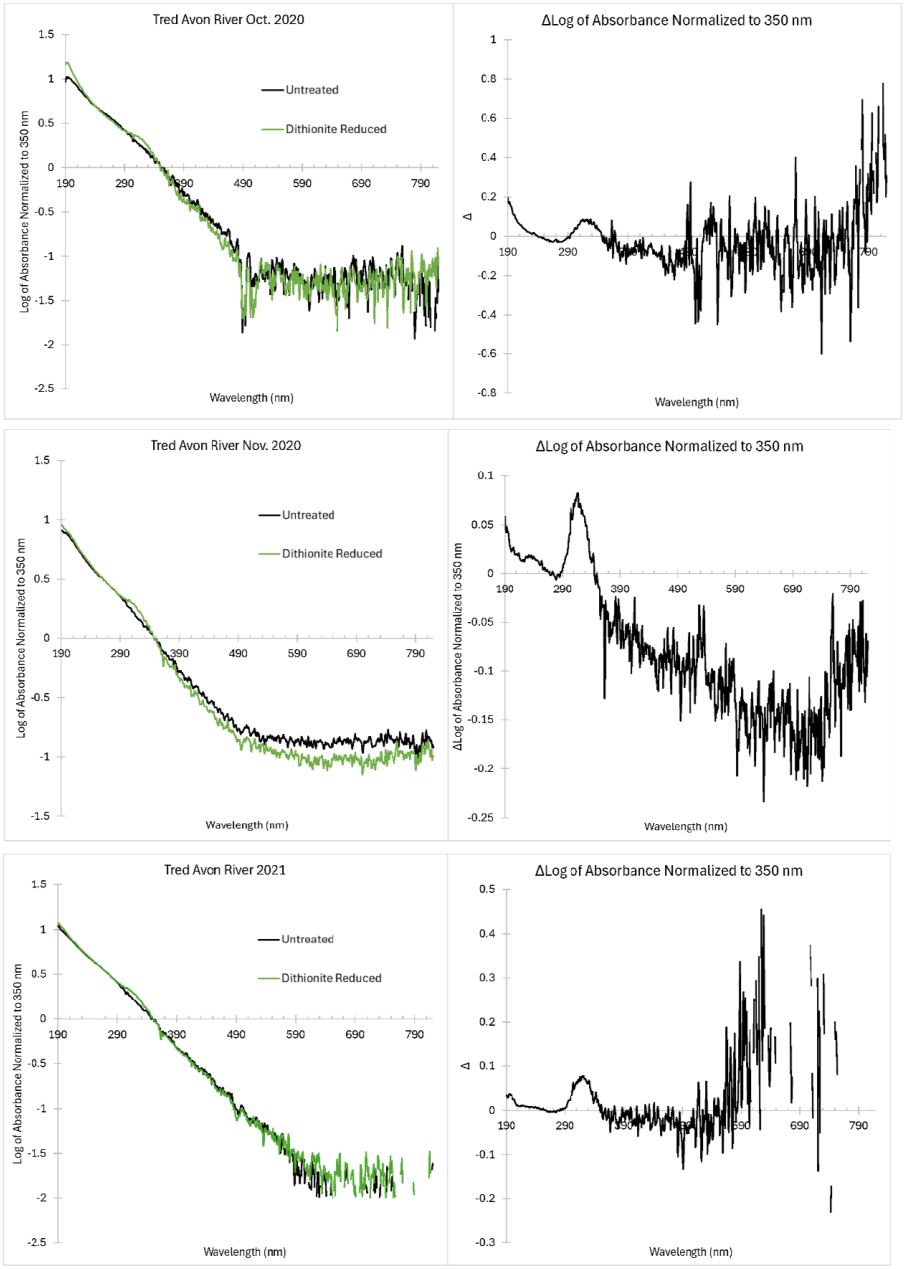


Figure 4.21: (Left) Log of Absorbance normalized to 350 for untreated and dithionite reduced Tred Avon River samples from October 2020, November 2020, and 2021. (Right) Change in log of absorbance normalized to 350 nm for Tred Avon River samples from October 2020, November 2020, and 2021.

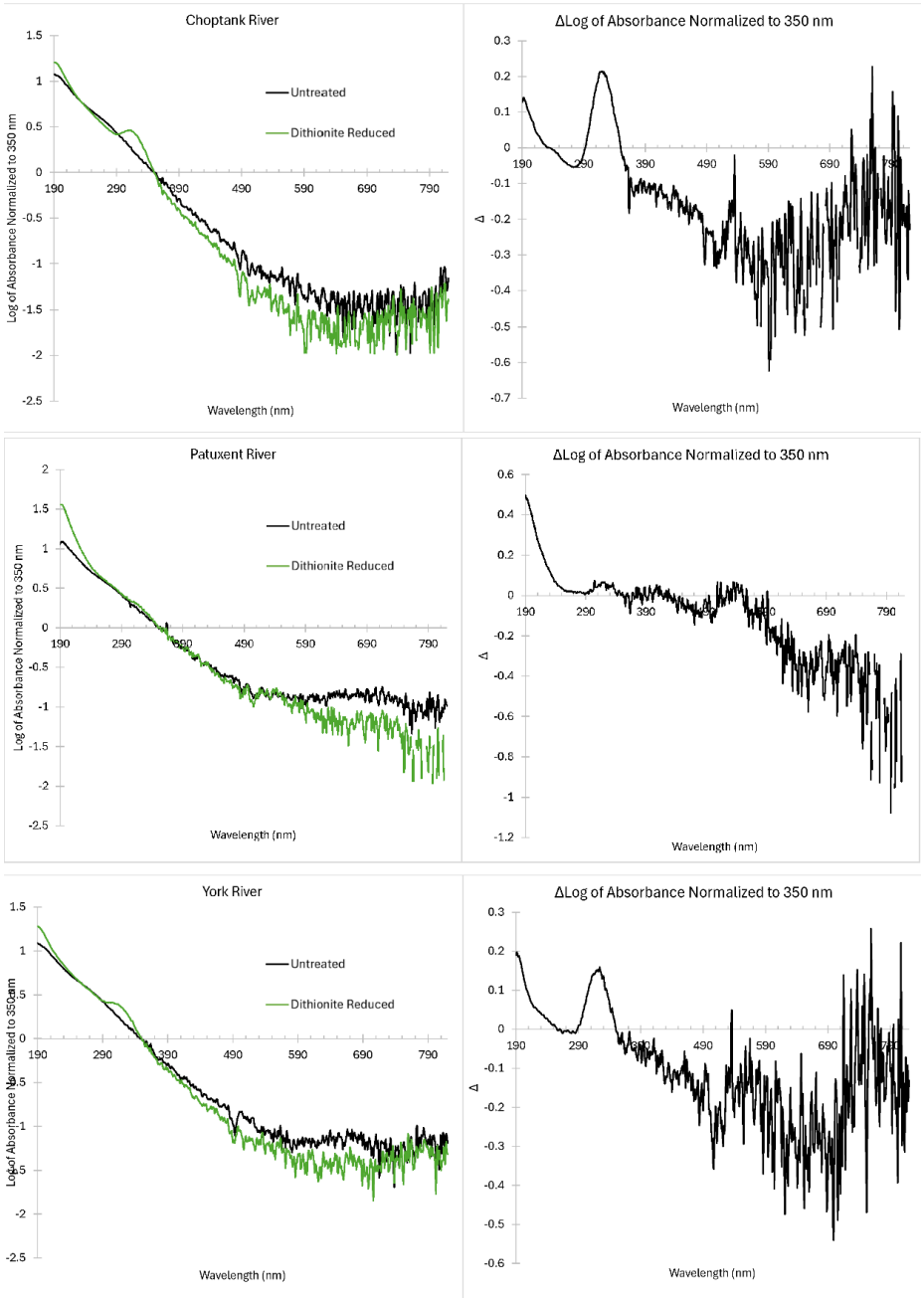


Figure 4.22: Log of Absorbance normalized to 350 for untreated and dithionite reduced Choptank River, Patuxant River, and York River samples. (Right) Change in log of absorbance normalized to 350 nm for Choptank River, Patuxant River, and York River samples

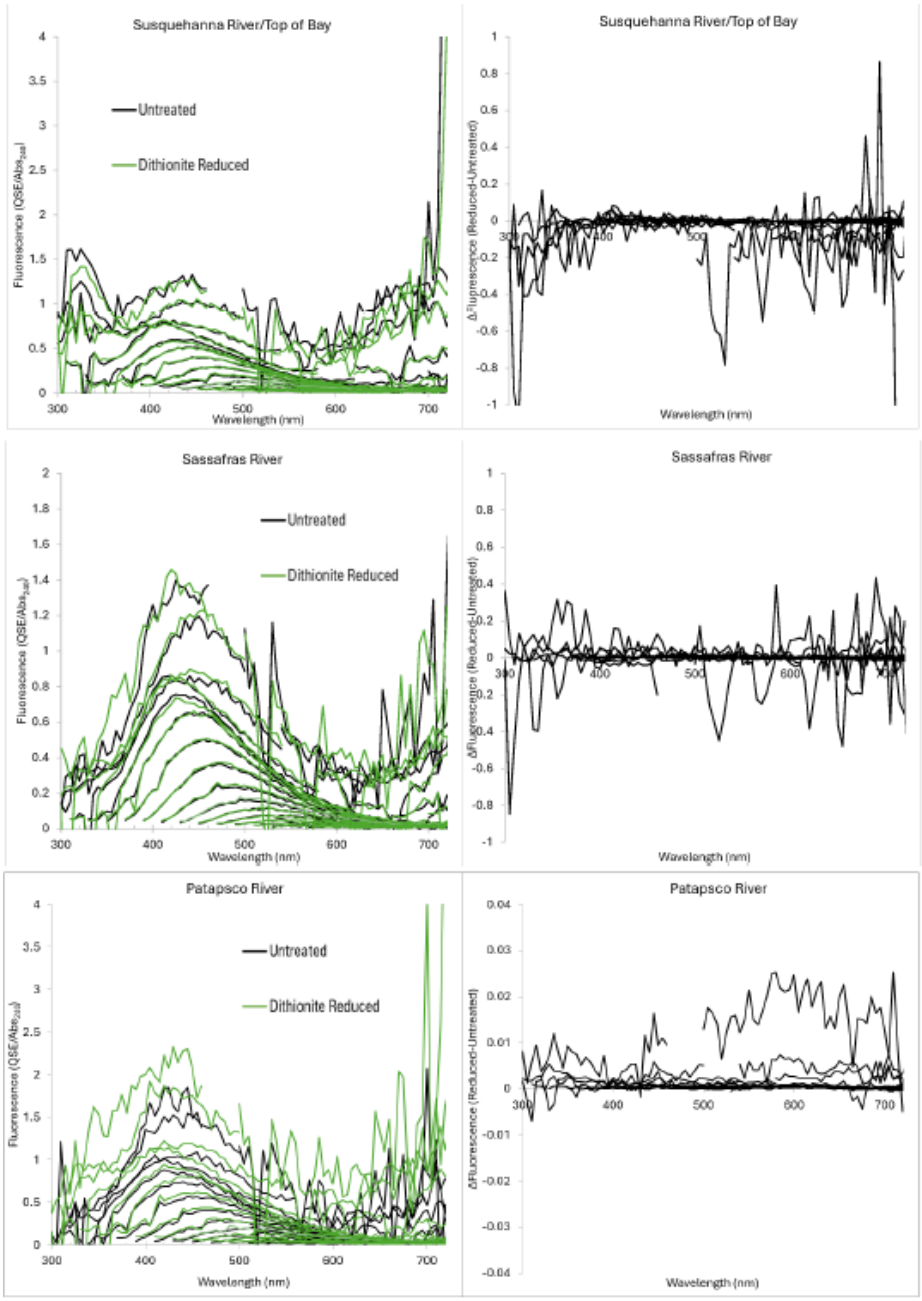


Figure 4.23: (Left) Fluorescence intensity normalized to the absorbance at 240 for the untreated sample, shown for untreated and dithionite reduced Susquehanna River, Sassafras River, and Patapsco River samples. (Right) Change in this fluorescence value due to dithionite reduction for Susquehanna River, Sassafras River, and Patapsco River samples. Fluorescence spectra were obtained using excitation wavelengths from 240-600 in 20nm increments and collecting the emission spectra from 290-800nm.

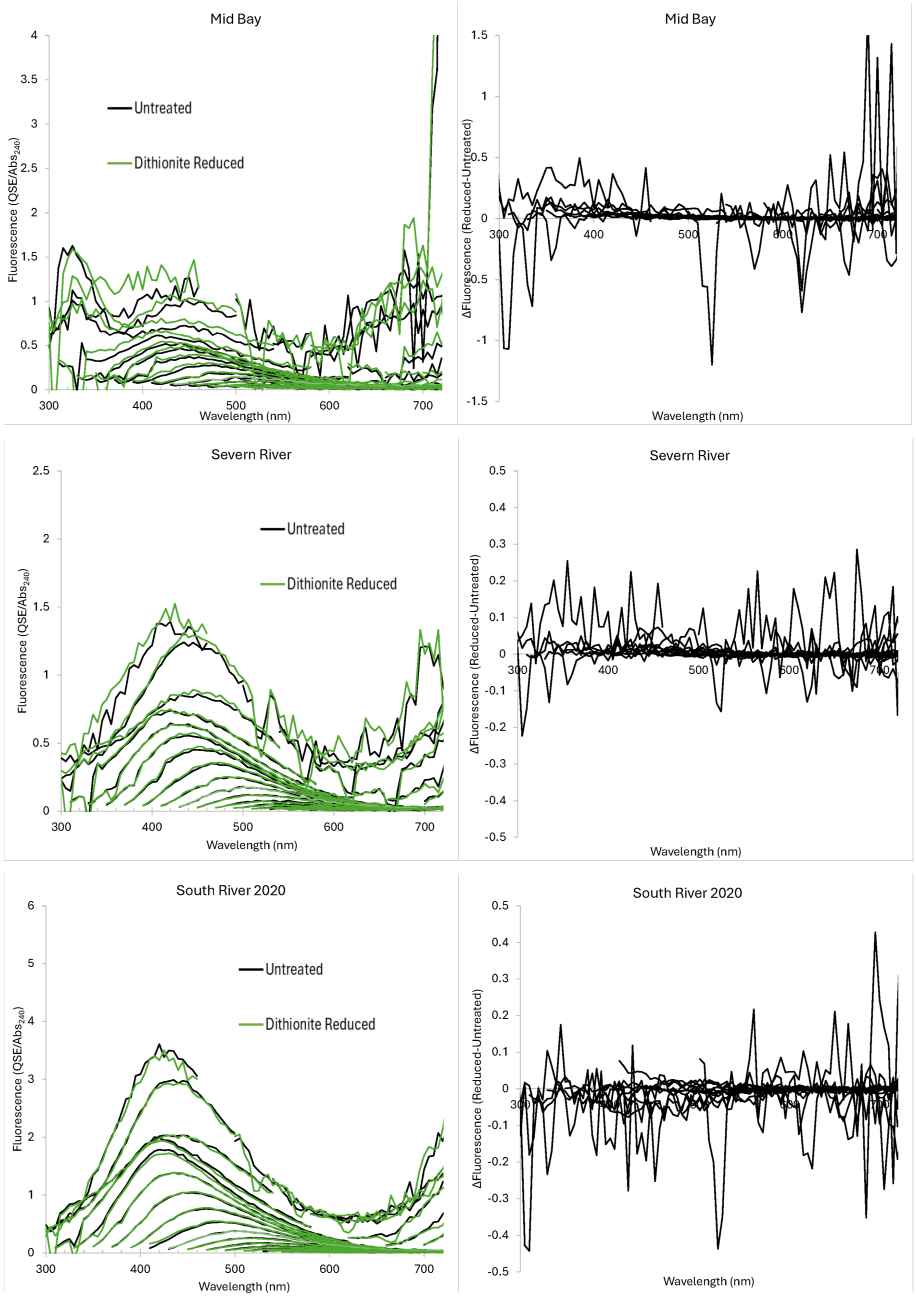


Figure 4.24: (Left) Fluorescence intensity normalized to the absorbance at 240 for the untreated sample, shown for untreated and dithionite reduced Mid Bay, Severn River, and South River 2020 samples. (Right) Change in this fluorescence value due to dithionite reduction for Mid Bay, Severn River, and South River 2020 samples. Fluorescence spectra were obtained using excitation wavelengths from 240-600 in 20nm increments and collecting the emission spectra from 290-800nm.

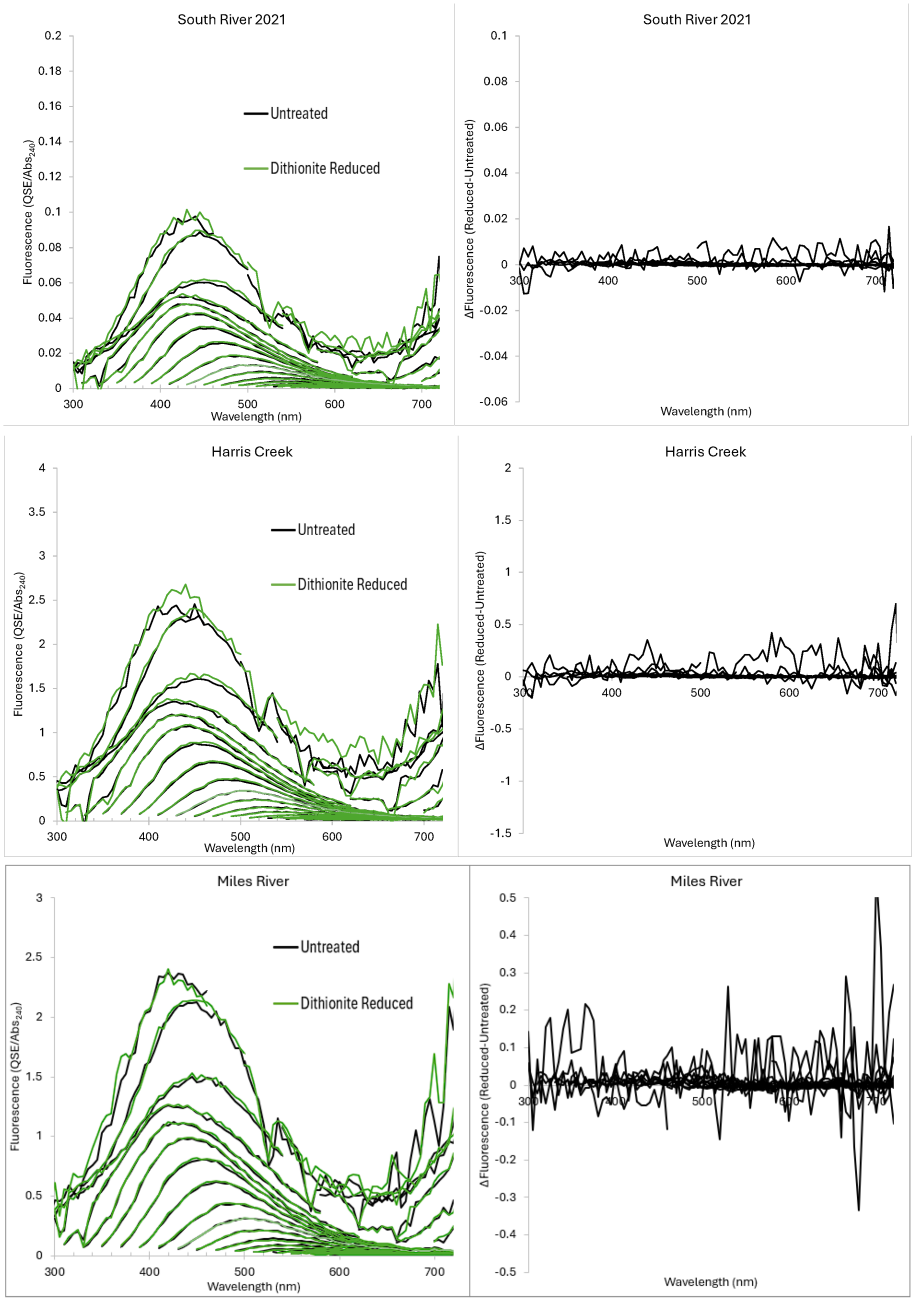


Figure 4.25: (Left) Fluorescence intensity normalized to the absorbance at 240 for the untreated sample, shown for untreated and dithionite reduced South River 2021, Harris Creek, and Miles River samples. (Right) Change in this fluorescence value due to dithionite reduction for South River 2021, Harris Creek, and Miles River samples. Fluorescence spectra were obtained using excitation wavelengths from 240-600 in 20nm increments and collecting the emission spectra from 290-800nm.

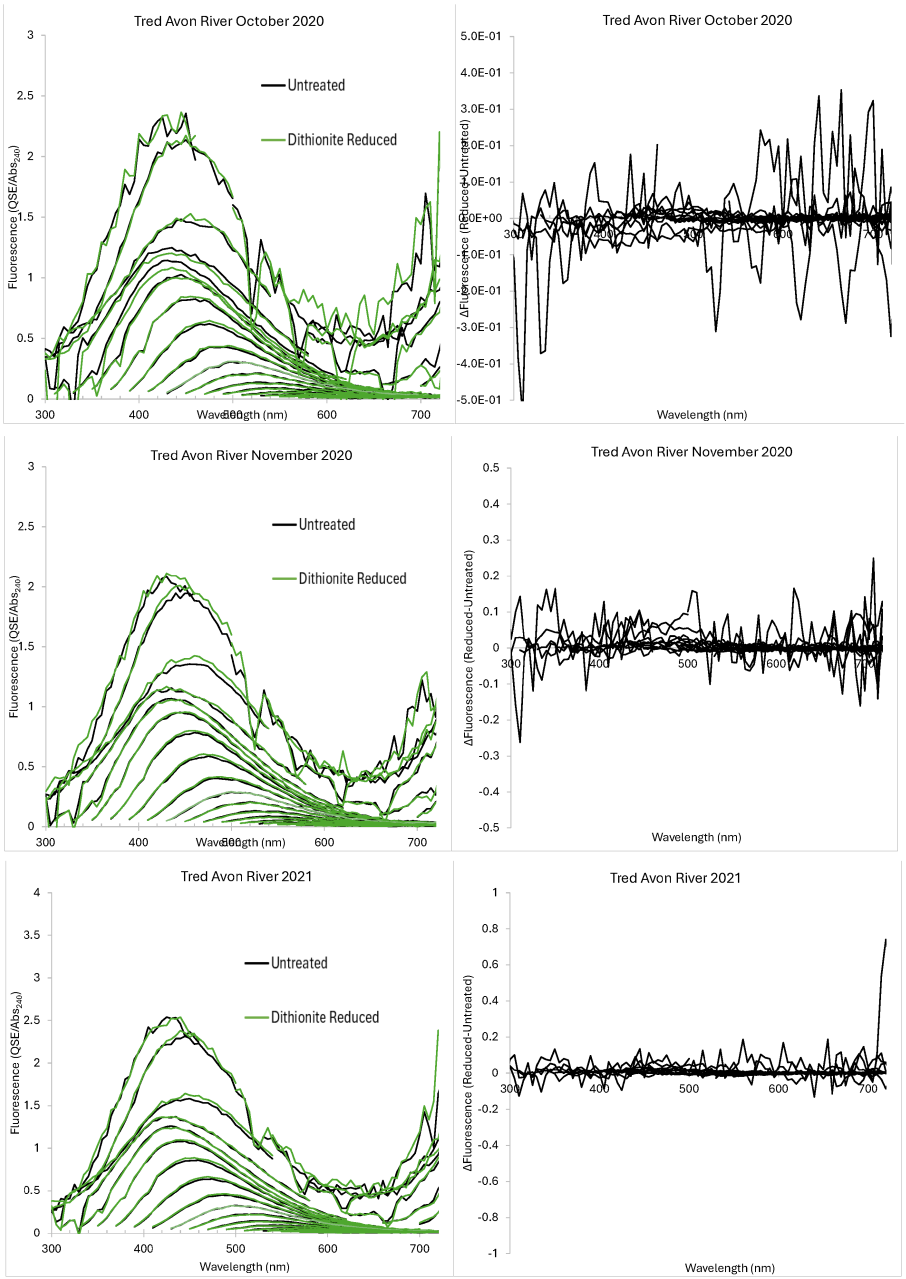


Figure 4.26: (Left) Fluorescence intensity normalized to the absorbance at 240 for the untreated sample, shown for untreated and dithionite reduced Tred Avon River samples from October 2020, November 2020, and 2021. (Right) Change in this fluorescence value due to dithionite reduction for Tred Avon River samples from October 2020, November 2020, and 2021. Fluorescence spectra were obtained using excitation wavelengths from 240-600 in 20nm increments and collecting the emission spectra from 290-800nm.

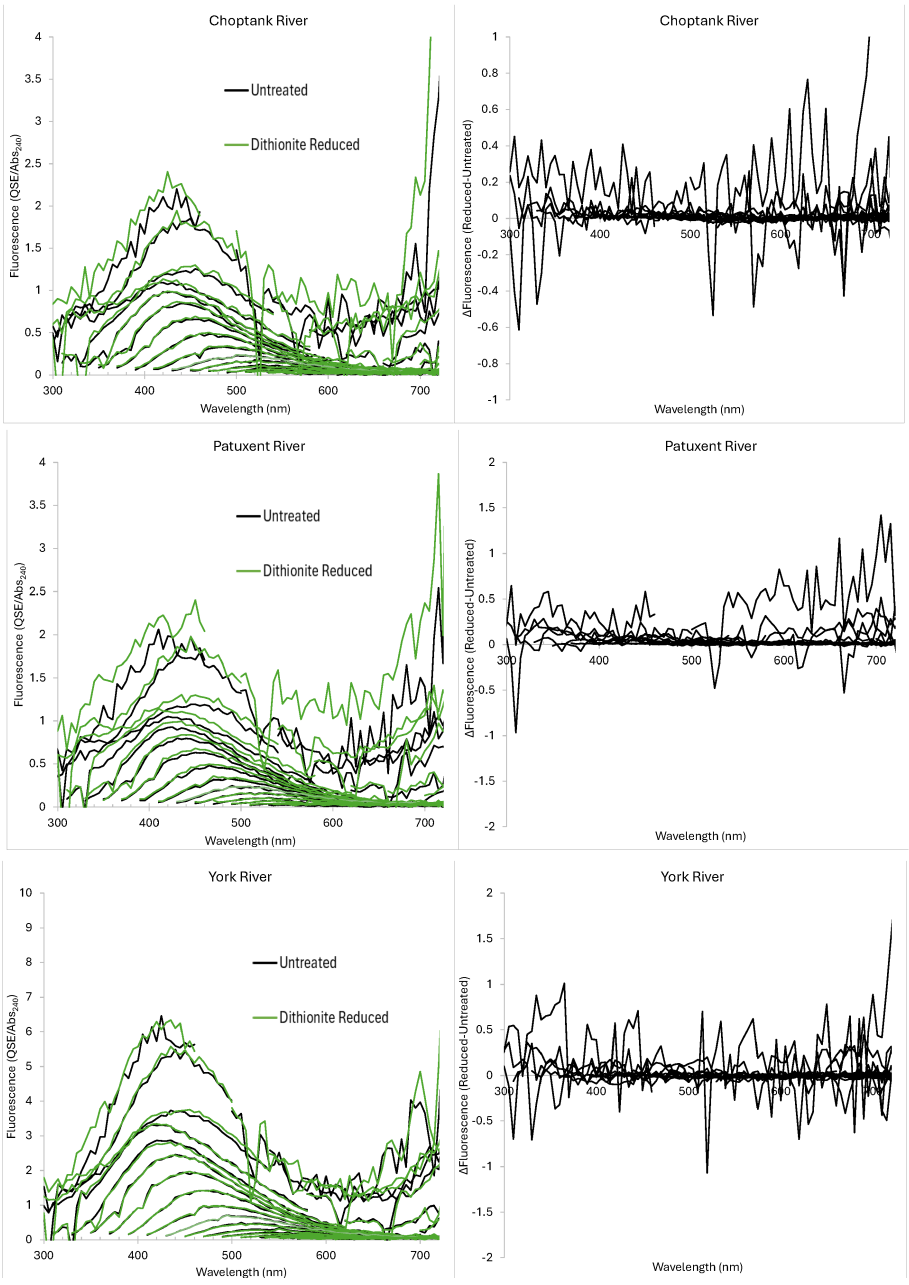


Figure 4.27: (Left) Fluorescence intensity normalized to the absorbance at 240 for the untreated sample, shown for untreated and dithionite reduced Choptank River, Patuxent River, and York River samples. (Right) Change in this fluorescence value due to dithionite reduction for Choptank River, Patuxent River, and York River samples. Fluorescence spectra were obtained using excitation wavelengths from 240-600 in 20nm increments and collecting the emission spectra from 290-800nm.

Not only does the comparison against borohydride reduction suggest little quinone contribution to these samples, but comparison against model quinone data supports this conclusion. Model quinones showed significant changes to fluorescence due to both borohydride and dithionite reduction, but CDOM samples showed little change due to dithionite reduction, suggesting dissimilarity between the two and suggesting any contribution of quinones to the optical properties of CDOM is small.

4.3.5 Estimated Quinone Content

The quinone content estimated for each CDOM standard is tabulated in table 4.1. As compared to previous results and electrochemical results, ESHA quinone content is underestimated; however it is more precisely determined than in previous work (*48*). LHA is closer to electrochemical results than previous work, but no more precise. (*48*) PLFA is also underestimated but more precise. SRHA is actually somewhat overestimated, although the electrochemically determined quinone value is within error. SRFA is underestimated as compared to electrochemical results. SRNOM and LAC have no electrochemical results for comparison, but the quinone content of LAC is found more precisely than previously (*48*), and SRNOM had not been determined in either data set.

It follows that the samples from the plains (ESHA) and from the Suwanee River contain higher quinone content, as quinones are expected to occur from plant sources. PLFA is a microbial source, and it shows generally less quinone content than these sources, but still a not insignificant amount. This may indicate some quinone content in CDOM due to microbial activity rather than simply from vegetation and anthropogenic sources. LAC shows very little quinone content. This would indicate that wood and bark sources do not contribute significantly to quinone content. Lastly, LHA from the mine source shows a great deal of quinone content, indicating coal may be a significant source of quinones. The

CDOM Standard	Quinone Content (μM) in 100mg/L	Del Vecchio et al.	Aeschbacher et al.
ESHA	64±9	94±26	98.1±0.75
LHA	90±35	75±33	86±2
PLFA	12±4	18±8	24.7±0.5
LAC	6±1	13±14	-
SRHA	63±15	-	48±1
SRFA	12±2	11±5	33.6±0.4
SRNOM	21±5	-	-

Table 4.1: Estimated quinone content in CDOM standards, compared to Del Vecchio et. al. (*48*) and Aeschbacher et. al. (*101*)

NPO Sample Depth	Estimated Quinone Content Scaled to 100 mg/L LAC
Surface	34 ± 29
500	Unmeasurable
600	40 ± 17
800	27 ± 5
1000	70 ± 7
1500	54 ± 30
2500	71 ± 47
3500	57 ± 39
4500	41 ± 27

Table 4.2: Estimated quinone content for NPO samples, scaled to match the absorbance of 100 mg/L LAC

estimated quinone content for the NPO samples is shown in table 4.2. Scaling is based on the ratio of absorbance in the untreated sample to that of a 100mg/L sample of LAC. Results should not be quantitatively compared to the CDOM standard results, since this is not a quantitative comparison of concentrations.

As discussed in chapter 3, these quinone contents should be regarded as estimates rather than exact values, as emphasized by their high errors.

4.4 Conclusions

For CDOM standards, it was observed that the utilized methodology increased precision of observed quinone content, but may not have improved accuracy as compared to electrochemical results. In terms of observed quionone content, the greatest values were by far LHA and ESHA, indicating that CDOM from coal/mine sources and prairie lands contains a good deal of quinone moieties. The natural water samples both from the ocean and the bay area were observed to have minimal contribution of quinones to their optical properties. If sources further inland were studied, especially in areas with dense vegetation, quinone content may be higher. But because the ocean (especially surface waters) largely lacks significant sources of quinones, they were not present in large amounts. In the bay area, ocean and terrestrial water is mixing, and so although there is some quinone input from terrestrial sources, it likely is diluted and quickly broken down in marine waters. If there are greater quinone concentrations found further inland, this may support that terrestrial sources of quinones are not long lived in marine systems. (*51*)

Sample	Estimated Quinone Content Scaled to 100 mg/L LAC
Susquehanna River	29 ± 11
Sassafras River	14 ± 12
Patapsco River	17 ± 0.2
Mid Bay	35 ± 10
Severn River	67 ± 54
South River 2020	31 ± 5
South River 2021	41 ± 17
Harris Creek	35 ± 27
Miles River	34 ± 21
Tred Avon River Oct 2020	34 ± 6
Tred Avon River Nov 2020	31 ± 18
Tred Avon River 2021	35 ± 5
Choptank River	Unmeasurable
Patuxent River	66 ± 38
York River	49 ± 46

Table 4.3: Estimated quinone content for Chesapeake Bay samples, scaled to match the absorbance of 100 mg/L LAC

Chapter 5: Conclusions and Future Work

5.1 Summary

The work presented in this thesis consists of a thorough characterization of a suite of model quinone compounds, the reduction products of these quinones using borohydride, dithionite, and sulfite, and an investigation of the contribution of quinones to the optical properties of Chromophoric Dissolved Organic Matter. In Chapter 2, absorption and fluorescence spectra for a suite of model quinones including *p*-benzoquinones with different numbers and arrangement of methyl-substitutions, 1,4-napthoquinones, and anthraquinones were presented. Molar absorptivities of these quinones at their absorbance peaks were calculated and presented. The quinones are reduced to their hydroquinone forms by borohydride, except for anthraquinones which were reduced with dithionite, and their absorption and fluorescence spectra presented. Molar absorptivities for the hydroquinone peaks were calculated and presented. Fluorescence quantum yields were calculated for both quinones and hydroquinones. *P*-bezoquinones showed little fluorescence, with quantum yields indistinguishable from instrument noise. *P*-benzohydroquinones showed greater fluorescence intensity and quantum yields on the order of 10^{-2}. Naphthoquinones and anthraquinones had slightly higher fluorescence. Juglone showed a fluorescence intensity comparable to the *p*-benzohydroquinones, with a quantum yield of 1.4×10^{-2}. The naphthohydroquinones and anthrahydroquinones had quantum yields on the same order of magnitude as the *p*-benzoquinones, with the exception of hydroxyjuglone, which had a

quantum yield of 0.16.

In Chapter 3, model quinones were reduced with sodium dithionite and sodium sulfite to investigate reaction products and stoichiometry. Quinone molar absorptivities from Chapter 2 were used in the experiments to quantify quinone stocks, and hydroquinone spectra were compared with dithionite and sulfite reduced spectra. HPLC was used to investigate products and stoichiometry of the dithionite reductions. Slight differences between the dithionite reduced absorption spectra and the expected combination of the quinone and hydroquinone spectra were observed. Sulfite reduction was used to explain these differences, although contribution of sulfonated hydroquionone byproducts was determined to be relatively small in dithionite reduced samples. Stoichiometry of dithionite reduction determined by HPLC chromatography supported that sulfite interference was likely small, as most quinones showed comparable quinone disappearance to hydroquinone appearance and those that did not had high degrees of uncertainty, with the sole exception of 2,3-dimethyl-*p*-benzoquinone. Given these results, the dithionite reduction procedure was used to evaluate the quionone content and impact on optical properties of CDOM.

In Chapter 4, dithionite reduction was used to evaluate quinone content and contribution to the optical properties of CDOM standards and natural water extracts. Dithionite reduction showed little impact on CDOM optical properties, especially for the natural water extracts. Estimated quinone contents were found to be high for CDOM sources dense in plant life or coal mining areas, whereas CDOM from bark and from microbial production was not as high. For ocean and bay area samples, little impact of quinones on the optical properties were observed, and small quinone contents were estimated for these samples. Therefore, quinones are less relevant to the optical properties of CDOM than ketones and aldehydes, especially for estuary and marine systems.

5.2 Future Directions

5.2.1 Model Quinones

Preliminary research on the model quinone compounds showed evidence of a difference in the products of the reaction of quinones with dithionite and sulfite. To further investigate this difference, HPLC fractions could be analysed to identify products. Mass-spectroscopy and Nuclear Magnetic Resonance (NMR) measurements would help elucidate the structures and masses of these products and any differences between the two reducing species. Additional substitution groups could be investigated in the same procedures as methyl-substitution and conjugated ring structures are in this work to investigate the effects of different groups. This can be extended to a range of different quinone compounds, especially those most relevant to CDOM properties, although quinones are also widely relevant in other contexts, including wine chemistry, organic chemistry reactions, and dyes. This analysis would include expanding to methoxy-substituted *p*-benzoquinones and *o*-quinones to further investigate effects of structure on reactivity to sulfite and products.

HPLC could be applied to the sulfite reduced model quinones to investigate quinone disappearance and hydroquinone appearance and compare to dithionite reduced quinone results. This comparison would help draw conclusions about the dithionite reduction products.

A separation method for the sulfonated hydroquinone product could be further investigated and developed, involving ion exchange in the separation method to isolate the sulfonated compounds.

5.2.2 CDOM Characterization in Lakes and Rivers

Characterization of CDOM in natural waters could be extended to include up the Susquehanna River, The Great Lakes, and other inland lakes and rivers. This characterization would include dithionite and borohydride reduction of CDOM and model compounds, pH titration of the untreated and reduced forms of these samples, and measurement of production of reactive oxygen species due to photochemistry. This could also include measurements of dissolved nitrogen, dissolved phosphorous, dissolved carbon, and iron and metal ion species in these natural water samples, and investigating the samples' reduction potential.

This would ultimately allow an overview and comparison of ocean, coastal, and inland waters' structure and optical properties, particularly in terms of ketones, aldehydes, and quinones.

5.2.3 Photochemical activity of Quinones in CDOM

Following the optical contribution of quinones in CDOM, the photochemical contribution of quinones in CDOM can be investigated. This has been completed on model quinone compounds (Clark, 2014). The effects of photochemistry on dithionite reduced CDOM samples could be investigated and compared to untreated samples. The difference between these reactions and products will show the contribution of quinones to the photochemistry of CDOM, which may offer a more concrete understanding of their activity and role in the environment.

Appendix A: Supporting Information

A.1 Chapter 1 Supplemental

A.1.1 Beer's Law

The Beer-Lambert law states that absorbance is proportional to concentration of the absorbing species. (*126*) This relationship is given in equation A.1., where A(λ) = the absorbance at a particular wavelength, $\varepsilon(\lambda)$ = the molar absorptivity of the absorbing species at that wavelength, and c = the pathlength through which the absorbance is measured.

$$A(\lambda) = \varepsilon(\lambda) * b * c \tag{A.1}$$

Therefore, as long as the absorbance due to the absorbing species and the molar absorptivity are known, the concentration of the absorbing species can be found, assuming all interferences, such as other absorbing species and pH and solvent effects, are minimized or accounted for. This concept was applied in Del Vecchio et al. to calculate the quinone content of the HA standards.(*48*)

Initial work involved repetition of the experiments of Del Vecchio et. al. to determine reproducability. The methods are described above. Results of these experiments and comparison to the work of Del Vecchio et. al. and Aeschbacher et. al. are shown in figure 1. These results were largely consistent with Del Vecchio et. al., although quinine content for ESHA was significantly underestimated as compared to Del Vecchio et. al.

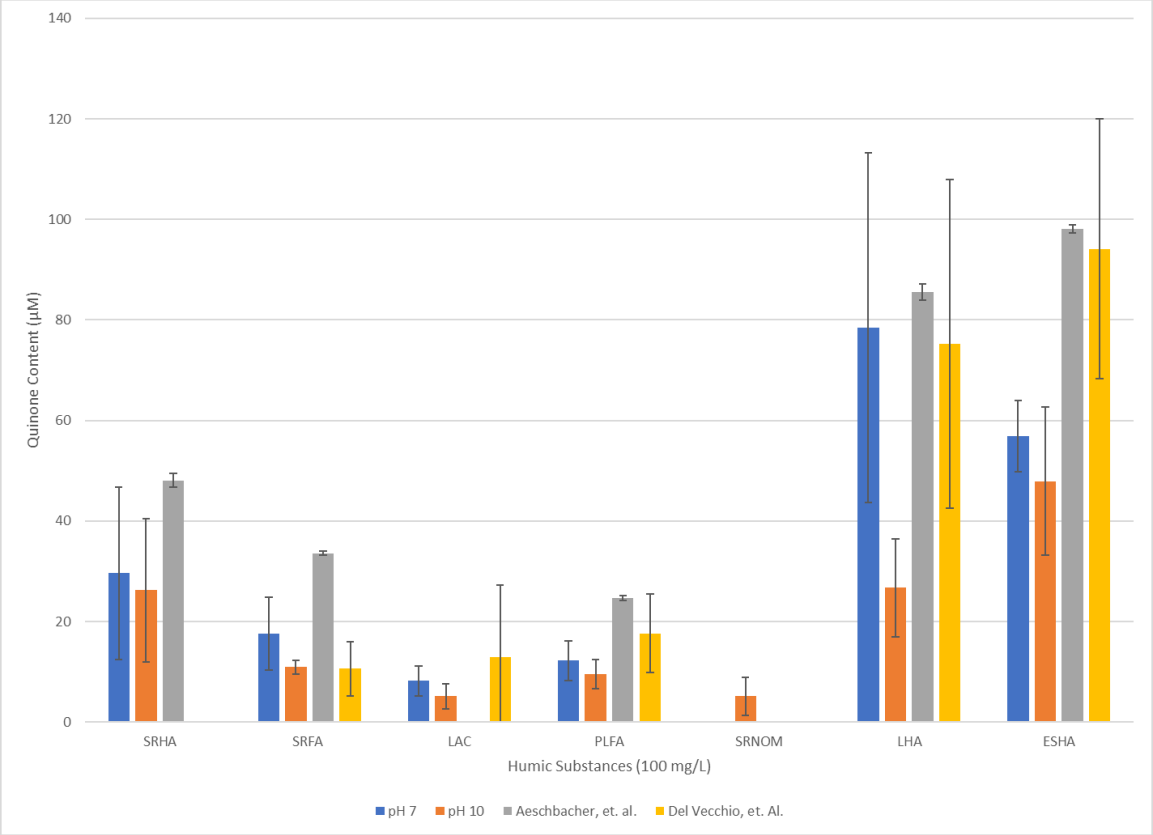


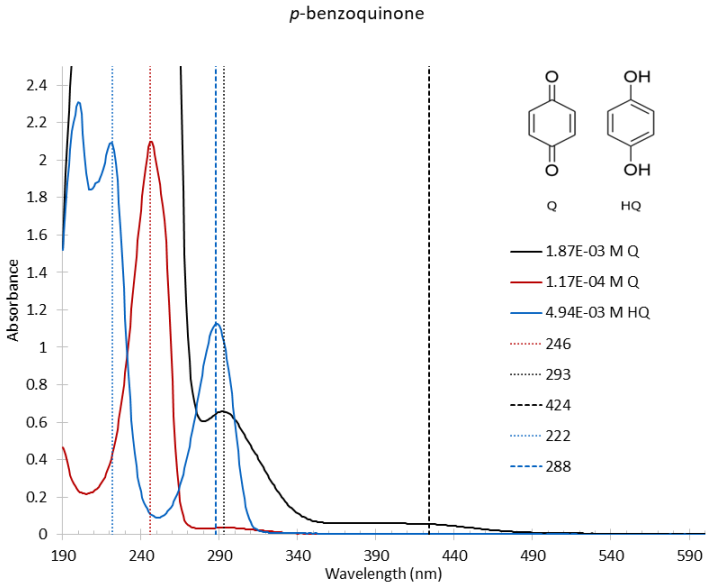
Figure 1: Preliminary results from replicating the work of Del Vecchio et. al. (*48*)

For SRHA, SRFA, and PLFA, quinone content was slightly underestimated as compared to Aeschbacher et. al. This may in part be due to the attribution of EAC completely to quinone content, but for LHA and ESHA the methods compare very well. This underestimation prompted consideration of the possible side reactions and initiated the model quinone study.

A.2 Chapter 2 Supplemental

A.2.1 Calibration Curve Concentrations and Representative Spectra

Wavelengths corresponding to absorbance peaks for which molar absorptivity is calculated are shown in dotted and dashed lines corresponding to the color in which the repre-



Concentration Q	A(293)	A(424)
1.87 mM	0.70274	0.05474
1.50 mM	0.56136	0.04344
1.12 mM	0.43201	0.03268
0.750 mM	0.29681	0.02077
0.375 mM	0.16515	0.01001

Concentration Q	A(246)
0.117 mM	2.09899
0.105 mM	1.93862
0.0937 mM	1.736
0.0820 mM	1.50772
0.0703 mM	1.29448

Concentration HQ	A(222)	A(288)
0.117 mM	0.52187	0.26265
0.105 mM	0.48153	0.24208
0.0937 mM	0.42835	0.2168
0.0820 mM	0.36691	0.18679
0.0703 mM	0.31883	0.15994

Figure 2: Calibration curve concentrations and representative spectra for *para*-benzoquinone.

sentative spectra is shown. The table of concentrations and absorbances used to find the molar absorptivity of that peak is shown in the corresponding color. Concentrated quinone spectra are shown in black, dilute quinone spectra are shown in red, and hydroquinone spectra are shown in blue. For 1,4-naphthoquinone, a dilute hydroquinone sample is shown in green to show the peak at 242 nm.

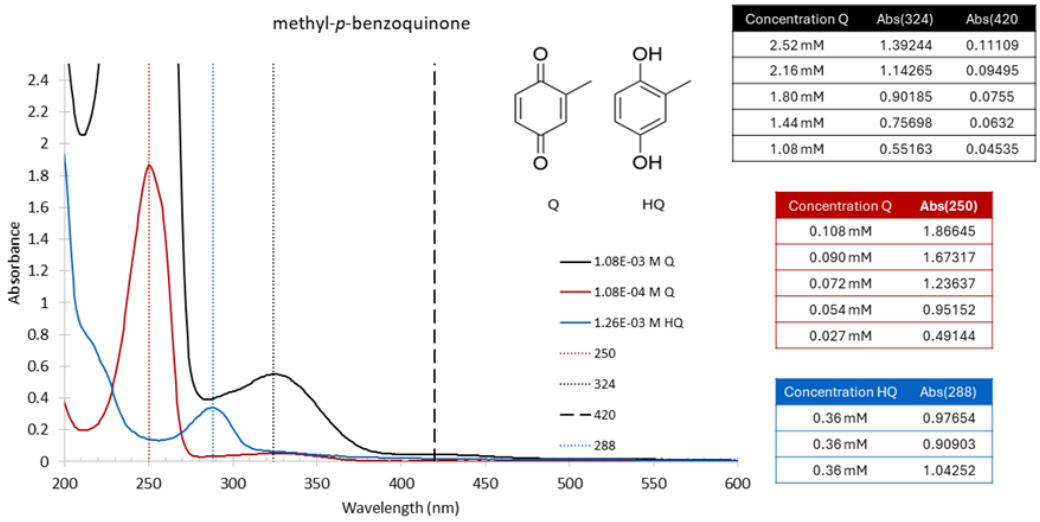
A.3 Chapter 3 Supplemental

A.3.1 Dithionite Quantification

Dithionite stock concentration Calculated:

Using dithionite absorbance at 316 nm and a molar extinction coefficient of 8000 M^{-1} cm^{-1} (*100*): 0.011 $\pm$ 0.001 M

Using ferricyanide absorbance at 420 nm and a molar extinction coefficient of 1020

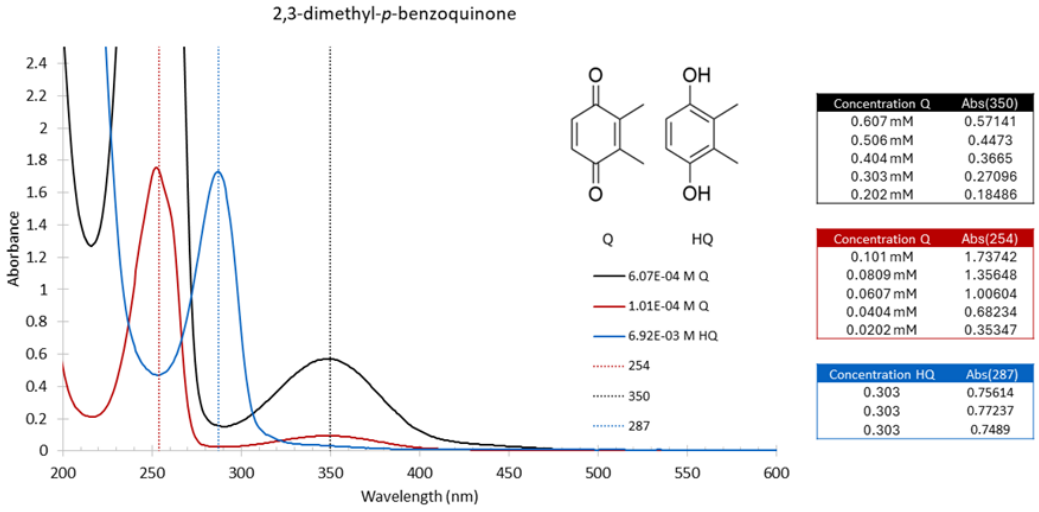


Concentration Q	Abs(324)	Abs(420
2.52 mM	1.39244	0.11109
2.16 mM	1.14265	0.09495
1.80 mM	0.90185	0.0755
1.44 mM	0.75698	0.0632
1.08 mM	0.55163	0.04535

Concentration Q	Abs(250)
0.108 mM	1.86645
0.090 mM	1.67317
0.072 mM	1.23637
0.054 mM	0.95152
0.027 mM	0.49144

Concentration HQ	Abs(288)
0.36 mM	0.97654
0.36 mM	0.90903
0.36 mM	1.04252

Figure 3: Calibration curve concentrations and representative spectra for methyl-*para*-benzoquinone.

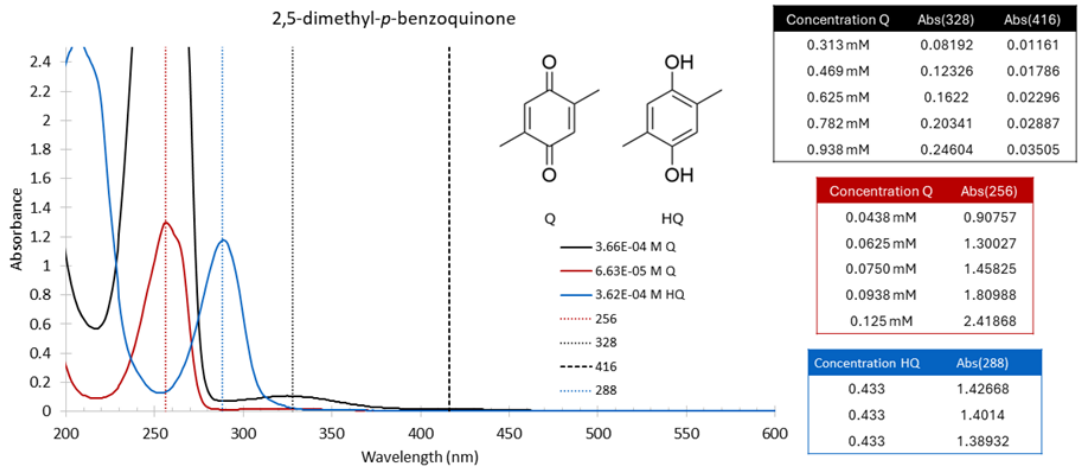


Concentration Q	Abs(350)
0.607 mM	0.57141
0.506 mM	0.4473
0.404 mM	0.3665
0.303 mM	0.27096
0.202 mM	0.18486

Concentration Q	Abs(254)
0.101 mM	1.73742
0.0809 mM	1.35648
0.0607 mM	1.00604
0.0404 mM	0.68234
0.0202 mM	0.35347

Concentration HQ	Abs(287)
0.303	0.75614
0.303	0.77237
0.303	0.7489

Figure 4: Calibration curve concentrations and representative spectra for 2,3-dimethyl-*para*-benzoquinone.

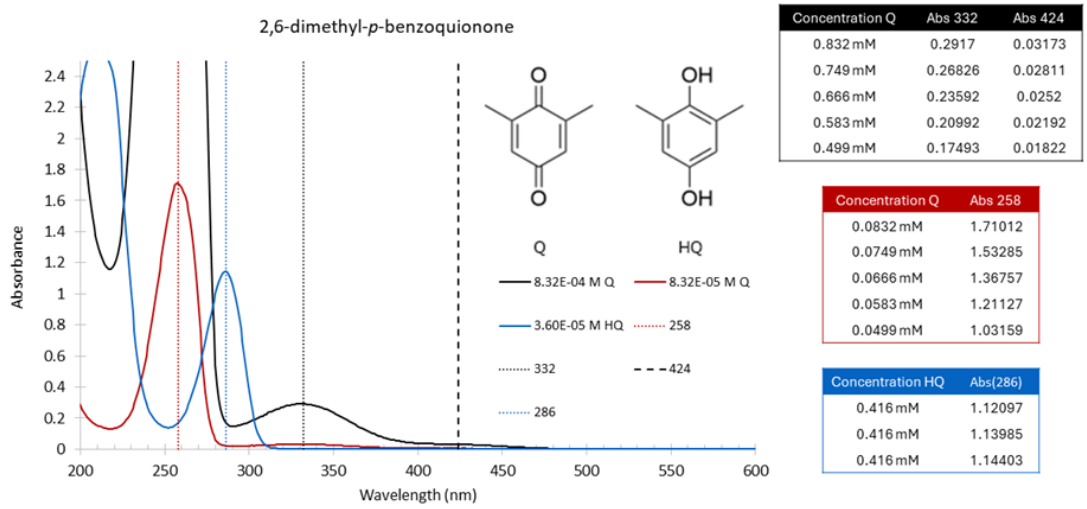


Concentration Q	Abs(328)	Abs(416)
0.313 mM	0.08192	0.01161
0.469 mM	0.12326	0.01786
0.625 mM	0.1622	0.02296
0.782 mM	0.20341	0.02887
0.938 mM	0.24604	0.03505

Concentration Q	Abs(256)
0.0438 mM	0.90757
0.0625 mM	1.30027
0.0750 mM	1.45825
0.0938 mM	1.80988
0.125 mM	2.41868

Concentration HQ	Abs(288)
0.433	1.42668
0.433	1.4014
0.433	1.38932

Figure 5: Calibration curve concentrations and representative spectra for 2,5-dimethyl-*para*-benzoquinone.



Concentration Q	Abs 332	Abs 424
0.832 mM	0.2917	0.03173
0.749 mM	0.26826	0.02811
0.666 mM	0.23592	0.0252
0.583 mM	0.20992	0.02192
0.499 mM	0.17493	0.01822

Concentration Q	Abs 258
0.0832 mM	1.71012
0.0749 mM	1.53285
0.0666 mM	1.36757
0.0583 mM	1.21127
0.0499 mM	1.03159

Concentration HQ	Abs(286)
0.416 mM	1.12097
0.416 mM	1.13985
0.416 mM	1.14403

Figure 6: Calibration curve concentrations and representative spectra for 2,6-dimethyl-*para*-benzoquinone.

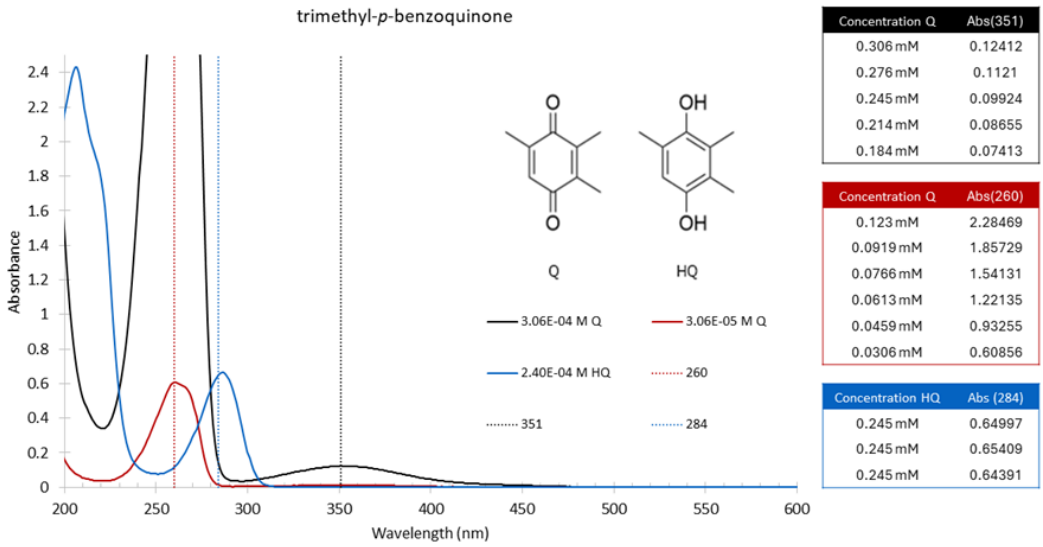


Figure 7: Calibration curve concentrations and representative spectra for trimethyl-*para*-benzoquinone.

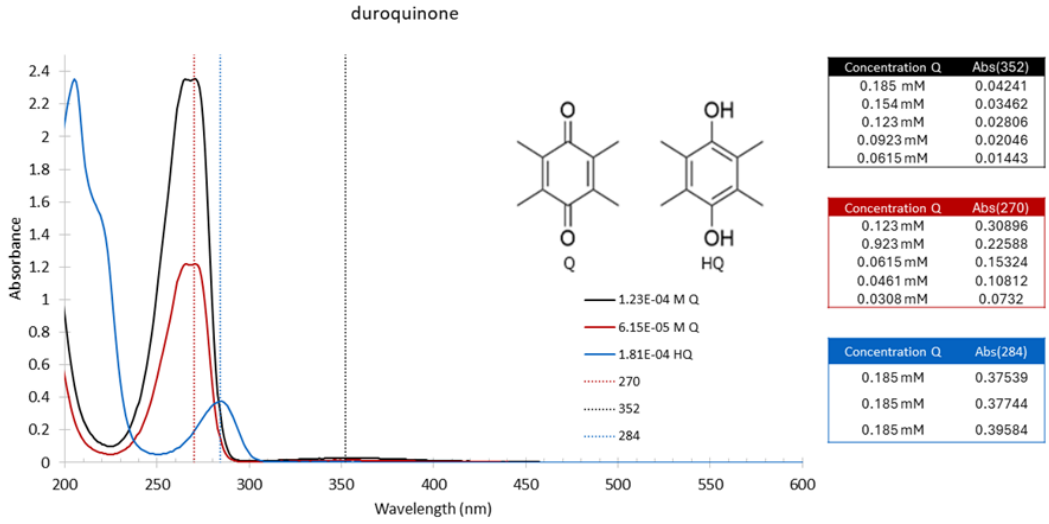
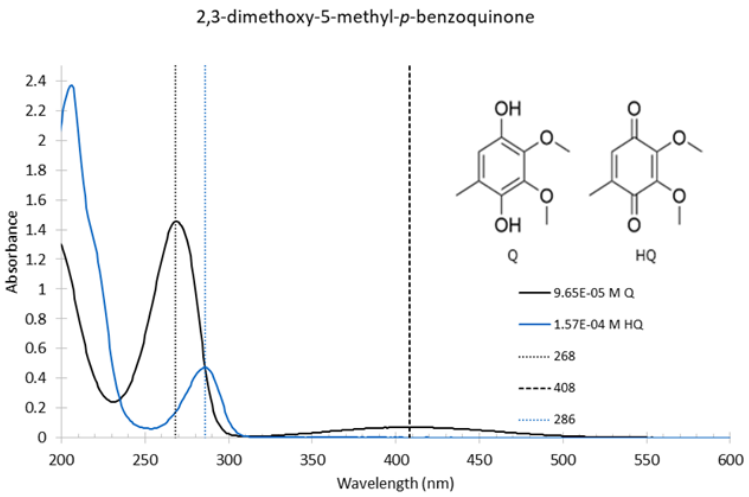


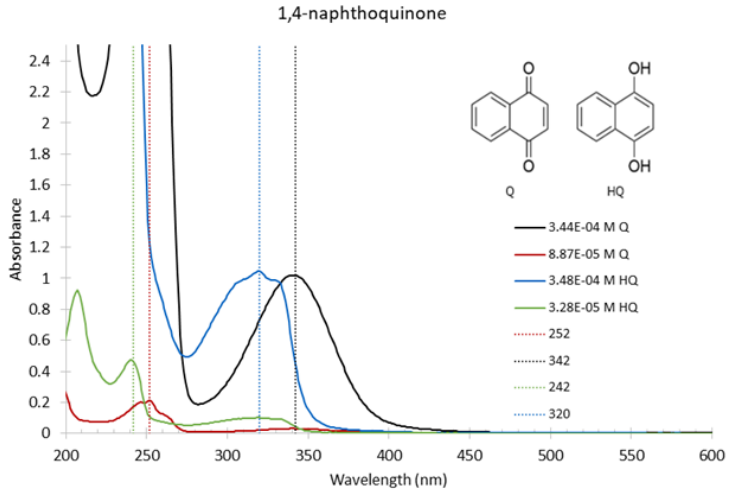
Figure 8: Calibration curve concentrations and representative spectra for duroquinone.



Concentration	Abs(268)	Abs(408)
0.158 mM	2.36455	0.1203
0.142 mM	2.15526	0.10753
0.126 mM	1.87608	0.09227
0.111 mM	1.68489	0.082
0.0947 mM	1.45579	0.07121

Concentration	Abs(286)
0.158 mM	0.47359
0.158 mM	0.47802
0.158 mM	0.47673

Figure 9: Calibration curve concentrations and representative spectra for 2,3-dimethoxy-5-mehtyl-*para*-benzoquinone.

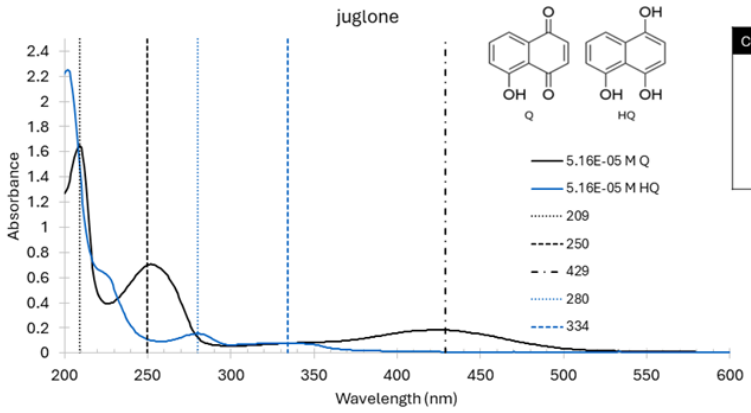


Concentration Q	(Abs)342
0.177 mM	0.51189
0.151 mM	0.4488
0.133 mM	0.38318
0.106 mM	0.33381
0.0887 mM	0.28075

Concentration	Abs(252)
0.0444 mM	1.00465
0.0355 mM	0.80796
0.0266 mM	0.60938
0.0177mM	0.40126
0.00887 mM	0.21045

Concentration HQ	Abs(242)	Abs(320)
0.102	0.98402	0.11545
0.102	0.6842	0.13012
0.102	0.43407	0.09158

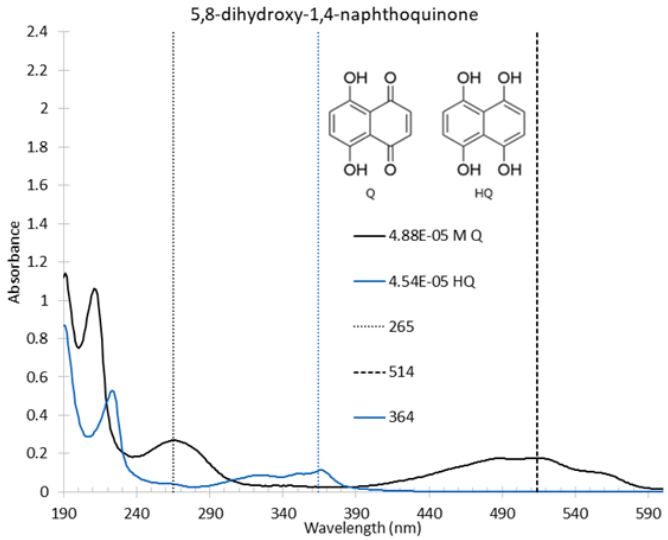
Figure 10: Calibration curve concentrations and representative spectra for naphthoquinone.



Concentration HQ	Abs(209)	Abs(250)	Abs(429)
4.96 µM	0.16111	0.06942	0.01711
3.97 µM	0.131365	0.057015	0.013785
2.97 µM	0.102292	0.042972	0.010282
7.25 µM	0.235091	0.096891	0.023011
5.83 µM	0.192776	0.080036	0.018486

Concentration Q	Abs(278)	Abs(334)
0.11 mM	0.23095	0.12446
0.11 mM	0.24078	0.14476
0.11 mM	0.24272	0.14931

Figure 11: Calibration curve concentrations and representative spectra for juglone

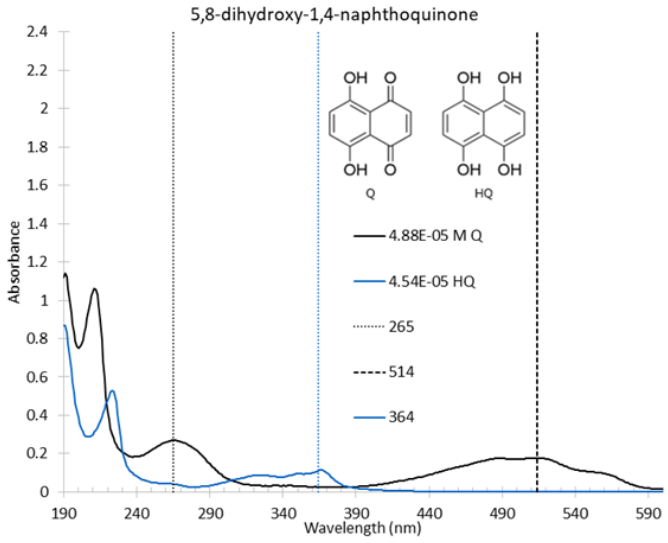


Concentration Q	Abs(265)
9.5 µM	0.05031
9.5 µM	0.04862
9.5 µM	0.05054
9.5 µM	0.05048
9.5 µM	0.05012
9.5 µM	0.04892

Concentration Q	Abs(514)
6.1 µM	0.02052
5.08 µM	0.01851
4.24 µM	0.01527
3.53 µM	0.01326
2.94 µM	0.01006
1.96 µM	0.00725

Concentration Q	Abs(364)
9.52 µM	0.02272
9.52 µM	0.01939
9.52 µM	0.019312

Figure 12: Calibration curve concentrations and representative spectra for 5,8-dihydroxy-napthoquinone

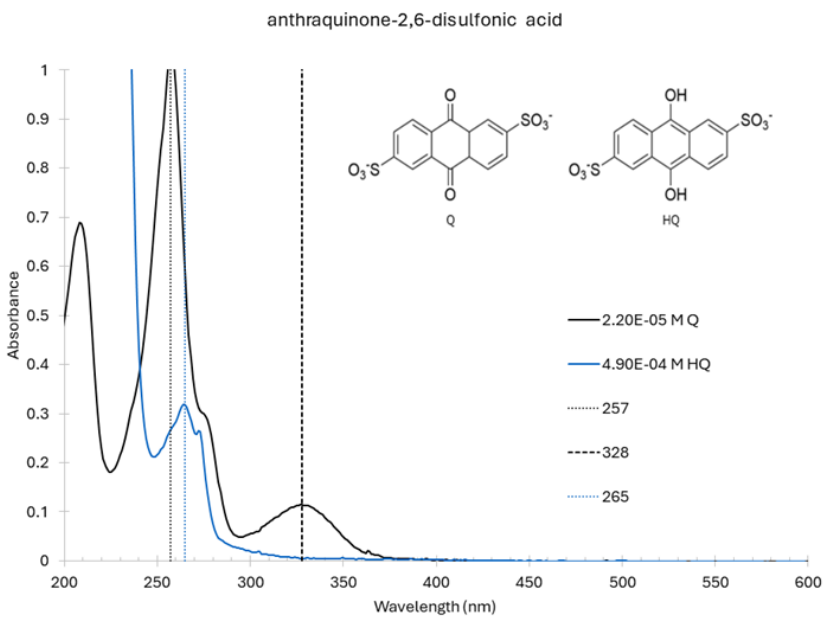


Concentration Q	Abs(265)
9.5 µM	0.05031
9.5 µM	0.04862
9.5 µM	0.05054
9.5 µM	0.05048
9.5 µM	0.05012
9.5 µM	0.04892

Concentration Q	Abs(514)
6.1 µM	0.02052
5.08 µM	0.01851
4.24 µM	0.01527
3.53 µM	0.01326
2.94 µM	0.01006
1.96 µM	0.00725

Concentration Q	Abs(364)
9.52 µM	0.02272
9.52 µM	0.01939
9.52 µM	0.019312

Figure 13: Calibration curve concentrations and representative spectra for anthraquinone-1,5-disulfonic acid.



Concentration Q	Abs(328)
0.423 mM	2.18998
0.254 mM	1.3368
0.282 mM	1.4839
0.211 mM	1.11921
0.352 mM	1.85368
0.423 mM	2.19454
0.0423 mM	0.21774
0.0338 mM	0.17422
0.0376 mM	0.19325
0.0308 mM	0.15832
0.0282 mM	0.14453

Concentration Q	Abs(208)
0.0423 mM	1.3016
0.0338 mM	1.05317
0.0376 mM	1.16539
0.0308 mM	0.95704
0.0282 mM	0.87684

Concentration HQ	Abs(257)
0.0423 mM	1.95017
0.0338 mM	1.58117
0.0376 mM	1.74808
0.0308 mM	1.43451
0.0282 mM	1.31553

Figure 14: Calibration curve concentrations and representative spectra for anthraquinone-2,6-disulfonic acid.

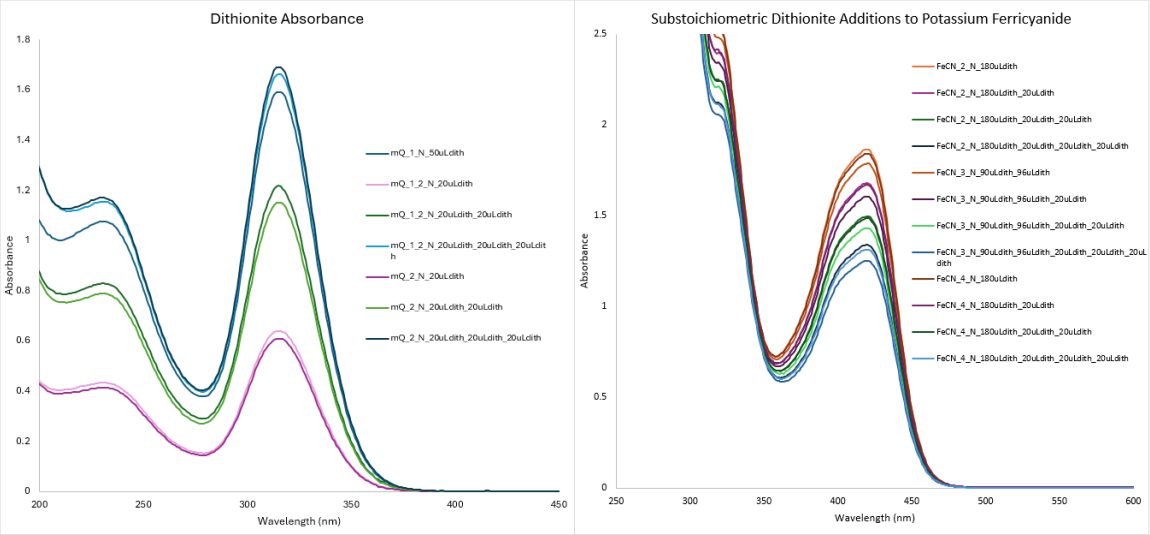


Figure 15: Absorption spectra for (Left) dithionite additions to a mQ blank and (Right) dithionite additions to a sample of potassium ferricyanide.

M^{-1} cm^{-1} (*100*): 0.0131 +/- 0.0006 M

A.3.2 HPLC Chromatographs

A.3.3 Comparison of 2,3-dimethyl-*p*-benzoquinone and duroquinone LC chromatographs

Duroquinone shows no difference between end of dithionite titration chromatogram and borohydride reduced chromatogram, consistent with hydroquinone formation from dithionite reduction. In comparison, 2,3-dimethyl-*p*-benzoquinone shows an additional small peak under excess dithionite reduction as compared to the hydroquinone chromatogram, and the end of dithionite titration chromatogram has additional small shoulders around this peak. This supports the conclusion that a small amount of additional products may be forming in the dithionite reduction, especially over time and multiple additions. These interferences remain small compared to the observed hydroquinone peak, however.

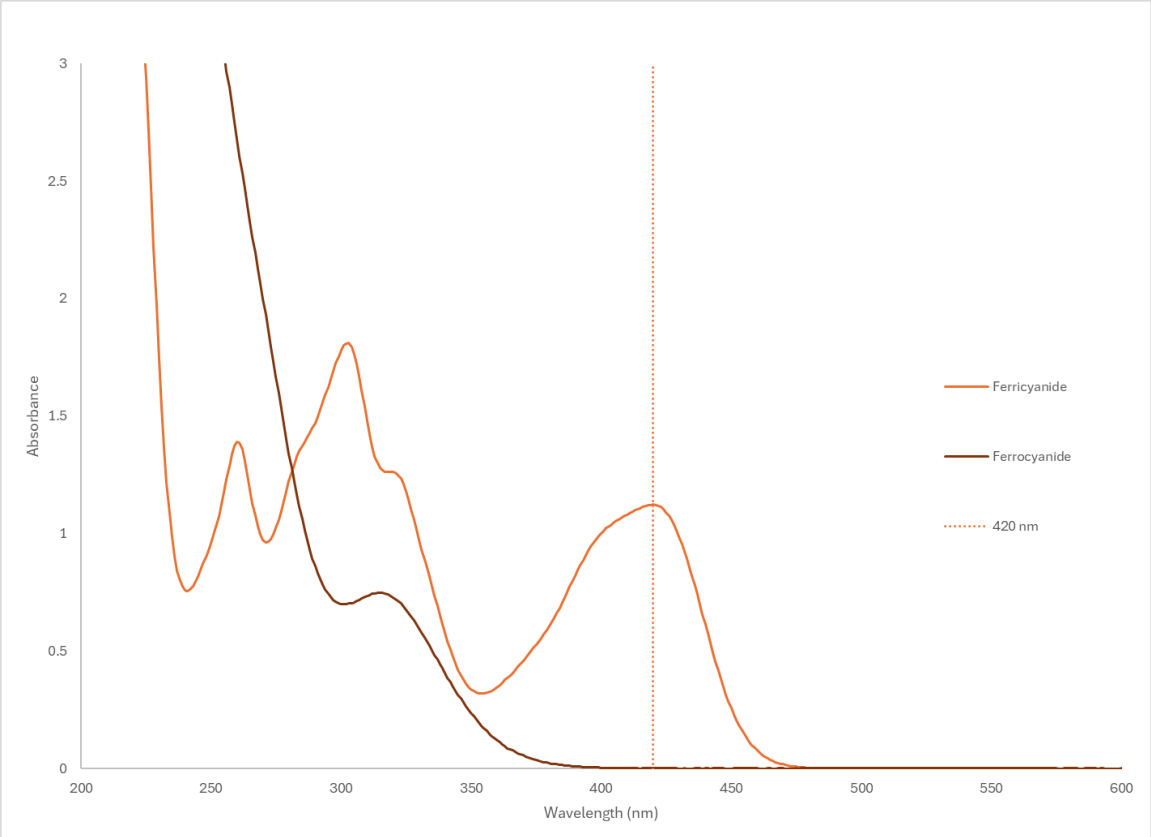


Figure 16: Absorption spectra of ferricyanide and ferrocyanide produced by dithionite reduction of ferricyanide. A line is placed at 420 nm to emphasize that only the ferricyanide absorbs at this wavelength.

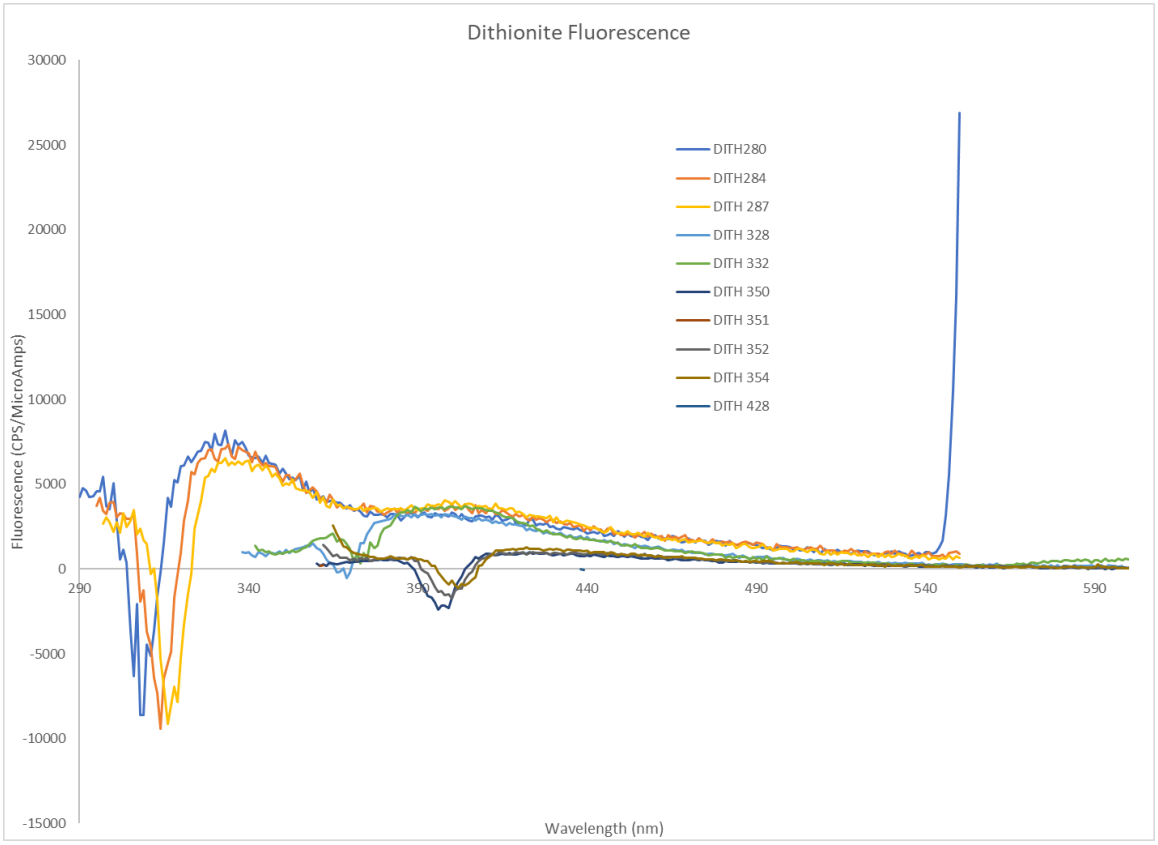


Figure 17: Blank subtracted dithionite fluorescence intensity presented as obtained.

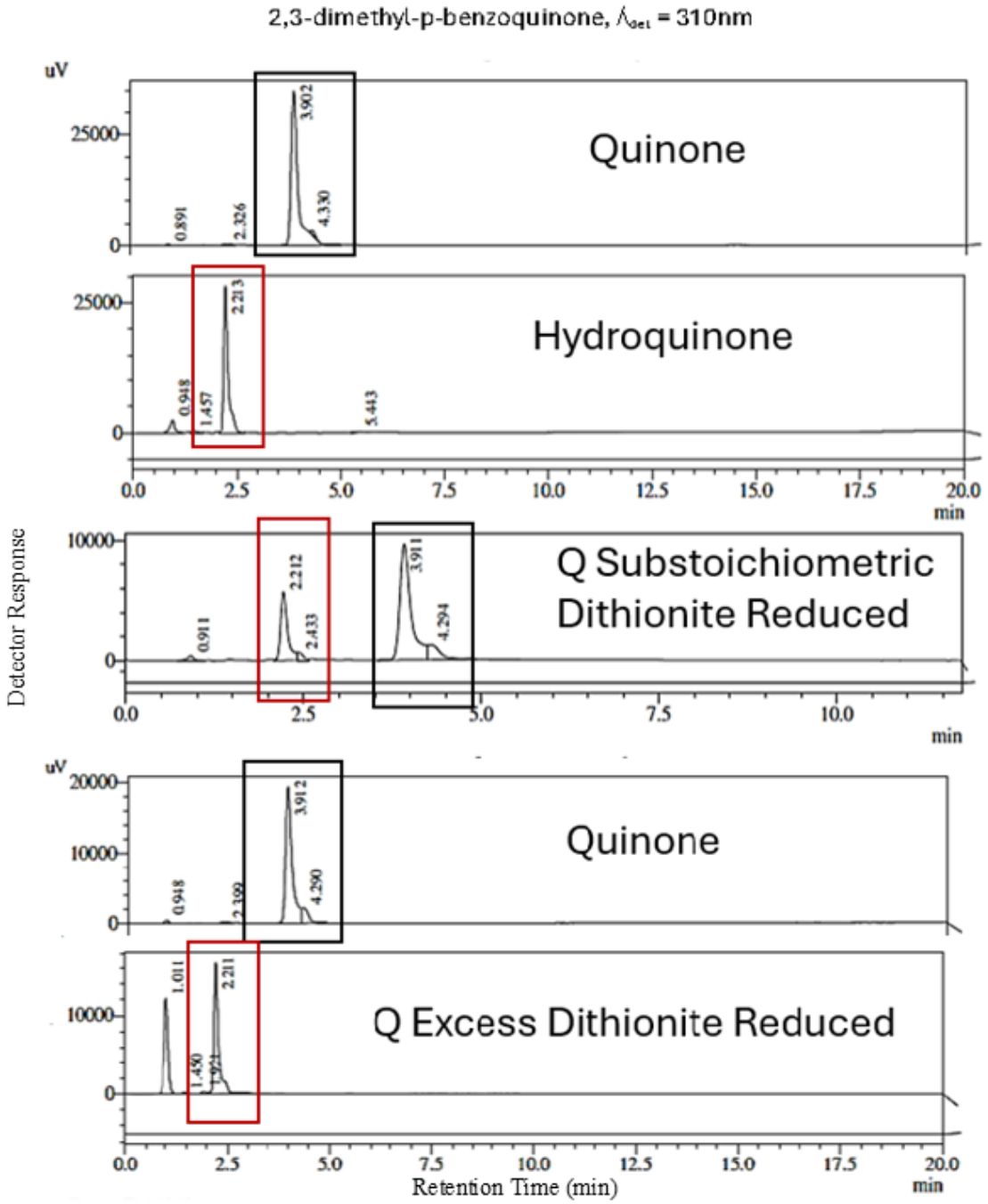


Figure 18: HPLC chromatographs of 2,3-dimethyl-*p*-benzoquinone, 2,3-dimethyl-*p*-benzohydroquinone, and dithionite reduced 2,3-dimethyl-*p*-benzoquinone. Quinone peak is highlighted by black box. Hydroquinone peak is highlighted by red box.

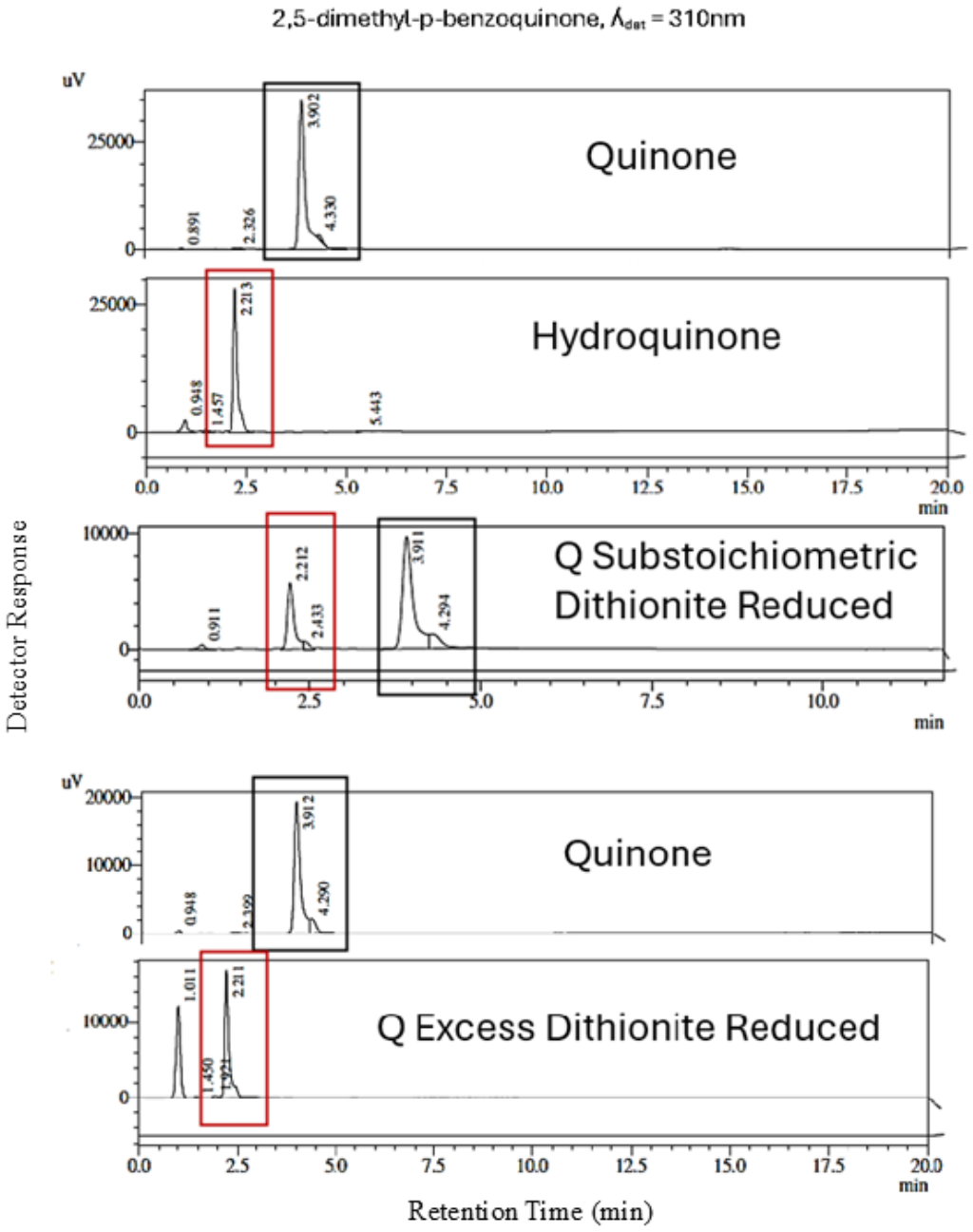


Figure 19: HPLC chromatographs of 2,5-dimethyl-*p*-benzoquinone, 2,5-dimethyl-*p*-benzohydroquinone, and dithionite reduced 2,5-dimethyl-*p*-benzoquinone. Quinone peak is highlighted by black box. Hydroquinone peak is highlighted by red box.

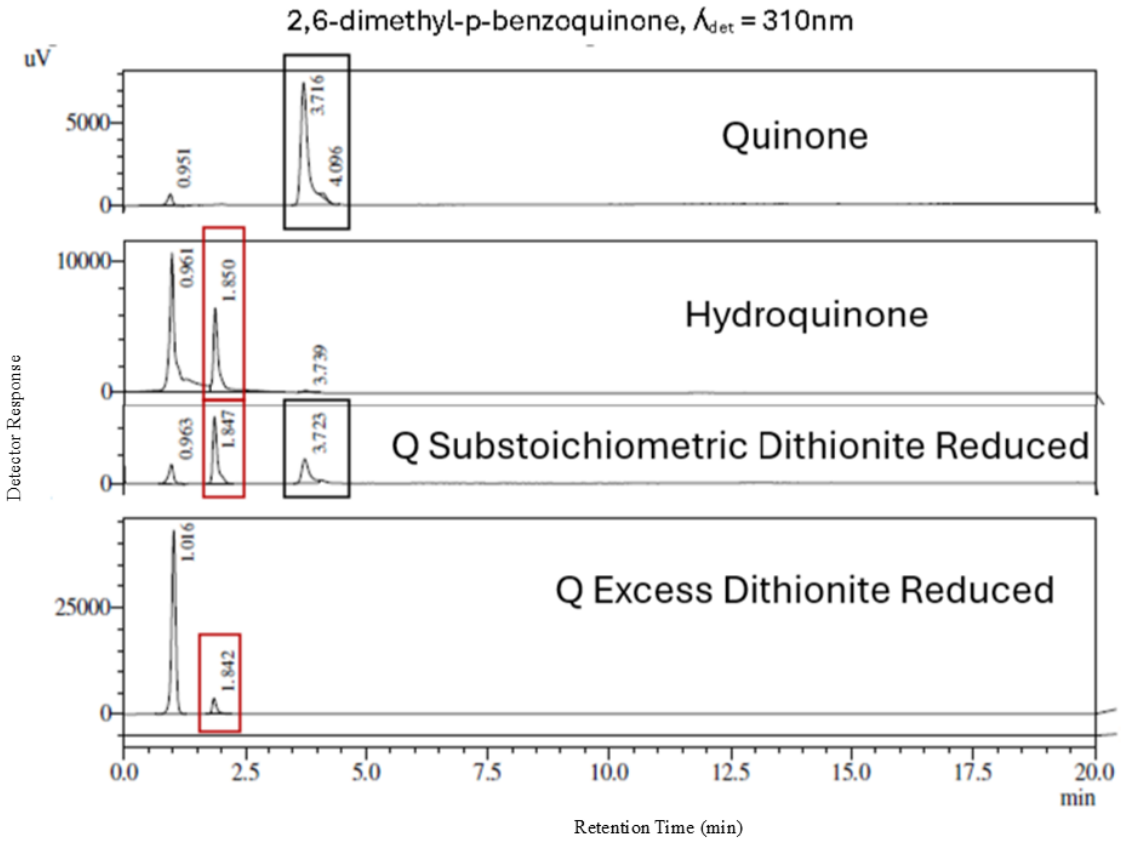


Figure 20: HPLC chromatographs of 2,6-dimethyl-*p*-benzoquinone, 2,6-dimethyl-*p*-benzohydroquinone, and dithionite reduced 2,6-dimethyl-*p*-benzoquinone. Quinone peak is highlighted by black box. Hydroquinone peak is highlighted by red box.

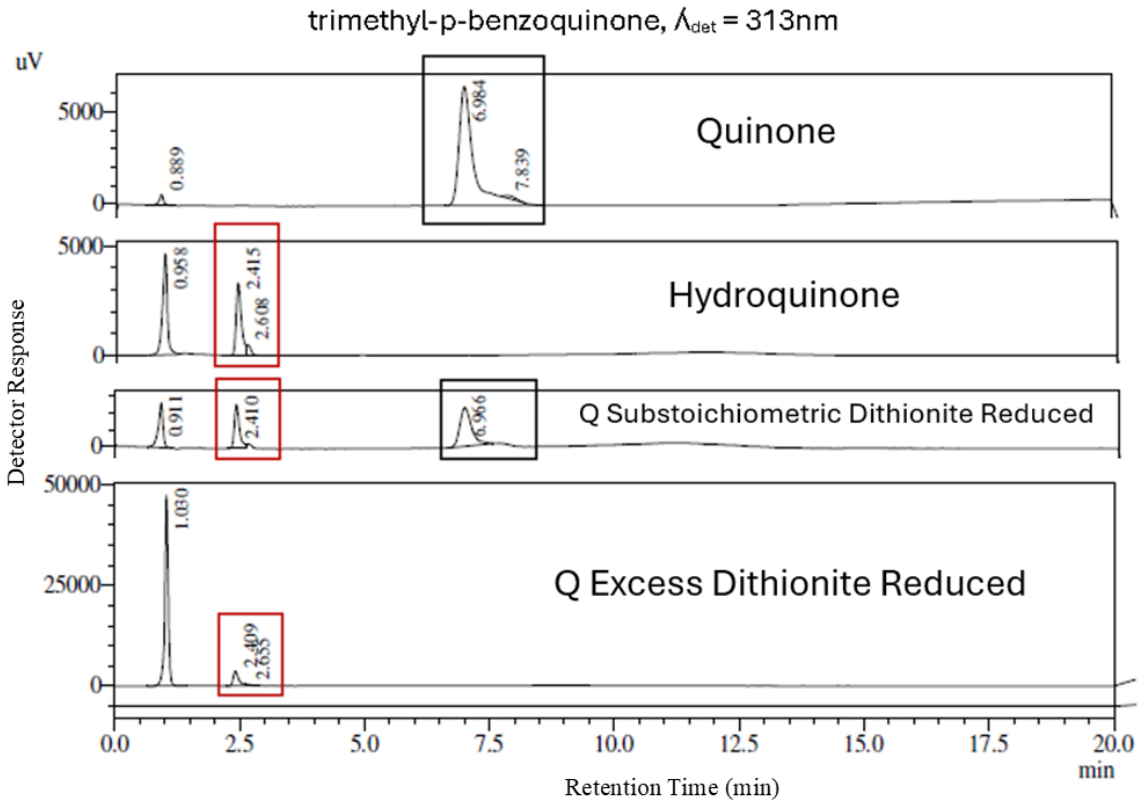


Figure 21: HPLC chromatographs of trimethyl-*p*-benzoquinone, trimethyl-*p*-benzohydroquinone, and dithionite reduced trimethyl-*p*-benzoquinone. Quinone peak is highlighted by black box. Hydroquinone peak is highlighted by red box.

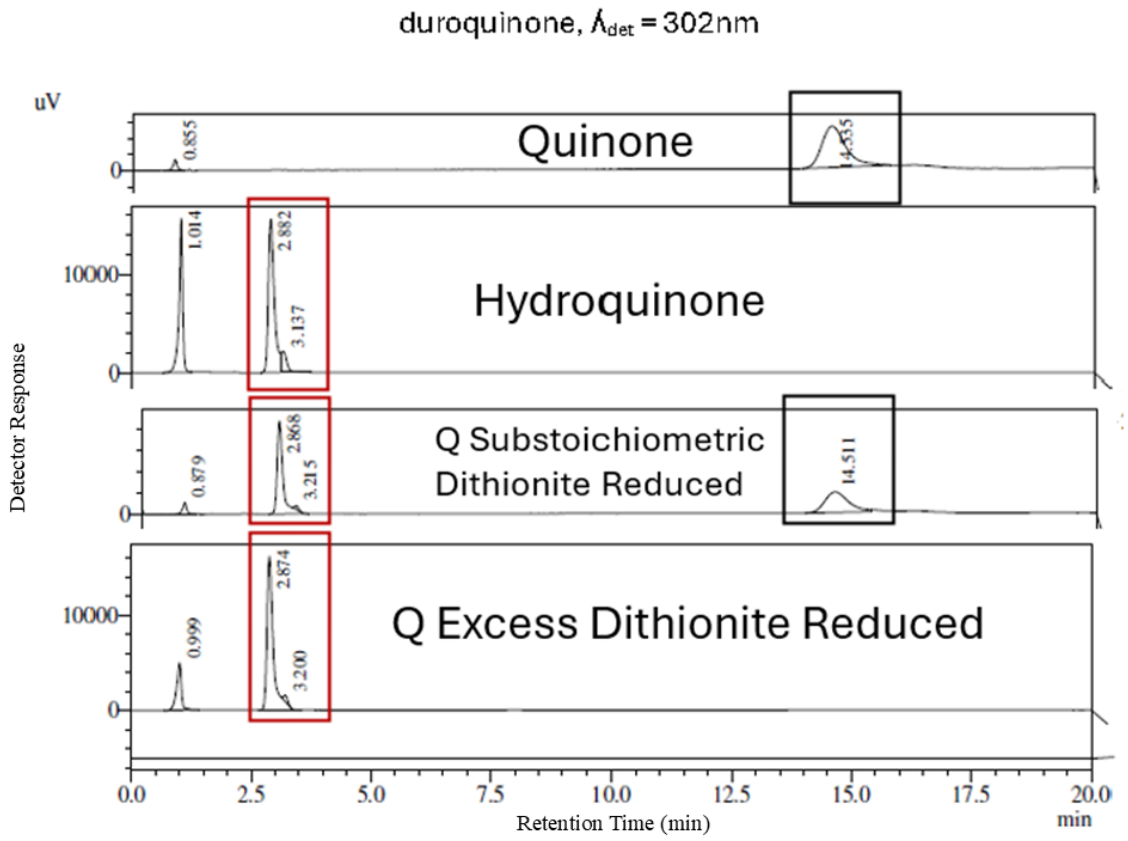


Figure 22: HPLC chromatographs of duroquinone, durohydrquinone, and dithionite reduced duroquinone. Quinone peak is highlighted by black box. Hydroquinone peak is highlighted by red box.

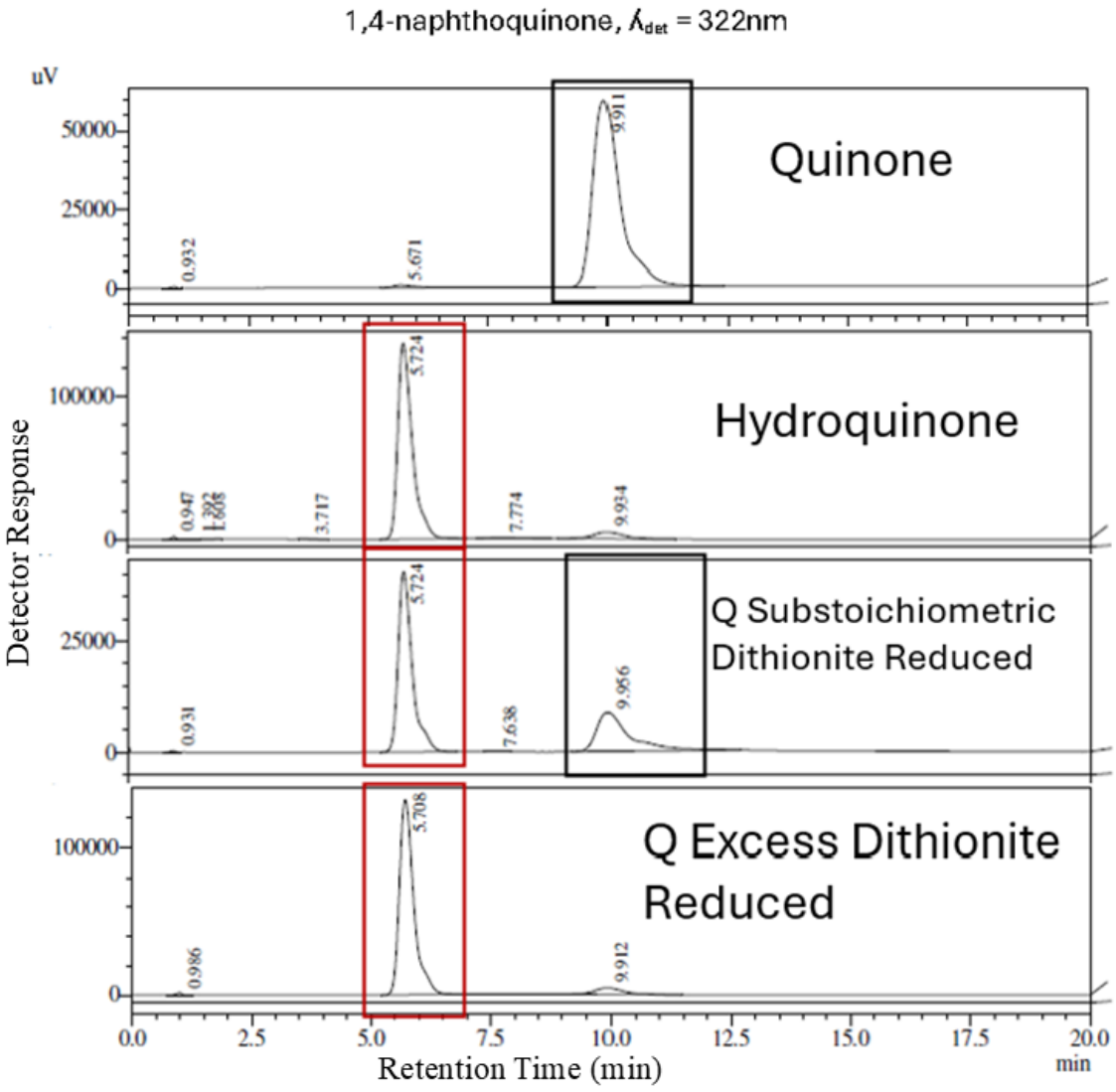


Figure 23: HPLC chromatographs of 1,4-naphtoquinone, naphthohydroquinone, and dithionite reduced 1,4-naphthoquinone. Quinone peak is highlighted by black box. Hydroquinone peak is highlighted by red box.

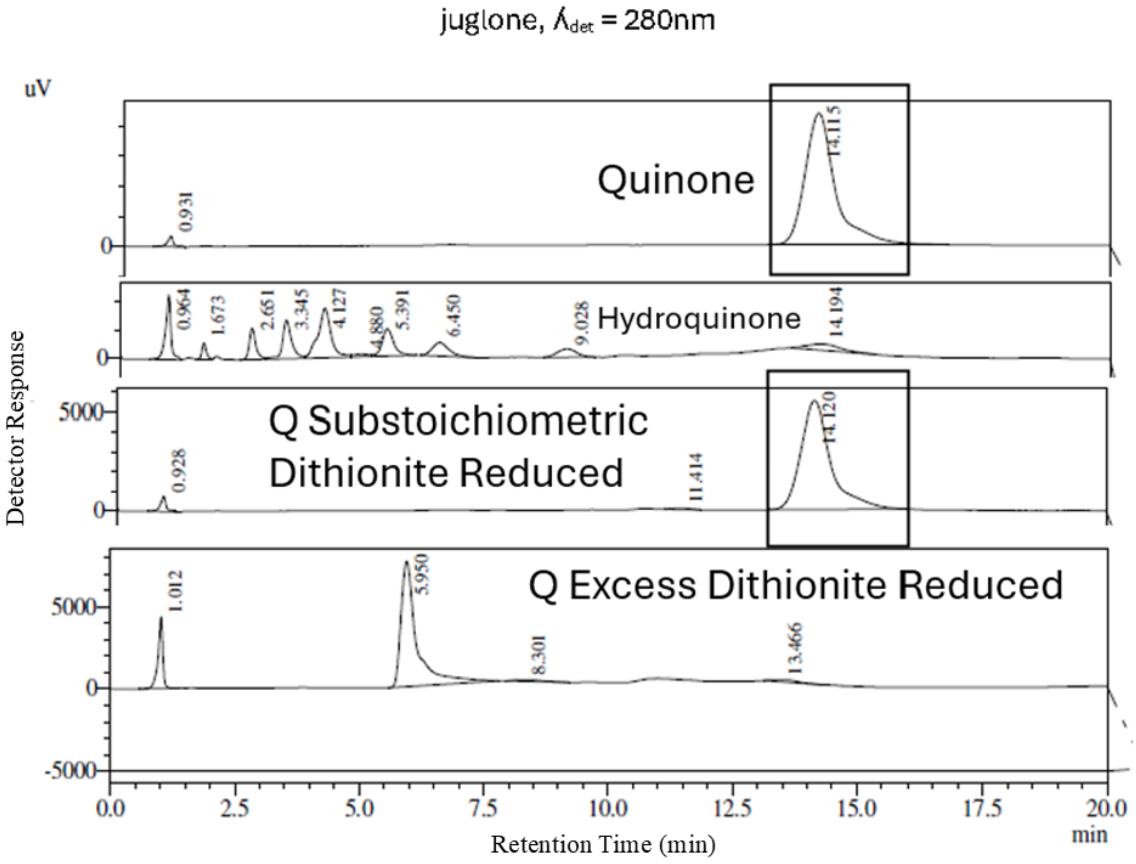


Figure 24: HPLC chromatographs of juglone, hydroxyjuglone, and dithionite reduced juglone. Quinone peak is highlighted by black box. Hydroquinone peak is highlighted by red box.

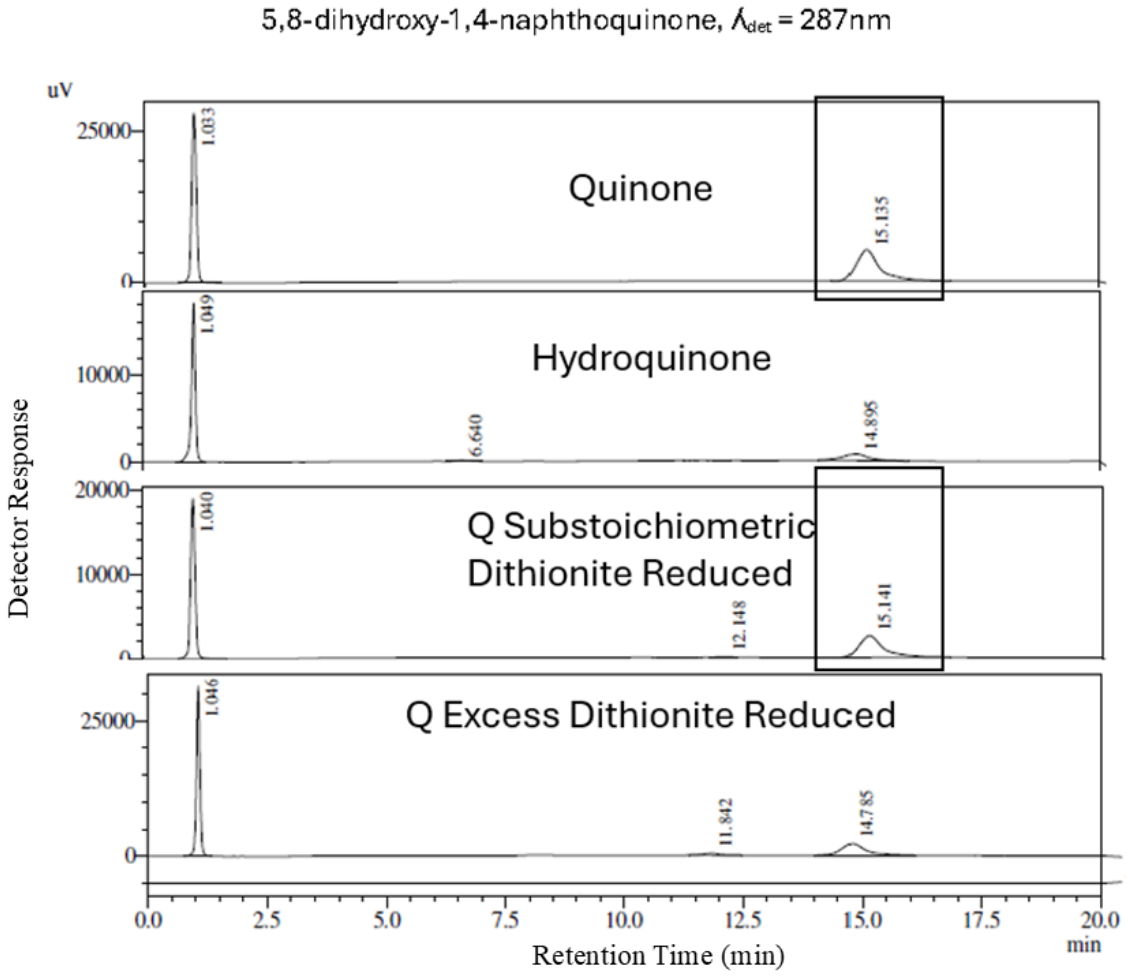
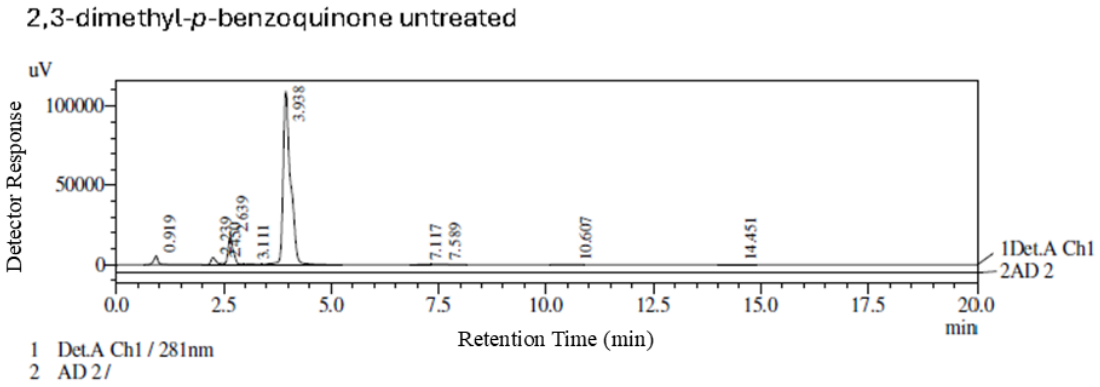
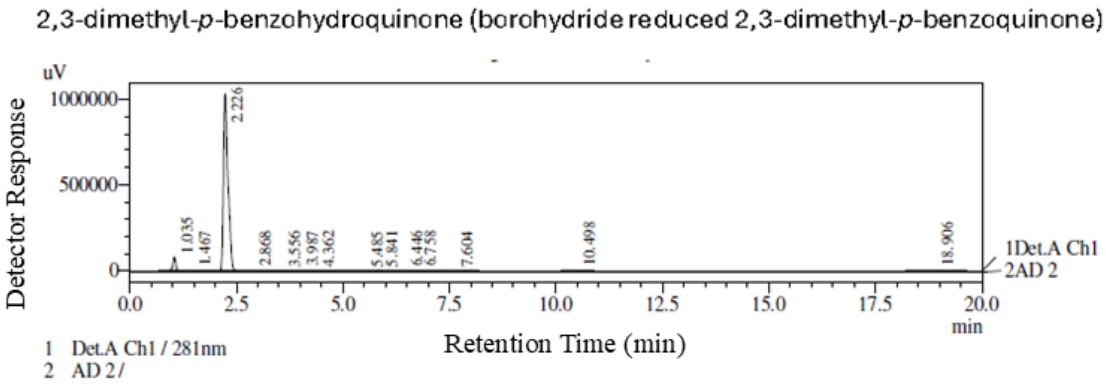


Figure 25: HPLC chromatographs of 5,8-dihydroxy-1,4-naphthoquinone, naphthalene-1,4,5,8-tetraol, and dithionite reduced 5,8-dihydroxy-1,4-naphthoquinone. Quinone peak is highlighted by black box. Hydroquinone peak is highlighted by red box.



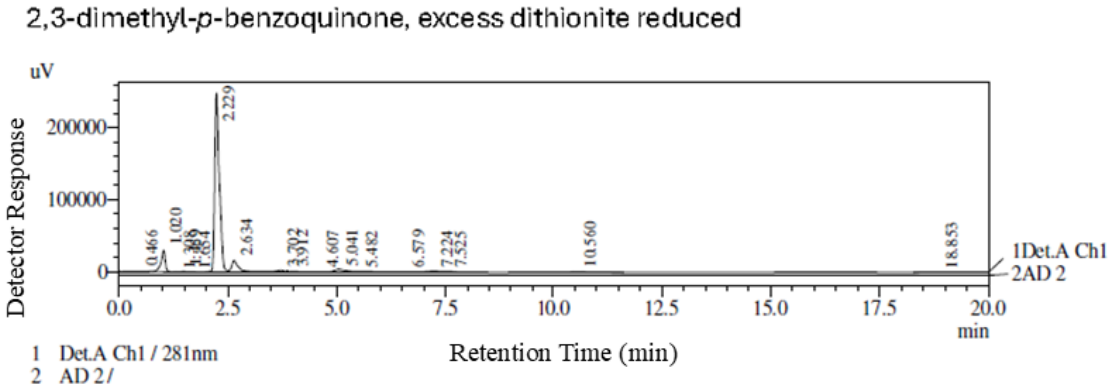
Peak#	Ret. Time	Area	Height	Area %	Height %
1	0.919	39974	5609	2.56	4.047
2	2.239	35573	4535	2.278	3.272
3	2.45	6284	996	0.403	0.719
4	2.639	144973	16993	9.286	12.261
5	3.111	7616	427	0.488	0.308
6	3.938	1308244	109218	83.794	78.804
7	7.117	4721	288	0.302	0.208
8	7.589	6950	273	0.445	0.197
9	10.607	2984	105	0.191	0.076
10	14.451	3944	150	0.253	0.108
Total		1561264	138594	100	100

Figure 26: HPLC Chromatagraph of 2,3-dimethyl-*p*-benzoquinone



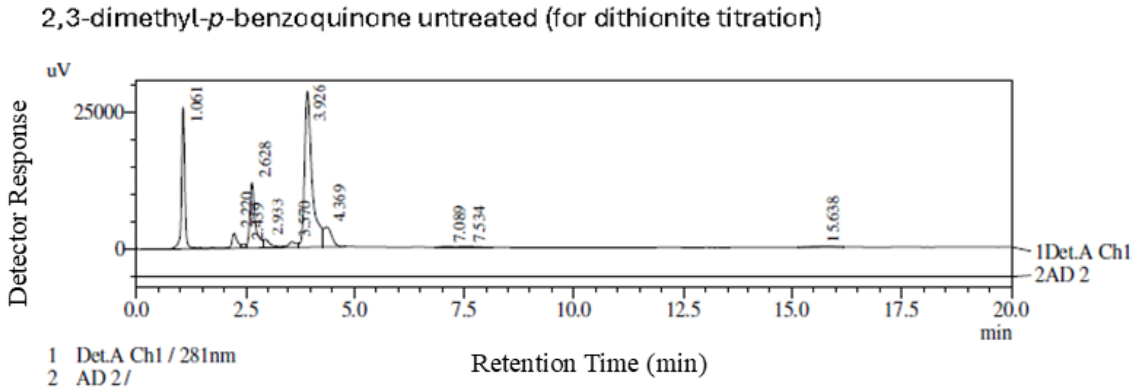
Peak#	Ret. Time	Area	Height	Area %	Height %
1	1.035	424561	82420	5.142	7.324
2	1.467	2222	448	0.027	0.04
3	2.226	7677463	1033630	92.975	91.852
4	2.868	4628	644	0.056	0.057
5	3.556	1635	102	0.02	0.009
6	3.987	4049	377	0.049	0.034
7	4.362	1364	146	0.017	0.013
8	5.485	16035	1107	0.194	0.098
9	5.841	94459	5140	1.144	0.457
10	6.446	4867	345	0.059	0.031
11	6.758	1155	103	0.014	0.009
12	7.604	3893	230	0.047	0.02
13	10.498	3392	163	0.041	0.014
14	18.906	17816	464	0.216	0.041
Total		8257539	1125318	100	100

Figure 27: HPLC Chromatagraph of 2,3-dimethyl-*p*-benzohydroquinone



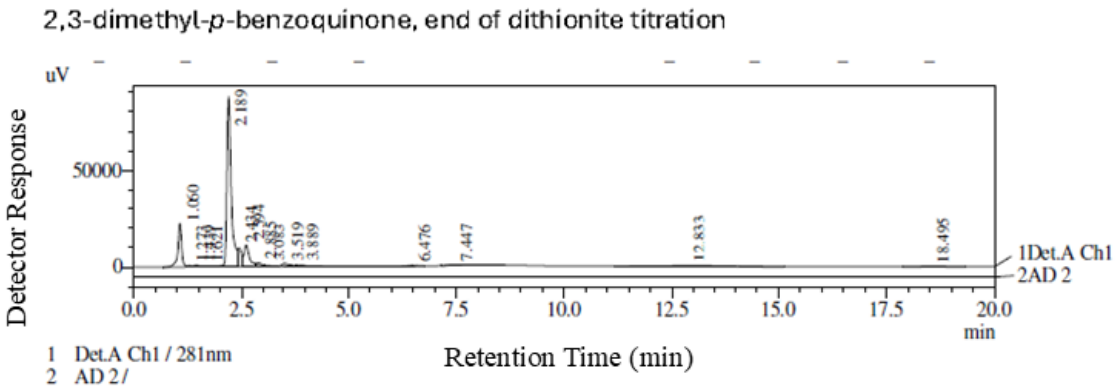
Peak#	Ret. Time	Area	Height	Area %	Height %
1	0.466	8448	285	0.333	0.092
2	1.02	207720	30254	8.184	9.728
3	1.308	3440	393	0.136	0.127
4	1.469	5102	628	0.201	0.202
5	1.654	1691	224	0.067	0.072
6	2.229	1841571	250136	72.559	80.428
7	2.634	195279	16189	7.694	5.205
8	3.702	37779	2365	1.489	0.76
9	3.912	23699	1317	0.934	0.423
10	4.607	3675	278	0.145	0.089
11	5.041	75092	3816	2.959	1.227
12	5.482	35461	1041	1.397	0.335
13	6.579	13484	513	0.531	0.165
14	7.224	40891	1697	1.611	0.546

Figure 28: HPLC Chromatagraph of 2,3-dimethyl-*p*-benzoquinone reduced with excess dithionite



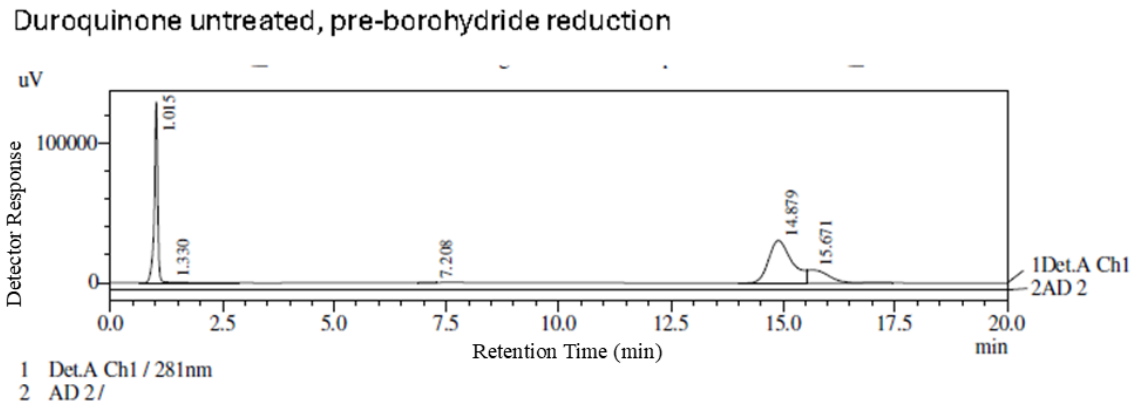
Peak#	Ret. Time	Area	Height	Area %	Height %
1	1.061	136596	25965	19.613	33.965
2	2.22	21867	2716	3.14	3.553
3	2.439	4731	727	0.679	0.951
4	2.628	103530	11982	14.865	15.674
5	2.933	19092	1539	2.741	2.014
6	3.57	13616	1020	1.955	1.334
7	3.926	343278	28493	49.289	37.271
8	4.369	44642	3628	6.41	4.746
9	7.089	2098	116	0.301	0.152
10	7.534	3416	148	0.491	0.194
11	15.638	3589	112	0.515	0.146
Total		696456	76447	100	100

Figure 29: HPLC Chromatagraph of 2,3-dimethyl-*p*-benzoquinone for dithionite titration



Peak#	Ret. Time	Area	Height	Area %	Height %
1	1.06	132642	22295	12.516	16.075
2	1.273	4472	714	0.422	0.515
3	1.439	10373	917	0.979	0.661
4	1.621	5152	516	0.486	0.372
5	2.189	621711	87648	58.662	63.197
6	2.434	60256	9591	5.685	6.915
7	2.594	97665	11139	9.215	8.031
8	2.885	17073	1777	1.611	1.281
9	3.083	7558	591	0.713	0.426
10	3.519	21921	1569	2.068	1.131
11	3.889	11809	674	1.114	0.486
12	6.476	6644	393	0.627	0.283
13	7.447	4139	246	0.391	0.178
14	12.833	50540	447	4.769	0.322
15	18.495	7864	174	0.742	0.126
Total		1059819	138691	100	100

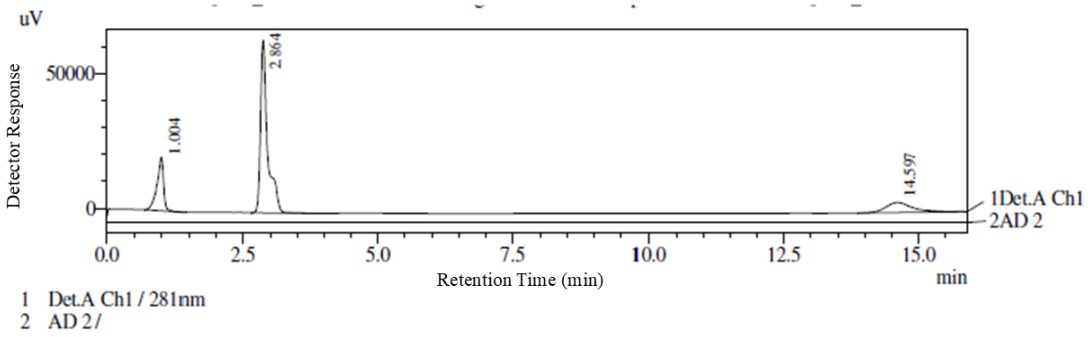
Figure 30: HPLC Chromatagraph of 2,3-dimethyl-*p*-benzoquinone following dithionite titration



Peak#	Ret. Time	Area	Height	Area %	Height %
1	1.015	671733	129902	31.598	76.28
2	1.33	22039	511	1.037	0.3
3	7.208	1150	50	0.054	0.029
4	14.879	1104735	30548	51.965	17.938
5	15.671	326245	9284	15.346	5.452
Total		2125901	170295	100	100

Figure 31: HPLC Chromatagraph of duroquinone

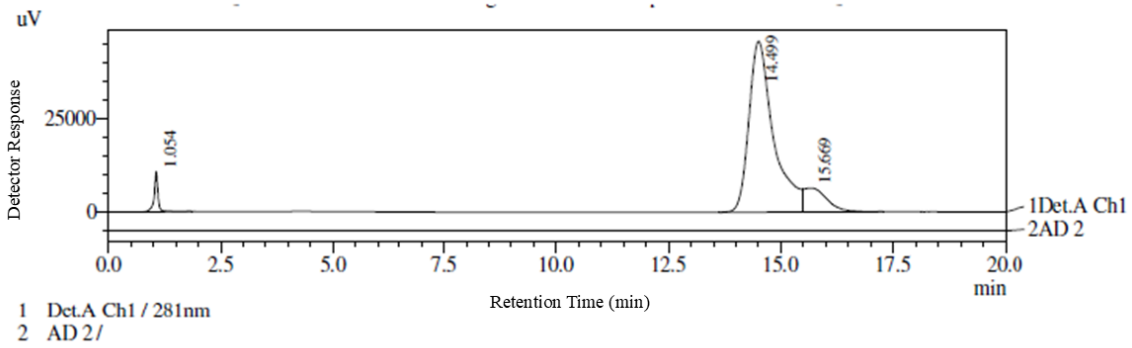
Durohydroquinone (borohydride reduced duroquinone)



Peak#	Ret. Time	Area	Height	Area %	Height %
1	1.004	165351	19462	18.839	22.36
2	2.864	578400	63838	65.898	73.344
3	14.597	133968	3739	15.263	4.296
Total		877720	87040	100	100

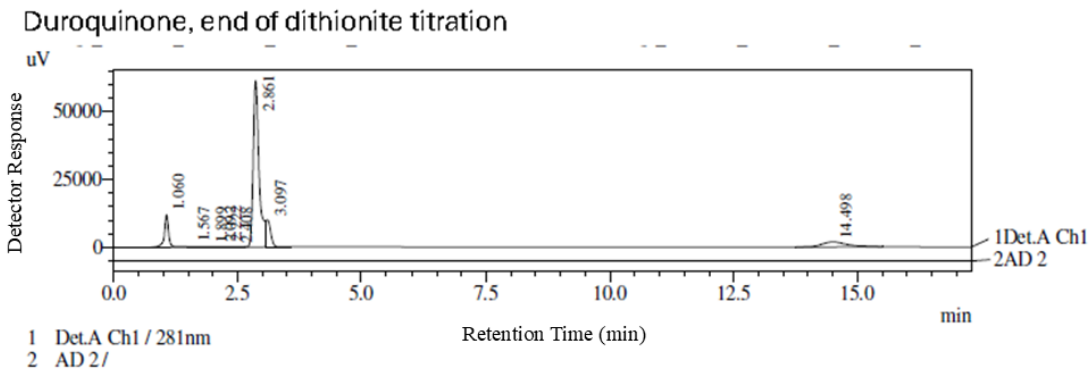
Figure 32: HPLC Chromatagraph of durohydroquinone

Duroquinone untreated (for dithionite titration)



Peak#	Ret. Time	Area	Height	Area %	Height %
1	1.054	64746	10799	3.177	17.132
2	14.499	1741787	45807	85.48	72.671
3	15.669	231131	6427	11.343	10.197
Total		2037664	63032	100	100

Figure 33: HPLC Chromatagraph of duroquinone for dithionite titration



Peak#	Ret. Time	Area	Height	Area %	Height %
1	1.06	71452	11970	9.927	13.951
2	1.567	1761	136	0.245	0.159
3	1.899	2638	144	0.367	0.168
4	2.092	1145	134	0.159	0.156
5	2.222	1351	138	0.188	0.161
6	2.408	1020	86	0.142	0.1
7	2.861	505563	61373	70.239	71.526
8	3.097	71073	10003	9.874	11.658
9	14.498	63773	1820	8.86	2.121
Total		719776	85805	100	100

Figure 34: HPLC Chromatagraph of duroquinone following dithionite titration

A.3.4 Quinone-Sulfite Reactions Over Time

Dithionite reactions were immediate upon addition to sample, while sulfite continued to react over time. Supporting information includes spectra of quinones over time after addition of sulfite. A.3.4 Duroquinone, while it shows no immediate reaction with sulfite, does appear to very slowly be reduced by sulfite, as the absorbance around the peak of the hydroquinone increases slightly over time. Based on the shape changes over time, 2,3-dimethyl and 2,5-dimethyl-*p*-benzoquinone appear to initially form the sulfonated hydroquinone, but over time produce more hydroquinone in solution. In contrast, the 2,6-dimethyl*p*-benzoquinone appears to form more sulfonated product over time, as the absorbance increases at the wavelength corresponding to the excess sulfite reduced sample rather than the hydroquinone (borohydride reduced sample). Trimethyl-*p*-benzoquinone appears to very slowly form more of the sulfonated product, but not to a great extent after the initial reaction. Naphthoquinone and juglone show greater formation of the assumed sulfonated product over time. Anthraquinone-1,5-disulfonic acid does not react with sulfite at all.

A.3.5 Sulfite Reduction Stoichiometry

A.3.6 *p*-benzoquinone and methyl-*p*-benzoquinone

P-benzoquinone and methyl-*p*-benzoquinone show optical changes on their own within the time frame of experimentation, so dithionite reduction and LC analysis could not be performed; however, the fluorescence of the quinone and hydroquinone forms was collected and the fluorescence quantum yields calculated in chapter 2. Both compounds are very photo-reactive.(*127*, *128*)

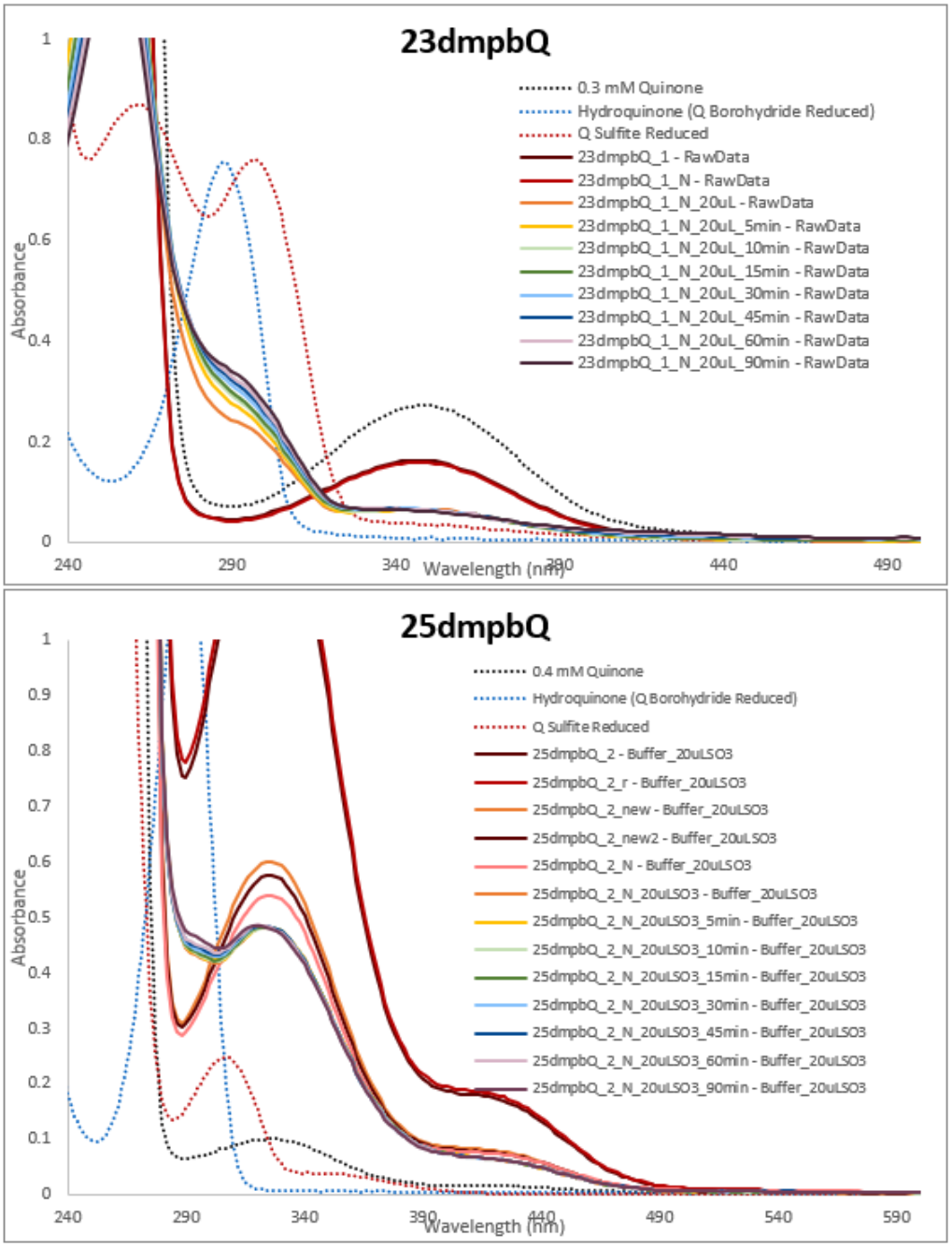


Figure 35: 2,3 and 2,5-dimethyl*p*-benzoquinone over time with substoichiometric sulfite addition. Quinone, hydroquinone, and excess sulfite spectra are shown for reference as dotted lines.

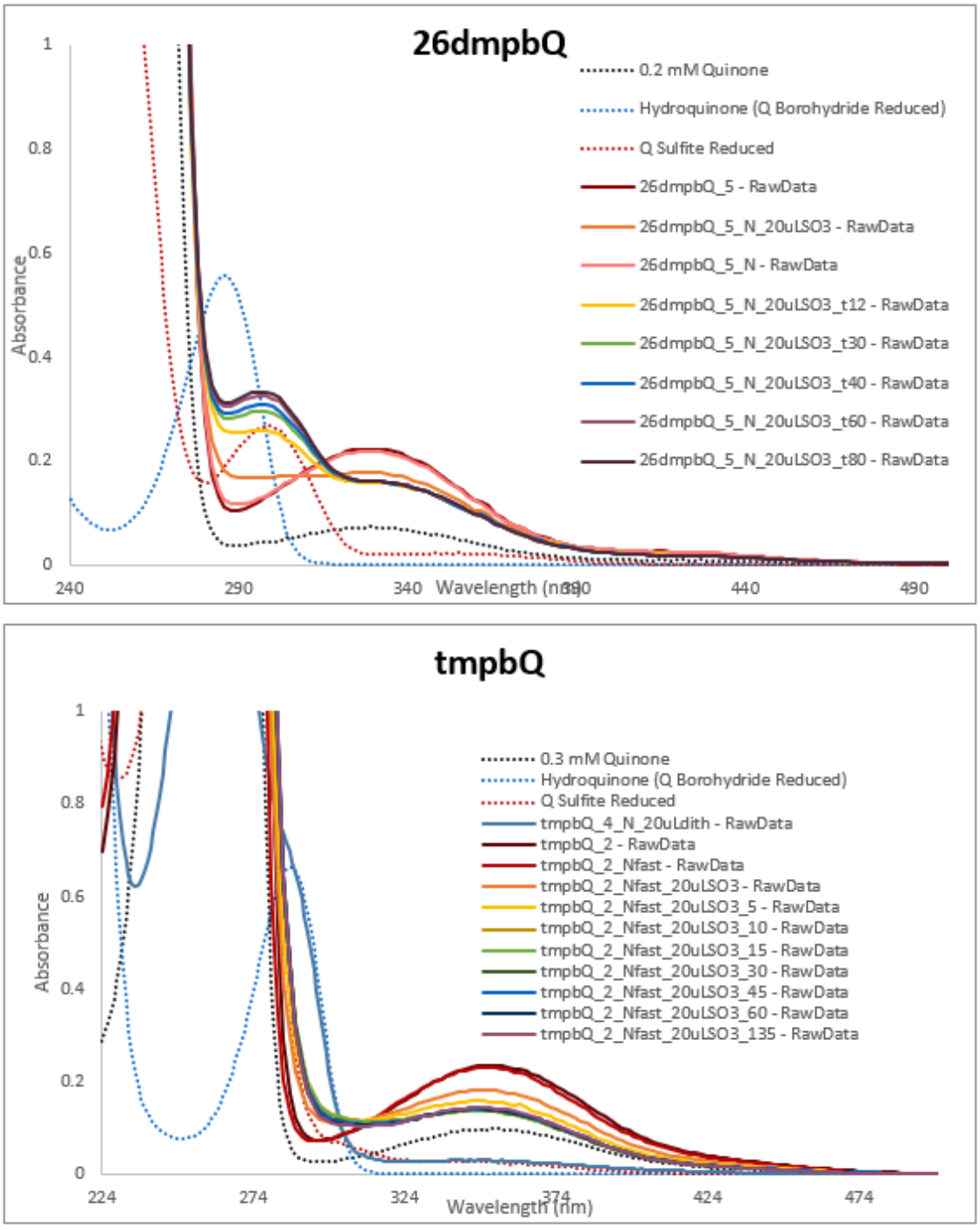


Figure 36: 2,6 and trimethyl*p*-benzoquinone over time with substoichiometric sulfite addition. Quinone, hydroquinone, and excess sulfite spectra are shown for reference as dotted lines.

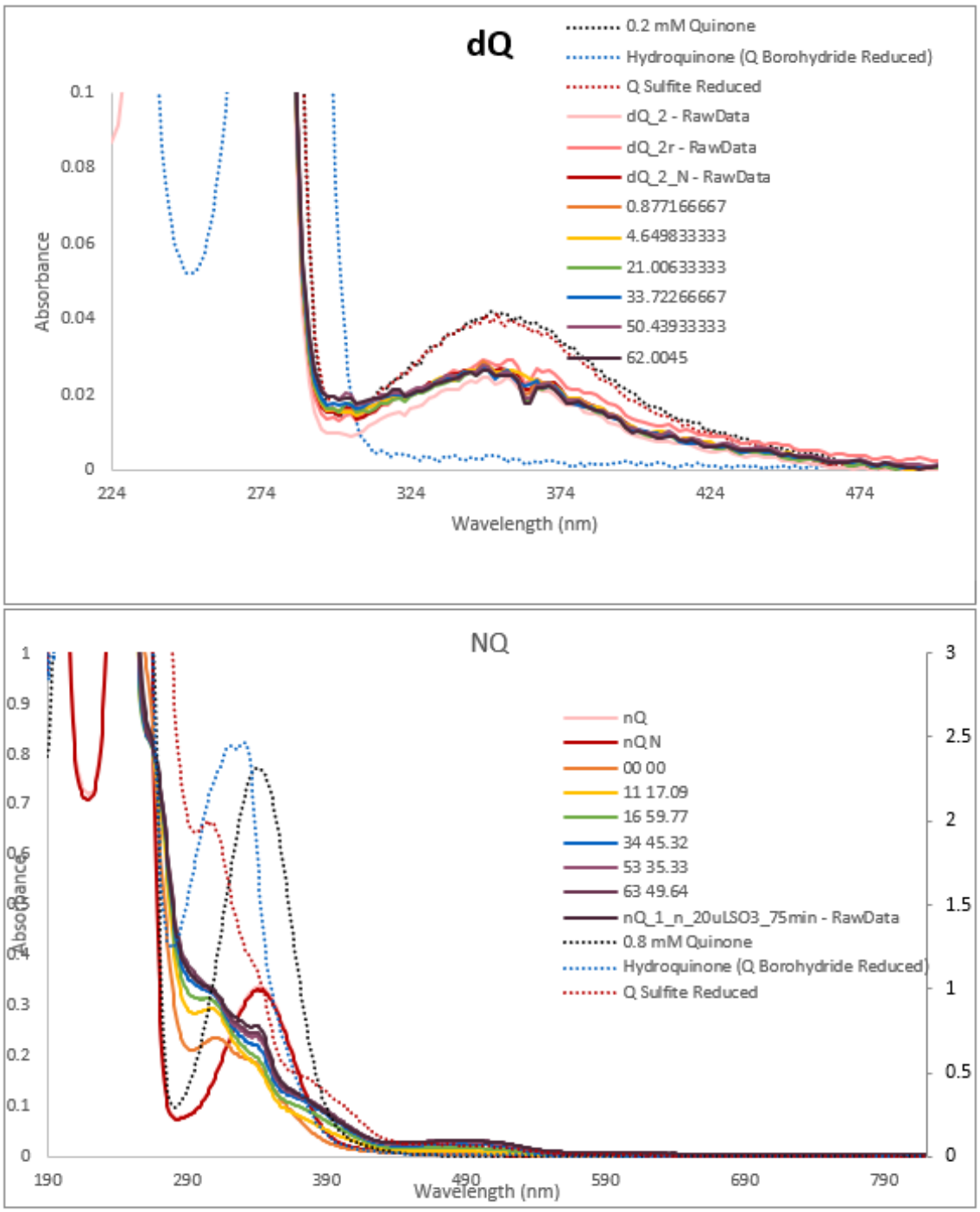


Figure 37: Duroquinone and napthoquinone over time with substoichiometric sulfite addition. Quinone, hydroquinone, and excess sulfite spectra are shown for reference as dotted lines.

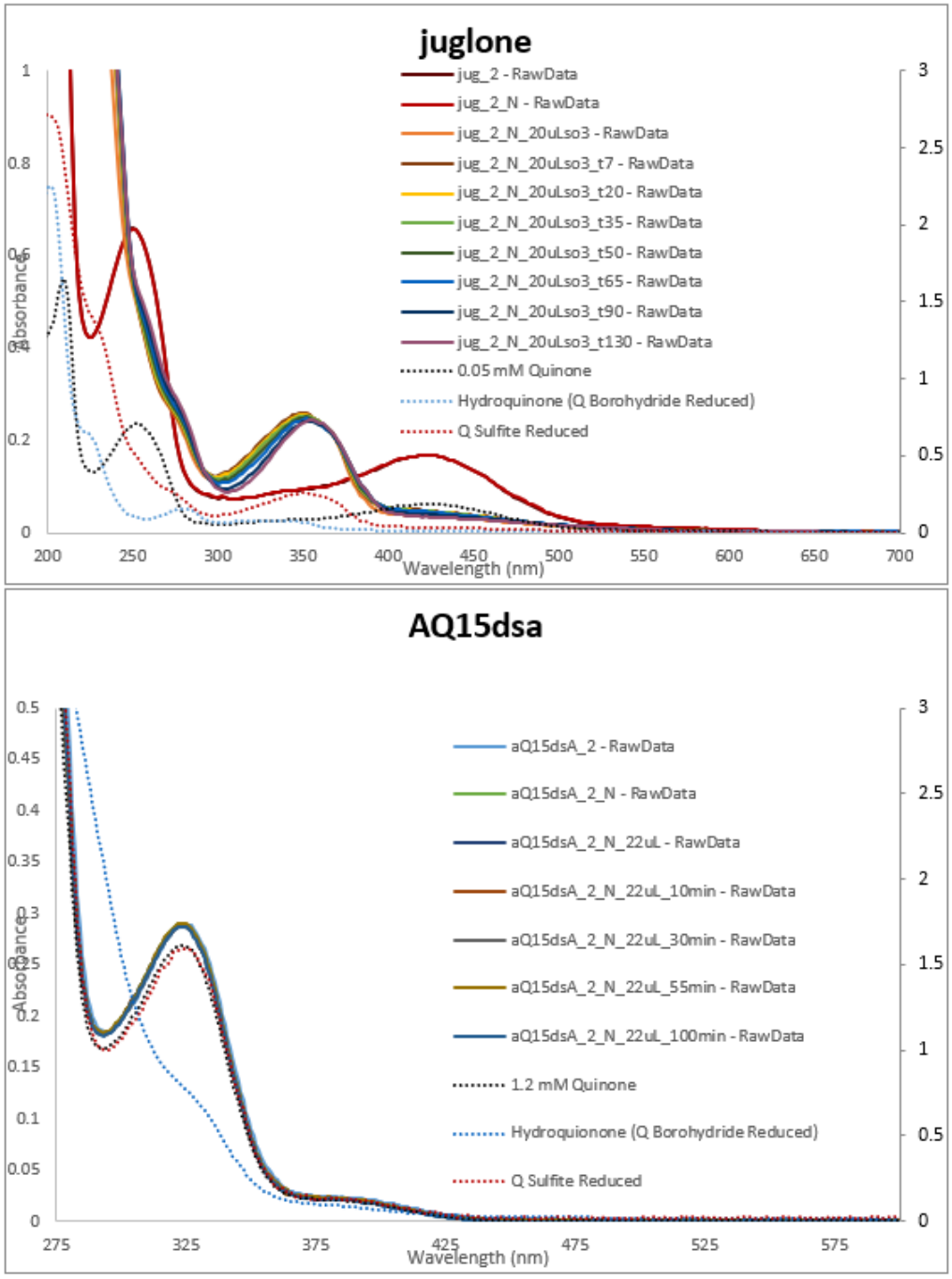


Figure 38: Juglone and anthraquinone-1,5-disulfonic acid over time with substoichiometric sulfite addition. Quinone, hydroquinone, and excess sulfite spectra are shown for reference as dotted lines.

Quinone	Stoichiometry of SO_3^{2-} Reduction (Q:R)
2,3-dimethyl-p-benzoquinone (23dmpbQ)	1.6:1
2,5-dimethyl-p-benzoquinone (25dmpbQ)	1.0:1
2,6-dimethyl-p-benzoquinone (26dmpbQ)	0.89:1
Trimethyl-p-benzoquinone (tmpbQ)	0.3-0.6:1
Duroquinone (dQ)	No reaction
2,3-dimethoxy-5-methyl-p-benzoquinone (23dmo5mpbQ)	1:1

Table A.1: Stoichiometry of reduction of quinones by sulfite, based on disappearance of quinone absorbance peak and sulfite concentration calculated from mass and volume.

A.4 General Supplemental

A.4.1 Ketone and Aldehyde Dithionite Reduction Controls

To show that ketones and aldehydes are not reduced by dithionite, dithionite was added to 2-acetylnaphthone and 4-hydroxybenzadehyde under anoxic conditions as described in Chapter 3. In figure 39, the spectra of dithionite added to the ketone produces simply the addition spectra of dithionite and the ketone. In figure 40, 4-hydroxybenzadehyde does not produce the simple addition spectra, but its pKa is 7.61 (*129*), so this may be attributed to pH effects. The difference in shape is not explained by the aldehyde being reduced, as conversion of the spectra to that of 4-hydroxybenzyl alcohol (figure 40 orange line) does not produce the dithionite addition spectra shape. Either a small amount of aldehyde is reduced, or more likely, this difference is simply due to pH effects as the sample moves

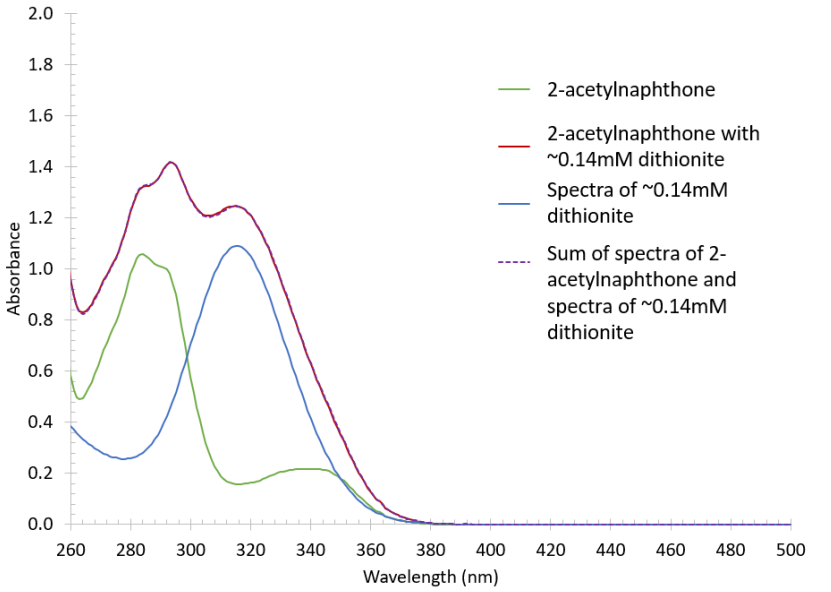


Figure 39: Absorption spectra of 2-acetylnaphthone with dithionite

from neutral pH to high pH ($\sim$10) with dithionite reduction.

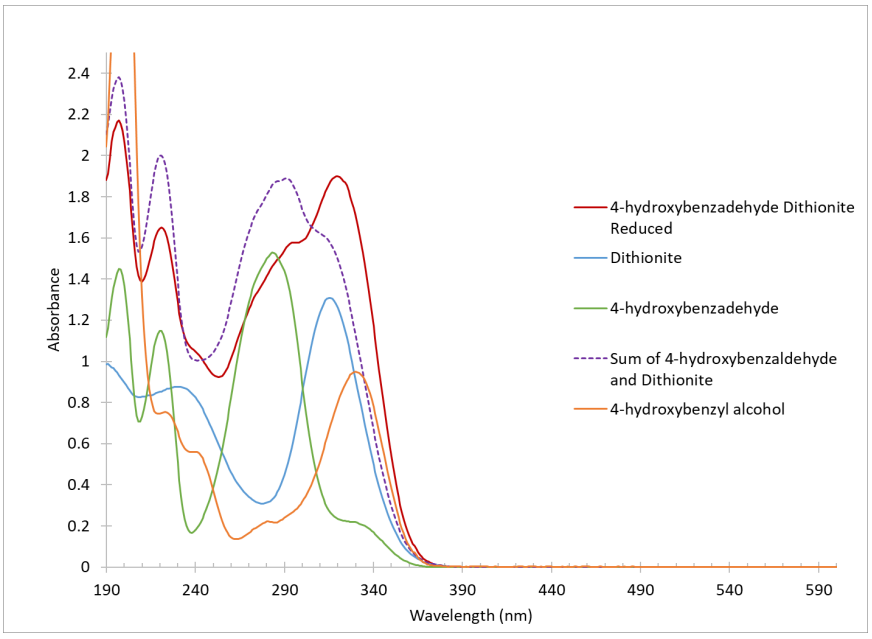


Figure 40: Absorption spectra of 4-hydroxybenzaldehyde with dithionite

Bibliography

(*1*) Cartisano, C. M., and Blough, N. V. Chromophoric Dissolved Organic Matter (CDOM) in the Open Ocean: Optical and Chemical Properties and Their Relation to CDOM Structure and Sources, Ph.D. Thesis, 2019.

(*2*) McDonnell, S. M. A Detailed Optical Analysis of Chromophoric Dissolved Organic Matter and C18 Extracted Organic Matter in the Chesapeake Bay, Ph.D. Thesis, College Park: University of Maryland, College Park, 2023.

(*3*) Hansell, D. A., and Carlson, C. A., *Biogeochemistry of Marine Dissolved Organic Matter*; Elsevier: 2014.

(*4*) Le Roux, D. Investigation of the Production and Decay Pathways of Superoxide by Chromophoric Dissolved Organic Matter, Ph.D. Thesis, College Park: University of Maryland, College Park, 2022.

(*5*) Bolan, N. S., Adriano, D. C., Kunhikrishnan, A., James, T., McDowell, R., and Senesai, N. In *Advances in Agronomy*, 2011; Vol. 110; Chapter 1.

(*6*) Twardowski, M. S., and Donaghay, P. L. (2001). Separating in situ and terrigenous sources of absorption by dissolved materials in coastal waters. *Journal of Geophysical Research: Oceans 106*, 2545–2560.

(*7*) Autochthonous and allochthonous production, 2024.

(*8*) Zhang, Y., Zhou, L., Zhou, Y., Zhang, L., Yao, X., Shi, K., Jeppesen, E., Yu, Q., and Zhu, W. Chromophoric dissolved organic matter in inland waters: Present knowledge and future challenges, 2021.

(*9*) Berg, S. M., Whiting, Q. T., Herrli, J. A., Winkels, R., Wammer, K. H., and Remucal, C. K. (2019). The Role of Dissolved Organic Matter Composition in Determining Photochemical Reactivity at the Molecular Level. *Environmental Science and Technology 53*, 11725–11734.

(*10*) Lou, T., and Xie, H. (2006). Photochemical alteration of the molecular weight of dissolved organic matter. *Chemosphere 65*, 2333–2342.

(*11*) Boyle, E. S., Guerriero, N., Thiallet, A., Del Vecchio, R., and Blough, N. V. (2009). Optical properties of humic substances and CDOM: Relation to structure. *Environmental Science and Technology 43*, 2262–2268.

(*12*) Ma, J., Del Vecchio, R., Golanoski, K. S., Boyle, E. S., and Blough, N. V. (2010). Optical properties of humic substances and CDOM: Effects of borohydride reduction. *Environmental Science and Technology 44*, 5395–5402.

(*13*) Vodacek, A., Blough, N. V., DeGrandpre, M. D., Peltzer, E. T., and Nelson, R. K. (1997). Seasonal variation of CDOM and DOC in the Middle Atlantic Bight: Terrestrial inputs and photooxidation. *Limnology and Oceanography 42*, 674–686.

(*14*) Andrew, A. A., Del Vecchio, R., Subramaniam, A., and Blough, N. V. (2013). Chromophoric dissolved organic matter (CDOM) in the Equatorial Atlantic Ocean: Optical properties and their relation to CDOM structure and source. *Marine Chemistry 148*, 33–43.

(*15*) Katahira, R., Elder, T. J., and Beckham, G. T. In *Lignin Valorization*, 2018.

(*16*) Sleighter, R. L., and Hatcher, P. G. (2008). Molecular characterization of dissolved organic matter (DOM) along a river to ocean transect of the lower Chesapeake Bay by ultrahigh resolution electrospray ionization Fourier transform ion cyclotron resonance mass spectrometry. *Marine Chemistry 110*.

(*17*) Tzortziou, M., Zeri, C., Dimitriou, E., Ding, Y., Jaffe, R., Anagnostou, E., Pitta, E., and Mentzafou, A. (2015). Colored dissolved organic matter dynamics and anthropogenic influences in a major transboundary river and its coastal wetland. *Limnology and Oceanography 60*, 1222–1240.

(*18*) IHSS What are Humic Substances?, 2024.

(*19*) Sutton, R., and Sposito, G. Molecular structure in soil humic substances: The new view, 2005.

(*20*) Leenheer, J. A., and Wilson, M. A. (1987). Presence and potential significance of aromatic-ketone groups in aquatic humic substances. *Org. Geochem 11*, 273–280.

(*21*) Peuravuori, J., and Pihlaja, K. (1997). Molecular size distribution and spectroscopic properties of aquatic humic substances. *Analytica Chimica Acta 337*, 133–149.

(*22*) Piccolo, A. (2001). The Supramolecular Structure of Humic Substances. *Soil Science 166*, 810–832.

(*23*) Del Vecchio, R., and Blough, N. V. (2004). On the origin of the optical properties of humic substances. *Environmental Science and Technology 38*, 3885–3891.

(*24*) Klapper, L., McKnight, D. M., Fulton, J. R., Blunt-Harris, E. L., Nevin, K. P., Lovley, D. R., and Hatcher, P. G. (2002). Fulvic acid oxidation state detection using fluorescence spectroscopy. *Environmental Science and Technology 36*, 3170–3175.

(*25*) Dryer, D. J., Korshin, G. V., and Fabbricino, M. (2008). In situ examination of the protonation behavior of fulvic acids using differential absorbance spectroscopy. *Environmental Science and Technology 42*, 6644–6649.

(*26*) Green, S. A., Morel, F. M., and Blough, N. V. (1992). Investigation of the Electrostatic Properties of Humic Substances by Fluorescence Quenching. *Environ. Sci. Technol. 26*, 294–302.

(*27*) Korshin, G. V., Benjamin, M. M., and Li, C. (1999). Use of Differential Spectroscopy to Evaluate the Structure and Reactivity of Humics. *Wat. Sci. Tech. 40*, 9–16.

(*28*) Ziechmann, W. (1972). Über die Elektronen-donator-und acceptor-eigenshaften von huminstoffen. *Geoderma*, 111–131.

(*29*) Swift, R. S. Macromolecular properties of soil humic substances: Fact, fiction, and opinion, 1999.

(*30*) Stenson, A. C., Landing, W. M., Marshall, A. G., and Cooper, W. T. (2002). Ionization and fragmentation of humic substances in electrospray ionization Fourier transform-ion cyclotron resonance mass spectrometry. *Analytical Chemistry 74*, 4397–4409.

(*31*) Kujawinski, E. B., Hatcher, P. G., and Freitas, M. A. (2002). High-resolution fourier transform ion cyclotron resonance mass spectrometry of humic and fulvic acids: Improvements and comparisons. *Analytical Chemistry 74*, 413–419.

(*32*) Bianca, M. Application Of Ultrahigh Resolution Mass Spectrometry and Deuterium Labeling to Determine the Contribution of Ketone/Aldehyde-Containing Species To The Composition And Optical Properties Of Dissolved Organic Matter, Ph.D. Thesis, 2020.

(*33*) IHSS Samples - A Retrospective, 2024.

(*34*) Source Materials for IHSS Samples, 2024.

(*35*) Andrew, A. A., Del Vecchio, R., Zhang, Y., Subramaniam, A., and Blough, N. V. (2016). Are Extracted Materials Truly Representative of Original Samples? Impact of C18 Extraction on CDOM Optical and Chemical Properties. *Frontiers in Chemistry 4*, 1–12.

(*36*) Twardowski, M. S., Boss, E., Sullivan, J. M., and Donaghay, P. L. In *Marine Chemistry*, 2004; Vol. 89, pp 69–88.

(*37*) Yacobi, Y. Z., Alberts, J. J., Takács, M., and Mcelvaine, M. Absorption spectroscopy of colored dissolved organic carbon in Georgia (USA) rivers: the impact of molecular size distribution, tech. rep. 1, 2003, pp 41–46.

(*38*) Lei, X., Pan, J., and Devlin, A. T. (2019). Characteristics of absorption spectra of chromophoric dissolved organic matter in the Pearl River Estuary in spring. *Remote Sensing 11*, DOI: 10.3390/rs11131533.

(*39*) Green, S. A., and Blough, N. V. (1994). Optical absorption and fluorescence properties of chromophoric dissolved organic matter in natural waters. *Limnology and Oceanography 39*, 1903–1916.

(*40*) Fellman, J. B., Hood, E., and Spencer, R. G. Fluorescence spectroscopy opens new windows into dissolved organic matter dynamics in freshwater ecosystems: A review, 2010.

(*41*) Baker, A. (2002). Fluorescence excitation-emission matrix characterization of river waters impacted by a tissue mill effluent. *Environmental Science and Technology 36*, 1377–1382.

(*42*) Boss, E. Colored Dissolved Organic Matter, 2021.

(*43*) Sharpless, C. M., and Blough, N. V. The importance of charge-transfer interactions in determining chromophoric dissolved organic matter (CDOM) optical and photochemical properties, 2014.

(*44*) Schendorf, T. M., Del Vecchio, R., Bianca, M., and Blough, N. V. (2019). Combined Effects of pH and Borohydride Reduction on Optical Properties of Humic Substances (HS): A Comparison of Optical Models. *Environmental Science and Technology 53*, 6310–6319.

(*45*) Furman, G. S., and Lonsky, W. F. (1988). Charge-transfer complexes in kraft lignin part 2: Contribution to color. *Journal of Wood Chemistry and Technology 8*, 191–208.

(*46*) Mignone, R. A., Martin, M. V., Morán Vieyra, F. E., Palazzi, V. I., Lõpez De Mishima, B., Mártire, D. O., and Borsarelli, C. D. In *Photochemistry and Photobiology*, 2012; Vol. 88, pp 792–800.

(*47*) Zepp, R. G., Schlotzhauer, P. F., and Sink, R. M. (1985). Photosensitized Transformations Involving Electronic Energy Transfer in Natural Waters: Role of Humic Substances. *Environ. Sci. Technol 19*, 74–81.

(*48*) Del Vecchio, R., Schendorf, T. M., and Blough, N. V. (2017). Contribution of Quinones and Ketones/Aldehydes to the Optical Properties of Humic Substances (HS) and Chromophoric Dissolved Organic Matter (CDOM). *Environmental Science and Technology 51*, 13624–13632.

(*49*) Tzortziou, M., Osburn, C. L., and Neale, P. J. (2007). Photobleaching of Dissolved Organic Material from a Tidal Marsh-Estuarine System of the Chesapeake Bay †. *Photochemistry and Photobiology 83*, 782–792.

(*50*) Helms, J. R., Stubbins, A., Ritchie, J. D., Minor, E. C., Kieber, D. J., and Mopper, K. (2008). Absorption spectral slopes and slope ratios as indicators of molecular weight, source, and photobleaching of chromophoric dissolved organic matter. L. *Limnol. Oceanogr. 53*, 955–969.

(*51*) Moran, M. A., Sheldon, W. M., and Zepp, R. G. (2000). Carbon loss and optical property changes during long-term photochemical and biological degradation of estuarine dissolved organic matter. *Limnology and Oceanography 45*, 1254–1264.

(*52*) Clark, C. D., De Bruyn, W., and Jones, J. G. (2014). Photoproduction of hydrogen peroxide in aqueous solution from model compounds for chromophoric dissolved organic matter (CDOM). *Marine Pollution Bulletin 79*, 54–60.

(*53*) Morris, D. P., and Hargreaves, B. R. (1997). The role of photochemical degradation of dissolved organic carbon in regulating the UV transparency of three lakes on the Pocono Plateau. *Limnology and Oceanography 42*, 239–249.

(*54*) Del Vecchio, R. D., and Blough, N. V. (2002). Photobleaching of chromophoric dissolved organic matter in natural waters: kinetics and modeling. *Marine Chemistry 78*, 231–253.

(*55*) Sharpless, C. M., Aeschbacher, M., Page, S. E., Wenk, J., Sander, M., and McNeill, K. (2014). Photooxidation-induced changes in optical, electrochemical, and photochemical properties of humic substances. *Environmental Science and Technology 48*, 2688–2696.

(*56*) Golanoski, K. S., Fang, S., Del Vecchio, R., and Blough, N. V. (2012). Investigating the mechanism of phenol photooxidation by humic substances. *Environmental Science and Technology 46*, 3912–3920.

(*57*) Gonsior, M., Peake, B. M., Cooper, W. T., Podgorski, D., D'Andrilli, J., and Cooper, W. J. (2009). Photochemically induced changes in dissolved organic matter identified by ultrahigh resolution fourier transform ion cyclotron resonance mass spectrometry. *Environmental Science and Technology 43*, 698–703.

(*58*) Wang, W., Johnson, C. G., Takeda, K., and Zafiriou, O. C. (2009). Measuring the photochemical production of carbon dioxide from marine dissolved organic matter by pool isotope exchange. *Environmental Science and Technology 43*, 8604–8609.

(*59*) Blough, N. V., and Green, S., *The Role of Nonliving Organic Matter in the Earth's Carbon Cycle*; Zepp, R. G., and Sonntag, C., Eds.; J. Wiley: Chichester, New York, 1995, pp 23–45.

(*60*) Chin, Y.-P., and Aiken, G. (1994). Molecular Weight, Polydispersity, and Spectroscopic Properties of Aquatic Humic Substances. *Environ. Sci. Technol 28*, 1853–1858.

(*61*) De Haan, H., and De Boer, T. (1987). Applicability Of Light Absorbance and Fluorescence as Measures pf Concentration and Molecular Size of Dissolved Organic Carbon in Humic Lake Tjeukemeer. *War. Res 21*, 731–734.

(*62*) Phillips, S. M., and Smith, G. D. (2015). Further evidence for charge transfer complexes in brown carbon aerosols from excitation-emission matrix fluorescence spectroscopy. *Journal of Physical Chemistry A 119*, 4545–4551.

(*63*) Coble, P. G. (2007). Marine optical biogeochemistry: The chemistry of ocean color. *Chemical Reviews 107*, 402–418.

(*64*) Bianca, M. R., Baluha, D. R., Gonsior, M., Schmitt-Kopplin, P., Del Vecchio, R., and Blough, N. V. (2020). Contribution of ketone/aldehyde-containing compounds to the composition and optical properties of Suwannee River fulvic acid revealed

by ultrahigh resolution mass spectrometry and deuterium labeling. *Analytical and Bioanalytical Chemistry 412*, 1441–1451.

(*65*) Zepp, R. G., Erickson, D. J., Paul, N. D., and Sulzberger, B. (2007). Interactive effects of solar UV radiation and climate change on biogeochemical cycling. *Photochemical and Photobiological Sciences 6*, 286–300.

(*66*) Blough, N. V., and Zepp, R. G., *Reactive Oxygen Species in Natural Waters, in Active Oxygen in Chemistry*; 0 2, 1995, pp 280–333.

(*67*) Salonen, K., and Hammar, T. (1986). On the importance of dissolved organic matter in the nutrition of zooplankton in some lake waters. *Oecologia (Berlin) 68*, 246–253.

(*68*) Waggoner, D. C., Wozniak, A. S., Cory, R. M., and Hatcher, P. G. (2017). The role of reactive oxygen species in the degradation of lignin derived dissolved organic matter. *Geochimica et Cosmochimica Acta 208*, 171–184.

(*69*) Scully, N. M., Cooper, W. J., and Tranvik, L. J. In *FEMS Microbiology Ecology*, Elsevier: 2003; Vol. 46, pp 353–357.

(*70*) Rose, A. L. (2016). The influence of reactive oxygen species on local redox conditions in oxygenated natural waters. *Frontiers in Earth Science 4*, 1–11.

(*71*) Voelker, B. M., Morel, F. M. M., and Sulzberger, B. (1997). Iron Redox Cycling in Surface Waters: Effects of Humic Substances and Light. *Environ. Sci. Technol. 31*, 1004–1011.

(*72*) Mopper, K., Zhou, X., Kieber, R. J., Kieber, D. J., Sikorski, R. J., and Jonest, R. D. (1991). Photochemical degradation of dissolved organic carbon and its impact on the oceanic carbon cycle. *Nature 353*.

(*73*) Zafiriou, O. C., Joussot-Dubien, J., Zepp, R. G., and Zika, R. G. (1984). Photochemistry of natural waters: Many compounds and environments are affected by sunlight-induced photochemistry. *Environmental Science and Technology 18*, 358–371.

(*74*) Gaberell, M., Chin, Y. P., Hug, S. J., and Sulzberger, B. (2003). Role of dissolved organic matter composition on the photoreduction of Cr(VI) to Cr(III) in the presence of iron. *Environmental Science and Technology 37*, 4403–4409.

(*75*) Garg, S., Rose, A. L., and Waite, T. D. (2007). Production of reactive oxygen species on photolysis of dilute aqueous quinone solutions. *Photochemistry and Photobiology 83*, 904–913.

(*76*) Uchimiya, M., and Stone, A. T. (2009). Reversible redox chemistry of quinones: Impact on biogeochemical cycles. *Chemosphere 77*, 451–458.

(*77*) Lee, S., Roh, Y., and Koh, D. C. (2019). Oxidation and reduction of redox-sensitive elements in the presence of humic substances in subsurface environments: A review. *Chemosphere 220*, 86–97.

(*78*) Scott, D. T., Mcknight, D. M., Blunt-Harris, E. L., Kolesar, S. E., and Lovley, D. R. (1998). Quinone moieties act as electron acceptors in the reduction of humic substances by humics-reducing microorganisms. *Environmental Science and Technology 32*, 2984–2989.

(*79*) MacAlady, D. L., and Walton-Day, K. (2009). New light on a dark subject: On the use of fluorescence data to deduce redox states of natural organic matter (NOM). *Aquatic Sciences 71*, 135–143.

(*80*) Aeschbacher, M., Vergari, D., Schwarzenbach, R. P., and Sander, M. (2011). Electrochemical analysis of proton and electron transfer equilibria of the reducible moieties in humic acids. *Environmental Science and Technology 45*, 8385–8394.

(*81*) Ratasuk, N., and Nanny, M. A. (2007). Characterization and quantification of reversible redox sites in humic substances. *Environmental Science and Technology 41*, 7844–7850.

(*82*) Bauer, M., Heitmann, T., Macalady, D. L., and Blodau, C. (2007). Electron transfer capacities and reaction kinetics of peat dissolved organic matter. *Environmental Science and Technology 41*, 139–145.

(*83*) Miller, M. P., McKnight, D. M., Cory, R. M., Williams, M. W., and Runkel, R. L. (2006). Hyporheic exchange and fulvic acid redox reactions in an alpine stream/wetland ecosystem, Colorado front range. *Environmental Science and Technology 40*, 5943–5949.

(*84*) Yang, Z., Kappler, A., and Jiang, J. (2016). Reducing capacities and distribution of redox-active functional groups in low molecular weight fractions of humic acids. *Environmental Science and Technology 50*, 12105–12113.

(*85*) Nurmi, J. T., and Tratnyek, P. G. In *Aquatic Redox Chemistry*; ACS Symposium Series: Washington, DC, 2011; Chapter 7, pp 129–151.

(*86*) Fimmen, R. L., Cory, R. M., Chin, Y. P., Trouts, T. D., and McKnight, D. M. (2007). Probing the oxidation-reduction properties of terrestrially and microbially derived dissolved organic matter¿. *Geochimica et Cosmochimica Acta 71*, 3003–3015.

(*87*) Hernández-Montoya, V., Alvarez, L. H., Montes-Morán, M. A., and Cervantes, F. J. (2012). Reduction of quinone and non-quinone redox functional groups in different humic acid samples by Geobacter sulfurreducens. *Geoderma 183-184*, 25–31.

(*88*) Aeschbacher, M., Graf, C., Schwarzenbach, R. P., and Sander, M. (2012). Antioxidant properties of humic substances. *Environmental Science and Technology 46*, 4916–4925.

(*89*) Dunnlvant, F. M., Schwarzenbach, R. P., and Macalady, D. L. (1992). Reduction of Substituted Nitrobenzenes in Aqueous Solutions Containing Natural Organic Matter. *Environ. Sci. Technol. 26*, 2133–2141.

(*90*) Jiang, Y., Xi, B., Li, R., Li, M., Xu, Z., Yang, Y., and Gao, S. (2019). Advances in Fe(III) bioreduction and its application prospect for groundwater remediation: A review. *Frontiers of Environmental Science and Engineering 13*, DOI: 10.1007/s11783-019-1173-9.

(*91*) Blough, N. V., and Del Vecchio, R. (2011). Comment on "hILIC-NMR: Toward the identification of individual molecular components in dissolved organic matter". *Environmental Science and Technology 45*, 5908–5909.

(*92*) Maurer, F., Christl, I., and Kretzschmar, R. (2010). Reduction and reoxidation of humic acid: Influence on spectroscopic properties and proton binding. *Environmental Science and Technology 44*, 5787–5792.

(*93*) Mladenov, N., Zheng, Y., Miller, M. P., Nemergut, D. R., Legg, T., Simone, B., Hageman, C., Rahman, M. M., Ahmed, K. M., and Mcknight, D. M. (2010). Dissolved organic matter sources and consequences for iron and arsenic mobilization in Bangladesh aquifers. *Environmental Science and Technology 44*, 123–128.

(*94*) Schendorf, T. M., Del Vecchio, R., Koech, K., and Blough, N. V. (2016). A standard protocol for NaBH4 reduction of CDOM and HS. *Limnology and Oceanography: Methods 14*, 414–423.

(*95*) de Vries, J. G., and Kellogg, R. M. (1980). Reduction of Aldehydes and Ketones by Sodium Dithionite. *Journal of Organic Chemistry 45*, 4126–4129.

(*96*) Dhillon, R. S., Singh, R. P., and Kaur, D. (1995). Selective 1,4-reduction of conjugated aldehydes and ketones in the presence of unconjugated aldehydes and ketones with sodium dithionite. *Tetrahedron Letters 36*, 1107–1108.

(*97*) Gassman, P. G., Rasmy, O. M., Murdock, T. O., and Saito, K. (1981). Mechanism of Sodium Dithionite Reduction of Aldehydes and Ketones. *Journal of Organic Chemistry 46*, 5457–5458.

(*98*) Camps, F., Coll, J., and Guitart, J. (1986). Regiospecific reduction of unsaturatied conjugated ketones with sodium dithionite under phase transfer catalysis. *Tetrahedron 42*, 4603–4609.

(*99*) Neyt, N. C., and Riley, D. L. (2018). Mild and selective reduction of aldehydes utilising sodium dithionite under flow conditions. *Beilstein Journal of Organic Chemistry 14*, 1529–1536.

(*100*) Dixon, M. (1971). The acceptor specificity of flavins and flavoproteins. III. Flavoproteins. *BBA - Bioenergetics 226*, 269–284.

(*101*) Aeschbacher, M., Sander, M., and Schwarzenbach, R. P. (2010). Novel electrochemical approach to assess the redox properties of humic substances. *Environmental Science and Technology 44*, 87–93.

(*102*) Uchimiya, M., and Stone, A. T. (2010). Reduction of substituted p-benzoquinones by FeII near neutral pH. *Aquatic Geochemistry 16*, 173–188.

(*103*) McKay, G. (2021). Autoxidized Hydroquinone Mimics the Optical Properties of Chromophoric Dissolved Organic Matter. *Environmental Science and Technology Letters 8*, 825–831.

(*104*) Tarakhno, Z. N., Pivnenko, N. S., Oleinik, L. S., Troyan, V. N., and Lavrushin, V. I. (1989). Spectral characteristics and structure of anthrones resulting from reduction of 9,10-anthraquinones with sodium borohydride. *Visnik Kharkivs'kogo Universitetu 340*, 77–80.

(*105*) Thomson, R., *Naturally Occurring Quinones*, 2nd ed.; Academic Press: 1971.

(*106*) Murillo-Gelvez, J., Hickey, K. P., Di Toro, D. M., Allen, H. E., Carbonaro, R. F., and Chiu, P. C. (2019). Experimental Validation of Hydrogen Atom Transfer Gibbs Free Energy as a Predictor of Nitroaromatic Reduction Rate Constants. *Environmental Science and Technology 53*, 5816–5827.

(*107*) Tro, N. J., *Chemistry Structure and Properties*, 2nd ed.; Pearson Education: 2018.

(*108*) LuValle, J. E. (1952). The Reaction of Quinone and Sulfite. I. Intermediates. *Journal of the American Chemical Society 74*, 2970–2977.

(*109*) Arai, G., and Suzuki, A. (1983). The Rate of the Addition Reactions between Quinones with Sodium Sulfite. *Nippon Kagaku Kaishi*, 465–469.

(*110*) Youngblood, M. P. (1986). Kinetics and Mechanism of the Addition of Sulfite to p -Benzoquinone. *Journal of Organic Chemistry 51*, 1981–1985.

(*111*) Burillo, J. C., Rodríguez, F., Adrados, L. F., and Tijero, J. F. (1988). Kinetics of Anthraquinone Reduction with Sodium Dithionite in Alkaline Medium. *AlChE 34*, 865–869.

(*112*) Nikolantonaki, M., and Waterhouse, A. L. (2012). A method to quantify quinone reaction rates with wine relevant nucleophiles: A key to the understanding of oxidative loss of varietal thiols. *Journal of Agricultural and Food Chemistry 60*, 8484–8491.

(*113*) Futami, A., and Hauska, N. (1979). Vectorial Redox Reactions of Physiological Quinones II. A Study of Transient Semiquinone Formation. *Biochimica et Biophysica Acta 547*, 597–608.

(*114*) De Barros, S. K., Stilson, A., Cardoso, V., and De Lima, C. G. (1994). Fluorimetric studies of some quinones and quinonoid compounds after reduction reaction. *Analytics Chimica Acta 289*, 273–290.

(*115*) Van Damme, J. G., and De Néve, R. E. (1979). Fluorescence Assay of Hydroxynaphthoquinones. *Journal of Pharmaceutical Sciences 68*, 16–19.

(*116*) Hosoya, S. (1976). Bleaching of high-yield pulp. Reactions of quinones and quinone polymers with some oxidizing and reducing reagents. *Mokuzai Gakkaishi 22*, 314–319.

(*117*) Gaudiano, G., Frigerio, M., Sangsurasak, C., Bravo, P., and Koch, T. H. (1992). Reduction of Daunomycin and 11-Deoxydaunomycin with Sodium Dithionite in DMSO. Formation of Quinone Methide Sulfite Adducts and the First NMR Characterization of an Anthracycline Quinone Methide. *Journal of the American Chemical Society 114*, 5546–5553.

(*118*) Danilewicz, J. C. (2016). Reaction of oxygen and sulfite in wine. *American Journal of Enology and Viticulture 67*, 13–17.

(*119*) Hosoya, S. (1980). Reactions of Lignin During High-Yield Pulp Bleaching. *Japan Tappi Journal 34*, 276–282.

(*120*) Moore, R. M. (2008). A photochemical source of methyl chloride in saline waters. *Environmental Science and Technology 42*, 1933–1937.

(*121*) Gieseking, J. E., *Soil Components*, 1975; Vol. 1.

(*122*) Jasińska, A., Burska, D., and Bolałek, J. (2012). Sulfur in the marine environment. *Oceanological and Hydrobiological Studies 41*, 72–82.

(*123*) Cory, R. M., and McKnight, D. M. (2005). Fluorescence spectroscopy reveals ubiquitous presence of oxidized and reduced quinones in dissolved organic matter. *Environmental Science and Technology 39*, 8142–8149.

(*124*) Ariese, F., Van Assema, S., Gooijer, C., Bruccoleri, A. G., and Langford, C. H. (2004). Comparison of Laurentian Fulvic Acid luminescence with that of the hydroquinone/quinone model system: Evidence from low temperature fluorescence studies and EPR spectroscopy. *Aquatic Sciences 66*, 86–94.

(*125*) McKay, G., and Leresche, F. (2022). Impacts of ozone oxidation and borohydride reduction on the optical properties of humic substance isolates. *Aquatic Sciences 84*, DOI: 10.1007/s00027-022-00892-1.

(*126*) Ball, D. W., *Field Guide to Spectroscopy*; SPIE Press: Bellingham, WA, 2006.

(*127*) Gan, D., Jia, M., Vaughan, P. P., Falvey, D. E., and Blough, N. V. (2008). Aqueous photochemistry of methyl-benzoquinone. *Journal of Physical Chemistry A 112*, 2803–2812.

(*128*) Gu, J., Yang, L., Ma, J., Jiang, J., Yang, J., Zhang, J., Chi, H., Song, Y., Sun, S., and Tian, W. Q. (2017). Hydrated electron (eaq) generation from p-benzoquinone/UV: Combined experimental and theoretical study. *Applied Catalysis B: Environmental 212*, 150–158.

(*129*) Zheng, J. W., and Lafontant-Joseph, O. IUPAC Digitized pKa Dataset, v2.1, 2024.